HIGH TEMPERATURE DEGRADATION OF GRAPHITE/EPOXY COMPOSITES

by

Lauren K. Crews

B.S., Aerospace Engineering, University of Maryland at College Park (1992)

S.M., Aeronautics and Astronautics, Massachusetts Institute of Technology (1995)

SUBMITTED TO THE DEPARTMENT OF AERONAUTICS AND ASTRONAUTICS IN PARTIAL FULFILLMENT OF THE REQUIREMENTS FOR THE DEGREE OF

DOCTOR OF PHILOSOPHY
AT THE
MASSACHUSETTS INSTITUTE OF TECHNOLOGY

AUGUST 1998
[September 1998]

Signature of Author _____
Department of Aeronautics and Astronautics
August 14, 1998

Certified by _____
Hugh L. McManus
Associate Professor of Aeronautics and Astronautics
Chairman, Thesis Committee

Certified by _____
Paul A. Lagace
MacVicar Faculty Fellow, Professor of Aeronautics and Astronautics
Thesis Committee

Certified by _____
S. Mark Spearing
Boeing Assistant Professor of Aeronautics and Astronautics
Thesis Committee

Accepted by _____
Jaime Peraire
Associate Professor of Aeronautics and Astronautics
Chairman, Department Graduate Committee

HIGH TEMPERATURE DEGRADATION OF GRAPHITE/EPOXY

by

Lauren K. Crews

Submitted to the Department of Aeronautics and Astronautics
on August 14, 1998 in partial fulfillment of the requirements
for the degree of Doctor of Philosophy

ABSTRACT

The problem of determining the response of a laminated composite plate exposed to a high temperature environment while mechanically loaded is approached by identifying the underlying mechanisms and addressing them separately. The approach is general, but the work focuses on the response of AS4/3501-6 graphite/epoxy composites. The mechanisms studied and modeled in this work are thermal response, degradation chemistry, and changes in mechanical material properties. The thermal response of an orthotropic plate exposed to convective heating is modeled using generalized heat transfer theory. The key parameters identified as controlling the thermal response include well-known parameters from heat transfer literature and a new parameter called the geometry-orthotropy parameter. From these parameters, the accuracy with which a multi-dimensional temperature distribution may be approximated using a one-dimensional thermal model is quantified. The degradation chemistry of 3501-6 epoxy is studied through thermogravimetric analysis (TGA) experiments conducted in an inert atmosphere. A model of degradation based on a single Arrhenius rate equation is developed. Reaction constants for the degradation model are determined empirically and the validity of the model is verified through separate TGA experiments. A novel method for assessing the degradation state of a sample with an unknown thermal history is proposed. Analyses employing the method achieve estimates of the degradation state within 0.3 to 28% of the actual values. Changes in mechanical material properties are quantified by measuring the modulus and tensile strength of unidirectional $[0]_4$ and $[90]_{12}$ coupons exposed to temperatures as high as 400°C in a furnace. Some coupons are loaded to failure while exposed to the test temperature, others are first cooled to room temperature, allowing at-temperature and residual properties to be directly compared. Transverse properties are very sensitive to temperature around the glass transition temperature, but may recover when the coupon cools. Transverse properties are also very sensitive to small values (~0.03) of degradation state. Longitudinal properties are less sensitive to these variables. Temperature and degradation state are identified as appropriate metrics for quantifying changes in material properties. Models of the measured properties as functions of these variables are developed. A methodology for integrating models of the various mechanisms underlying structural response is presented. The thermal response model, degradation chemistry model, and material property models developed in this work are integrated with a thermomechanical response model based on classical laminated plate theory and implemented in a one-dimensional predictive code. This work establishes a foundation upon which a complete mechanism-based integrated model of the response of mechanically-loaded composites exposed to high temperatures may be developed. Specific recommendations for further work are provided.

Thesis supervisor: Prof. Hugh L. McManus

ACKNOWLEDGMENTS

Wow... I have seen the light at the end of the tunnel and it's WONDERFUL! I haven't stopped grinning since the end of my defense. I'd like to try to thank all the people who have made this endeavor possible, and helped me see it through.

I'd first like to thank my thesis committee. I had the great fortune to have a committee of colleagues who were interested in and knowledgeable about the work I wanted to do, as well as concerned about me and my development as a researcher. Each brought something different to the table, and through clear exchanges of ideas we figured out together how the project should go. In particular, I'd like to thank my advisor of six years, Hugh McManus, for sparking my interest in the environmental behavior of materials, for giving enough guidance that I could get started and enough freedom that I could test my wings, and (most especially) for seeing my potential and having the patience to help me reach it. My thanks to Paul Lagace, for keeping the TELAC standard so high. Earning his approval has always been an achievement to be proud of, and he will always have my deepest respect. I'm very grateful for his help in the editing of this thesis. I learned a lot about technical writing, and appreciated his interest and time. Thanks also to Mark Spearing, for his example of scholarship, diplomacy, professionalism, and for his friendship.

I'd like to thank Deb Bowser, most especially for her friendship, and also for more than once helping me achieve the impossible – getting all my committee members in the same place at the same time. Thanks also to Ping Lee, who helped with the

financial details (and would scold me but not wring my neck when I forgot another receipt), and to John Kane and Al Supple, who kept the lab going and offered guidance and expertise.

Several undergraduates contributed their time and talents in the laboratory and made the experiments possible. Thanks go to my UROPers, Cheryl Howell, Mario Gonzalez, and Rasa Biciunas, for suffering with me as we figured out how all that equipment down in the lab was supposed to work, and for performing an occasional victory dance with me when it actually did. Thanks also to Victor Aviles, for performing many of the TGA experiments, for being my guinea pig as I learned how to be a research advisor, and for being a good friend. I'm so glad you got rid of the earring.

I'd like to thank some of the people who helped me make it past the difficult point when I had slogged half-way through and was running out of steam. To Paula Peche, who always kept her door open, listened to the problem-of-the-day, and encouraged me. To Prof. Richard McCuen at the University of Maryland, who helped convince me to stay the course, and to Kristie Bosko, who, in her wisdom, said that being a mom with a PhD will be a very cool thing.

I'd also like to thank my friends here at MIT who have made the time bearable, and occasionally even fun. Thanks to all my fellow graduate students in TELAC, especially my "pace car," Brian Wardle, fellow baseball fan Dennis Burianek, math whiz Chris Dunn (who has generously hunted down more than one of my notorious math errors), class clown Steve Czepiela, and all-around good guy Tom Reynolds. Good luck to all of you (especially Chris, who needs it.) Thanks to the students at Baker House,

who gave me something to look forward to when I went home in the evening, and to my many far-flung friends.

My family has supported me throughout. Thanks to Mom for the brains and Dad for the charm and good looks (oops – did I get that backwards?) and all the love that have helped me succeed. Thanks to my brother Bobby for being a fan, Steven, who remembered to call on my birthday(!), and to Grandma and Grandpa. Thanks to my second family, Mom and Dad Crews, for their love and encouragement, and for making me probably the only MIT grad to receive a cow as a graduation gift. Thanks also to Laura, Nathan, and Martha. The biggest thanks of all goes to my husband and best friend, Dan Crews, for supporting and encouraging me throughout the whole process and helping me achieve this dream. I couldn't have done it without you, and I love you so much!! This work is dedicated to you.

Finally, I offer my thanks to God, for granting me the courage to start this work, the strength to see it through, and just enough wisdom to finish it. I am truly blessed.

For Dan, with love.

FOREWORD

This research was completed at the Technology Laboratory for Advanced Composites at the Massachusetts Institute for Technology. The work was funded by the National Science Foundation under NSF Grant 9257612-CMS. This work made use of MRSEC Shared Facilities supported by the National Science Foundation under Award Number DMR-9400334.

TABLE OF CONTENTS

TABLE OF FIGURES

TABLE OF TABLES

NOMENCLATURE

A	area of heat transfer
$\mathbf{A}$	matrix of extensional stiffnesses
$\mathbf{B}$	matrix of extension-bending coupling stiffnesses
Bi_i	Biot number in the i-direction
c	specific heat
$c_{effective}$	effective specific heat
c_o	baseline specific heat
$\mathbf{D}$	matrix of bending stiffnesses
E	activation energy
E_L	longitudinal ply modulus
E_T	transverse ply modulus
Fo_i	Fourier number in the i-direction
G_{LT}	shear modulus of ply
h	thickness of tensile coupon
h_{ci}	convection heat transfer coefficient in the i-direction
H_{latent}	latent heat of reaction
Int	axis intercept of linear plot
k	reaction constant
k_i	thermal conductivity in the i-direction
k_{yo}	through-thickness thermal conductivity of virgin material
$knockdown$	thermal conductivity knockdown factor
L_i	reference length in the i-direction
$\mathcal{L}ij$	geometry-orthotropy parameter relating the i- and j-directions
m	mass
m_f	mass of nonreactive material
m_o	initial mass
M	number of nodes in the x-direction
M	moisture content
$\mathbf{M}$	vector of resultant moments
$\mathbf{M}^{\mathbf{C}}$	vector of degradation-induced resultant moments

$\mathbf{M}^{\mathbf{H}}$	vector of moisture-induced resultant moments
$\mathbf{M}^{\mathbf{mech}}$	vector of mechanically applied resultant moments
$\mathbf{N}^{\mathbf{M}}$	vector of pressure-induced resultant moments
$\mathbf{M}^{\mathbf{T}}$	vector of thermally-induced resultant moments
n	reaction order
N	number of nodes in the y-direction
$\mathbf{N}$	vector of resultant forces
$\mathbf{N}^{\mathbf{C}}$	vector of degradation-induced resultant forces
$\mathbf{N}^{\mathbf{H}}$	vector of moisture-induced resultant forces
$\mathbf{N}^{\mathbf{mech}}$	vector of mechanically applied resultant forces
$\mathbf{N}^{\mathbf{P}}$	vector of pressure-induced resultant forces
$\mathbf{N}^{\mathbf{T}}$	vector of thermally-induced resultant forces
P	pressure
P_{ult}	ultimate tensile load
q	rate of heat flow
q_{ci}	rate of heat flow via convection in i-direction
$\dot{q}_G$	rate of heat generation per unit volume
q_k	rate of heat flow via conduction
q_{ki}	rate of heat flow via conduction in the i-direction
Q	heating rate
$\mathbf{Q}$	matrix of reduced stiffnesses in ply coordinate system
$\overline{\mathbf{Q}}$	matrix of reduced stiffness in structural coordinate system
R	universal gas constant
R_{ij}	failure ratio in ij-direction
S	shear strength
t	time
t_i	time at time step i
t_{ref}	reference time
T	temperature
$\mathbf{T}$	transformation matrix

T_∞	ambient temperature
T_f	flame temperature
T_g	glass transition temperature
T_{max}	temperature at which maximum degradation rate occurs
T_o	initial temperature
$T_{i,j,m}$	temperature at node *i,j* at time *m*
v_f	fiber volume fraction
w	width of tensile coupon
X^c	longitudinal compressive strength
X^t	longitudinal tensile strength
y_p	mass fraction
Y^c	transverse compressive strength
Y^t	transverse tensile strength
z_i^+	vertical location of top of node *i*
z_i^-	vertical location of bottom of node *i*

α	degradation state
$\alpha_{i,j,m}$	degradation state at node *i,j* at time *m*
$\boldsymbol{\alpha}$	vector of ply thermal expansion coefficients
$\boldsymbol{\beta}$	vector of ply moisture expansion coefficients
$\boldsymbol{\varepsilon}$	vector of strains in ply coordinate system
$\boldsymbol{\varepsilon}^o$	vector of laminate middle surface strains
ζ	dimensionless *z*-direction length
η	dimensionless *y*-direction length
θ	ply angle
θ_i	angle of ply *i*
Θ	dimensionless temperature
$\boldsymbol{\kappa}$	vector of laminate curvatures
$\boldsymbol{\lambda}$	vector of ply pressure expansion coefficients
ν_{LT}	major Poisson's ratio

ν_{TL}	minor Poisson's ratio
ξ	dimensionless x-direction length
ρ	density
ρ_f	fiber density
ρ_m	matrix density
$\boldsymbol{\sigma}$	vector of stresses in ply coordinate system
σ_{ult}	strength of coupon
τ	dimensionless time
$\boldsymbol{\chi}$	vector of ply char expansion coefficients

CHAPTER 1

INTRODUCTION

Advanced composite materials are used in a variety of areas, particularly aerospace and marine applications. Materials such as graphite/epoxy have a high specific strength and stiffness, good corrosion and fatigue performance, and can be infinitely tailored to meet design requirements. For these reasons, composite materials are increasingly being used in structural applications.

In service, however, structures made of composite materials may experience fires [1], repair mishaps [2], ordnance misfires, engine exhaust impingement [3], and other exposures to temperatures above their recommended service temperature. These events, while they generally do not affect graphite fibers, can cause degradation* of polymeric matrix materials (such as epoxy) [4] and organic fibers (such as Kevlar) [5], resulting in diminished material properties and a loss of structural performance. [6]

The high temperature degradation of composite laminates raises concern about both the transient structural response to heat and the integrity of the laminate after the heat source is removed. For example, it may be important to estimate how long a load-bearing structure will survive in a fire before failing. If the structure survives the incident, accurate assessment of the extent of degradation and its effects on future performance is key.

---

* For definitions of terminology, see Glossary.

Degradation of composite materials such as graphite/epoxy occurs via a series of physical mechanisms. When a graphite/epoxy structure is exposed to a high temperature environment, heat enters through the surface and diffuses through the structure. The heat can cause the epoxy matrix to degrade. Elevated temperature and matrix degradation can induce changes in material properties, expansion or contraction of the laminate, and other effects that alter the stress/strain response of the laminate and can result in failure of the structure. The objectives of this work are to develop an understanding of the basic mechanisms behind the high temperature response of composites and to build a model of the degradation and its effects on mechanical response, thus providing the foundation for a complete mechanism-based model for analyzing the structural response of composite laminates exposed to high temperature environments.

To achieve these objectives, mechanisms involved in the high-temperature response of graphite/epoxy composites, including heat transfer, matrix degradation, and changes in material properties, are studied. Links between the different mechanisms are also considered. Previous work is reviewed to evaluate the existing knowledge, and areas requiring further study are identified. Experiments designed to address some of these needs are carried out. The test program includes thermogravimetric analysis tests to characterize the degradation behavior of epoxy resin, and elevated temperature tensile tests to quantify the mechanical properties of graphite/epoxy composites exposed to high temperatures. Models of the mechanisms are developed and then integrated into a computational tool for analyzing the temperature distribution, extent of degradation, and stress/strain response of graphite/epoxy laminates exposed to high temperature environments.

In Chapter 2, previous work relevant to the high temperature degradation of graphite/epoxy and its effects on structural performance is reviewed. The current level of understanding of the response of composite laminates to high temperature environments and the current predictive capability are summarized. Also, areas requiring further study are identified. Chapter 3 provides a concise statement of the problem addressed in this thesis and describes the solution approach. The approach combines experimental studies and analytical modeling. This approach was designed to complement the previous work and address some of the needs identified. The mathematical development of the analytical models is given in Chapter 4. Models of the individual mechanisms are described separately, followed by a discussion of the development of integrated models. Experimental procedures are detailed in Chapter 5. Experimental and analytical results are presented in Chapter 6. An integrated model that combines the models developed in this work and implements them in a computer code is presented in Chapter 7. Chapter 8 is a discussion of the significance of the results. Finally, conclusions and recommendations for future work are presented in Chapter 9.

CHAPTER 2

BACKGROUND

The work done to date toward developing an understanding of the effects of high-temperature environments on composite laminates is summarized in this chapter. A wide range of subjects is covered in this review, reflecting the broad scope of the topic. As such, it is not intended to be an exhaustive discussion of all relevant literature, but to summarize the knowledge on which the current investigation is built, highlighting major conclusions and areas requiring further research.

The review is divided into six sections. In the first section, the thermal response of graphite/epoxy laminates exposed to high temperature environments is discussed, and models of the response are reviewed. In section two, the chemistry behind the thermal degradation of epoxy is discussed briefly and degradation models are reviewed. Data on the changes in mechanical material properties caused by high temperature exposure, and models of the material property response, are reviewed in section three. Integrated approaches for modeling the thermal, degradation, and material property responses together with mechanics and failure models are discussed in section four. Section five includes a brief review of inspection techniques used to detect thermal degradation in composites. Each of these sections begins with an overview of the physical mechanisms that govern the response, followed by a description of previous work on the subject and a summary of the accomplishments and remaining needs. In section six, areas requiring further study are summarized.

2.1 THERMAL RESPONSE

When graphite/epoxy laminates are exposed to high temperature environments, heat transfer can occur via conduction, convection, and radiation. Conduction occurs inside the laminate, while convection and radiation couple the laminate with the environment. Boundary conditions can be specified as a surface temperature (K), heat flux (W/m^2), or heat transfer coefficient (W/m^2K).

The thermal response of the laminate, i.e. the temperature distribution inside, is complicated by the anisotropy of graphite/epoxy and by variable material properties. Graphite/epoxy is a composite composed of two dissimilar materials, and the material properties of the composite depend on both the properties of the constituents and the architecture in which the two constituents are combined. One material property to consider is thermal conductivity. Graphite has a much higher thermal conductivity than epoxy. [7] The thermal conductivity of a graphite/epoxy ply with continuous fibers embedded in epoxy matrix is much higher in the direction parallel to the fibers than in the directions normal to the fibers [8]. Furthermore, material properties, including thermal conductivity, vary as the epoxy matrix degrades [9]. These complications must be considered when modeling the thermal response.

The thermal response models described in the literature are all based on the fundamental principles of heat transfer. Fourier's law of heat conduction, Newton's law of heat convection, and the Stefan-Boltzmann law of radiation describe heat flows resulting from the various modes of heat transfer. The first law of thermodynamics enforces the condition that energy can neither be created nor destroyed. The resulting

transient heat transfer equations can then be solved to determine the internal temperature of the laminate.

Finite difference formulations are often used to solve for the temperature distribution. The volume of interest is divided into smaller volumes of finite size, and the heat flow into and out of these smaller volumes and the resulting temperatures inside each volume are calculated. One- [10,11,12,13], two- [14], and three-dimensional [15] finite difference solutions for heated graphite/epoxy laminates have been developed. Some of these models account for additional features, such as the ablation of the graphite fibers and resulting surface recession at extreme (>3000°C) temperatures.

Griffis, Masumura, et al. [10] and Griffis, Nemes, et al. [14] found good agreement between experimental data and their one- and two-dimensional thermal models, respectively. Both groups of authors modeled a graphite/epoxy coupon heated in the center by a laser beam. Milke and Vizzini [15] noted, however, that a fully three-dimensional analysis would be necessary to determine both in-plane and through-thickness temperature profiles in a composite with an arbitrary heat flux. They modeled a graphite/epoxy coupon suspended in front of a propane-heated radiant panel. The coupon modeled by Milke and Vizzini had the same thickness (~3 mm) as the coupons modeled by Griffis, Masumura, et al. and Griffis, Nemes, et al., but had a larger area. The radiant panel heat source used by Milke and Vizzini produced a heat flux that varied across the surface by as much as 20%; the laser beams used by the other authors had a much more uniform output.

All of the thermal response models include variable material properties. Both changes in temperature and the thermal degradation of the matrix that may result can

cause changes in material properties. For example, temperature-dependent data from Menousik and Monin [9] showed that through-thickness thermal conductivity decreases linearly from 1.4 W/m·K to 0.2 W/m·K between 343°C and 510°C. These temperatures were assumed to correspond with the onset and completion of matrix degradation. Fanucci [16] also showed a linear decrease in this same temperature range. This data is compiled with other experimentally measured values in Table 2.1.

The data in Table 2.1 shows that there is disagreement in the literature over the conductivity of non-degraded epoxy and over the factor by which the conductivity decreases when the epoxy degrades. Most of the authors indicate a through-thickness thermal conductivity of approximately 0.7 W/m·K, but the cited values differ by a factor of 2.5. The values may reflect different types of graphite/epoxy and different measurement techniques. The particular graphite/epoxy used in the current investigation, AS4/3501-6, was studied extensively by Farmer and Covert [17], who measured conductivity values ranging from 0.62-0.77 W/m·K. This latter data is considered the most reliable for describing the material of interest in this investigation.

Not all authors modeled thermal conductivity with a linear temperature dependence. Henderson and Wiecek [12] modeled the thermal conductivity of glass/phenolic as a cubic function of temperature, and McManus [13] modeled the thermal conductivity of carbon/phenolic as varying linearly with both temperature and degradation.

Changes in density were modeled either as linear functions of temperature [10,14,15] or as linear functions of degradation [11,12,13]. In all cases, the density of non-degraded graphite/epoxy was 1.5-1.6 g/cm^3.

Table 2.1 Through-thickness thermal conductivity of graphite/epoxy

Authors	Non-degraded (W/m·K)	Fully degraded (W/m·K)
Menousik and Monin (1979)[9]	1.4	0.2
Fanucci (1987) [16]	0.75	0.173
Han, et al. (1986) [8]	0.77	---
Sigur (1986) [18]	0.56	---
Berlin, et al. (1992)[19]	0.75	---
Scott and Beck (1992)[20]	0.7-0.9	---
Farmer and Covert (1994)[17]	0.62-0.77	---

In some cases, changes in specific heat were modeled. Most authors cited specific heat values that increased with temperature. Typical values for graphite/epoxy ranged between 1.2 and 1.8 J/g·K at room temperature and increased to 1.8-2.1 J/g·K at 340°C [9,16].

Furthermore, as the matrix undergoes degradative reactions, it absorbs additional heat (i.e. the latent heat of reaction.) To account for this, some authors included in their models large spikes in specific heat in the temperature range over which degradation was assumed to occur [10,14,15]. Others used more sophisticated degradation models and accounted for the additional heat absorbed at each step by multiplying the rate of degradation by the latent heat [11,12,13]. Values cited for the latent heat of graphite/epoxy have a range of 996-1675 J/g [9,11]. Degradation models are discussed at length in the next section.

In summary, the thermal response of heated graphite/epoxy laminates can be determined from the classic equations of heat transfer. Finite difference approaches incorporating variable material properties are a popular method for solving for the internal temperature distribution.

One-, two-, and three-dimensional finite difference solutions have been developed by various authors. While a fully three-dimensional solution may be necessary for determining the complete temperature distribution in a laminate exposed to an arbitrary thermal environment, simpler models should suffice in some cases. One-dimensional thermal models are desirable because they are less computationally intensive, and may enable the use of one-dimensional models for the determination of effects that depend on temperature, such as mechanical behavior. The conditions under which one-dimensional

models provide good estimates of the through-thickness temperature distribution in heated graphite/epoxy laminates should be investigated.

Material properties that vary as the epoxy matrix degrades are included in all of the models reviewed. However, the values of some of these properties are disputed. It should be kept in mind that the accuracy of models of the thermal response will be limited by the accuracy of the material properties.

2.2 EPOXY DEGRADATION CHEMISTRY

The composite material under consideration in this investigation is AS4/3501-6, manufactured by Hercules (now Hexcel) and consisting of AS4 graphite fibers and 3501-6 epoxy matrix. 3501-6 is a tetraglycidyl-4-4'-diaminodiphenylmethane epoxy cured with diaminodiphenylsulfone (TGDDM-DDS) at a processing temperature of 177°C [21]. The three principal cure reactions are described in detail by Morgan and Mones [21]. The polymer crosslinks as it cures, creating a network of intertwined polymer chains linked together. The crosslink density increases as the cure advances. The crosslinking greatly reduces the ability of the polymer to flow, making the fully cured epoxy dimensionally stable and elastic, and causes stiffening of the polymer chains, increasing the tensile, compressive, and flexural strength of the epoxy while reducing the maximum tensile elongation. Due to the complexity of the crosslinking process, it is impractical to establish a definitive structure for the cured polymer [22].

When the cured epoxy is heated, it will undergo a reversible transition from its stiff "glass-like" behavior to rubber-like behavior. The temperature at which this transition occurs is termed the glass transition temperature, T_g. The transition is

accompanied by long-range molecular motion, increased rotational freedom, and a resultant decrease in modulus [22]. It can be difficult to identify the glass transition temperature of epoxy because it increases with crosslink density, can change with aging and moisture content, and depends on both the measurement method and criterion employed. Morgan and Mones [23] cite 225-250°C (437-482°F) as the T_g range for fully cured TGDDM-DDS epoxy, while MIL-HDBK-17 [24] cites 199°C (390°F) as the T_g for AS4/3501-6 graphite epoxy under ambient conditions.

At slightly higher temperatures, permanent degradation of the epoxy polymer begins to occur, yielding gaseous pyrolysis products and solid carbonaceous residue. Thermal degradation may be brought about by either a breaking (scission) of the main polymer chains or by reactions (usually bond rearrangements) which modify the chain substituents but leave the chain itself intact [25]. Bishop and Smith [26] note that in the early stages of degradation, "the predominant breakdown mechanisms are... reactions leading to the formation of hydrogen, water, and methane. At higher temperatures the polymer chain breaks down." Specific decomposition mechanisms have been suggested by a number of researchers, including Bishop and Smith [26] and Lee [27].

The thermal stability of epoxy, i.e. its resistance to degradation, is affected by a number of variables, including the structure of the particular resin, the type of curing agent, the chlorine content, and the cure schedule [27]. Thermal stability also increases with increasing crosslink density [28]. One measure of the thermal stability of a polymer is the activation energy, E_a, of the degradation. Published values for the activation energy of epoxy range from 126 kJ/mol (30.2 kcal/mol) [11] to 213 kJ/mol (51 kcal/mol) [4].

While the epoxy matrix can be severely degraded by exposure to elevated temperatures, the graphite fibers are much more durable. De Pruneda and Morgan [29] found that the strength and structural integrity of graphite fibers with low nitrogen content, such as AS4, were unaffected when the fibers were exposed at 2500°C in an inert atmosphere for up to 30 minutes. In an inert atmosphere at ambient pressure, the fibers will sublimate around 3400°C [25].

Some models of the degradation of epoxy make the crude assumption that degradation is strictly a function of temperature. For example, degradation models based on temperature-dependent specific heat data [10,14,15] implicitly assume that degradation does not occur at temperatures below 343°C and that the matrix is fully degraded at temperatures above 510°C. The temperature-dependent specific heat data used in these models, taken from Menousik and Monin [9], is shown in Figure 2.1. The plot shows a large increase in specific heat between 343°C and 510°C, representing the additional heat absorbed by the composite as the matrix degrades, i.e. the latent heat of reaction.

This temperature-dependent degradation model may be useful when considering very severe environments in which the material becomes very hot and degradative reactions occur very quickly. For lower temperature regimes and slower heating rates, however, a more sophisticated model of the degradation is necessary. One such model is the Arrhenius reaction model employed by Pering, et al. [11], Henderson and Wiecek [12], and McManus [13]. The Arrhenius model determines degradation as a function of both temperature and time, hence different heating rates can be accounted for. Pering, et al. [11] used a single Arrhenius reaction to model the degradation of epoxy, but did not

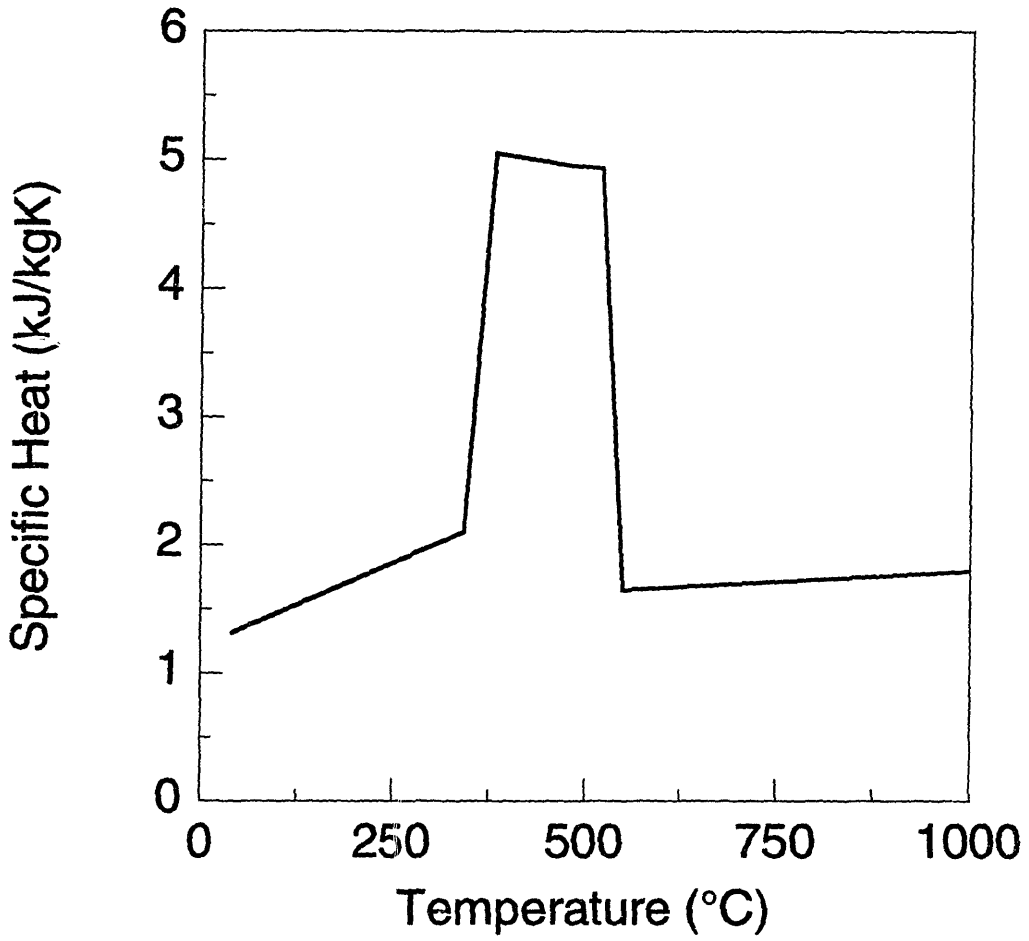

Figure 2.1 Specific heat of graphite/epoxy as a function of temperature (from Menousik and Monin [9]).

describe the process whereby the reaction constants used in their model were determined or provide comparisons with data. Cunningham [30] found that multiple Arrhenius reactions had to be superimposed to model the thermal degradation behavior of PMR-15, a polyimide resin, based on extensive thermogravimetric analysis of the resin. Cunningham's model predicted the degradation caused by exposures lasting up to 250 hours at relatively low temperatures.

Cunningham also included oxidative degradation in his model. In all of the other models described, it is assumed that the effects of oxidative degradation are negligible compared to the effects of thermally-induced degradation. This is reasonable in cases in which the environment is harsh enough that thermal degradation occurs much more quickly than oxygen can diffuse into the laminate. For the conditions considered in this investigation, in which thermal degradation occurs in a matter of minutes, this is a reasonable assumption. Oxygen will be a factor only at the surface, as diffusion of oxygen into the laminate is very slow compared to the rate of heat conduction [30].

In summary, the chemistry of epoxy and the process by which it thermally degrades are complex. Models of the degradation behavior have been developed, including models based on temperature-dependent specific heat and Arrhenius reaction models based on degradation rate. While the specific heat-based models are limited to severe environments with rapid heating rates, the Arrhenius models are more flexible and can account for different heating rates and temperature profiles. More work is needed to determine if an Arrhenius model is appropriate for modeling the degradation of 3501-6 epoxy and, if so, to establish reliable reaction constants based on data. Experiments specifically designed to quantify the degradation behavior of 3501-6 epoxy are needed.

2.3 CHANGES IN MATERIAL PROPERTIES

When graphite/epoxy composites are exposed to high temperature environments, changes in the temperature and degradation state of the epoxy matrix result in changes in the mechanical properties of the epoxy. Two primary mechanisms control the property changes: glass transition and thermal degradation. Some of the glass transition effects may be reversible, but thermal degradation causes permanent property loss. Since the mechanical properties of the graphite/epoxy composite plies depend on the mechanical properties of the constituents, the temperature- and degradation-induced changes in the mechanical properties of the epoxy result in temperature- and degradation-induced changes in the properties of the graphite/epoxy plies, even though the graphite fibers are relatively insensitive to high temperatures.

Mechanical properties of graphite/epoxy plies at various temperatures have been experimentally measured by a number of investigators [31,32,33,34]. The data reflect different testing environments and different types of graphite/epoxy, but show common trends. Weems and Rini [32] and Hinger [33] studied AS1/3501-6. Ha and Springer [34] studied T300/976. The material system studied by Greszczuk [31] is unknown. Published experimental values of transverse, shear, and longitudinal strength and moduli of graphite/epoxy at temperatures up to 400°C are compiled and plotted in Figures 2.2a-b, 2.3a-b, and 2.4a-b, respectively. The transverse and longitudinal property data was collected from unidirectional coupons. Shear properties were determined either from Iosipescu tests on unidirectional coupons [34] or derived from data from $[\pm 45]_s$ tests [32,33].

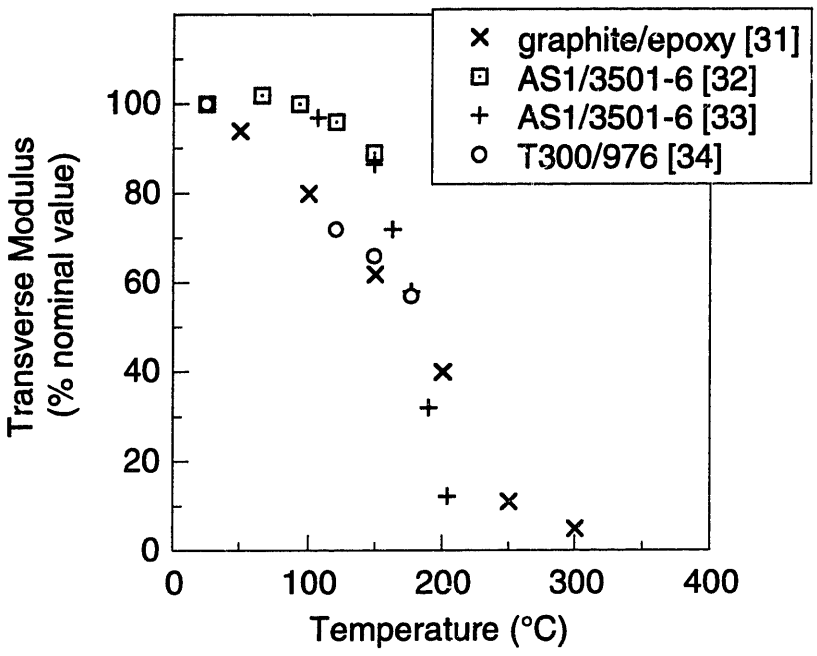

Figure 2.2a Published values of transverse modulus of graphite/epoxy versus temperature.

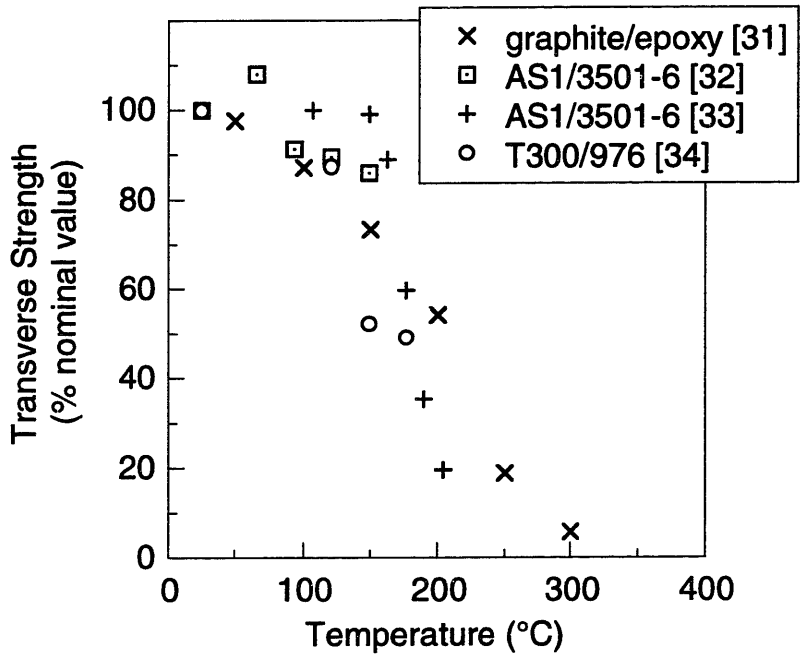

Figure 2.2b Published values of transverse strength of graphite/epoxy versus temperature.

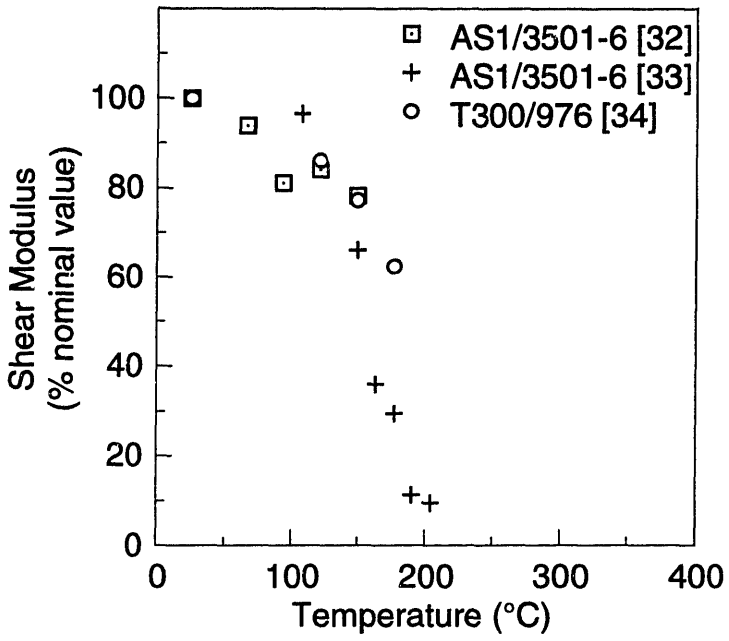

Figure 2.3a Published values of shear modulus of graphite/epoxy versus temperature.

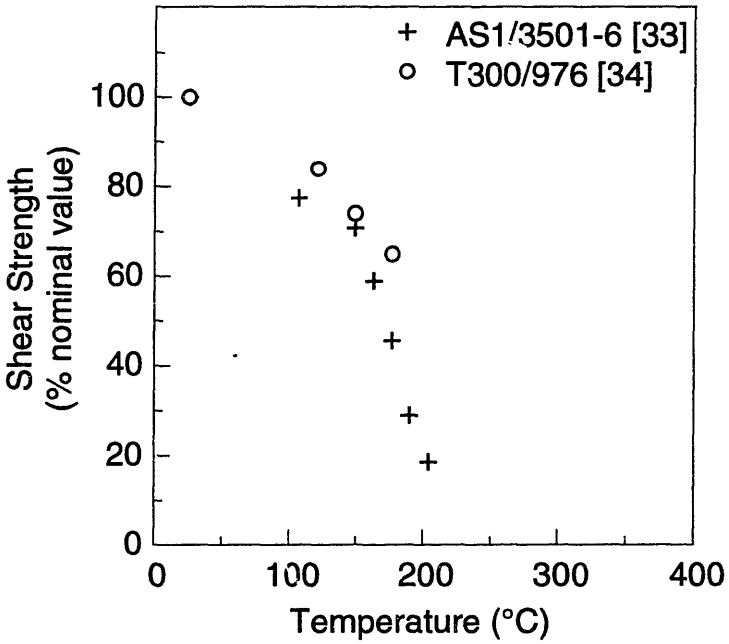

Figure 2.3b Published values of shear strength of graphite/epoxy versus temperature.

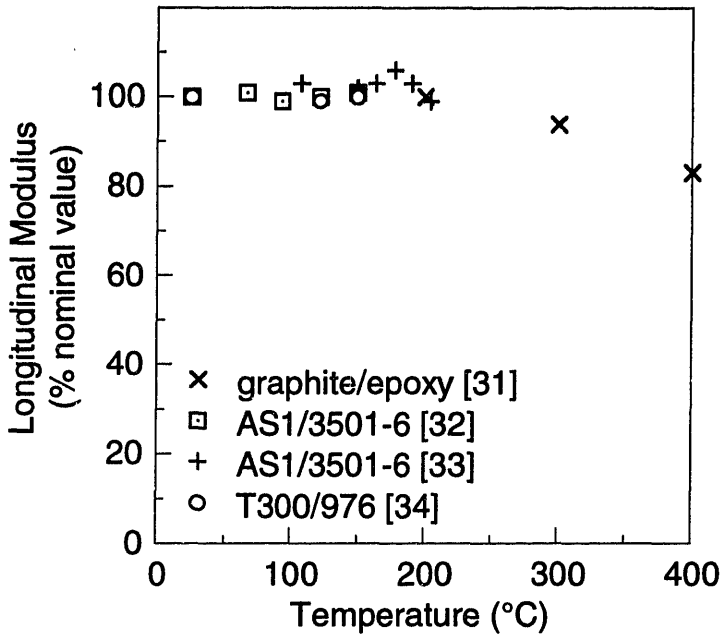

Figure 2.4a Published values of longitudinal modulus of graphite/epoxy versus temperature.

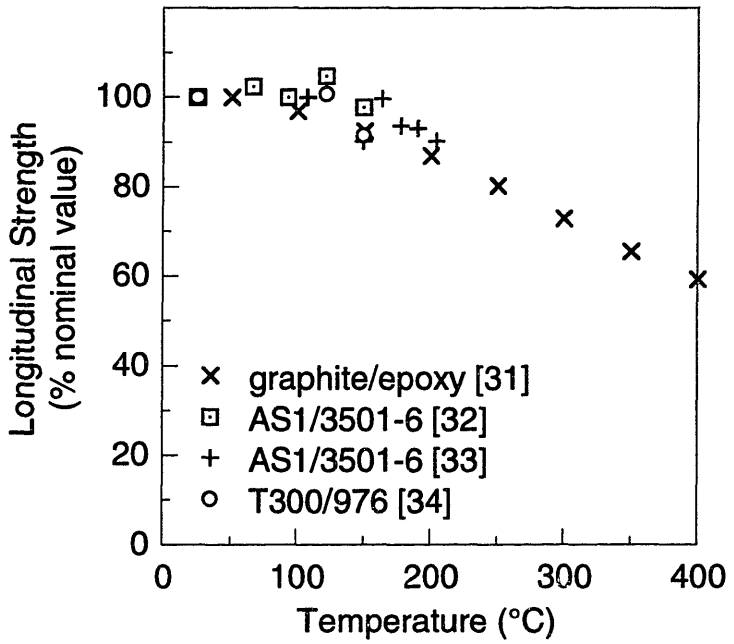

Figure 2.4b Published values of longitudinal strength of graphite/epoxy versus temperature.

The plots in Figures 2.2a, 2.2b, 2.3a, and 2.3b show that matrix-controlled transverse and shear properties are very sensitive to temperature. Substantial decreases in transverse and shear strengths and moduli are evident as the temperature approaches 200°C, the approximate glass transition temperature of epoxy, and these properties rapidly decrease to zero at temperatures above 200°C. In contrast, the fiber-controlled longitudinal stiffness and strength, shown in Figures 2.4a and 2.4b, are fairly constant up to 200°C. Above this temperature they decrease linearly to approximately 80% and 60% of their nominal values, respectively, at 400°C.

A number of authors [32,33,34,35] measured the Poisson's ratios of graphite/epoxy as functions of temperature up to 200°C and found that both ν_{12} and ν_{21} are temperature-invariant while the matrix is below its glass transition temperature. No data was available for higher temperatures.

All the data cited refers to at-temperature properties. Very little data describing residual property behavior is available. Residual strengths of quasi-isotropic laminates were reported by Frame, et al. [36] and Grimsley and Michaels [37], who tested laminates that had been cooled to room temperature after being exposed to a radiant heating chamber and a heating blanket, respectively. Frame, et al. found that the residual compressive and shear strengths of specimens exposed at 287°C decreased by up to 90% as the duration of exposure increased from 5 minutes to one hour. Strength loss occurred more rapidly at 343°C. Furthermore, specimens preconditioned for several weeks in a 98% relative humidity environment suffered greater strength loss than dry specimens. Grimsley and Michaels observed a drop in the residual properties of specimens exposed to temperatures above 250°C, with compression and fatigue performance dropping faster

than tensile strength. The fact that residual compressive strength was consistently lower than residual tensile strength suggests that while the fibers can continue to carry tensile loads after the matrix degrades, the matrix loss makes it difficult for the fibers to support compressive loads.

Because the data from Frame, et al. and Grimsley and Michaels was collected from quasi-isotropic laminates, no ply properties can be extracted. No direct comparisons can thus be made between at-temperature properties and residual ply properties. In order to determine the extent to which thermally-induced property changes are reversible, more data must be collected to permit direct comparisons of at-temperature and residual properties.

Several micromechanics models have been proposed to determine at-temperature material properties. Chen, et al. [38] used the rule of mixtures to estimate graphite/epoxy ply strengths and stiffnesses up to 3000°C. The graphite fibers were assumed to be unaffected by temperature, but the epoxy properties changed with temperature, particularly above the glass transition temperature of 200°C. No correlation with data was provided. Ha and Springer [34] collected data at temperatures up to 180°C from which to build a model. The model used the rule of mixtures to determine longitudinal and transverse stiffnesses and longitudinal tensile strength, and Tsai-Hahn formulae [39] to determine other properties as functions of temperature. Fitting parameters for the Tsai-Hahn model were extracted from the data.

Barker and Vangerko [35] also found good agreement between experimental data and rule of mixtures predictions of E_x, E_y, ν_{xy}, and G_{xy} as functions of temperature up to 120°C. They then used classical laminated plate theory (CLPT) in conjunction with the

temperature-dependent stiffnesses to predict the stiffness response of laminates heated up to 120°C. Excellent agreement between measured and predicted stiffnesses was observed for specially orthotropic ($[0_m/90_n]_s$) laminates, and reasonably good agreement was observed for generally orthotropic ($[\pm\theta]_s$) laminates.

An alternative to the temperature-based models was proposed by Springer [40], who hypothesized that changes in the strength and modulus of thermally degraded composites are related to mass loss. A model was developed stating that reductions in strength and stiffness are proportional to degradation (as determined by an Arrhenius model) raised to an exponent. The exponent is independent of temperature, but a different exponent must be empirically determined for each property. The form of the model was suggested, but no data was collected and no values were suggested for the exponents.

In summary, the strength and stiffness of graphite/epoxy plies are reduced when laminates are exposed to high temperatures. While the graphite fibers in the plies are relatively insensitive to high temperature exposure, the epoxy matrix may undergo a glass transition or thermally degrade, which compromises its mechanical properties. This loss of mechanical properties is evident in the loss of mechanical properties of the graphite/epoxy plies, which depend on the properties of the constituents. A number of studies have provided data regarding the loss of stiffness and strength of graphite/epoxy as a function of temperature up to 200°C. The data is fairly consistent and shows that transverse and shear properties are very sensitive to temperature, much more so than longitudinal properties. There is also evidence that compressive strength is more sensitive than tensile strength to the effects of high temperature exposure. A few models have been suggested that relate changes in stiffness and strength to temperature or matrix

degradation. However, correlations between models and data, when available, did not extend above 180°C. An attempt to determine laminate stiffness using classical laminate plate theory in conjunction with temperature-dependent stiffnesses showed good results.

More studies of material properties are needed. Residual (post cool-down) ply properties need to be measured to distinguish between temporary effects caused by the glass transition and permanent effects caused by thermal degradation. Furthermore, the previous work needs to be extended above 200°C. The collection of more data, particularly residual property data, will make it possible to determine how temperature and degradation influence material properties and to build better models of the material property response.

2.4 INTEGRATED MODELS

One of the goals of building models of the thermal response, matrix degradation, and changes in material properties is to integrate them along with stress-strain and failure models in order to predict the complete structural behavior. Such integrated models are considered here.

A general iterative approach for integrating models was suggested by McManus, et al. [41]. In this scheme, temperatures calculated from a thermal response model serve as an input to a model of diffusion and reaction chemistry. Based on the degradation state of the laminate predicted by the chemistry model, a thermomechanical response model is used to determine stresses and strains, which are then checked against models of damage mechanisms and failure. If failure does not occur, then the properties changed by

the progressive degradation and damage serve as inputs to the next round of modeling, beginning once again with thermal response.

This iterative approach is exemplified by the code developed by Chen, et al. [38]. They integrated a one-dimensional (through-thickness) thermal response model with implicit temperature-dependent degradation [10], a rule of mixtures material property model, classical laminated plate theory, and the maximum stress failure criterion in a one-dimensional finite element code. The time to failure of a quasi-isotropic graphite/epoxy coupon exposed on one surface to a laser while loaded in tension was determined given a specified heat flux and loading. The predicted times to failure were much lower than experimentally observed, varying by as much as 70%. The authors found that the out-of-plane deflections predicted by the code, based on an assumption of small deflections, were invalid. They improved the accuracy of the failure time predictions to within 10% of the measured times by artificially suppressing out-of-plane deflection.

Modeling a nearly identical problem, Griffis, Nemes, et al. [14] integrated a two-dimensional (through-thickness and radial) thermal response model with implicit temperature-dependent degradation, temperature-dependent material properties, classical laminated plate theory, and the maximum stress and Tsai-Wu failure criteria in a two-dimensional finite element code. The time to failure was predicted given a specified loading and heat flux. Mechanical material properties were based on data from Greszczuk [31]. Longitudinal strength and modulus values were extrapolated above 500°C. Predicted failure times were lower than experimentally measured times by as much as 25%. Some of the sources of disagreement cited were inaccurate temperature

calculations resulting from the specific heat-based degradation model, extrapolated material property data, and difficulties in modeling the complex stress state around the degraded material.

Ottaviano and Yeh [42] developed a relatively simple model to estimate the residual tensile strength of laminates exposed to fire. A temperature-dependent strength model was combined with the maximum stress failure criterion to predict the failure stress of graphite/epoxy laminates exposed to a propane flame for up to 45 seconds. The temperature distribution was not modeled, but was determined experimentally from thermocouples embedded in the laminates. The strength model consistently underestimated the laminate strengths. The authors concluded that strength data from isothermally heated specimens could not accurately predict the strength of fire-exposed laminates because of the difference in the thermal histories.

The model incorporating the most mechanisms was developed by McManus [13], who modeled the response of a solid rocket motor exit cone lining exposed to high-temperature, high-pressure engine exhaust. The material modeled was carbon/phenolic. The "CHAR" code integrated a one-dimensional (through-thickness) thermal response model with models of material degradation, material property loss, and elastic structural response. The thermal boundary conditions could be defined as a fixed surface temperature, flux, or temperature and heat transfer coefficient, and these parameters could vary with time. Temperature dependent or Arrhenius type degradation reactions could be defined. The material property input file included tables of material properties as functions of temperature and degradation, and properties that changed when the material delaminated could be specified. An elasticity model for a constrained plate was

used to determine stresses and strains. The effects of temperature, moisture, matrix degradation, and internal pressure on stresses and strains were considered.

In CHAR, the iterative approach suggested by McManus [41] was used. The volume was discretized through the thickness into a finite number of elements. At each time step, the temperature at the center of each element, as calculated by the thermal model, was used as an input to the degradation model, which determined the degradation state of the material in the element. The properties of the material in each element were determined from the tables of material properties, based on the temperature and degradation state of the element and whether or not the material in the element had delaminated. Stresses and strains in each element were calculated from the elasticity model. If the through-thickness stress in any element exceeded the failure strength of the element, the material in the element was assumed to delaminate. A time increment was then added, and all calculations were repeated for the next time step. Outputs of the code included the temperature, degradation state, pressure, strains, and stresses in each element.

In summary, a few models have been developed that integrate models of the thermal response, matrix degradation, and mechanical response. Of these, the CHAR code by McManus is the most advanced in terms of the number of effects modeled. However, the code is only one-dimensional and is not set up to analyze laminated plates. Furthermore, CHAR does not have a database of the properties of AS4/3501-6 graphite/epoxy.

An integrated model capable of determining the temperature, degradation, and mechanical response of a graphite/epoxy laminate, given a specified thermal environment

and loading, is needed. A model such as that designed by McManus [13] is desirable because it incorporates mechanism-based models of thermal reponse, matrix degradation, and material property changes. However, composite laminate mechanics need to be included and a database of graphite/epoxy properties needs to be constructed.

2.5 INSPECTION OF THERMALLY DEGRADED LAMINATES

Not only is it necessary to be able to predict the response of heat-exposed laminates, but methods are needed by which degradation that has already occurred can be detected and repaired. Since thermal degradation is related to material property loss, the need to detect degradation is driven by the need to detect losses in mechanical properties that will affect structural performance. Techniques currently available for the inspection of thermally degraded laminates are reviewed in this section.

Thermal degradation of composite laminates is difficult to detect using traditional non-destructive inspection techniques such as visual inspection, ultrasonics, tap testing, and radiography [43]. While the changes caused by thermal degradation are extensive, studies have shown that the *onset* of property loss is associated with low levels of degradation. Berlin, et al. [19] and Smith and Schwartz [44] both noted that strength loss preceded visibly evident degradation in fire-exposed graphite/epoxy laminates and sandwich panels, respectively.

Kistner, et al. [3] noted that standard ultrasonic C-scanning detects heat damage only after delamination has occurred, however up to 30% of the interlaminar shear strength may be lost before that point. Mehrkam, et al. [2] correlated changes in C-scan signal quality with reductions in the flexure strength of 0° coupons. They also noted

changes in the appearance of paint and sealant layers with exposure temperature, and a decrease in Barcol hardness at exposures above 620°C. Kucner [45] used Vickers microhardness to inspect the cross-sections of thermally degraded laminates and found that the microhardness of graphite/epoxy decreased near regions with visibly evident degradation. Microhardness was taken to be a metric of the integrity of the matrix in the composite.

The level of degradation in environmentally exposed insulating paper was monitored using thermogravimetry by Gedemer [46], who noted a change in the mass loss rate curves produced by degraded materials. The "TGA index," a ratio of the peak mass loss rate over the original sample weight, was suggested as a degradation metric.

In summary, inspection of thermally degraded laminates is challenging since properties may be permanently degraded before any changes are visibly apparent. Mixed results have been achieved using ultrasonic inspection. Some investigators have shown a correlation between ultrasonic signal response and flexure strength. However, others suggest that ultrasonic inspection is not sensitive enough to detect the onset of property loss. Microhardness has been shown to be sensitive to thermal degradation. However, the relationship between decreases in microhardness and losses in properties important to structural performance, like strength and stiffness, is not known. Furthermore, measurements were taken along laminate cross-sections, making this a destructive inspection technique. A method employing thermogravimetric analysis has been used to evaluate degradation of other materials, and while the technique is also destructive, it requires only small samples and may prove useful for assessing the degradation of epoxy.

2.6 AREAS FOR FURTHER RESEARCH

In the preceding five sections, previous work quantifying, modeling, and inspecting the effects of high temperature exposure on composite laminates has been reviewed. Areas requiring further study are summarized here.

Temperature and thermally-induced degradation are the dominant variables controlling the response of laminates to high temperature environments. The thermal response of heated composite laminates can be modeled using a finite difference formulation based on fundamental heat transfer principles. Thermal material properties that vary as the material degrades need to be included. The temperature distribution in a real laminated plate may vary in three dimensions. However, because of the advantages associated with the use of a one-dimensional model, the accuracy with which a one-dimensional thermal model can determine the through-thickness temperature distribution in the center of a multi-dimensional temperature field needs to be investigated. Experimental studies focused on the thermal degradation of epoxy need to be carried out to determine if the degradation can be effectively modeled using an Arrhenius equation and, if so, what reaction constants are appropriate.

The effects of temperature and degradation on the mechanical material properties of graphite/epoxy need to be systematically studied. Available mechanical material property data should be supplemented with studies that explore changes in material properties above 200°C and the extent to which property loss caused by the glass transition of the epoxy matrix is reversible. The residual (post cool-down) properties of laminates should be measured to distinguish between temporary (caused by the glass transition) and permanent (caused by thermal degradation) property loss. From the data,

models describing the dependencies of mechanical material properties on temperature and degradation should be developed.

New methods to quantitatively assess the degradation of epoxy should be developed. In particular, the use of mass loss-based analyses such as thermogravimetric analysis, which may be able to detect small degradation levels, needs to be investigated. When combined with models of the degradation dependence of mechanical material properties, new techniques for detecting degradation could address the need for a method to detect degradation-induced losses in mechanical properties.

Finally, models of the thermal response, degradation, and material property response should be integrated with classical laminated plate theory to develop a complete, accurate integrated model of the structural response of heated laminated plates.

CHAPTER 3

PROBLEM STATEMENT AND APPROACH

3.1 PROBLEM STATEMENT

The general problem which motivates the current work is a laminated graphite/epoxy plate exposed to a high temperature environment while being mechanically loaded. The specimen geometry, environmental conditions, and applied mechanical loads are specified. It is necessary to determine the temperature, degradation state, and stresses within the plate as functions of time and location. These stresses can then be used to assess damage and failure.

The geometry of the specific case to be considered is shown in Figure 3.1. The plate is exposed on the lower surface to a heat source, in this case a flame with temperature T_f and heat transfer coefficient h_{cz}. The portion of the lower surface exposed to the flame nominally measures L_x by L_y, and the thickness of the plate is L_z. The length and width of the plate are much greater than the dimensions of the area exposed to the flame. All other surfaces of the plate are insulated. The plate is mechanically loaded by force resultants N_x, N_y, N_{xy} and moment resultants M_x, M_y, M_{xy}.

3.2 PHILOSOPHY OF APPROACH

This overall problem can be addressed by answering the fundamental question of how the state of the laminate is changed by simultaneous exposure to a high temperature environment and mechanical loading. The state of the laminate is a full description of the

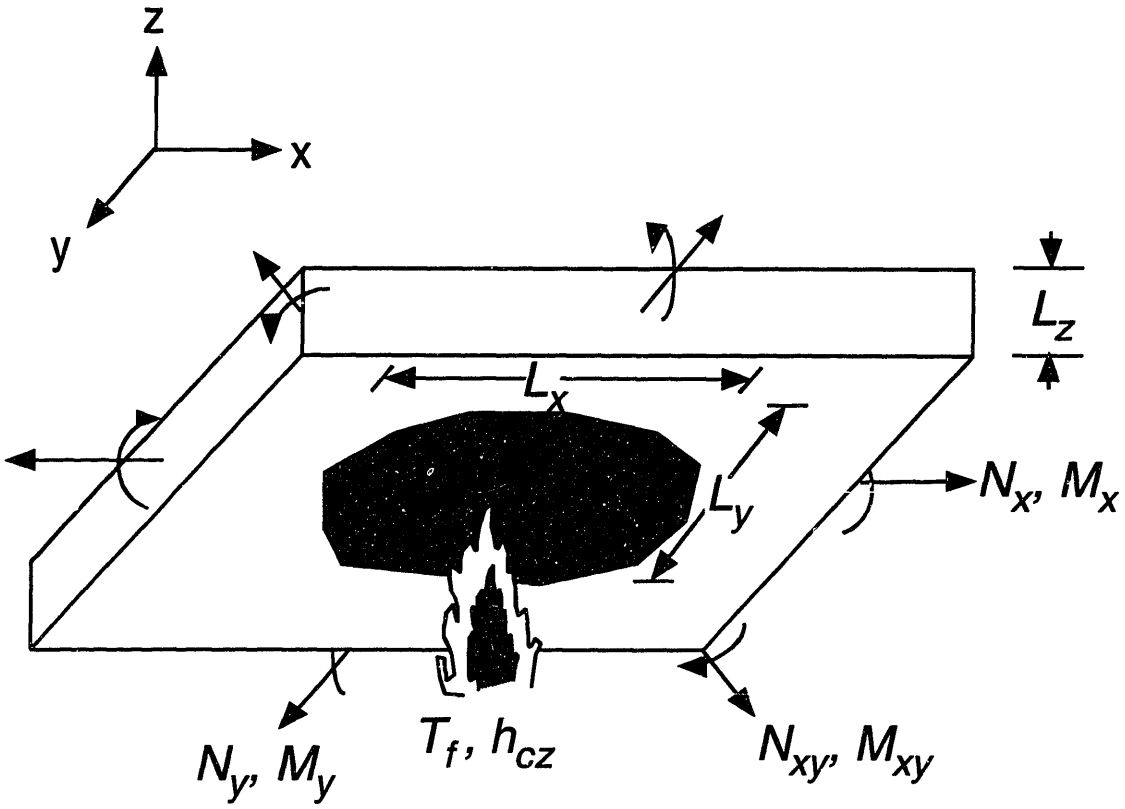

Figure 3.1 Problem geometry

material properties, temperature distribution (i.e. thermal state), level of degradation (i.e. degradation state), stresses and strains, and extent of mechanical damage, such as delamination (i.e. mechanical damage state). Figure 3.2 presents an original framework for addressing how the state of the laminate changes via various mechanisms. Each of the boxes represents a mechanism that affects the state of the laminate. The mechanisms can be studied and modeled independently.

The thermal state of the laminate (i.e. the temperatures inside the laminate) will depend on the environment outside the laminate and on the properties of the laminate which are related to its thermal response, including thermal conductivity and specific heat. Therefore, a thermal response model for the laminate requires input information about the environmental boundary conditions and the thermal material properties, which may change with the thermal state. Additionally, if delamination or other types of mechanical damage change the thermal response of the laminate, information about the mechanical damage state is also required as an input to the model.

Knowledge of the degradation chemistry of the material from which the laminate is composed is needed to determine the degradation state of the laminate. If thermal degradation is modeled, the thermal state is needed as an input to the degradation model. If degradation caused by oxidation or other mechanisms is modeled, information about the environment will also be required as input to the model.

Stresses and strains depend upon the thermo-mechanical response. A model for such response requires information about the applied mechanical loads. If stresses induced by effects due to temperature are modeled, then the thermal state is also needed as input. Mechanical material properties such as the modulus of the material must also be

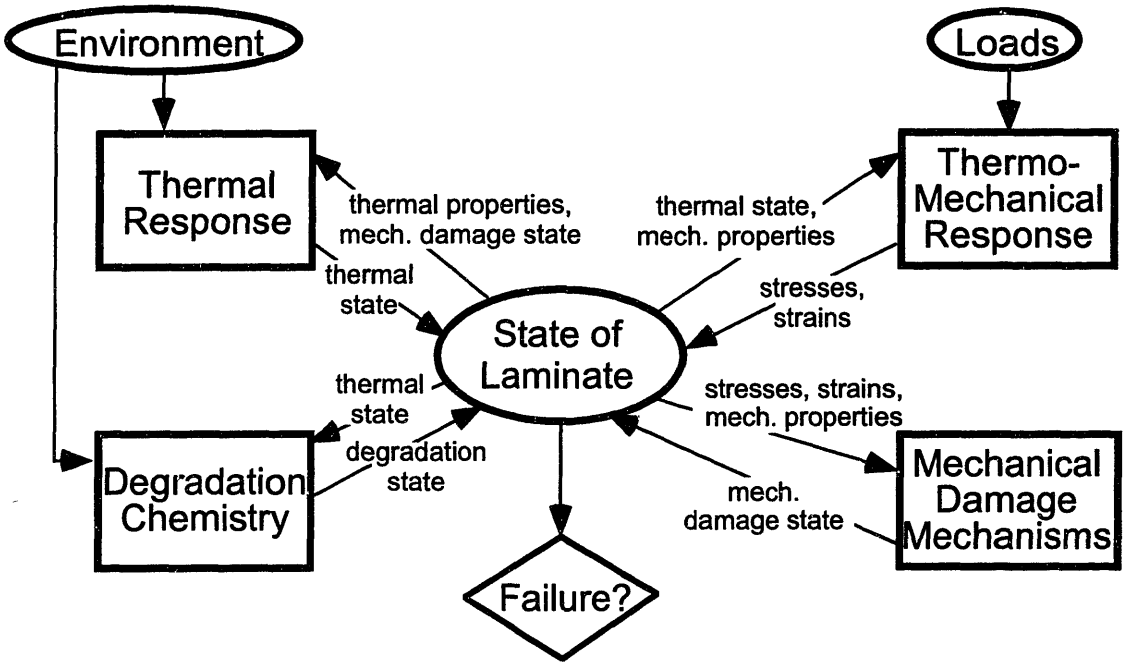

Figure 3.2 Illustration of the modeling framework

described. Since these properties can change as the state of the laminate changes, it may be necessary to provide a model that describes changes in the mechanical material properties as functions of the state of the laminate.

The occurrence of mechanical damage can be determined from a model of mechanical damage mechanisms, which uses as input the stresses and strains of the laminate and its mechanical properties. If the state of the laminate is such that a criterion for damage growth is exceeded, then the mechanical damage state of the laminate will be changed.

With an understanding of all the mechanisms that influence changes in the state of the laminate in response to the environment and mechanical loading, it is possible to develop a solution to the general problem shown in Figure 3.1. The objectives of the current work are to study three aspects of the problem: thermal response, degradation chemistry, and changes in mechanical material properties; and to model these mechanisms.

3.3 APPROACH

The thermal response, degradation chemistry, and mechanical material properties of graphite/epoxy are studied separately in order to evaluate how temperature and degradation affect the state of the laminate. In some cases, available models are applied; in others, new models are developed to describe these mechanisms. The models are then combined with a thermomechanical response model based on classical laminated plate theory to create an integrated model from which the response of laminates subjected to simultaneous heating and mechanical loading can be determined. The integrated model

is implemented in a FORTRAN code in order to demonstrate the predictive capability of the models. The process by which this is accomplished is outlined here.

The thermal response of a graphite/epoxy laminate exposed to a high temperature environment is analytically modeled using a discretized form of the conduction and convection equations from classical heat transfer theory. The theory is developed in a three-dimensional form. However, a one-dimensional approximation of the thermal response is desired because it is less computationally intensive and may enable the use of one-dimensional models for the determination of effects that depend on temperature. Therefore, the accuracy of a one-dimensional approximation of the through-thickness temperature distribution under various conditions is explored.

The effects of material orthotropy, laminate geometry, and flame intensity on the temperature distribution are evaluated through parametric studies. These parametric studies are conducted using a finite difference computer code that implements the heat transfer equations in two-dimensional form. Nondimensional parameters controlling the thermal response of an orthotropic laminate heated by convection are derived from heat transfer theory. The conditions under which the through-thickness temperature distribution in a two-dimensional temperature field can be accurately approximated using a one-dimensional model are identified in terms of these nondimensional parameters. The lessons learned regarding these parameters can be extended to determine the conditions under which a three-dimensional temperature field can be approximated with a one-dimensional model. The temperature distribution inside a partially insulated orthotropic laminate heated on one surface by convection is considered as a test case because it approximates the geometry of an aircraft skin partially exposed to a fire.

The degradation behavior of 3501-6 epoxy is studied through a series of thermogravimetric analysis (TGA) experiments. Reaction constants for a model based on a single Arrhenius rate equation are determined from mass loss data from TGA experiments performed on neat 3501-6 epoxy resin. The TGA experiments are selected because they allow precise measurement of mass loss (±0.001 μg) from a heated sample as a function of exposure temperature and time. It is assumed that mass loss correlates with degradation and that TGA is effective as a test of degradation. A series of dynamic heating TGA experiments is conducted in which samples are heated at different constant rates from room temperature up to a temperature at which the sample has completely degraded. From the results of the dynamic heating tests, a set of reaction constants describing the degradation behavior of 3501-6 epoxy is obtained. A second series of tests involving samples held at various constant elevated temperatures is conducted to verify the degradation model. The amount of degradation induced in the samples by the isothermal exposures is determined experimentally and compared with predictions from the model.

In a third set of tests, the usefulness of a new method for assessing the unknown degradation state of material with an unknown thermal history is evaluated. The method is based on fully degrading a sample of material and measuring its char yield. Char yield is defined as the mass fraction of nonreactive material that remains after a sample is fully degraded. Char yields are measured from samples with a variety of *known* thermal histories and the result from each sample is correlated with the degradation state of the sample, which is also known.

The changes in mechanical material properties due to changes in the temperature and degradation state of the material are quantified through a series of tensile tests performed on unidirectional $[0]_4$ and $[90]_{12}$ graphite/epoxy coupons exposed to temperatures up to 400°C. In half of the tests, coupons are loaded to failure at the testing temperature and at-temperature modulus and strength are measured. In the other half, coupons are cooled from the test temperature before being loaded to failure and residual modulus and strength are measured. At-temperature and residual mechanical material properties are directly compared, enabling a separation of temporary temperature-induced effects from permanent degradation-induced effects. To evaluate the level of correlation between degradation state and residual properties, a second series of residual property tests is conducted on a group of $[90]_{12}$ coupons. The coupons are all subjected to conditions that induce the same calculated degradation state as a ten-minute exposure at 300°C, but at different temperatures and exposure times. Stiffness and strength results from these tests are compared with the results from coupons exposed at 300°C for ten minutes.

From the material property data, models of the transverse and longitudinal stiffnesses and tensile strengths of graphite/epoxy plies as functions of temperature and degradation state are developed. For temperatures ranging from 25 to 400°C and for a full range of degradation states, the models provide predictions of the mechanical material properties.

To tie together the different aspects of the work and begin to address the stated problem, the thermal response, degradation, and mechanical material property models developed in this work are integrated with a thermomechanical response model based on

classical laminated plate theory. The one-dimensional integrated model is implemented in a code entitled CHARplus which is written in the FORTRAN programming language. The inputs to the code include laminate geometry, environmental conditions, and applied mechanical loads. The distributions of temperature, degradation state, stresses, and strains through the thickness of a laminate as functions of time are determined. The calculated stresses are compared to ply strength values determined from strength models developed in this work. However, models of mechanical damage mechanism and failure are not yet included.

Nevertheless, the integrated models in CHARplus show the capabilities of the approach developed in this work and thereby represent the foundation upon which a complete mechanism-based model of the problem shown in Figure 3.1 can be constructed, using the framework of Figure 3.2.

CHAPTER 4

THEORY AND ANALYSIS

Models of thermal response and degradation chemistry are outlined in this chapter. Governing equations and their discretized forms are presented for each model. The implementation of the thermal model in a finite difference code is described. The method by which data from thermogravimetric analysis experiments was processed to obtain values for the semi-empirical degradation model is also described.

4.1 THERMAL RESPONSE MODEL

A laminated plate made of a composite material is subjected to heating via conduction and convection. The material is orthotropic, hence its properties are different in different directions. It is necessary to determine the temperature distribution inside the plate. Heat transfer theory, modified to include variable orthotropic material properties, forms the basis of the thermal response model. The full three-dimensional governing equations are developed, and then a two-dimensional discretized form of the equations is presented.

4.1.1 Heat Transfer Theory

To derive the general heat conduction equation for a three-dimensional system, the law of conservation of energy is applied to the infinitesimal three-dimensional control

volume (CV) in Figure 4.1. The arrows in Figure 4.1 indicate heat flow into and out of the control volume. The law of conservation of energy can be stated as follows:

$$\begin{aligned} &\textit{rate of heat conduction into CV} + \textit{rate of heat generation inside CV} \\ &= \textit{rate of heat conduction out of CV} + \textit{rate of energy storage inside CV} \end{aligned} \tag{4.1}$$

According to Fourier's Law, the rate of heat conduction in a particular direction is proportional to the temperature gradient in that direction. For an orthotropic material, the conduction heat flow along the principal axes of the material can be expressed as follows:

$$q_{kx} = -k_x \Delta y \Delta z \frac{\partial T}{\partial x} \qquad q_{ky} = -k_y \Delta x \Delta z \frac{\partial T}{\partial y} \qquad q_{kz} = -k_z \Delta x \Delta y \frac{\partial T}{\partial z} \tag{4.2}$$

where q_{ki} and k_i are the rate of heat conduction (W) and thermal conductivity (W/m·K), respectively, in the i direction.

The other terms in Equation 4.1 can be expressed as follows:

$$\textit{rate of heat generation in CV} = \dot{q}_G \Delta x \Delta y \Delta z \tag{4.3}$$

$$\textit{rate of energy storage in CV} = \rho c \Delta x \Delta y \Delta z \frac{\partial T}{\partial t} \tag{4.4}$$

where $\dot{q}_G$ is the rate of heat generation per unit volume (W/m^3), and ρ and c are the density (kg/m^3) and specific heat (J/kg·K), respectively, of the material in the control volume.

Putting Equations 4.1, 4.2, 4.3, and 4.4 together, dividing through by the volume of the control volume, and taking the limit as the volume approaches zero, the conduction equation is obtained:

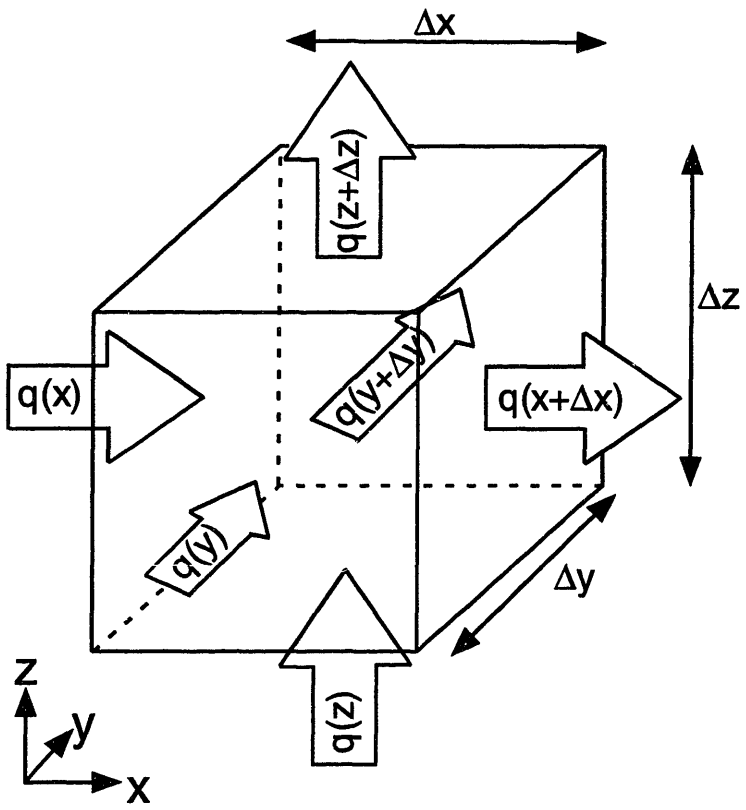

Figure 4.1 Central control volume element.

$$\frac{k_x}{\rho c}\frac{\partial^2 T}{\partial x^2}+\frac{k_y}{\rho c}\frac{\partial^2 T}{\partial y^2}+\frac{k_z}{\rho c}\frac{\partial^2 T}{\partial z^2}+\frac{\dot{q}_G}{\rho c}=\frac{\partial T}{\partial t} \tag{4.5}$$

If any of the surfaces of the control volume experience heat transfer via convection, the rate of heat transfer by convection can be calculated from the relation

$$q_{ci} = h_{ci} A \Delta T \tag{4.6}$$

where h_{ci} is the convection heat transfer coefficient (W/m^2K) in the i-direction, A is the area of heat transfer (m^2), and ΔT is the difference between the temperature of the surface of the control volume, $T\big|_{surface}$, and the ambient temperature, T_∞. At the surfaces, the equilibrium equation between conduction and convection at the surface can be written

$$\begin{aligned}
-k_x \left.\frac{\partial T}{\partial x}\right|_{x=surface} &= h_{cx}\left(T\big|_{x=surface} - T_\infty\right) \\
-k_y \left.\frac{\partial T}{\partial y}\right|_{y=surface} &= h_{cy}\left(T\big|_{y=surface} - T_\infty\right) \\
-k_z \left.\frac{\partial T}{\partial z}\right|_{z=surface} &= h_{cz}\left(T\big|_{z=surface} - T_\infty\right)
\end{aligned} \tag{4.7}$$

At an insulated boundary, the heat transfer coefficient h_{ci} is zero, which implies that

$$-k_{x_i} \left.\frac{\partial T}{\partial x_i}\right|_{x_i=boundary} = 0 \tag{4.8}$$

where x_i is x, y, or z.

It is sometimes convenient to express governing equations in dimensionless form in order to identify dimensionless parameters that control the response. To express the

thermal equilibrium equations in dimensionless form, dimensionless variables for space, temperature, and time are first defined as follows:

$$\xi = \frac{x}{L_x} \quad \text{(a)} \qquad \eta = \frac{y}{L_y} \quad \text{(b)} \qquad \zeta = \frac{z}{L_z} \quad \text{(c)}$$
$$\Theta = \frac{(T - T_\infty)}{(T_o - T_\infty)} \quad \text{(d)} \qquad \tau = \frac{t}{t_{ref}} \quad \text{(e)} \tag{4.9}$$

where L_x, L_y, and L_z are reference lengths in the x-, y-, and z-directions, respectively; T_o is the initial temperature, and t_{ref} is a reference time. Using these dimensionless variables, Equation 4.5 becomes

$$\frac{\partial \Theta}{\partial \tau} = \frac{t_{ref} k_x}{\rho c L_x^2}\left(\frac{\partial^2 \Theta}{\partial \xi^2} + \left(\frac{k_y L_x^2}{k_x L_y^2}\right)\frac{\partial^2 \Theta}{\partial \eta^2} + \left(\frac{k_z L_x^2}{k_x L_z^2}\right)\frac{\partial^2 \Theta}{\partial \zeta^2}\right) + \frac{\dot{q}_G t_{ref}}{\rho c (T_o - T_\infty)} \tag{4.10}$$

and Equation 4.7 can be written

$$\left.\frac{\partial \Theta}{\partial \xi}\right|_{\xi=0} = -\frac{h_{cx} L_x}{k_x}\Theta$$
$$\left.\frac{\partial \Theta}{\partial \eta}\right|_{\eta=0} = -\frac{h_{cy} L_y}{k_y}\Theta \tag{4.11}$$
$$\left.\frac{\partial \Theta}{\partial \varsigma}\right|_{\varsigma=0} = -\frac{h_{cz} L_z}{k_z}\Theta$$

Three sets of non-dimensional parameters are apparent in Equations 4.10 and 4.11. The first parameter, seen in Equation 4.10 as the first term on the right side, is a well-known heat transfer parameter, the Fourier number, for an orthotropic control volume:

$$Fo_x = \frac{t_{ref} k_x}{\rho c L_x^{\,2}} \tag{4.12}$$

Physically, the Fourier number is the ratio of the rate of heat transfer by conduction to the rate of energy storage in the system. Also, one can consider the quantity $\rho c L_x^{\,2} k_x^{-1}$ to be the time constant of the conduction problem [47]. Because of the way Equation 4.10 was written, with x-direction terms first, the first term on the right side was the x-direction Fourier number. By rearranging the variables in Equation 4.10, one could easily obtain expressions for the y- or z-direction Fourier numbers.

The second set of non-dimensional parameters is the set of Biot numbers for an orthotropic control volume, seen in Equation 4.11:

$$Bi_x = \frac{h_{cx} L_x}{k_x} \qquad Bi_y = \frac{h_{cy} L_y}{k_y} \qquad Bi_z = \frac{h_{cz} L_z}{k_z} \tag{4.13}$$

There are three Biot numbers that may be considered, depending on which surface (or surfaces) are exposed to convective heating. The Biot number is the ratio of conduction thermal resistance per unit area, L_i/k_i, to convection thermal resistance per unit area, $1/h_{ci}$. Like the Fourier number, the Biot number is well known in heat transfer literature [47,48].

The final set of non-dimensional parameters come about as a result of the thermal orthotropy of the material. The terms incorporate ratios of the thermal conductivities and reference lengths in different directions. For three-dimensional heat transfer, there are three of these geometry-orthotropy parameters:

$$\mathcal{L}_{xy}=\frac{k_y L_x^2}{k_x L_y^2} \qquad \mathcal{L}_{yz}=\frac{k_z L_y^2}{k_y L_z^2} \qquad \mathcal{L}_{xz}=\frac{k_z L_x^2}{k_x L_z^2} \tag{4.14}$$

The geometry-orthotropy parameters are the ratios of the Fourier numbers in two directions, i.e. the ratios of heat transfer by conduction in the two directions:

$$\mathcal{L}_{xy}=\frac{Fo_y}{Fo_x} \qquad \mathcal{L}_{yz}=\frac{Fo_z}{Fo_y} \qquad \mathcal{L}_{xz}=\frac{Fo_z}{Fo_x} \tag{4.15}$$

The larger the parameter $\mathcal{L}_{ij}$, the more conduction in the j direction dominates over conduction in the i direction, meaning that heat will flow more easily in the j-direction than in the i-direction.

Using the non-dimensional parameters, Equations 4.10 and 4.11 can be written

$$\frac{\partial\Theta}{\partial\tau}=Fo_x\left(\frac{\partial^2\Theta}{\partial\xi^2}+\mathcal{L}_{xy}\frac{\partial^2\Theta}{\partial\eta^2}+\mathcal{L}_{xz}\frac{\partial^2\Theta}{\partial\varsigma^2}\right)+\frac{\dot{q}_G t_{ref}}{\rho c(T_o-T_\infty)} \tag{4.16}$$

$$\left.\frac{\partial\Theta}{\partial\xi}\right|_{\xi=0}=-Bi_x\Theta \qquad \left.\frac{\partial\Theta}{\partial\eta}\right|_{\eta=0}=-Bi_y\Theta \qquad \left.\frac{\partial\Theta}{\partial\varsigma}\right|_{\varsigma=0}=-Bi_z\Theta \tag{4.17}$$

Equations 4.16 and 4.17 provide a complete description of the three-dimensional thermal response of a control volume exposed to convective heating. In the absence of heat generation, the thermal response at a given reference time (i.e. at a given Fourier number) is fully determined by the Biot numbers and the geometry-orthotropy parameters. As stated earlier, the material properties may change as the material is heated and undergoes thermal degradation. Equations 4.16 and 4.17 are still valid in this case, but the solution of the equations is more complicated.

4.1.2 Finite Difference Discretization

Due to the orthotropy of the material in the control volume described in the previous section, an analytical solution of the temperature distribution determined by Equations 4.16 and 4.17 is infeasible. However, a numerical solution can be developed by use of a finite difference approach. The development given is derived from Kreith and Bohn [48].

One objective of developing a model of the thermal response is to characterize the thermal response in terms of the non-dimensional parameters. For the fully three-dimensional case, this becomes a bit unwieldy because there are three Biot numbers and three geometry-orthotropy parameters to consider. To focus on the role of the non-dimensional parameters, a two-dimensional case is considered. For a two-dimensional case with conduction heat transfer in the x- and z-directions and convection through the thickness (z-direction) only, the thermal response is determined wholly by two parameters: Bi_z and $\mathcal{L}_{xz}$. The lessons learned about the roles of these two parameters can be extended to the three-dimensional case to explain the roles of the other Biot numbers and geometry-orthotropy parameters in determining the temperature distribution.

An element in the interior of a discretized two-dimensional control volume (CV) is shown in Figure 4.2. The control volume is divided along the x-direction into M-1 equal segments of length Δx and along the z-direction into N-1 equal segments of length Δz:

$$\Delta x = \frac{L_x}{M-1} \qquad \Delta z = \frac{L_z}{N-1} \tag{4.18}$$

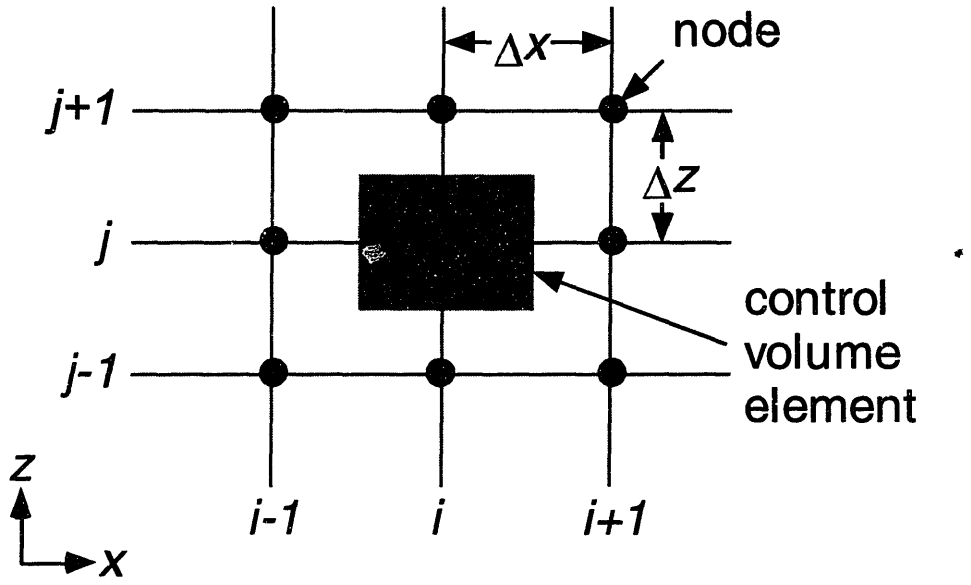

Figure 4.2 Illustration of control volume for conduction in rectangular coordinates.

The boundaries of each rectangular element are denoted by:

$$\begin{aligned} x_i &= (i-1)L_x \qquad i = 1,2,...,M \\ z_j &= (j-1)L_z \qquad j = 1,2,...,N \end{aligned} \tag{4.19}$$

The element measures Δx by Δz and is centered about node *i,j*. The smaller the elements, the more closely the discretized temperature distribution will approximate the continuous temperature distribution in the actual structure. There is no lower limit to the size of the elements, however the use of smaller elements will require the use of a smaller time step, Δt. The time step must be selected such that

$$\Delta t < \frac{1}{2}\left[\frac{\Delta x^2}{k_x/\rho c} + \frac{\Delta z^2}{k_z/\rho c}\right]^{-1} \tag{4.20}$$

otherwise, the solution will exhibit growing oscillations and become unstable.

The temperature of node *i,j* at time *m* is denoted $T_{i,j,m}$. To write the conduction equation in finite difference form, the temperature between nodes is assumed to vary linearly. Thus, the expressions for the rate of heat conduction, rate of heat generation, and rate of energy storage can be written as follows:

$$q_{kx} = -k_x \frac{2T_{i,j,m} - T_{i-1,j,m} - T_{i+1,j,m}}{\Delta x} \qquad q_{kz} = -k_z \frac{2T_{i,j,m} - T_{i,j-1,m} - T_{i+1,j,m}}{\Delta z} \tag{4.21}$$

$$\textit{rate of heat generation inside CV} = \dot{q}_G \Delta x \Delta z \tag{4.22}$$

$$\textit{rate of energy storage inside CV} = \rho c \Delta x \Delta z \frac{T_{i,j,m+1} - T_{i,j,m}}{\Delta t} \tag{4.23}$$

The properties of the material in the control volume element, k_x, k_z, c, and ρ, may vary as the element heats up and undergoes thermal degradation.

Assembling Equations 4.1, 4.21, 4.22, and 4.23, we obtain the finite difference equation for the temperature of nodes inside the control volume:

$$T_{i,j,m+1} = T_{i,j,m} + \Delta t \left[\begin{array}{l} \dfrac{k_x / \rho c}{\Delta x^2} \left(T_{i-1,j,m} - 2T_{i,j,m} + T_{i+1,j,m} \right) \\ + \dfrac{k_z / \rho c}{\Delta z^2} \left(T_{i,j-1,m} - 2T_{i,j,m} + T_{i,j+1,m} \right) + \dfrac{\dot{q}_{G,i,j,m}}{\rho c} \Delta x \Delta z \end{array} \right] \tag{4.24}$$

Nodes on the edge of the control volume must also be considered. Figure 4.3a shows a boundary element of the control volume. The lower surface is exposed to convection heat transfer, with a convection coefficient h_{cz} and ambient temperature T_∞. The conservation of energy statement in Equation 4.1 can be modified to account for heat flow by convection:

$$\begin{array}{c} \textit{rate of heat conduction/convection into CV + rate of heat generation inside CV} \\ = \\ \textit{rate of heat conduction/convection out of CV + rate of energy storage inside CV} \end{array} \tag{4.25}$$

The heat conduction terms can be written as before, with the conduction term for heat flow into the element from the surface replaced by a convection term:

$$q_{ix} = -k_x \frac{2T_{i,1,m} - T_{i-1,1,m} - T_{i+1,1,m}}{\Delta x} \qquad q_{kz} = h_{cz} \Delta x \left(T_\infty - T_{i,1,m} \right) + k_z \frac{T_{i,2,m} - T_{i,1,m}}{\Delta z / 2} \tag{4.26}$$

The heat generation and energy storage terms are modified to account for the smaller size of the control volume:

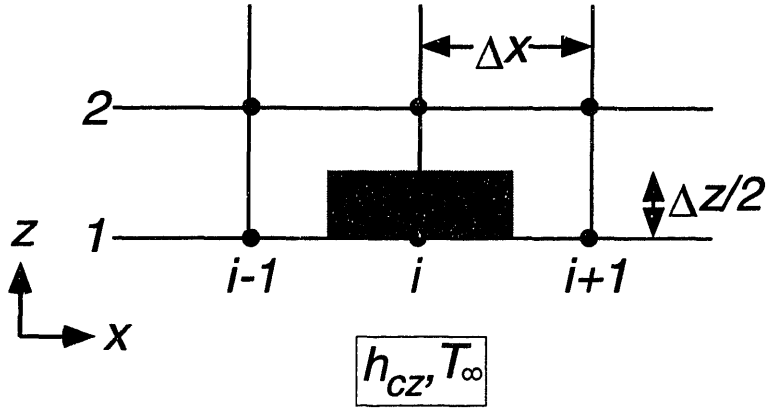

Figure 4.3a Boundary control volume element.

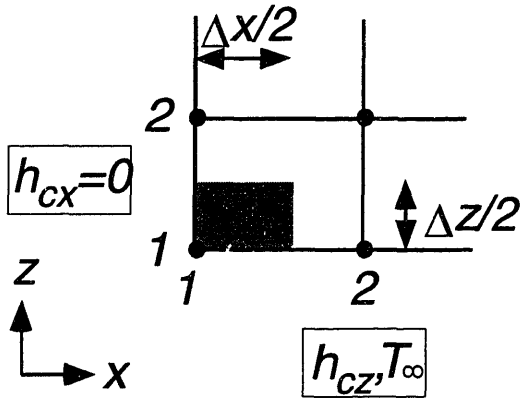

Figure 4.3b Corner control volume element.

$$rate\ of\ heat\ generation\ inside\ CV = \frac{1}{2}\dot{q}_G \Delta x \Delta z \tag{4.27}$$

$$rate\ of\ energy\ storage\ inside\ CV = \frac{\rho c \Delta x \Delta z}{2}\left(T_{i,1,m+1} - T_{i,1,m}\right) \tag{4.28}$$

Assembling Equations 4.25, 4.26. 4.27, and 4.28, the finite difference equation for the temperature of nodes on the edge of the control volume can be written:

$$T_{i,1,m+1} = T_{i,1,m} + \Delta t\left[\begin{array}{l} \dfrac{k_x/\rho c}{\Delta x^2}\left(T_{i-1,1,m} - 2T_{i,1,m} + T_{i+1,1,m}\right) + \dfrac{2k_z/\rho c}{\Delta z^2}\left(T_{i,2,m} - T_{i,1,m}\right) \\ + \dfrac{2h_{cz}}{\rho c \Delta z}\left(T_\infty - T_{i,1,m}\right) + \dfrac{\dot{q}_{G,i,j,m}}{2\rho c}\Delta x \Delta z \end{array}\right] \tag{4.29}$$

Finally, following a similar development, the finite difference equation for the temperature of nodes in the corner of the control volume, such as the one shown in Figure 4.3b, can be written:

$$T_{1,1,m+1} = T_{1,1,m} + \Delta t\left[\begin{array}{l} \dfrac{2k_x/\rho c}{\Delta x^2}\left(T_{2,1,m} - T_{1,1,m}\right) + \dfrac{2k_z/\rho c}{\Delta z^2}\left(T_{1,2,m} - T_{1,1,m}\right) \\ + \dfrac{2h_{cz}}{\rho c \Delta z}\left(T_\infty - T_{1,1,m}\right) + \dfrac{\dot{q}_{G,i,j,m}}{4\rho c}\Delta x \Delta z \end{array}\right] \tag{4.30}$$

Given initial temperatures $T_{i,j,m=0}$ at all nodes i,j and boundary conditions h_{cx}, h_{cz}, and T_∞, Equations 4.24, 4.29, and 4.30 can be used to determine the temperatures $T_{i,j,m=1}$ at the next time step. Repeatedly marching forward in time, one can determine $T_{i,j,m+1}$ for all times. As noted, the model is flexible enough to account for material properties that vary as the material heats up and undergoes thermal degradation.

4.1.3 The Temper Code

The two-dimensional finite difference thermal model derived in Section 4.1.2 is implemented in a FORTRAN code known as "Temper." The source code is listed in Appendix A. Temper determines the temperature distribution in a cross-section of a plate that is heated via convection along part of one surface. This geometry was selected because it is similar to that of an aircraft skin partially exposed to a localized fire. The heat source does not vary in the *y*-direction, hence the temperature distribution is two-dimensional. The geometry is illustrated in Figure 4.4. The area modeled is circled in Figure 4.4; due to symmetry, only one-half of the cross-section is modeled. The area is discretized into M nodes laterally and N nodes through the thickness, as illustrated in Figure 4.5. The heat source is specified as an ambient temperature, T_∞, and heat transfer coefficient, h_{cz}. The unheated surfaces are modeled as being insulated ($h_{ci} = 0$). The code predicts the temperature distribution $T_{i,j,m}$ in the material at all nodes i,j and time steps m. Through-thickness and lateral heat flow are considered.

The inputs required from the user of Temper include the dimensions of the volume, the number of nodes along each axis, the location of the first insulated node, the time step increment, and the initial temperature at each node. Material properties, including density, thermal conductivity, and specific heat must also be specified. The user also specifies boundary conditions, including the ambient temperature and convection coefficients along each boundary. The end condition for the program execution can be specified in various ways, such as the maximum time for which the temperature distribution is desired or the maximum temperature for a specified node. Given these inputs, Temper provides the temperature at each node in the mesh as a

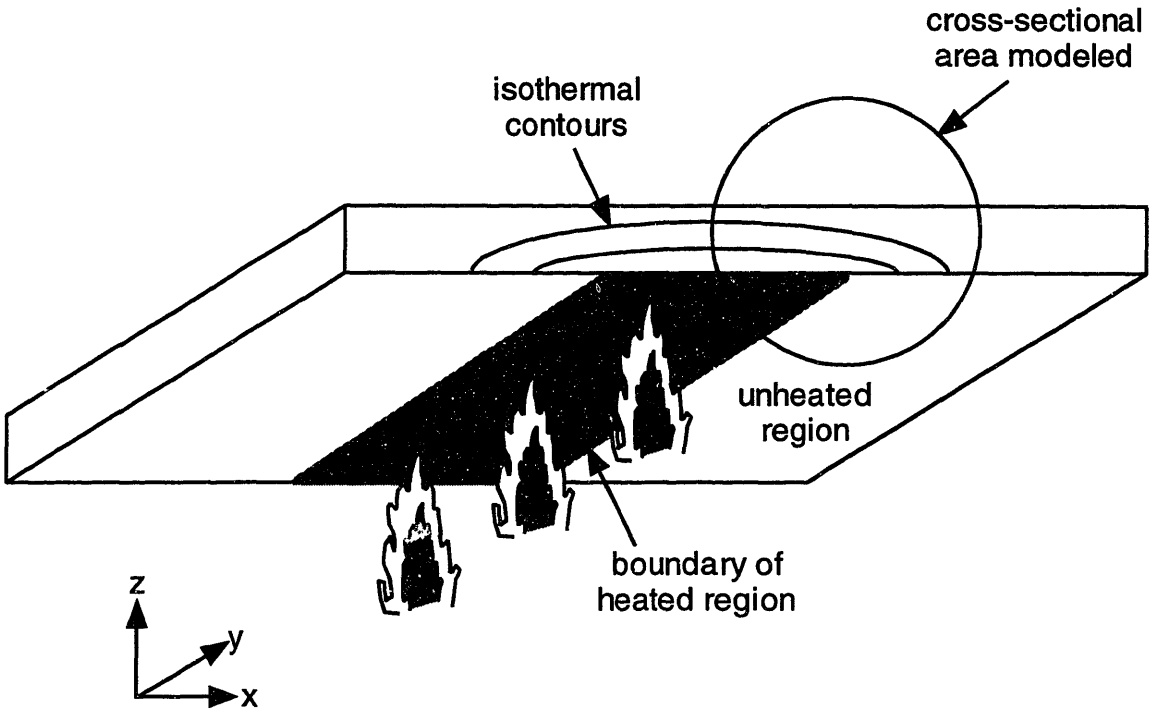

Figure 4.4 Illustration of geometry modeled in Temper code.

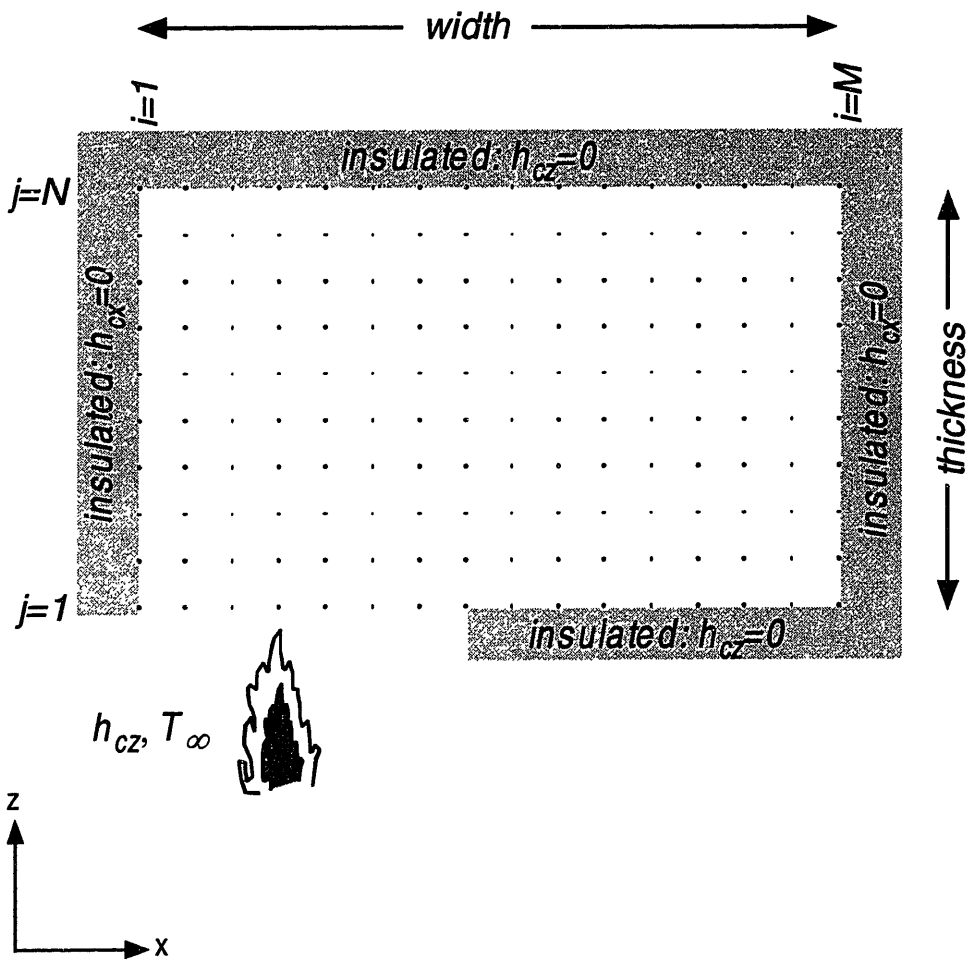

Figure 4.5 Illustration of mesh used in Temper code.

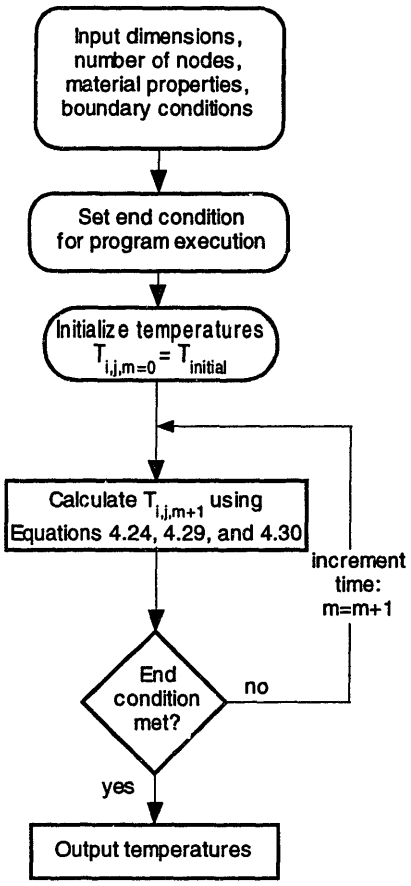

Figure 4.6 Algorithm used in the Temper code.

function of time. The computational algorithm is sketched in flowchart form in Figure 4.6.

4.2 DEGRADATION MODEL

A sample of polymeric material is exposed to a high temperature environment that causes it to thermally degrade. As the material degrades, volatile reaction products are released, resulting in mass loss. A carbonaceous residue, called char, is left behind as a reaction product. It is assumed that the concentration of oxygen is low and the rate of thermal degradation is high such that the effects of oxidative degradation can be disregarded. It is necessary to determine the degradation state of the material at a point within the sample as a function of the temperature history at that point. Mass loss is used as a metric of degradation. Arrhenius reaction kinetics forms the basis of the degradation model.

4.2.1 Arrhenius Reaction Kinetics

A control volume initially containing mass m_o of matrix material is considered. As the control volume is heated, it loses mass as the matrix material thermally degrades and volatile reaction products are released. A conversion metric α is used to track the degradation process. When α is zero, no reactions have yet taken place. When α reaches one, the material in the control volume is fully degraded and no more reactions are possible. It is assumed that mass loss correlates with degradation. The degradation state

of the control volume is equated with the conversion metric α, which is defined in terms of the normalized mass loss:

$$\alpha = \frac{m_o - m}{m_o - m_f} \tag{4.31}$$

where m is the mass at the time of interest, m_o is the initial mass, and m_f is the final mass of the fully degraded material, i.e. the mass of nonreactive material in the control volume, referred to as char.

Arrhenius reaction kinetics is used to model the thermal degradation reactions that occur when the material is heated. The rate of degradation is exponentially dependent on the temperature of the control volume and has an nth order dependence on its degradation state:

$$\frac{\partial \alpha}{\partial t} = k(1-\alpha)^n \, exp\left[\frac{-E}{RT}\right] \tag{4.32}$$

where k is the reaction constant (1/min), n is the reaction order, and E is the activation energy (kJ/mol). These three constants must be determined experimentally. R is the universal gas constant, equal to 8.314 kJ/mol·K. For some materials, there may be multiple reactions occurring simultaneously [30]. Some reactions may work independently on different mass fractions y_p, where

$$\sum_p y_p = 1 \tag{4.33}$$

A conversion metric, α_p, along with initial and final masses, are defined for each mass fraction. Some mass fractions may be attacked by multiple reactions, q in number.

Equations of the form of Equation 4.32 can be written for each mass fraction y_p and each reaction q:

$$\frac{\partial \alpha_{pq}}{\partial t} = k_{pq}\left(1-\alpha_p\right)^{n_{pq}} exp\left[\frac{-E_{pq}}{RT}\right] \tag{4.34}$$

Reaction constants k_{pq}, n_{pq}, and E_{pq} must be determined for each reaction. Note that tensor summation notation is not used here. The degradation state of each mass fraction at time t is found by summing the progress of each reaction:

$$\alpha_p(t) = \int_o^t \sum_q \frac{\partial \alpha_{pq}}{\partial t} dt \tag{4.35}$$

See Cunningham [30] for a more complete development of the procedure required for tracking the progression of multiple reactions.

4.2.2 Finite Difference Discretization

Equation 4.32 cannot be solved directly for the degradation state, $\alpha(t)$, of the control volume, so a finite difference approach is taken in which the equation is discretized in time. The equation is also discretized with respect to space to account for two-dimensional spatial variations in temperature. Each spatial node i,j is located at the center of an element containing a finite amount of material. Assuming a single reaction, the finite difference form of Equation 4.32 is written

$$\left.\frac{\partial \alpha}{\partial t}\right|_{i,j,m} = k\left(1-\alpha_{i,j,m}\right)^n \frac{-E}{RT_{i,j,m}} \tag{4.36}$$

where $\partial\alpha/\partial t|_{i,j,m}$, $\alpha_{i,j,m}$, and $T_{i,j,m}$ are the rate of degradation, degradation state, and temperature at node i,j at time m. These parameters may vary with i and j, but are assumed to be uniform within the element associated with each node. Equation 4.36 is applied to each element separately, and the degradation state $\alpha_{i,j,m}$ of each element is calculated independently.

To determine the conditions at time $m+1$, the temperature, and degradation state are calculated as follows:

$$T_{i,j,m+1} = T_{i,j,m} + \left.\frac{\partial T}{\partial t}\right|_{i,j,m} \Delta t \tag{4.37}$$

$$\alpha_{i,j,m+1} = \alpha_{i,j,m} + \left.\frac{\partial \alpha}{\partial t}\right|_{i,j,m} \Delta t \tag{4.38}$$

where Δt is the discretization time step (sec). Equation 4.37 is used when the heating rate $\partial T/\partial t|_{i,j,m}$ at time m is known (as in the case of the thermogravimetric analysis experiments conducted in this investigation.) If the temperatures are calculated using a finite difference analysis, the temperatures $T_{i,j,m+1}$ are determined from Equations 4.24, 4.29, and 4.30. Once the temperature and degradation state are calculated, the degradation rate at time $m+1$ can then be determined:

$$\left.\frac{\partial \alpha}{\partial t}\right|_{i,j,m+1} = k\left(1-\alpha_{i,j,m+1}\right)^n \frac{-E}{RT_{i,j,m+1}} \tag{4.39}$$

By specifying initial conditions $\alpha_{i,j,m=0}$ and $T_{i,j,m=0}$ and using Equations 4.37-4.39 while marching forward in time, one can determine degradation state α as a function of time and location.

4.2.3 Determination of Reaction Constants

Thermogravimetric analysis (TGA) experiments performed at a constant heating rate (such that $\frac{\partial T}{\partial t} = Q$ = constant) provide the data for the determination of the reaction constants characteristic of a particular material. The procedure for such experiments is described in detail in Chapter 5. In the experiments, the mass of a sample is monitored while the sample is heated and thermally degrades. Mass loss rate is continuously calculated. Mass loss is used as a metric of degradation and the degradation state of the sample as a function of temperature is determined from the mass loss data. Constants for the Arrhenius reaction model in Equation 4.32 are determined from the degradation state versus temperature data using Kissinger's method [49] as described by Cunningham [30]. To convert the raw mass loss and mass loss rate data into a form useful for analysis, normalized mass loss and normalized mass loss rate are calculated. In order to calculate these values, the sample used in the thermogravimetric analysis experiments must be heated until it is fully degraded.

Mass loss and mass loss rate are normalized by dividing the amount of mass loss at a given time or temperature by the total mass lost when the material has fully degraded. The normalized variables are the degradation state, α, and the rate of change of degradation state, $\frac{\partial \alpha}{\partial t}$, respectively.

$$\alpha(T) = \frac{m_o - m(T)}{m_o - m_f} \tag{4.40}$$

$$\frac{\partial \alpha}{\partial t}(T) = \frac{\frac{\partial m}{\partial t}(T)}{m_o - m_f} \tag{4.41}$$

For a given constant heating rate Q, the material's maximum degradation rate will occur at temperature T_{max}. At this temperature, by definition,

$$\frac{\partial}{\partial t}\left(\frac{\partial \alpha}{\partial t}\right)=0 \tag{4.42}$$

Substituting the degradation rate expression in Equation 4.32 and taking the time derivative, it can be stated that

$$\left[\begin{array}{l} kn(1-\alpha(T_{max}))^{n-1}\, exp\left(\frac{-E}{RT_{max}}\right)\left(\frac{-\partial \alpha}{\partial t}(T_{max})\right) \\ +k(1-\alpha(T_{max}))^{n}\, exp\left(\frac{-E}{RT_{max}}\right)\frac{E}{RT_{max}^2}\frac{dT}{dt} \end{array}\right]=0 \tag{4.43}$$

Canceling terms and substituting the degradation rate expression from Equation 4.32 gives

$$nk(1-\alpha(T_{max}))^{n}\, exp\left(\frac{-E}{RT_{max}}\right)=(1-\alpha(T_{max}))\frac{E}{RT_{max}^2}\frac{dT}{dt} \tag{4.44}$$

Substituting in the constant heating rate Q and taking the logarithm of both sides, the following expression can be obtained:

$$ln\left(\frac{Q}{T_{max}^2}\right)=ln\left(\frac{nkR}{E}(1-\alpha(T_{max}))^{n-1}\right)-\frac{E}{RT_{max}} \tag{4.45}$$

Equation 4.45 can be used to determine reaction constants k, n, and E from experimental data that provides mass and mass loss rate as functions of temperature. From the experimental data, the temperature T_{max} at which the maximum degradation rate

occurs, the degradation state at the maximum degradation rate, $\alpha(T_{max})$, and the value of the maximum degradation rate, $\frac{\partial \alpha}{\partial t}(T_{max})$, are noted for different heating rates Q. A linear fit through the data in a plot of $ln(QT_{max}^{-2})$ versus T_{max}^{-1} provides sufficient information to find all three reaction constants. Explicitly, a line can be fitted through an x-y plot with $x = T_{max}^{-1}$ and $y = ln(QT_{max}^{-2})$:

$$y = -\frac{E}{R}x + ln\left[\frac{nkR}{E}\left(1-\alpha(T_{max})^{n-1}\right)\right] \tag{4.46}$$

The activation energy, E, can be obtained from the slope of the line, $-E/R$. Constants k and n are obtained from the intercept of the line,

$$Int = ln\left[\frac{nkR}{E}(1-\alpha(T_{max}))^{n-1}\right] \tag{4.47}$$

Solving for k,

$$k = \frac{E\,exp(Int)}{R}\frac{1}{n(1-\alpha(T_{max}))^{n-1}} \tag{4.48}$$

Substituting Equation 4.48 into Equation 4.32, an expression for n can be obtained:

$$n = \left(\frac{\partial \alpha}{\partial t}(T_{max})\right)^{-1}\frac{E\,exp(Int)}{QR}(1-\alpha(T_{max}))exp\left(\frac{-E}{RT_{max}}\right) \tag{4.49}$$

The value of n is determined from the experimentally determined values of T_{max}, $\alpha(T_{max})$, and $\frac{\partial \alpha}{\partial t}(T_{max})$ and the plot intercept value. The value of k can then be determined from Equation 4.48.

Another piece of information that can be derived from TGA data is the char yield of the sample. Char yield is the fraction of nonreactive material in a sample. In experiments conducted in an inert atmosphere up to a temperature at which the sample has completely reacted, the char yield should be a constant material property [25]. It is calculated by taking a ratio of the masses of the sample before and after heating:

$$char\ yield = \frac{m_f}{m_o} \tag{4.50}$$

where m_o and m_f are the initial and final masses of the specimen, respectively.

4.2.4 Determination of Degradation State using Char Yield

When a sample of epoxy is partially degraded by exposure to a high temperature environment, it will lose a fraction of its mass, giving it a residual degradation state α_{res}. By definition, in a partially degraded sample $\alpha_{res}<1$. The degradation state α_{res} can be measured by taking a fraction of the sample, fully degrading it, measuring the resulting "effective" char yield, and comparing the effective char yield to the nominal char yield of epoxy.

If a sample of partially degraded epoxy with mass m_{ro} is heated in an inert atmosphere until it is completely degraded, the effective char yield from that partially degraded sample can be computed from its final mass m_{rf}:

$$effective\ char\ yield = \frac{m_{rf}}{m_{ro}} \tag{4.51}$$

The effective char yield of the partially degraded sample will be higher than the nominal char yield of a non-degraded sample. From the ratio of the effective char yield to the nominal char yield, the initial degradation state α_{res} of the sample can be determined:

$$\alpha_{res} = \frac{1 - \frac{nominal\ char\ yield}{effective\ char\ yield}}{1 - nominal\ char\ yield} \tag{4.52}$$

If the partially degraded epoxy sample in question is reinforced with graphite fibers to form a composite, the initial degradation state can be calculated in the same way. However, the mass of the inert graphite fibers must be figured into the char yield. The effective char yield from a partially degraded fiber-reinforced composite sample with initial mass m_{roc} will be higher because the mass of the fully degraded composite sample, m_{rfc}, will include the masses of both the fibers and nonreactive char. The ratio of sample masses before and after the degradation in the inert atmosphere will be an effective "char/fiber yield:"

$$effective\ char/fiber\ yield = \frac{m_{rfc}}{m_{roc}} \tag{4.53}$$

The effective char/fiber yield is compared with the nominal char/fiber yield from a non-degraded composite sample to determine the degradation state α_{res}. The nominal char/fiber yield can be measured experimentally or calculated from the fiber volume fraction v_f, fiber and matrix densities ρ_f and ρ_m, and nominal matrix char yield by using the rule of mixtures:

$$nominal\ char/fiber\ yield = \frac{v_f \rho_f + nominal\ char\ yield(1 - v_f)\rho_m}{v_f \rho_f + (1 - v_f)\rho_m} \tag{4.54}$$

The degradation state calculation has the same form as before:

$$\alpha_{res} = \frac{1 - \dfrac{nominal\ char/fiber\ yield}{effective\ char/fiber\ yield}}{1 - nominal\ char/fiber\ yield} \tag{4.55}$$

CHAPTER 5

EXPERIMENTAL PROCEDURE

The procedures used to perform experiments to study the degradation of epoxy and the effects of temperature and matrix degradation on the mechanical properties of graphite/epoxy plies are detailed in this chapter. The design of the test matrices is discussed, and the test matrices themselves are presented.

5.1 EPOXY DEGRADATION STUDIES

5.1.1 Procedure

The samples used in the TGA tests were made of cured, powdered, and desiccated neat 3501-6 epoxy resin. To prepare the samples, a layer of uncured resin pellets (made by Hercules) was placed in a 40 cm x 33 cm galvanized steel pan lined with a sheet of guaranteed non-porous Teflon (GNPT). The layer of resin pellets had to be thin to prevent a runaway exotherm during curing. The pan was placed in a preheated 180°C oven. No pressure or vacuum was used. Once exposed to the heat of the oven, the pellets melted together and formed a plaque. After eight hours, the oven was turned off and the plaque of cured epoxy was allowed to gradually cool to room temperature. This was not a standardized cure procedure. It was chosen because the time at 180°C was similar to the time at 180°C in a standard cure and postcure cycle for AS4/3501-6 graphite/epoxy.

Once cooled, the plaque of cured epoxy was broken into small pieces, placed in a clean household coffee grinder along with dry ice (to make the resin more brittle and prevent overheating,) and milled into a powder. The powder was sifted through a No. 40 U.S.A. Standard Testing Sieve (425 micron grating) and then placed in a sealed jar with anhydrous calcium sulfate desiccant for a minimum of 24 hours before testing.

Thermogravimetric analysis tests were performed using a Seiko TG/DTA 320 thermogravimetric analyzer with a Seiko SSC/5200H data collection computer. The machine consists of two sample holders inside a furnace instrumented with a precision microbalance and thermocouples. The sample holders are mounted at the end of 10 cm-long, 1.6 mm-diameter hollow rods made of alumina with platinum-platinum rhodium R-type thermocouples inside. The sample cups measure 5 mm in diameter and are 2 mm deep. One sample cup is left empty, as a control, and the other is filled with the material to be tested. A horizontal differential system balance mechanism with an optical position sensor measures the deflection of each rod, which correlates with the mass inside the sample cup. The mass is measured to a precision of 0.001 mg. The maximum temperature of the furnace is 1500°C, and the heating rate can be varied between 0.01°C/min and 100°C/min. The furnace chamber is continuously flushed with a gas selected by the user, typically nitrogen, air, or oxygen, at a flow rate selected by the user. Figure 5.1 shows a photograph of the thermogravimetric analyzer with the furnace chamber open.

The heating profile of the machine is fully programmable. The user selects start temperature, heating rate, hold temperature, hold time, and cooling rate. While the machine executes the heating profile, the mass and temperature of the sample are

measured at a sampling rate of 2 Hz. The computer calculates mass loss rate from the mass data and records time, temperature, mass, and mass loss rate in a data file.

To perform the TGA experiments, the thermogravimetric analyzer was set up and the flow rate from the nitrogen tank set at 200 mL/min. The inert nitrogen atmosphere was selected in order to isolate the effects of temperature on degradation. Two empty pans, a reference and sample pan, were placed in their respective holders and balanced. Alumina pans were used for this series of experiments because they could withstand the high temperatures and did not react chemically with the epoxy sample. Once the pans were balanced, the sample pan was removed, filled with grains of powdered epoxy, and returned to the holder. The mass of the epoxy sample was then measured. Typical sample masses ranged from 5000 μg to 6000 μg.

In the first series of experiments, the furnace controller was programmed to perform a single ramp (i.e. dynamic heating test) from 25°C to 800°C. The sample was then cooled back to 25°C at approximately 50°C/min. Tests were performed at three heating rates: 5°, 10°, and 15°C/min, with multiple tests performed at 10°C/min to evaluate the repeatability of the tests.

The data collection computer recorded time, temperature, mass, and mass loss rate in spreadsheet form. The files could not be directly accessed by a Macintosh or Windows-based PC because the Seiko SSC/5200H runs on a proprietary operating system. To circumvent this difficulty, plots of temperature vs. mass and temperature vs. mass loss rate resulting from each experiment were printed, and then each plot was scanned using a Hewlett Packard Scanjet 4C scanner and Adobe Photoshop image editing software. Data from these plots was extracted using DataThief, a software program that

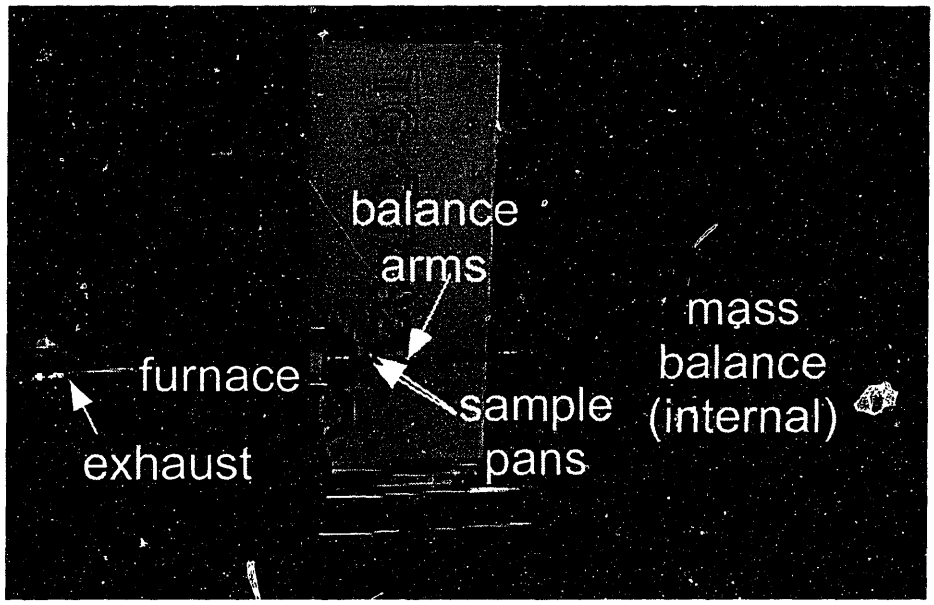

Figure 5.1 Photograph of thermogravimetric analyzer (furnace in open position).

allows the user to trace a series of data points on a two-axis graph and determines their x-y coordinates. To verify the integrity of data obtained via this indirect method, the DataThief output from one test was compared with data for the same test that had been translated from the Seiko operating system into the Windows operating system by a Seiko technician at the company headquarters. The data processed through DataThief agreed with the translated data with an accuracy of ±2%.

In the second series of tests, the furnace controller was programmed to perform an isothermal exposure. The temperature was ramped from room temperature to the programmed test temperature at 25°C/min. The temperature was held at the test temperature for the scheduled exposure time and then ramped down to room temperature at 25°C/min.

As each sample was heated, held at temperature, and cooled, the temperature and sample mass were recorded at a sampling rate of 2 Hz. The sample masses before and after heating were of particular interest. The actual heating profiles, as measured by the furnace thermocouple, did not exactly match the programmed profiles, a problem not encountered in the dynamic heating tests. The actual exposure temperatures were consistently lower than the programmed exposure temperatures. A sample plot of actual exposure temperature data as a function of time is shown in Figure 6.13. The differences between the programmed and actual exposure temperatures ranged from 18 to 34°C. Calculations of the degradation state induced by each test were based on the actual thermocouple data, not the nominal test conditions.

When each of the samples in the second series of tests reached room temperature after cooling down from the test temperature, a dynamic heating TGA test was

immediately performed without opening the furnace or otherwise disturbing the samples. The furnace computer was reprogrammed to generate a single ramp from room temperature to 800°C at 10°C/min. Once the furnace reached 800°C, the sample was cooled to room temperature.

As before, the temperature, mass, and mass loss rate were recorded at a rate of 2 Hz. Plots of these variables were printed and then scanned in order to extract the data using DataThief, as previously described.

5.1.2 Test Matrices

The test matrix for the initial series of dynamic heating TGA tests was designed to explore the degradation behavior of epoxy over a range of heating rates. Rates of 5°C/min, 10°C/min, and 15°C/min were chosen, and multiple tests were performed at 10°C/min to evaluate the repeatability of the tests. The test matrix is shown in Table 5.1.

The purpose of the second series of tests was to verify the predictions of the degradation model generated from the results of the initial series of TGA tests. The test matrix was designed based on predictions from the degradation model. The model was used to predict the degradation state that would result if a sample were exposed to a high-temperature isothermal exposure. The exposure temperature profile included a 25°C/min ramp from room temperature to a prescribed exposure temperature, a hold at the exposure temperature for a prescribed time, and a 25°C/min ramp back to room temperature. A sketch of the temperature profile is shown in Figure 5.2.

Table 5.1 Initial TGA test matrix

Heating rate (°C/min)	Number of specimens
5	1
10	3
15	1

Table 5.2 Model verification test matrix

Exposure temperature	Hold time (min)	# specimens	Predicted α
250	10	1	0.001
350	1	1	0.168
335	10	1	0.295
375	1	1	0.552
335	25	1	0.559
350	10	1	0.576
350	20	1	0.805
375	10	1	0.974

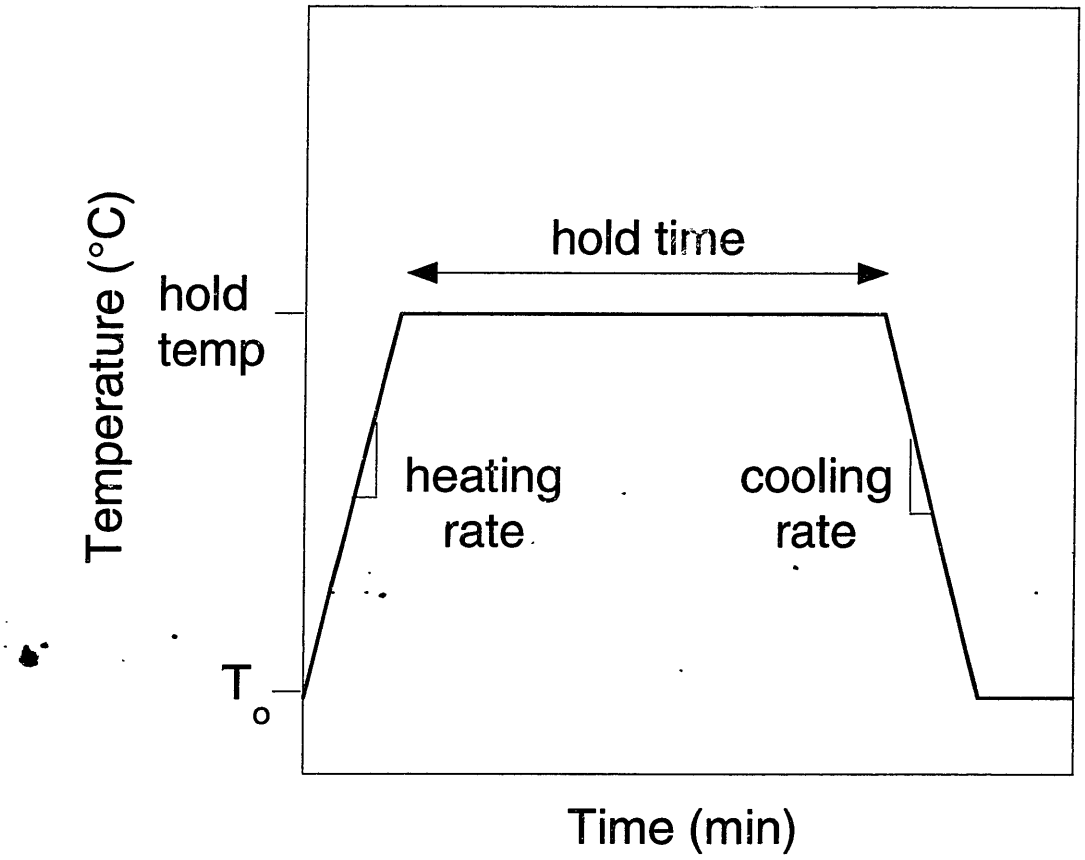

Figure 5.2 Heating profile used in degradation model verification tests.

The degradation states predicted by the model for a variety of hold times and exposure temperatures are plotted as a function of time and temperature on a contour map in Figure 5.3. The contours of the plot show the degradation states, α, predicted to result from the exposures, and the dots indicate exposure time-temperature combinations that were selected for the test matrix. The times and temperatures selected for each test are tabulated in Table 5.2, along with the degradation state predicted by the model for each test. The test conditions were selected to show the effects of increasing hold time or temperature while the other variable remains constant and to determine whether identical degradation states could be obtained from specimens with different exposure conditions. For example, the 10-minute exposure at 350°C, 25-minute exposure at 335°C, and 1-minute exposure at 375°C were all predicted to cause a degradation state of approximately 0.55. All three points lie along the same contour in Figure 5.3.

5.2 MATERIAL PROPERTY STUDIES

5.2.1 Procedure

The laminates used for tensile testing were manufactured from Hercules AS4/3501-6 graphite epoxy tape. Individual plies were cut from a single roll of preimpregnated unidirectional tape (pre-preg) and were laid up into $[0]_4$ and $[90]_{12}$ panels measuring 71.1 cm long by 30.5 cm wide. These panels were twice as long as the laboratory standard, a variation necessitated by the experimental setup. The cure plate was assembled following the specifications of TELAC Report 88-4b [50] for a net resin cure and the panels were cured in the TELAC autoclave using the standard cycle for

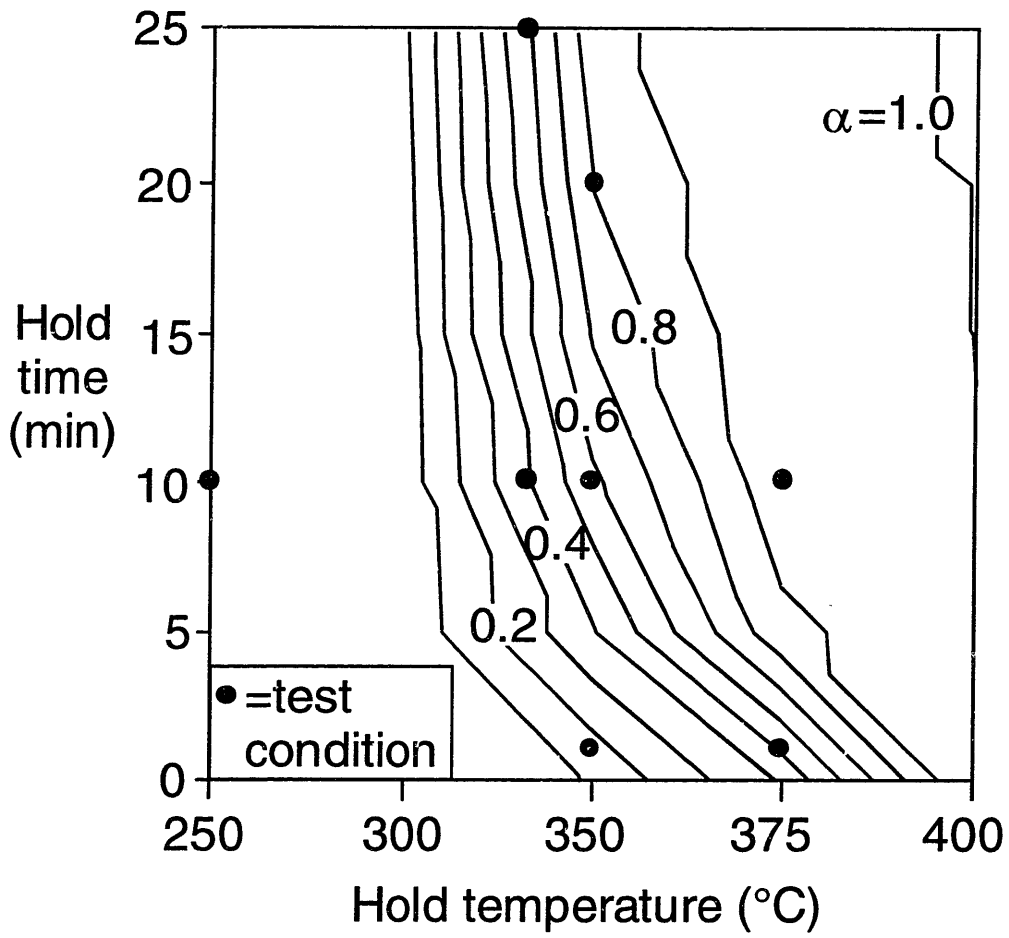

Figure 5.3 Contour map of predicted degradation state as a function of temperature and time of exposure.

AS4/3501-6 epoxy, as shown in Figure 5.4. The autoclave temperature was held at 115°C for one hour, increased to 180°C, held for three hours, and then cooled to room temperature. The applied pressure and vacuum were maintained at 0.59 MPa and 600 mm Hg, respectively, throughout the cure. After the laminates were cured and removed from the cure plate, they were postcured in an oven at 180°C for eight hours.

Each post-cured laminate was cut using a water-cooled diamond-wheel milling machine into five coupons measuring 71.1 cm long by 5.1 cm wide. The thickness and width of each coupon were measured with a micrometer at a minimum of four points, at least one of which was in each third of the laminate, as divided from top to bottom. The measurements were averaged and recorded. The average thickness of the $[90]_{12}$ coupons was 1.66 mm ± 0.16 mm. The average thickness of the $[0]_4$ coupons was 0.59 mm ± 0.044 mm. This works out to an average ply thickness of 0.138 mm ± 0.014 mm for the $[90]_{12}$ coupons and 0.146 mm ± 0.011 mm for the $[0]_4$ coupons. These average ply thicknesses are on the low end of the range defined by MIL-HDBK-17 for plies of AS4/3501-6 [24], 0.139mm – 0.160 mm.

To prepare the coupons for use in a tensile test, fiberglass loading tabs measuring 7.6 in length and 5.1 cm in width were bonded to the end of each coupon using Dexter Epoxi-Patch two-part room temperature-cure epoxy. Weights placed on the loading tabs while the epoxy cured ensured that the tabs were parallel and bonded well. K-type thermocouples were bonded to the surface of each coupon using Omega CC High Temperature Cement. To ensure that the thermocouples remained in place throughout testing, a thin 28-gage stainless steel wire was wrapped around the specimen to mechanically hold each bonded thermocouple in place. Three thermocouples were

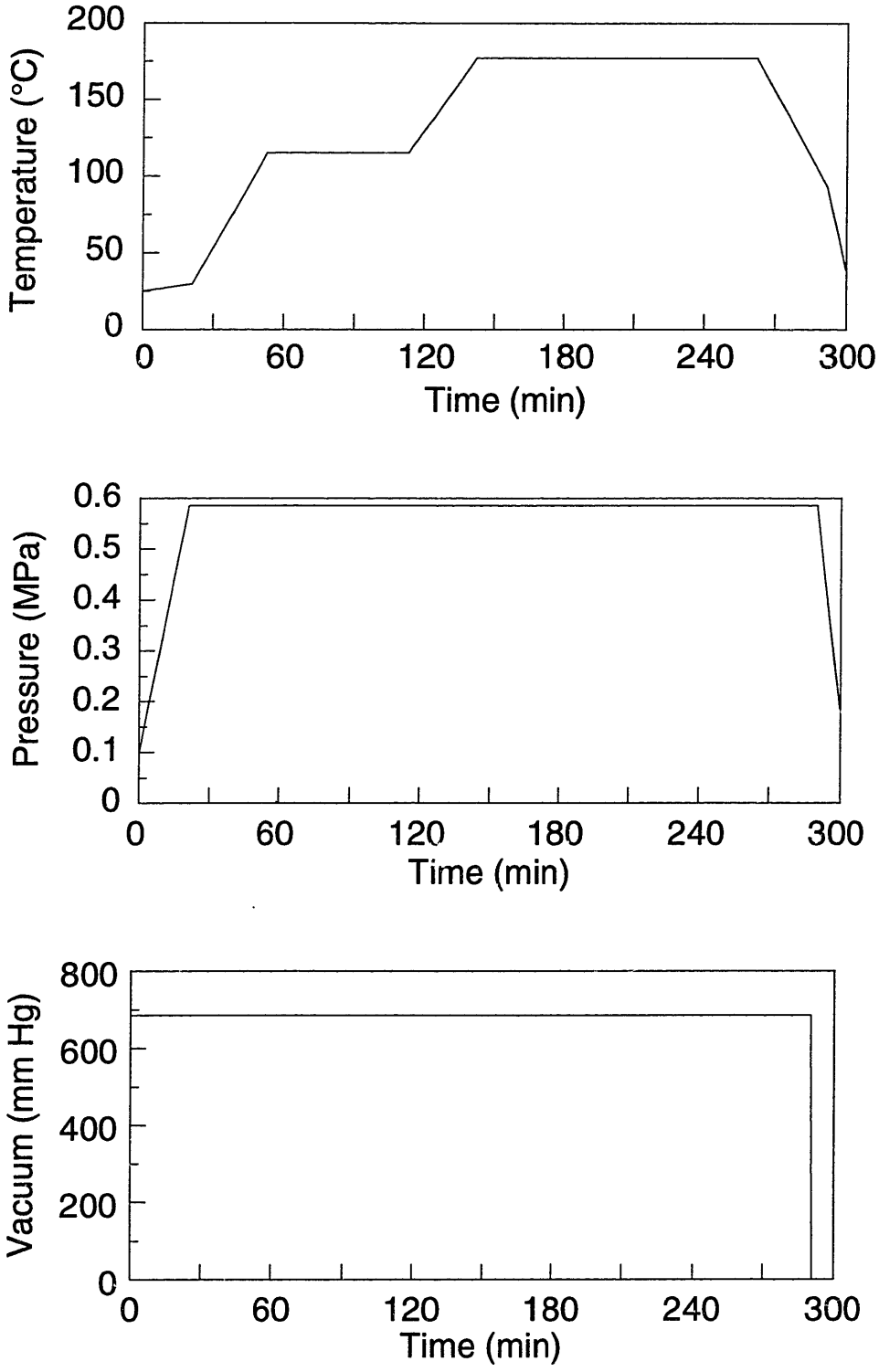

Figure 5.4 Cure cycle for AS4/3501-6 graphite/epoxy: (*top*) Temperature cycle (*center*) Pressure cycle (*bottom*) Vacuum cycle

placed along one face of the coupon: one in the center, and one 12.7 cm longitudinally above and below the center. When placed this way, each of the thermocouples was positioned in the center of a heating zone of the furnace when the coupon was clamped for testing. Until testing, the laminates were stored under ambient laboratory conditions of 25°C and 55 to 65% RH.

Tensile testing was performed using an Instron 1332 servohydraulic testing machine with a maximum capacity of 222 kN. The testing machine was controlled using an Instron 8500+ digital controller. The hydraulic grips of the testing machine were actively cooled with chilled water.

An Applied Test Systems Series 2961 split cylinder test furnace was mounted onto the side of the testing machine and positioned between the grips of the testing machine. A photograph of the testing machine and furnace is shown in Figure 5.5. The furnace had a 38.4 cm-high test section with three heating sections, and a 12.7 cm inner diameter. A photograph of the interior of the furnace is shown in Figure 5.6. The furnace was controlled using an Applied Test Systems Series 230 furnace controller that could be set in 1°C increments up to 499°C. The controller determined the voltage input to each heating zone of the furnace based on the set temperature and measurements from a thermocouple inside the furnace. Individual rheostats for each heating zone allowed for manual control of the voltage input to each zone.

The furnace had a window in one side through which an extensometer was attached to the coupons. The Epsilon Technology Model 3448 High Temperature Extensometer had 13.3 cm-long ceramic rods with chisel points which were fitted against the edge of the coupon. Spring-loaded ceramic cords held the extensometer in place.

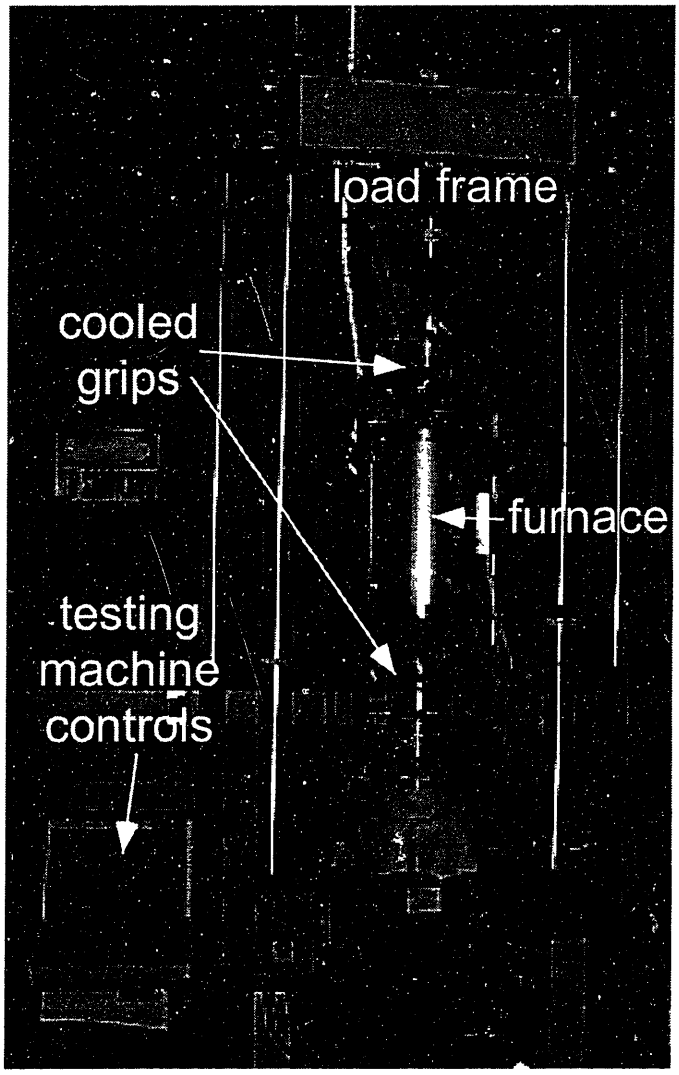

Figure 5.5 Photograph of testing machine and furnace.

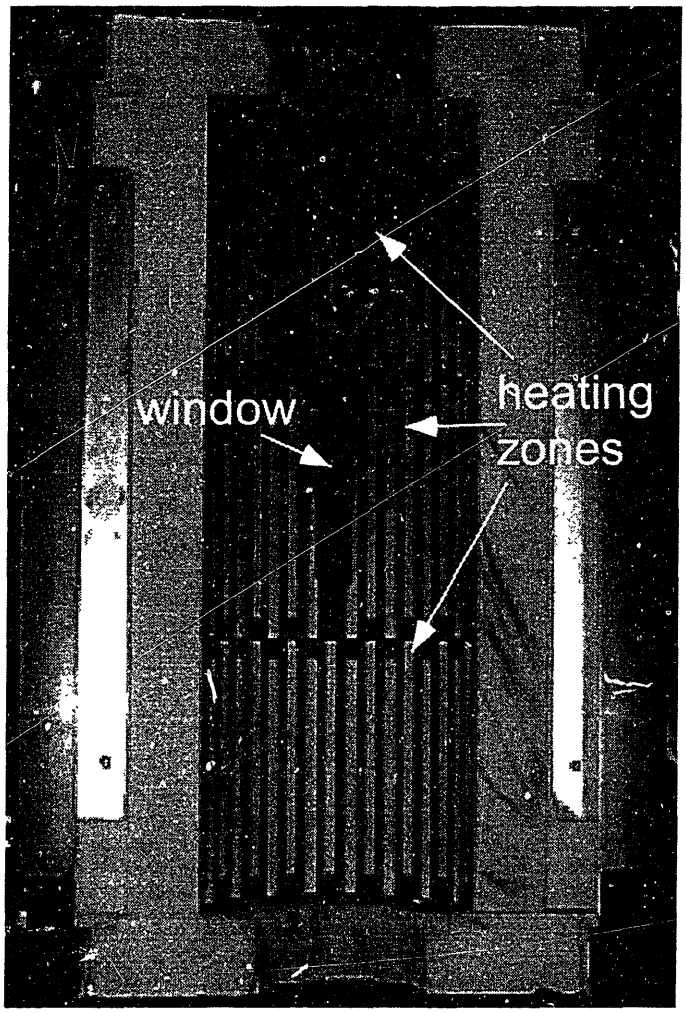

Figure 5.6 Photograph of interior of split-cylinder furnace.

Once in position with the 25.4-mm gage length set, the extensometer was calibrated by the Instron 8500+ calibration program using a ±10% shunt calibration jumper supplied by Epsilon Technology.

Detailed illustrations of the positioning of the coupon inside the test furnace are shown in Figures 5.7 and 5.8. The two figures are identical one-quarter-scale sketches that contain different information about the setup. In Figure 5.7, the various components, including the thermocouples and extensometer, are labeled. In Figure 5.8, the dimensions of the setup are specified.

At the beginning of each test, a coupon was clamped in the upper grip of the testing machine and the thermocouples were wired to the data acquisition board. In tests measuring at-temperature properties, the extensometer was attached to the edge of the specimen and calibrated before the furnace was closed. In tests measuring residual properties, the extensometer was not attached until after the specimens had cooled and the furnace was opened.

With the coupon in place, the furnace was latched and insulation placed over its top opening. A plastic tent vented by an elephant trunk-style hood was closed around the furnace to ventilate fumes and the furnace was turned on. Rheostats on the furnace controller were adjusted as necessary to keep the temperature in the three heating zones, as measured by the thermocouples attached to the coupon, as even as possible while the furnace heated up to the testing temperature. When the temperature reached within 10°C of the testing temperature, a timer was started. The temperature was kept constant (within 10°C of the testing temperature) for 10 minutes.

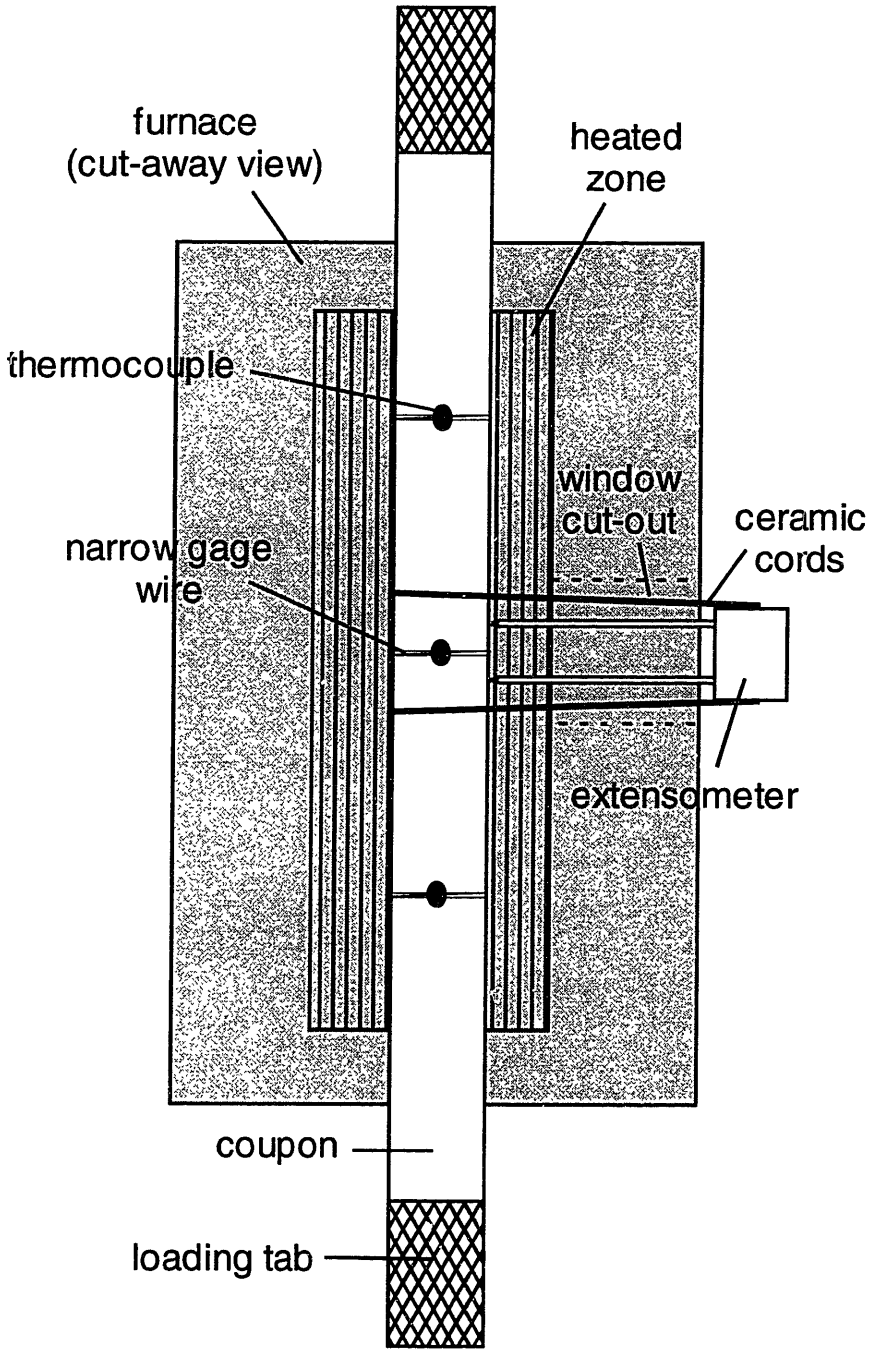

Figure 5.7 Labeled illustration of tensile specimen configuration.

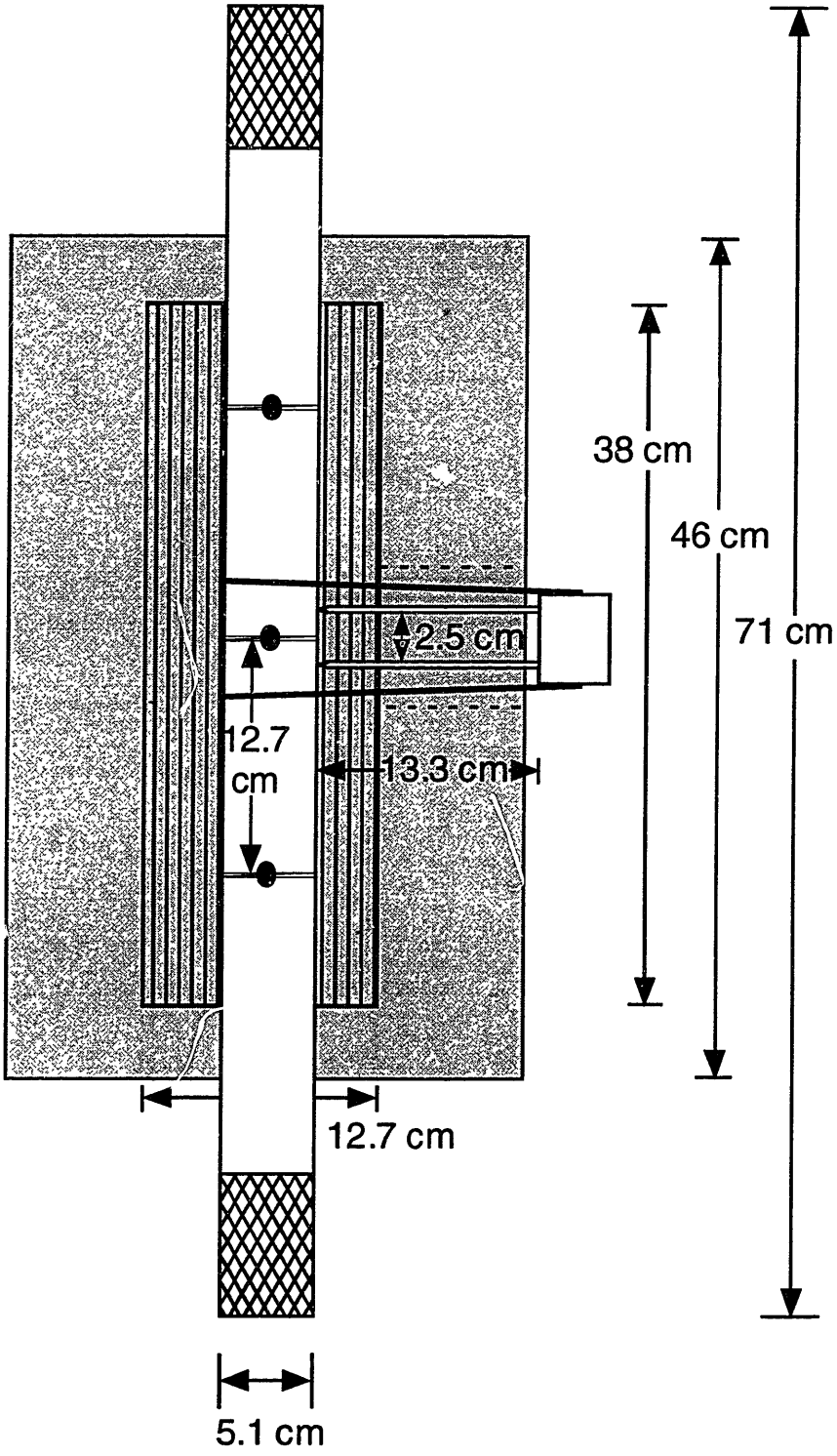

Figure 5.8 Dimensions of tensile specimen configuration.

In Figure 5.9a, typical thermocouple data from a test in which loading was carried out at temperature, an "at-temperature" test, is plotted. In Figure 5.9b, typical thermocouple data from a test in which loading was carried out after the coupon cooled, a "residual" test, is plotted. In both of the plots, the temperature at the start of the test was above room temperature, around 50°C. This occurred because, in each case, the furnace had retained heat from a previous test conducted on the same day. Hence, when the furnace was closed around the specimen at the start of the test, the residual heat of the furnace raised the initial temperature of the specimens. The plots show that the control of the temperature in the furnace was generally good, although not perfect. The temperature within different zones of the furnace varied by as much as 15°C, and the average furnace temperature during the ten-minute hold at the test temperature varied from the nominal test temperature by ±10°C.

After the ten-minute exposure period elapsed, if the coupon was designated for testing at-temperature properties, the bottom tab of the coupon was gripped and loading commenced under position control. The furnace remained at the testing temperature throughout loading. The loading was a 1mm/min stroke-controlled ramp, and continued until failure occurred. For $[90]_{12}$ coupons, failure was defined as the point when the load dropped to zero, signaling that the coupon had fractured into two pieces. For $[0]_4$ coupons, failure was defined as the point when the coupon could no longer bear a load greater than the maximum load achieved.

If the coupon was designated for testing residual properties, the furnace was turned off immediately after the exposure period, the insulation at the top of the furnace was removed, and the furnace was allowed to gradually cool to room temperature. The

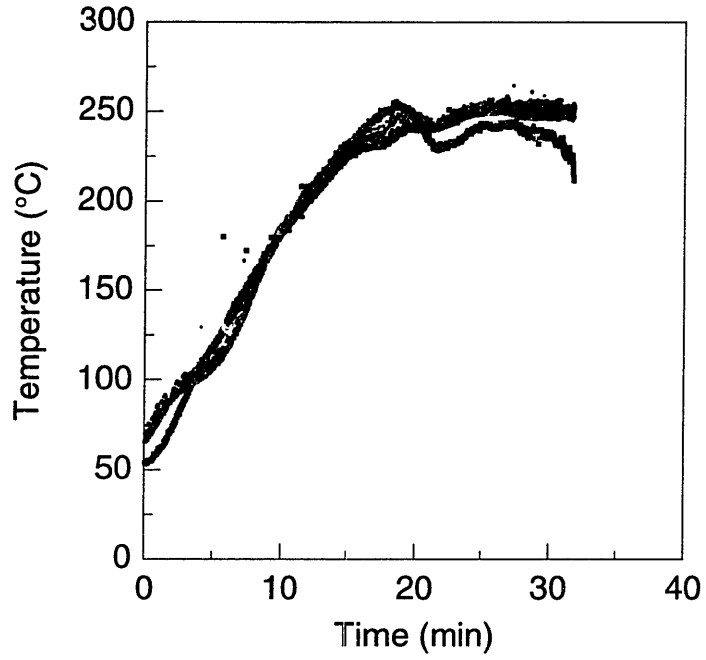

Figure 5.9a Typical temperature data for an at-temperature property test with exposure at 250°C.

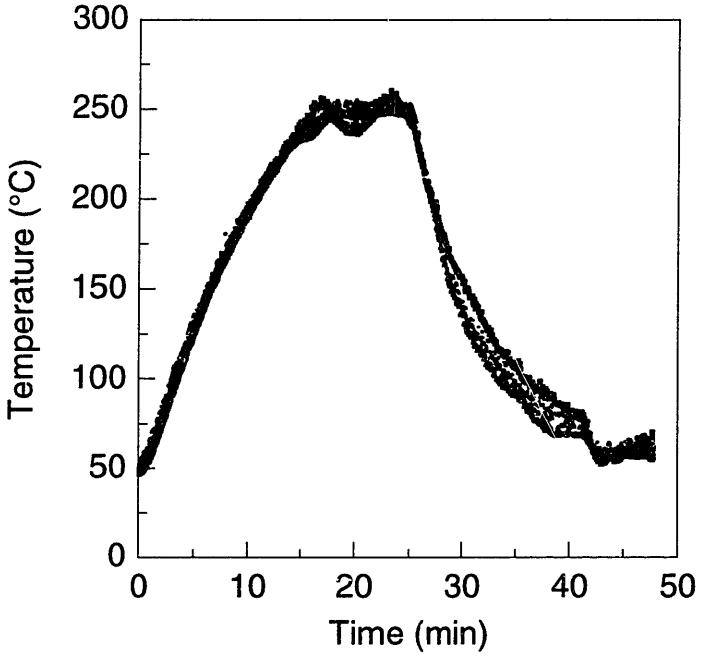

Figure 5.9b Typical temperature data for a residual property test with exposure at 250°C.

coupon cooling rate was kept approximately constant at 10-15°C/min, controlled by gradually opening the furnace wider, opening the plastic tent, and turning on a fan. Once the coupon had reached approximately 50°C, the extensometer was mounted onto the side of the coupon, the bottom tab of the coupon was clamped, and loading commenced as in the at-temperature tests.

Data collection was carried out using a Power Macintosh 7500/100 running a customized LabVIEW virtual instrument. Load, stroke, and strain were recorded from the Instron 8500+, and temperature was recorded from the three thermocouples mounted on the specimen. Data collection rate varied from 0.5 Hz during heating and cool down to 2 Hz during tensile loading.

Strength was calculated from the load data by taking the maximum load carried by the coupon, P_{ult}, and dividing by the average width, w, and thickness, h, of the coupon, which were measured before testing began:

$$\sigma_{ult} = \frac{P_{ult}}{wh} \tag{5.1}$$

Stiffness was calculated by performing a linear fit to stress data plotted against strain data. The curve fit was done using the linear curve fit feature of the Kaleidagraph® software program. Details of the curve fits are described in Chapter 6.

The degradation state of the epoxy matrix in each coupon at the end of testing was calculated using the thermocouple data. The temperatures of the upper, middle, and lower thermocouples at each time were averaged, and a spreadsheet based on the thermal degradation model developed in Section 4.2.2 was used to calculate the degradation state

as a function of time up to the end of testing. For at-temperature tests, the degradation state at the end of the ten-minute temperature hold was calculated. For residual tests, the degradation state at the end of the cool down period was calculated.

5.2.2 Test Matrices

The test matrix for the tensile tests was designed to show the full spectrum of transverse and longitudinal material property behavior and to contrast at-temperature and residual properties. The results of previous studies guided the test matrix development.

As noted earlier, previous studies showed complete transverse property loss by 300°C. This temperature was therefore chosen as the maximum exposure temperature for the transverse coupons. The maximum exposure temperature for the longitudinal coupons was 400°C. This was chosen primarily because a ten-minute exposure at 400°C would induce complete matrix degradation. Longitudinal properties were therefore measured from coupons with degradation states ranging from 0 up to 1.

The test matrix is shown in Table 5.3. Tests were conducted at intervals of 50°C, except between room temperature and 150°C, in which range no property changes were anticipated based on previous studies. Three at-temperature property tests and three residual property tests were conducted for each type of coupon for each exposure temperature. In each case, the coupon was held at the test temperature for ten minutes.

A supplementary test matrix was developed to evaluate the residual properties of transverse coupons with different thermal histories but equivalent degradation states. The degradation model was used to determine exposure time and temperature combinations

that would induce the same amount of degradation as a ten-minute exposure at 300°C. A shorter exposure at a temperature higher than 300°C and a longer exposure at a temperature below 300°C were chosen. These test conditions are tabulated in Table 5.4. Degradation that occurred during the cool down following the at-temperature exposure was considered in selecting test conditions.

Table 5.3 Tensile test matrix

Lay-up	Test condition	25°C	150°C	200°C	250°C	300°C	350°C	400°C
$[0]_4$	At-temperature	3[a]	3	3	3	3	3	3
$[0]_4$	Residual	3	3	3	3	3	3	3
$[90]_{12}$	At-temperature	3	3	3	3	3	0	0
$[90]_{12}$	Residual	3	3	3	3	3	0	0

[a] Number of coupons tested
Exposure time 10 minutes.

Table 5.4 Supplementary tensile test matrix

Lay-up	Test condition	Exposure temperature (°C)	Exposure time (min)	Number of coupons	Predicted degradation state
$[90]_{12}$	Residual	317	0.1	3	0.022
$[90]_{12}$	Residual	275	55	3	0.023

CHAPTER 6

RESULTS

Experimental and analytical results are presented in this chapter. The first section includes analytical predictions of the thermal response. Nondimensional parameters controlling the thermal response are identified, and charts summarizing the conditions under which a one-dimensional thermal model can accurately model a multi-dimensional temperature field are presented in terms of those parameters. The second section contains results from thermogravimetry experiments conducted to explore the thermal degradation characteristics of epoxy. Degradation is modeled by applying an Arrhenius rate equation and determining reaction constants from experimental data. A procedure for assessing the degradation state of a heat-exposed composite laminate is presented. Finally, results from a series of tensile tests conducted to evaluate changes in the ply strength and stiffness are given in the third section. Empirical models of material properties as functions of temperature and degradation state are developed.

6.1 THERMAL RESPONSE

Parametric studies exploring the role of nondimensional parameters in determining the temperature distribution inside a plate heated via convection along part of the lower surface were conducted. The geometry of the plate is shown in Figure 4.4. The goals of the parametric studies were to determine how changing the values of the nondimensional parameters affects the heat flow through the cross-section and to

identify, in terms of the nondimensional parameters, the conditions under which the through-thickness temperature distribution in the center of the plate can be accurately modeled using a one-dimensional thermal model. This is an important consideration because a one-dimensional model is less computationally intensive and may enable the use of one-dimensional models for the determination of effects that depend on temperature, thereby enabling more efficient evaluations of such effects. The actual temperature distribution in the plate shown in Figure 4.4 varies in two dimensions: laterally, in the x-direction, and through the thickness, in the z-direction. In a physical sense, the question of, "How accurately can one determine the through-thickness temperature distribution in a heated structure while ignoring lateral heat flow?" needs to be answered.

It should be recalled that in Section 4.1.1, three nondimensional parameters, the geometry-orthotropy parameter, $\mathcal{L}_{xz}$, Biot number, Bi_z, and Fourier number, Fo_z, were identified as controlling the temperature distribution in a two-dimensional temperature field. Those parameters, defined in Equations 4.14, 4.13, and 4.12, respectively, are repeated here for convenience:

$$\mathcal{L}_{xz} = \frac{k_z L_x^2}{k_x L_z^2} \tag{6.1}$$

$$Bi_z = \frac{h_{cz} L_z}{k_z} \tag{6.2}$$

$$Fo_z = \frac{t_{ref} k_z}{\rho c L_x^2} \tag{6.3}$$

In the parametric study, the reference lengths L_x and L_z are the heated width w and thickness h, respectively, of the plate, as shown in Figure 4.4, and the reference time, t_{ref},

is the duration of the simulation. The effects of varying the geometry-orthotropy parameter and the Biot number were investigated in the parametric study. The parameters varied in the course of the study were the axial thermal conductivity, k_x, the thickness, L_z, the heated width, L_x, and the heat transfer coefficient, h_c. Other parameters were held constant.

To conduct the study, the Temper finite difference thermal code described in Section 4.1.3 was used to calculate the cross-sectional temperature distribution inside the plate. The structure is 500 mm wide and the width of the heated area is varied from 50 mm to 100 mm; the width of the structure is much larger than the width of the heated region, thus the structure can be considered semi-infinite in regards to the heat flow. The thickness of the structure is varied from 5 to 10 mm. The mesh used to discretize the cross-section in the Temper code is shown in Figure 4.5. Thirteen through-thickness nodes and sixty-one lateral nodes were used in the discretization. The structure is initially at 0°C, and is heated at the start of the simulation by a 1000°C flame with a heat transfer coefficient that is varied from 50 W/m^2·K to 200 W/m^2·K. Round numbers were selected for these parameters out of convenience.

These exercises are intended to explore the roles of various parameters in determining the thermal response, and not to provide realistic temperature predictions that could be correlated with experimental data. Thus, the material properties selected for the series of parametric studies were also round numbers. It should be noted, however, that the material properties selected are of the same order of magnitude as the properties of graphite/epoxy. The through-thickness thermal conductivity, k_z, is set at 1 W/m·K; density, ρ, at 1000 kg/m^3; and specific heat, c, at 1000 J/kg·K. The axial thermal

conductivity, k_x, is varied between 10 W/m·K and 40 W/m·K as part of the parametric study.

The output from the Temper code, i.e. the cross-sectional temperature distribution in the mesh shown in Figure 4.6, can be presented graphically as a contour plot, such as the one shown in Figure 6.1a. Since the structure is much wider than the heated area, the plot is truncated along the width to focus on the temperature distribution in the material surrounding the heated area. The heated area is denoted in the plot with upward-pointing arrows. The axes of the plot show the dimensions of the cross-section, and the contours inside represent regions of equal temperature. The vertical axis is a line of symmetry, hence the physical structure modeled is twice as wide. The different scales of the two axes should be noted: while the contour plot appears nearly square, the width of the structure is much greater than the thickness. The thickness to width ratio of each element in the plot is approximately 1:5.

In the next three sub-sections, the results of the parametric studies are described.

6.1.1 Role of the Geometry-Orthotropy Parameter

The role of the geometry-orthotropy parameter, $\mathcal{L}_{xz}$, in determining the cross-sectional temperature distribution was studied in the course of two parametric studies. The Biot number and Fourier number of the structures modeled were held constant while the geometry-orthotropy parameter was varied. The parameter was varied in two ways: by changing the ratio of the axial thermal conductivity to the through-thickness thermal

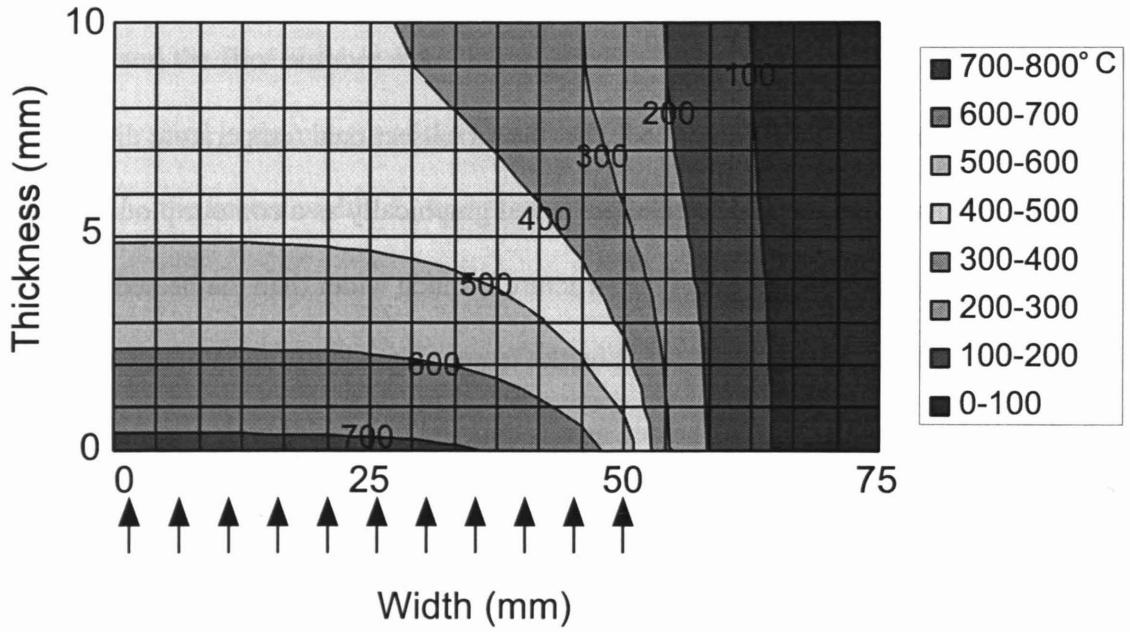

Figure 6.1a Temperature distribution in half of 10 mm thick plate with orthotropy ratio of 10 heated along 100 mm of its width (geometry-orthotropy parameter of 10).

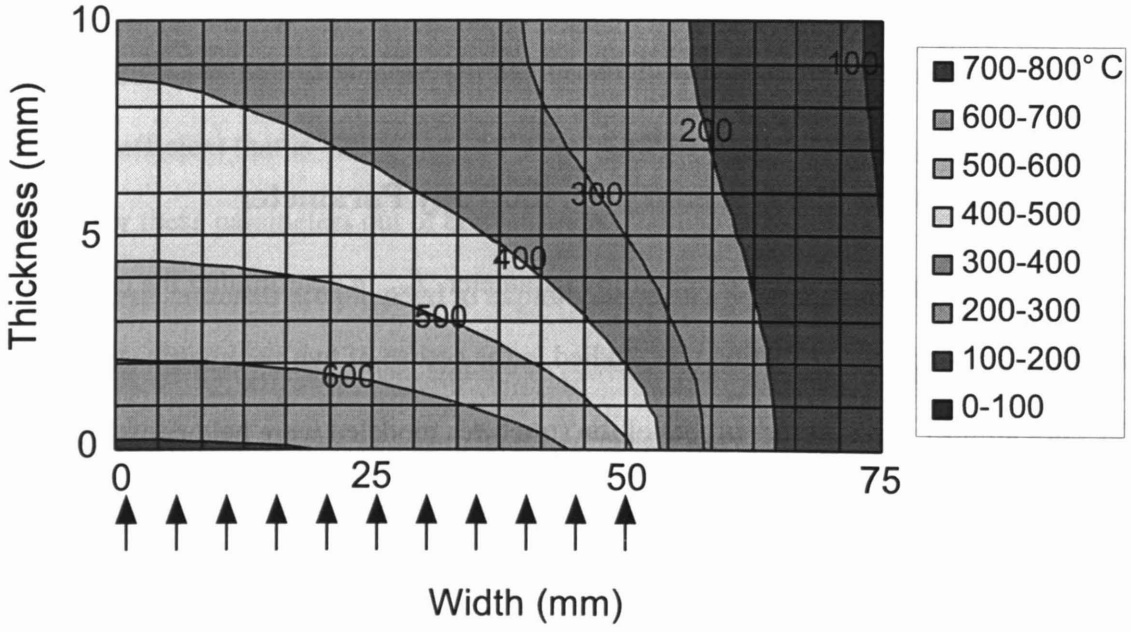

Figure 6.1b Temperature distribution in half of 10 mm thick plate with orthotropy ratio of 40 heated along 100 mm of its width (geometry-orthotropy parameter of 2.5).

conductivity, k_x/k_z (the "orthotropy ratio"), and by changing the ratio of the thickness of the structure to the heated width of the structure, L_z/L_x. The effect of changing the orthotropy ratio is considered first.

In Figures 6.1a and 6.1b, two temperature contour plots are shown. The two cases vary only in the ratio of axial thermal conductivity, k_x, to through-thickness thermal conductivity, k_z. In Figure 6.1a, the axial thermal conductivity is 10 W/m·K, ten times the through-thickness thermal conductivity. In the temperature contour plotted in Figure 6.1b, k_x is raised to 40 W/m·K, making the orthotropy ratio 40. In each of the cases, the heat transfer coefficient of the flame is set at 200 W/m^2·K. Expressing the parameters of the two cases nondimensionally, the Biot number for both cases is 2 and the Fourier number for both cases is 0.6. In the first case, the geometry-orthotropy parameter is 10, in the second case it is 2.5.

The shape of the temperature contours is used as a basis for comparing the two plots. Heat flows along the temperature gradient, perpendicular to the contours, hence the shape of the contours illustrates the direction of heat flow. In Figure 6.1a, there is a wide region, out to approximately 25 mm, in which there is minimal lateral temperature variation. Within this 25 mm-wide region, the temperature contours are nearly flat, indicating that heat flows straight through the structure. Further out, the temperature contours curve downward and become nearly vertical as the heat marches laterally into the insulated part of the volume. The plot in Figure 6.1b has no wide region with flat temperature contours. From the very center of the structure, the temperature contours are curved. This indicates that there is significant heat flow in both the through-thickness and lateral directions. Since the only difference between the two cases is the value of the

geometry-orthotropy parameter, it can be stated that the lower the geometry-orthotropy parameter, the more important lateral heat flow is relative to through-thickness heat flow.

In the second parametric study, the geometry-orthotropy ratio was varied by changing the geometry of the structure. In Figures 6.2a, 6.2b, and 6.2c, the temperature contours of structures with three different geometries are compared. The plot in the center, Figure 6.2b, is identical to Figure 6.1a: a 10 mm-thick laminate with an orthotropy ratio of 10. Figure 6.2a and 6.2c show the effect of varying the ratio of the laminate thickness to the width of the heated area while keeping other parameters constant. In Figure 6.2a, the geometry ratio is varied by halving the thickness of the specimen to 5 mm. In Figure 6.2c, the ratio is varied by reducing the half-width of the heated area from 50 mm to 25 mm. The ratios of the widths of the heated areas to the plate thicknesses in Figures 6.2a, b, and c are 20, 10, and 5, respectively. This results in respective geometry-orthotropy parameters of 40, 10, and 2.5.

In order to keep the Biot number and Fourier numbers constant in all three cases, it was necessary to adjust both the heat transfer coefficient and the duration of the simulation in the case of the thinner structure. That is because the thickness of the structure, L_z, figures into the calculations of both parameters. To maintain constant Biot and Fourier numbers of 2 and 0.6, respectively, it was necessary to raise the heat transfer coefficient to 400 $W/m^2 \cdot K$ and reduce the duration of the simulation from 60 seconds to 15 seconds for the case of the structure with a thickness of 5 mm.

In Figure 6.2a, there is a region nearly 40 mm wide in which the temperature contours are flat and through-thickness heat flow dominates. This region in which through-thickness heat flow dominates is nearly twice as wide as the comparable region

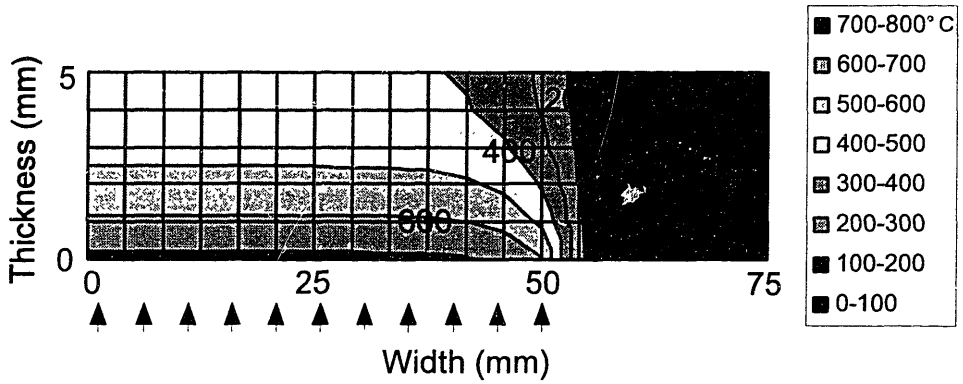

Figure 6.2a Temperature distribution in half of 5 mm thick plate with orthotropy ratio of 10 heated along 100 mm of its width (geometry-orthotropy parameter of 40).

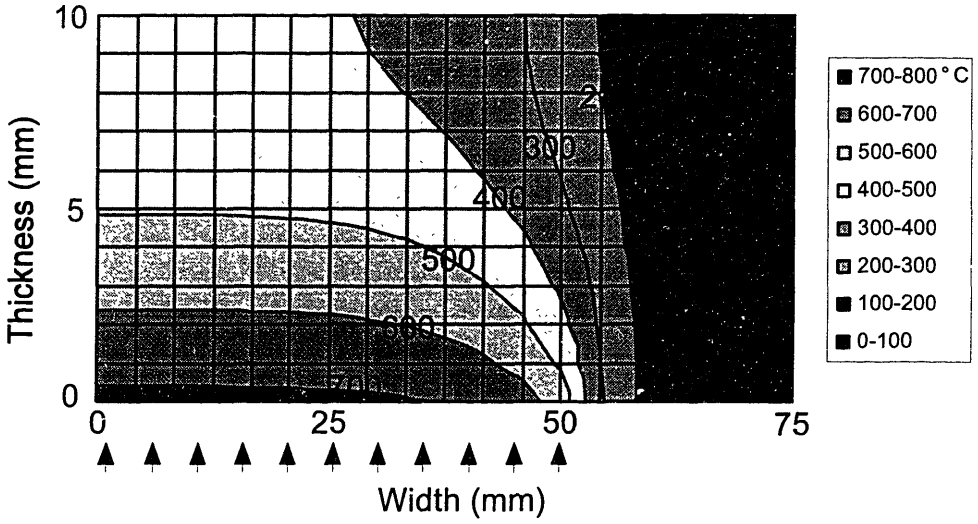

Figure 6.2b Temperature distribution in half of 10 mm thick plate with orthotropy ratio of 10 heated along 100 mm of its width (geometry-orthotropy parameter of 10).

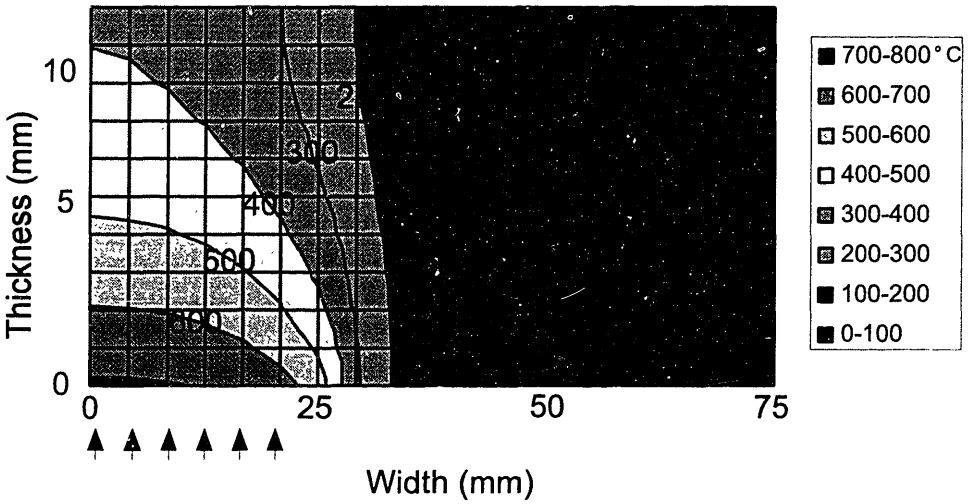

Figure 6.2c Temperature distribution in half of 10 mm thick plate with orthotropy ratio of 10 heated along 50 mm of its width (geometry-orthotropy parameter of 2.5).

in Figure 6.2b, in which the thickness-to-width ratio is lower. When the ratio is reduced further, as in the case shown in Figure 6.2c, the region of flat temperature contours is nearly nonexistent. The result obtained in the first example is reinforced here: decreasing the geometry-orthotropy ratio, in this case by decreasing the ratio of the thickness of the structure to the width of the heated area, increases the importance of lateral heat flow relative to through-thickness heat flow.

6.1.2 Role of the Biot Number

The role of the Biot number, Bi_z, in determining the cross-sectional temperature distribution was studied by varying the Biot number while holding the geometry-orthotropy parameter and the Fourier number constant. The Biot number was varied by changing the flame intensity, i.e. the heat transfer coefficient. The flame temperature, orthotropy ratio, and geometry were not changed.

Figure 6.3a is the familiar contour plot from Figures 6.1a and 6.2b. Figure 6.3b is an identical structure heated for the same duration by a flame of the same temperature, but with a heat transfer coefficient reduced by a factor of four, from 200 $W/m^2 \cdot K$ to 50 $W/m^2 \cdot K$. In these cases, the geometry-orthotropy parameter is 10 and the Fourier number is 0.6. The Biot number varies from 2 in the first case to 0.5 in the second.

The shapes of the contours in Figure 6.3b are generally similar to the shapes of the contours in Figure 6.3a. The difference in the two plots is that in Figure 6.3b the temperatures associated with these contours are much lower than in Figure 6.3a. Reducing the Biot number slows down the rate at which the plate heats up, meaning that for a given Fourier number the temperature throughout the plate will be lower.

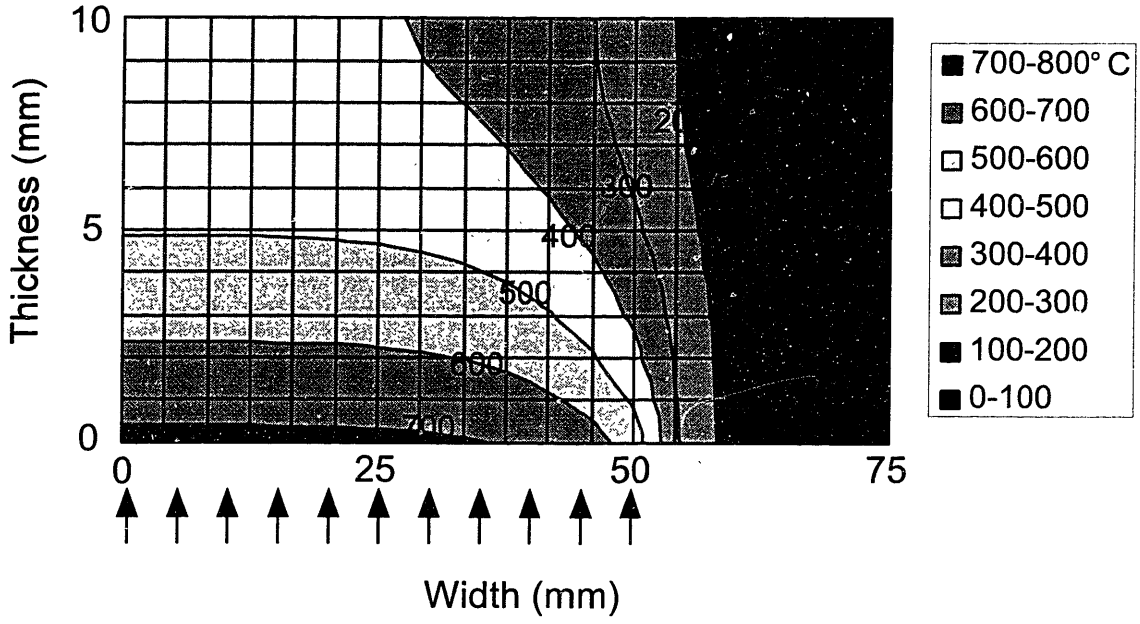

Figure 6.3a Temperature distribution in half of 10 mm thick plate heated along 100 mm of its width by flame with heat transfer coefficient of 200 W/m^2·K (Biot number of 2).

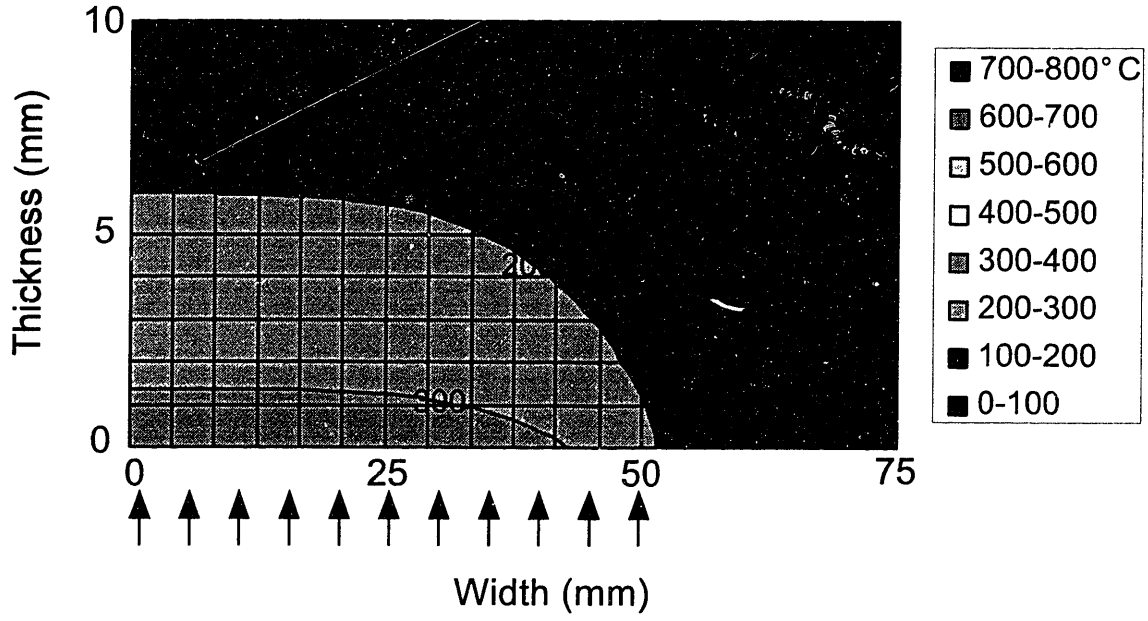

Figure 6.3b Temperature distribution in half of 10 mm thick plate heated along 100 mm of its width by flame with heat transfer coefficient of 200 W/m^2·K (Biot number of 0.5).

It is useful to consider how the shape of the temperature contours is related to the magnitude of the internal temperatures. This can be done by extending the simulation that produced the contour plot in Figure 6.3b until the temperature of a particular point is equal to the temperature of the same point in the case shown in Figure 6.3a. The point in the center of the back face of the plate (at *width* equal to 0 mm, *thickness* equal to 10 mm) is considered. In the case shown in Figure 6.3a, the temperature of the point at the end of the simulation is 412°C. If the simulation shown in case Figure 6.3b is run until the temperature of the center point on the back face reaches 412°C, the result is the temperature distribution shown in Figure 6.4. The Biot number and geometry-orthotropy parameter for the case shown in Figure 6.4 are 0.5 and 10, respectively, the same as those for the case shown in Figure 6.3b. However, the Fourier number of the case shown in Figure 6.4 is now 1.4, over twice as large as in the previous case.

The plot in Figure 6.4 lacks the flat temperature contours indicative of straight through-thickness heat flow. The above exercise demonstrates that while reducing the Biot number does not change the shape of the temperature distribution for a given Fourier number, the smaller Biot number reduces the magnitude of the temperatures in the temperature distribution. If the magnitude of the temperatures is held constant when two cases are compared, then the case with the smaller Biot number will have more significant lateral heat flow relative to the through-thickness heat flow.

6.1.3 Approximation Error and Nondimensional Parameters

The lessons learned about the roles of the nondimensional parameters in determining the shape of the temperature distribution can be applied to assess the

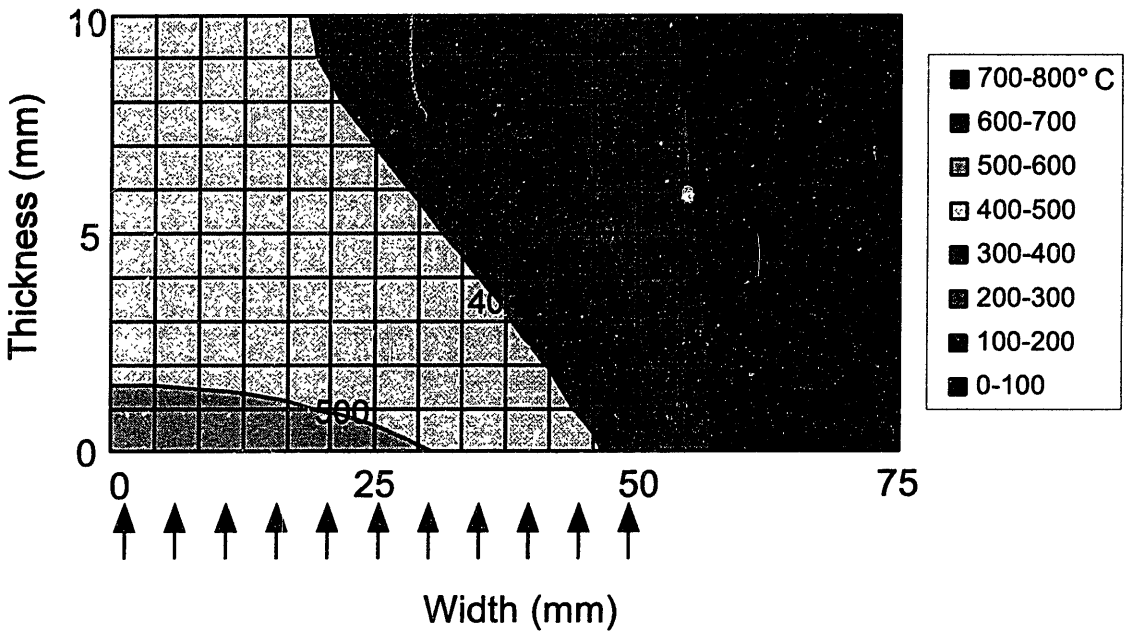

Figure 6.4 Temperature distribution in half of 10 mm thick plate heated along 100 mm of its width by flame with heat transfer coefficient of 50 $W/m^2 \cdot K$ until back face temperature reaches 412°C.

accuracy of a one-dimensional approximation of the through-thickness temperature distribution in center of such a configuration. In a one-dimensional model, no lateral heat flow is modeled. Therefore, cases that demonstrated wide regions with flat temperature contours would be good candidates for accurate one-dimensional modeling approximations, as wide flat temperature contours are associated with flow straight through the thickness.

The parametric studies demonstrated that the higher the geometry-orthotropy parameter and the higher the Biot number, the more important through-thickness heat flow is relative to lateral heat flow. By extension, then, the higher the geometry-orthotropy parameters and Biot number, the more accurate a one-dimensional modeling approximation would be. The accuracy of such an approximation can be quantified by comparing the results of a one-dimensional model with the "correct" results from a two-dimensional model. The metric used here is the time required for the point in the center of the back face of the plate to reach a given temperature. When lateral heat flow is considered, as in a two-dimensional model, the time required for the point on the back face to reach the target temperature will be longer. The error metric is

$$\%\ Error = \frac{Time_{2-Dmodel} - Time_{1-Dmodel}}{Time_{2-Dmodel}} \tag{6.4}$$

In Figures 6.5a and 6.5b, the error associated with a one-dimensional approximation is quantified as a function of the geometry-orthotropy parameter and the Biot number. In Figure 6.5a, the Biot number is held constant at 1 while the geometry-orthotropy parameter is varied, and in Figure 6.5b the reverse is true, with the geometry-

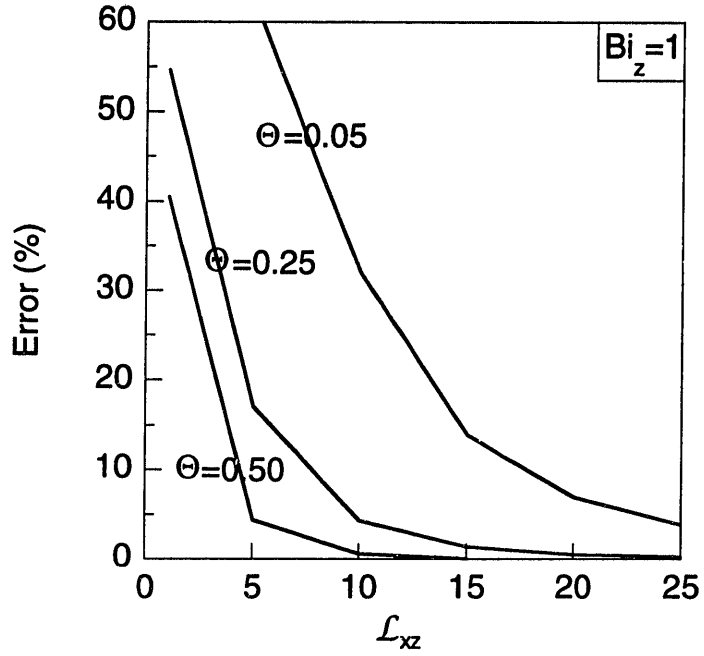

Figure 6.5a Error associated with a one-dimensional modeling approximation as a function of geometry-orthotropy parameter for different nondimensional back face temperatures (constant Biot number of 1).

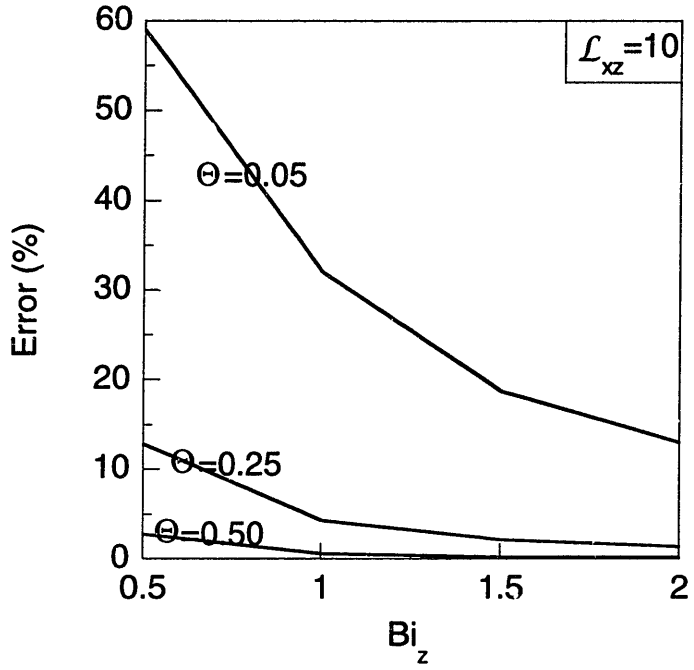

Figure 6.5b Error associated with a one-dimensional modeling approximation as a function of Biot number for different nondimensional back face temperatures (constant geometry-orthotropy parameter of 10).

orthotropy parameter held constant at 10. To make the plots more general, the back face temperature used in the error criterion is expressed in nondimensional form. From Equation 4.9, the nondimensional temperature is:

$$\Theta = \frac{(T - T_\infty)}{(T_o - T_\infty)} \tag{6.5}$$

where T is the temperature of the back face, T_∞ is the flame temperature (1000°C in this case) and T_o is the initial temperature (0°C in this case). Initially, the nondimensional temperature Θ is equal to 1, since T and T_o are equal. As the temperature of the back face increases, Θ approaches zero. In the plots in Figures 6.5a and 6.5b, Θ is varied from 0.5 to 0.05.

The plots in Figures 6.5a and 6.5b demonstrate what was qualitatively demonstrated before: increasing the geometry-orthotropy parameter and the Biot number improves the accuracy of a one-dimensional modeling approximation of the through-thickness temperature distribution by reducing the associated approximation error. The plot also shows that for a given geometry-orthotropy parameter and Biot number, the higher the nondimensional temperature, i.e. the further the temperature distribution is from equilibrium, the better the approximation. This indicates that a one-dimensional approximation is better for determining transient temperature solutions.

The two plots can be unified in a three-dimensional surface plot for a particular value of the nondimensional back face temperature. In Figure 6.6, the error associated with a nondimensional back face temperature of 0.5 is shown as a function of geometry-orthotropy parameter and Biot number.

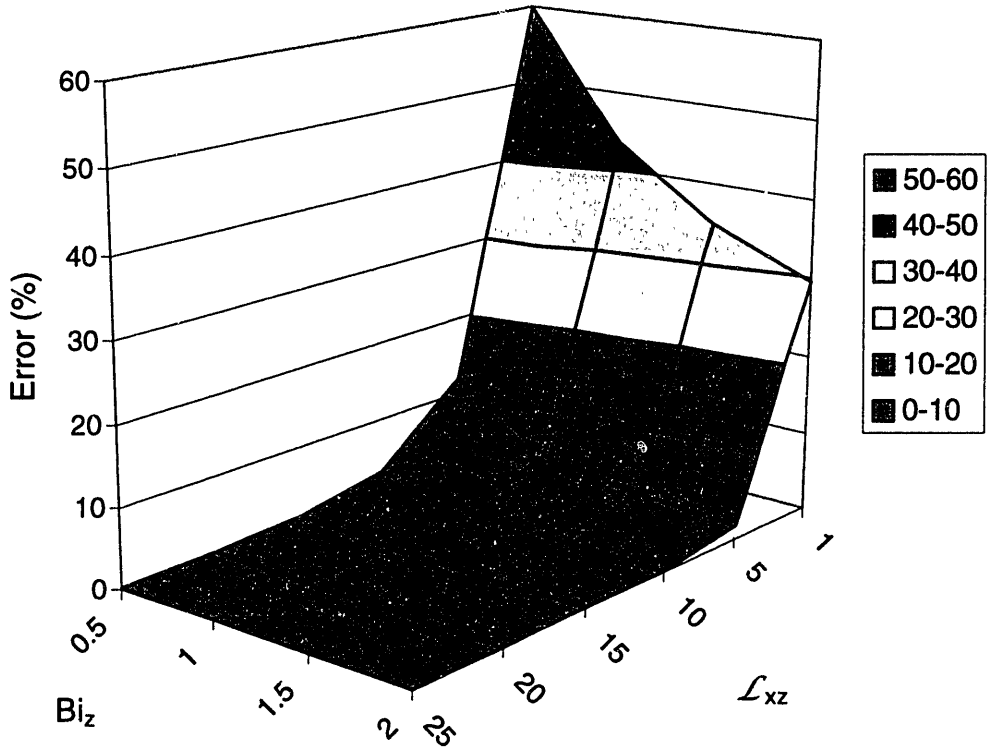

Figure 6.6 Error associated with a one-dimensional modeling approximation as a function of geometry-orthotropy parameter and Biot number for a nondimensional back face temperature of 0.5.

Finally, if a maximum allowable approximation error is established, it is possible to determine the conditions under which a one-dimensional approximation is valid. As an example, the maximum allowable approximation error is set at 5%. Figure 6.7 shows the minimum allowable nondimensional back face temperature for which the approximation error is less than 5% for a range of geometry-orthotropy parameters and Biot numbers. The curves in Figure 6.7 were generated by repeatedly running the Temper code for longer simulations that reached higher back face temperatures until the error reached 5%, for various discrete combinations of Biot number and geometry-orthotropy parameter. Using Figure 6.7, one can determine whether or not a one-dimensional approximation of the through-thickness temperature distribution is accurate within 5% for a given Biot number, geometry-orthotropy parameter, and maximum back face temperature.

If the approximation is sufficiently accurate, then the structure depicted in Figure 4.5 can be treated as an infinite plate exposed to the environment on one entire surface. Solutions to this classical one-dimensional transient heat conduction problem appear in the form of charts in many heat transfer textbooks [47,48]. These charts can be used to determine the temperature distribution through the structure.

6.2 DEGRADATION STUDIES

The results from the thermogravimetric analysis (TGA) studies are presented in this section. Degradation was modeled using an Arrhenius rate equation. Experimental results from the TGA studies were used to determine appropriate reaction constants for the model. These results are presented, along with the results of experiments designed to

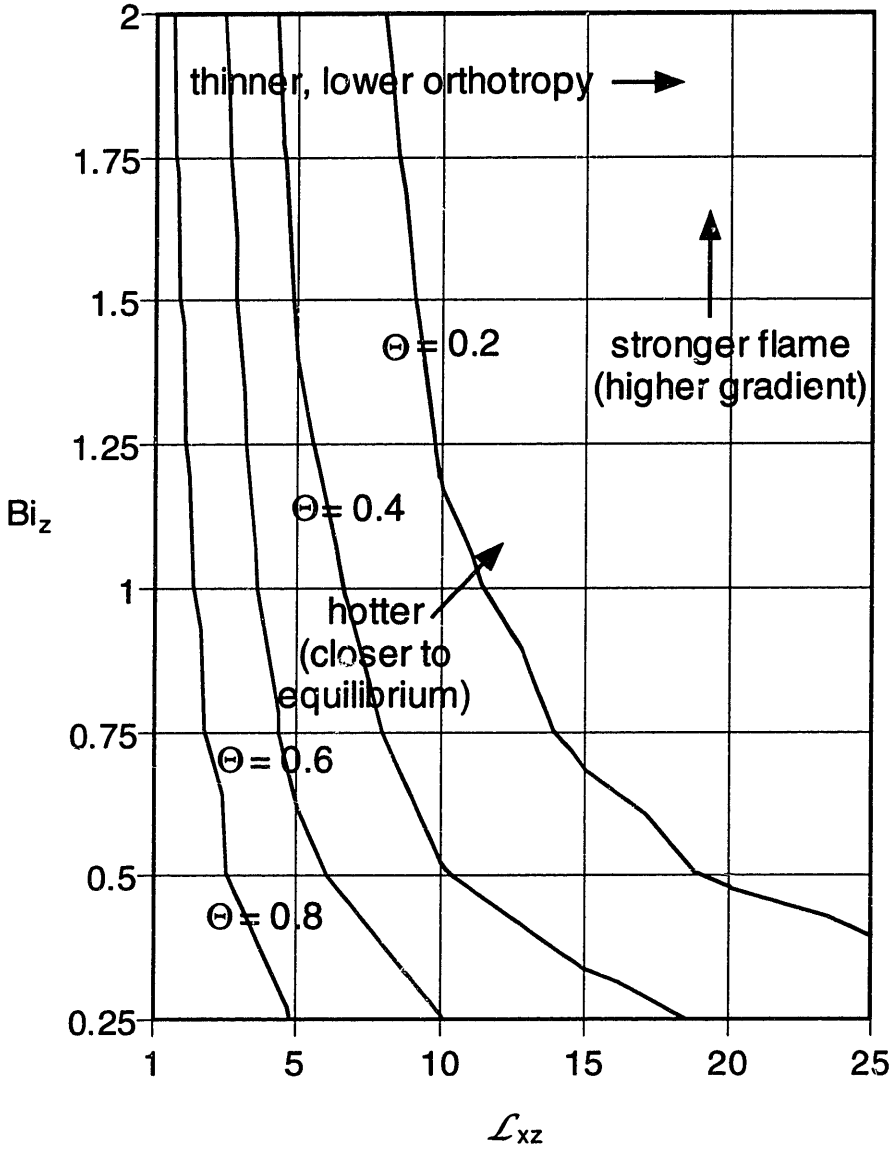

Figure 6.7 Contour map showing minimum nondimensional back face temperature for which error associated with one-dimensional modeling approximation is less than 5%, as a function of geometry-orthotropy parameter and Biot number.

verify the model and experiments designed to evaluate a degradation assessment technique.

6.2.1 Results of TGA Tests and Development of Degradation Model

Dynamic heating thermogravimetric analysis experiments on 3501-6 epoxy produced mass and mass loss rate data as functions of temperature. From each set of raw data, normalized mass loss and normalized mass loss rate were calculated using Equations 4.40 and 4.41. As discussed in Chapter 4, normalized mass loss is assumed to equate with degradation state, α, and hence normalized mass loss rate is equated with the rate of degradation, $\partial\alpha/\partial t$. Figure 6.8 shows a typical plot of normalized TGA data from a test conducted at 10°C/min. Results from all other tests are cataloged in Appendix B. The degradation state stays is very small up to 250°C, at which temperature detectable degradation begins, with the rate increasing rapidly with increasing temperature. The rate of degradation peaks at 0.198/min at a temperature of 373°C and then decreases as the degradation state becomes large. The rate of degradation is very small by the time the temperature reaches 500°C as the degradation state of the sample is over 0.9 by this point.

Another piece of data collected from the dynamic heating tests is char yield. The char yields from each test, calculated using Equation 4.50, are tabulated in Table 6.1. The average char yield was 0.233, with a coefficient of variation of 7.6%.

Figures 6.9 and 6.10 show the degradation state and rate of degradation results from tests at different heating rates. While all the tests were performed from 25°C up to

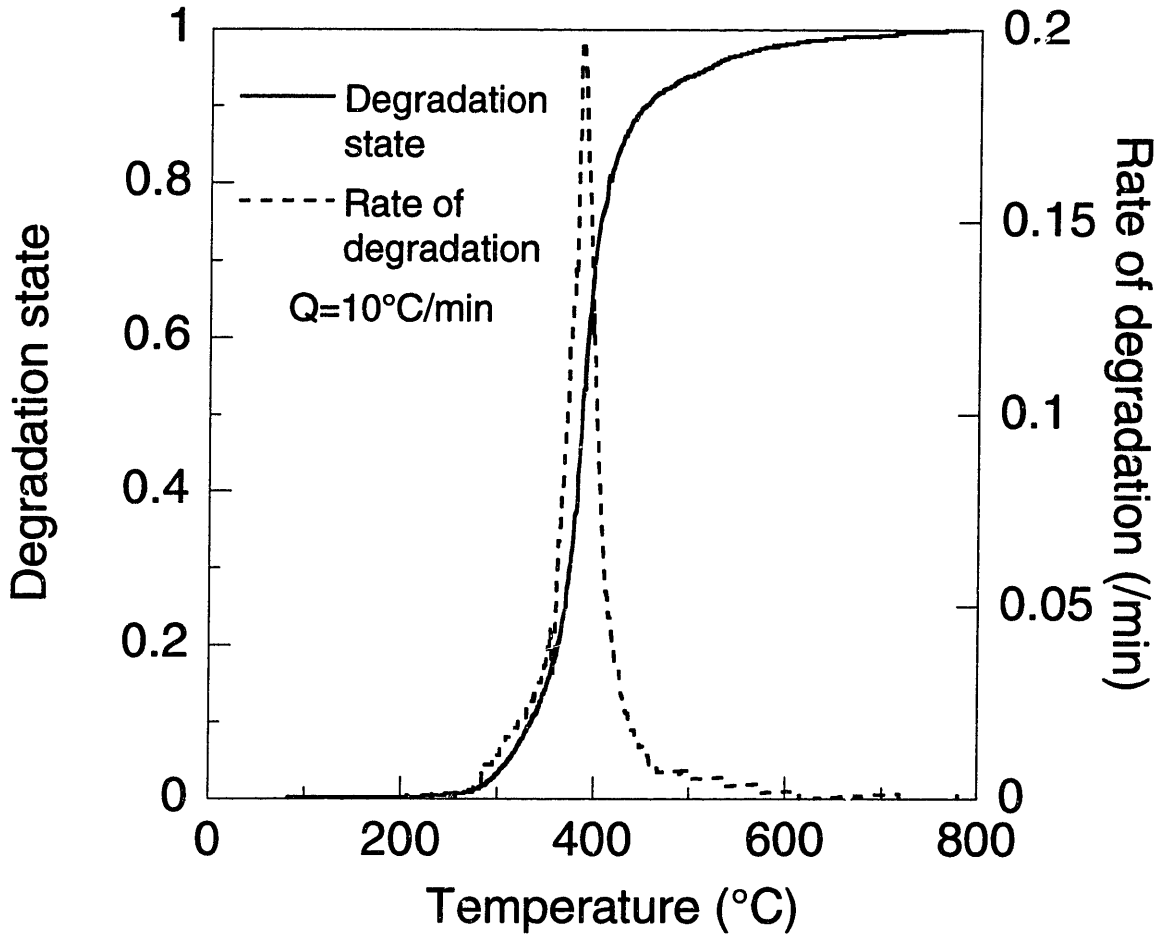

Figure 6.8 Typical plot of degradation state and rate of degradation data versus temperature for a TGA test conducted at 10°C/min.

Table 6.1 Char yields from dynamic heating tests

Heating Rate (°C/min)	Char yield (%)
5	22.7
10 (Trial 1)	21.4
10 (Trial 2)	25.5
10 (Trial 3)	22.1
15	24.8

Table 6.2 Summary of maximum degradation rate data from dynamic heating tests

Heating rate (°C/min)	Maximum normalized mass loss rate (/min)	Temperature at max. mass loss rate (°C)	Degradation state at max. mass loss rate
5	0.100	373	0.444
10 (Trial 1)	0.195	389	0.480
10 (Trial 2)	0.191	390	0.485
10 (Trial 3)	0.198	386	0.473
15	0.312	393	0.492

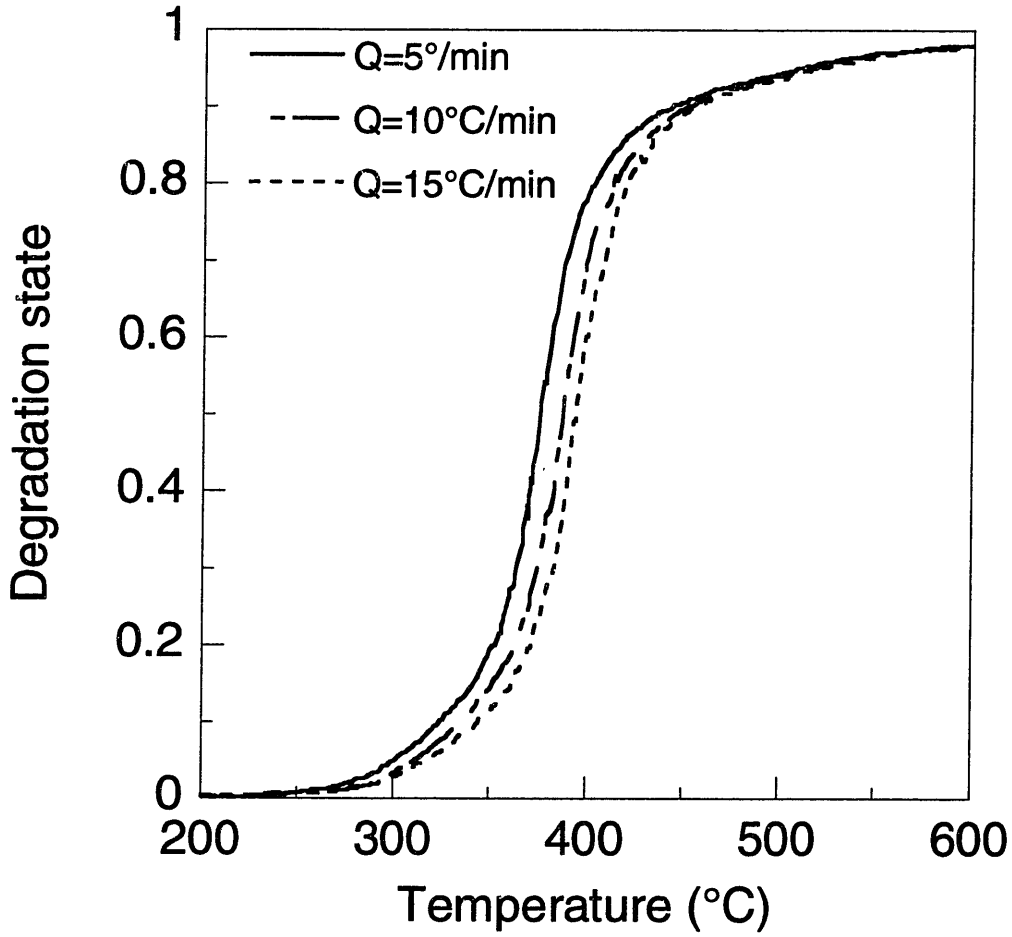

Figure 6.9 Degradation results versus temperature for TGA tests conducted at heating rates of 5°, 10°, and 15°C/min.

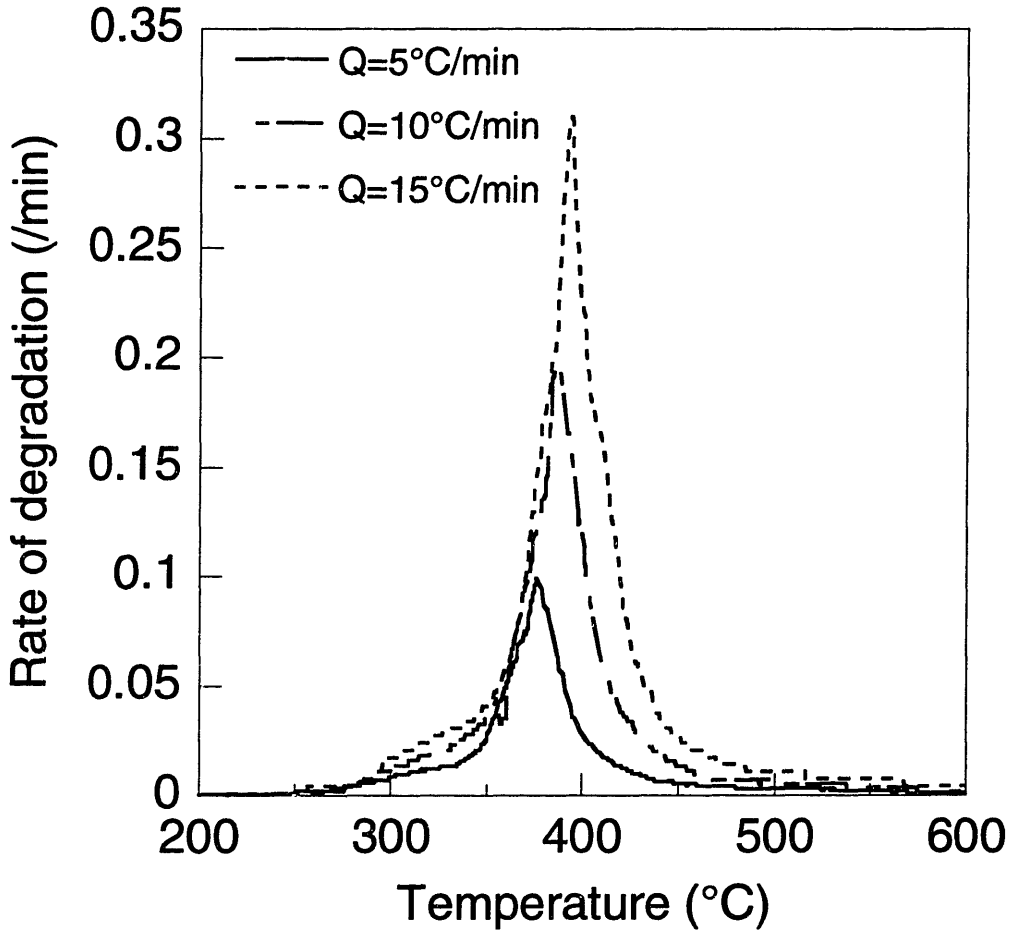

Figure 6.10 Rate of degradation results versus temperature for TGA tests conducted at heating rates of 5°, 10°, and 15°C/min.

800°C, only the data between 200°C and 600°C is presented. Below 200°C, the degradation state and rate of degradation are nearly zero and above 600°C, the degradation state curve asymptotes to one and the rate of degradation curve to zero. The shifts in the curves with increasing heating rate are typical of an Arrhenius-type rate dependent reaction. At higher heating rates, rapid degradation begins at a higher temperature, and the temperature at which the maximum rate of degradation occurs and the magnitude of the maximum rate of degradation are also higher. These values are tabulated in Table 6.2 for the various heating rates. Multiple tests were conducted at 10°C/min to evaluate the repeatability of the results. The data in Table 6.2 indicates that the results from the three tests at 10°C/min are very consistent, lending confidence to the results.

The data in Table 6.2 was used to determine the appropriate reaction constants for a degradation model of 3501-6 epoxy based on an Arrhenius rate equation. Using Kissinger's method [51] as described in Section 4.2.3, a single set of reaction constants was obtained. An optimal fit to the data was obtained with an activation energy, E, of 184.9 kJ/mol, frequency factor, k, of 2.338×10^{14}/min, and a reaction order, n, of 1.

Predictions of the rate of degradation as a function of temperature made using the Arrhenius model and the test conditions from the dynamic heating tests were calculated for epoxy heated from 25°C to 800°C at constant heating rates of 5°, 10°, and 15°C/min. These are presented in Figures 6.11a, 6.11b, and 6.11c and compared with normalized experimental data. The model predictions slightly overestimate the degradation rate between approximately 325°C and 400°C and underestimate the degradation rate at higher temperatures. The R-values for these cases were calculated using a Pearson's R

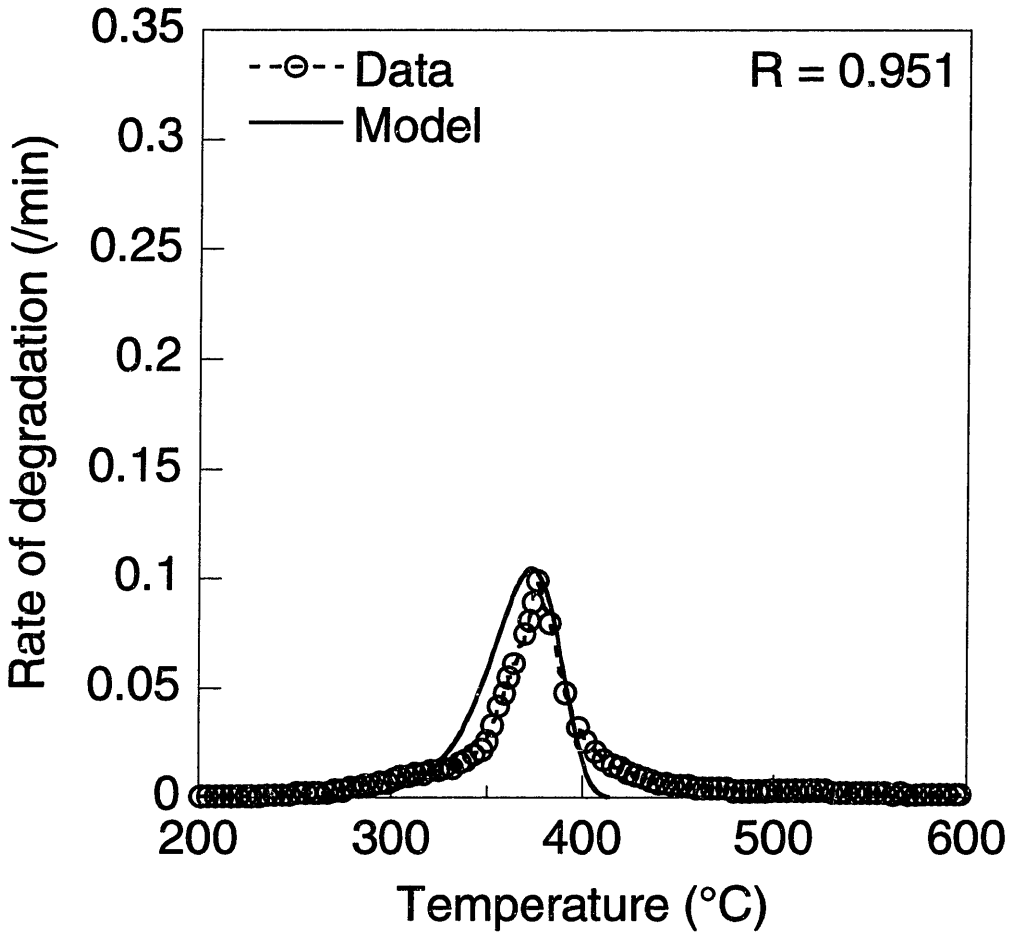

Figure 6.11a Predictions of degradation rate versus temperature compared with data for a heating rate of 5°C/min.

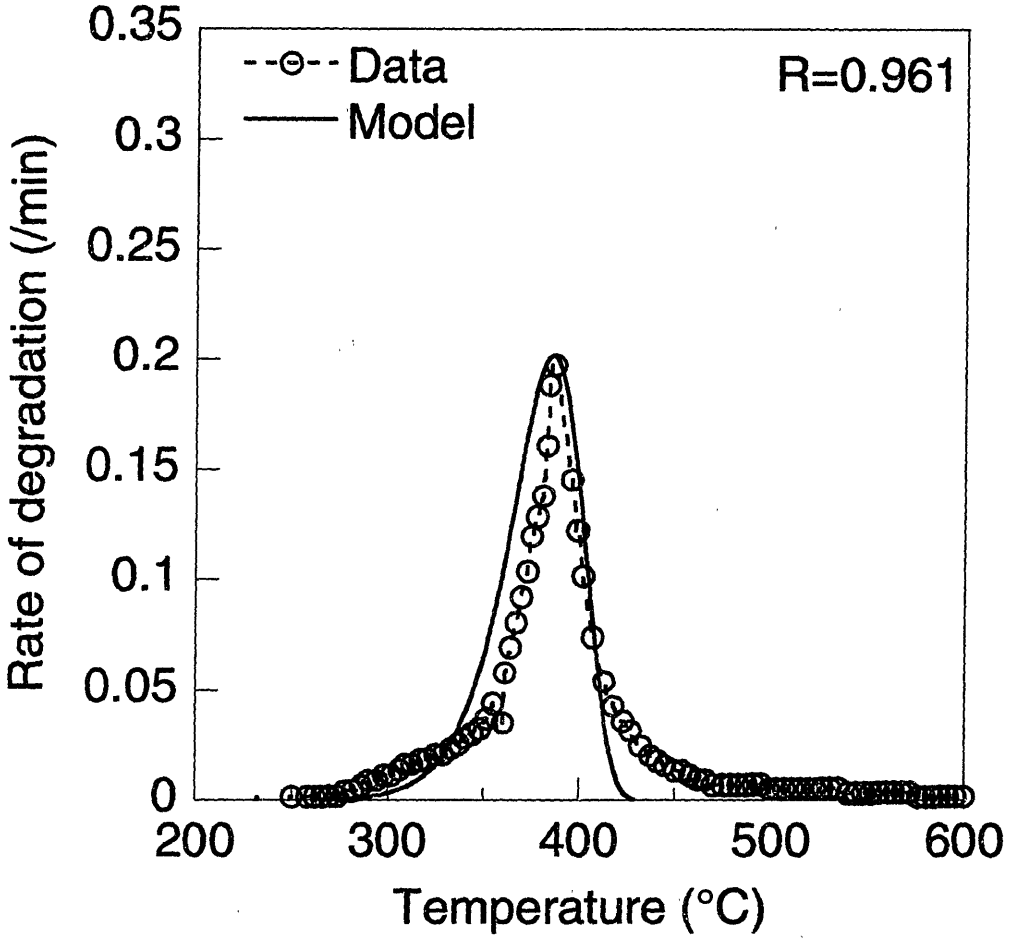

Figure 6.11b Predictions of degradation rate versus temperature compared with data for a heating rate of 10°C/min.

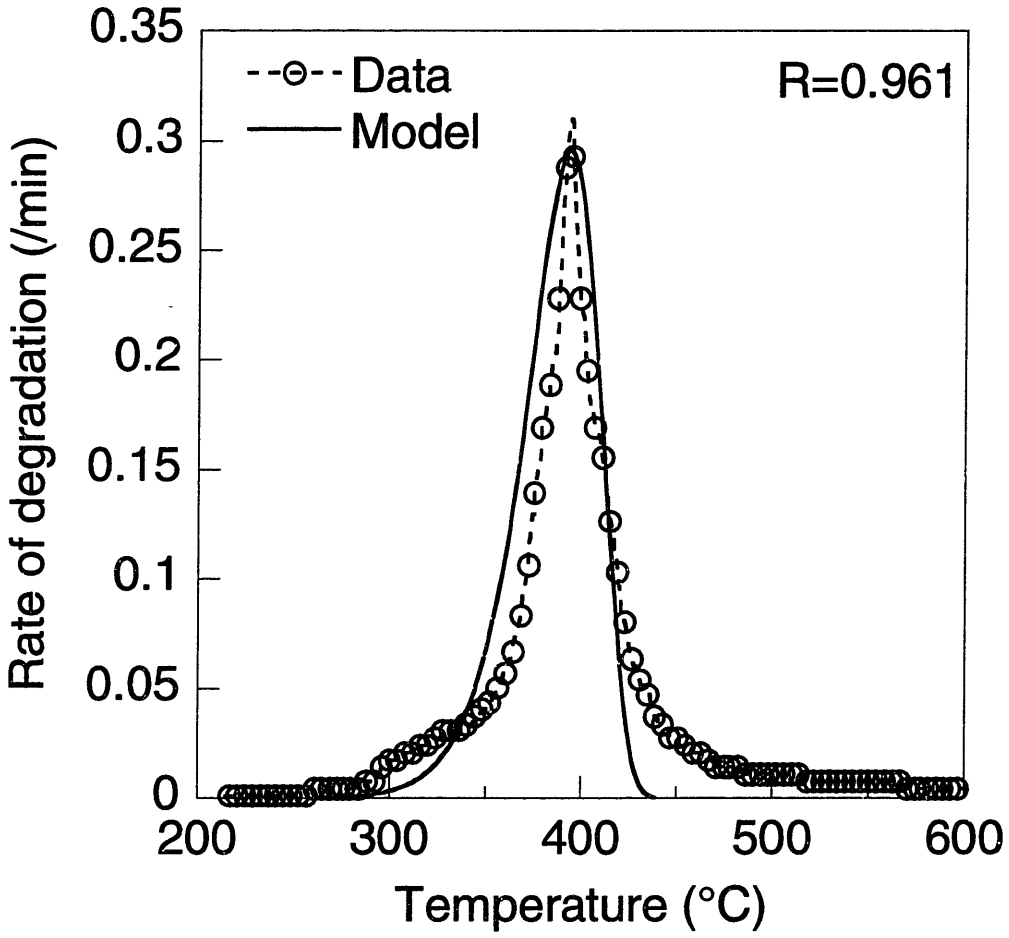

Figure 6.11c Predictions of degradation rate versus temperature compared with data for a heating rate of 15°C/min.

formula for Least Squares curve fits [52] (see Appendix C.) The values, shown on the plots, ranged from 0.951 to 0.961.

Predictions of the degradation state as a function of temperature for epoxy heated from 25°C to 800°C at 10°C/min are compared with experimental data in Figure 6.12. The model underestimates the degradation state up to a degradation state of 0.15. The match between data and model is very good for degradation states between 0.15 and 0.6. At higher degradation levels, the model overestimates the degradation state. This plot is typical of the match between data and model for other heating rates.

6.2.2 Verification of Degradation Model

In order to verify the degradation model, the residual degradation states predicted via the model for samples held at elevated temperatures were compared with the degradation state calculated from experimental data. Various hold times and temperatures were investigated, as described in Section 5.1.3. The testing conditions are tabulated in Table 5.2.

The temperature control of the thermogravimetric analyzer used to conduct the experiments proved to be imperfect. Thus, the actual temperatures at which the samples were held were consistently lower than the programmed temperatures. Figure 6.13 shows a sample of temperature and degradation state data from a high temperature isothermal exposure. Data from other tests is cataloged in Appendix B. For the test shown, the programmed hold temperature was 350°C, however the actual hold temperature was only 327°C. The differences in programmed and actual hold temperatures for each of the high temperature isothermal exposure tests are summarized in Table 6.3, along with the

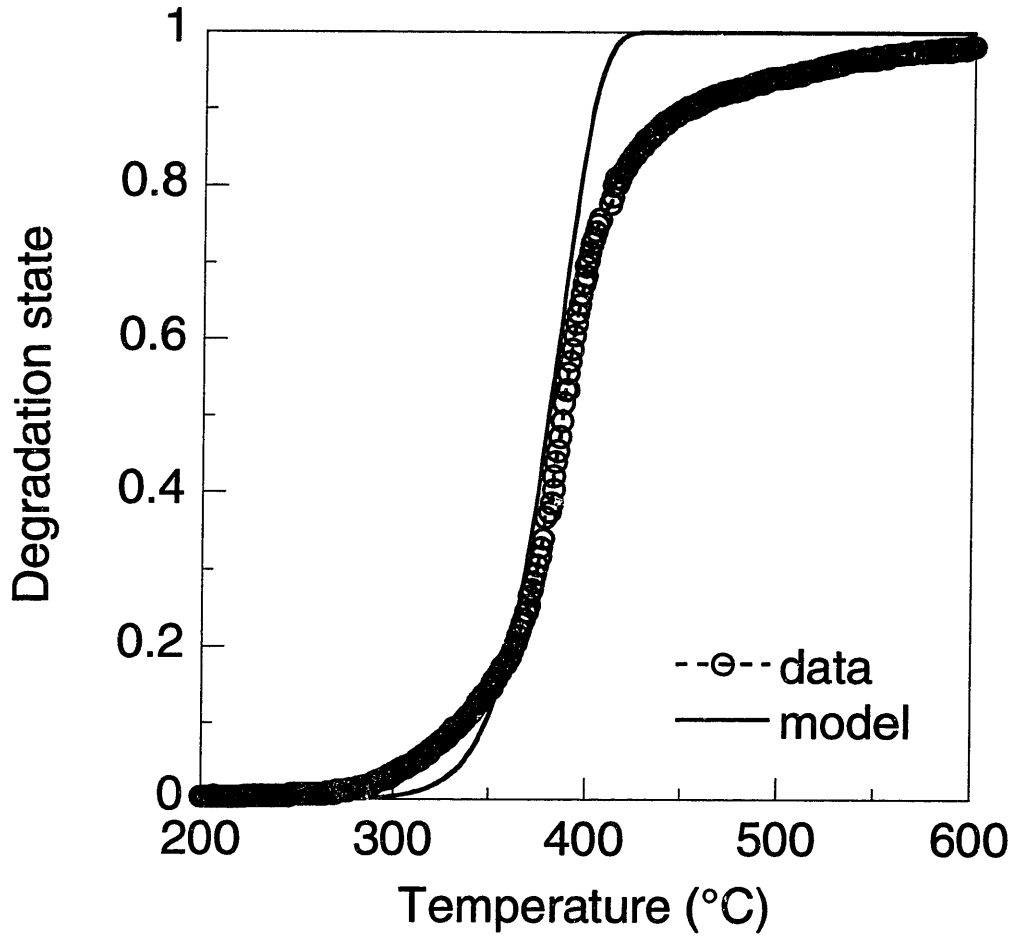

Figure 6.12 Predictions of degradation state versus temperature compared with data for a heating rate of 10°C/min.

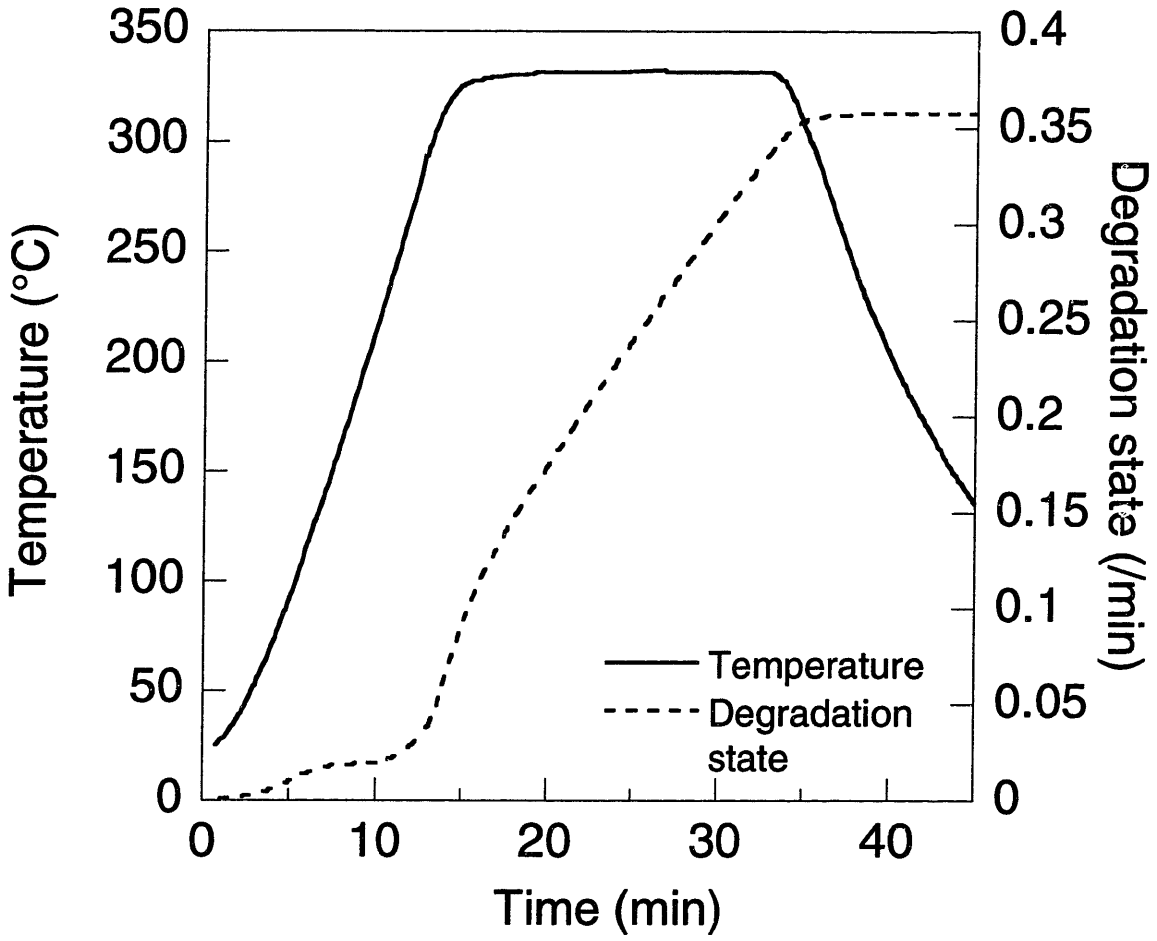

Figure 6.13 Typical sample of high temperature isothermal exposure degradation data versus time (nominal temperature of 350°C).

Table 6.3 Experimental summary of degradation state verification tests

Test	Hold Temperature (°C)		Hold Time (min)	Residual Degradation State α_{res}		Error from model
	Programmed	Actual		Experimental	Calculated	
1	350	331	10	0.232	0.248	6.9%
2	250	227	10	0.013	0.000	-100%
3	350	327	20	0.356	0.386	8.4%
4	350	316	1	0.111	0.032	-71.2%
5	375	354	10	0.564	0.637	12.9%
6	335	314	25	0.254	0.231	-9.1%
7	335	317	10	0.164	0.118	-28.0%
8	375	346	1	0.222	0.187	-15.8%

duration of each hold and the resulting residual degradation state. The residual degradation state for each sample was calculated using Equation 4.31. In order to make this calculation, it was necessary to know the mass, m_f, of the nonreactive fraction of each sample. This data was not available directly from the verification tests, but was determined experimentally from dynamic TGA tests conducted on the samples after they had undergone the isothermal exposure. This data appears in Appendix B.

Predicted values of the residual degradation state for each sample were calculated using thermocouple data from the isothermal exposure experiments in conjunction with the degradation model. These calculations are compared with experimentally measured values of degradation state in Table 6.3. The model tends to underestimate degradation states below 0.2 and overestimate degradation states above 0.3. The differences between measured and calculated values for exposures that resulted in small values of degradation state are sometimes large compared to the magnitude of the residual degradation state, which makes the error large for these calculated values. Results are also shown in a bar chart plot in Figure 6.14.

The verification tests were also designed to demonstrate that equivalent residual degradation states can be obtained from different thermal histories. Three different exposures, a 1-minute hold at 375°C, a 25-minute hold at 335°C, and a 10-minute hold at 350°C, all produced approximately the same residual degradation state, with values of 0.222, 0.254, and 0.232, respectively.

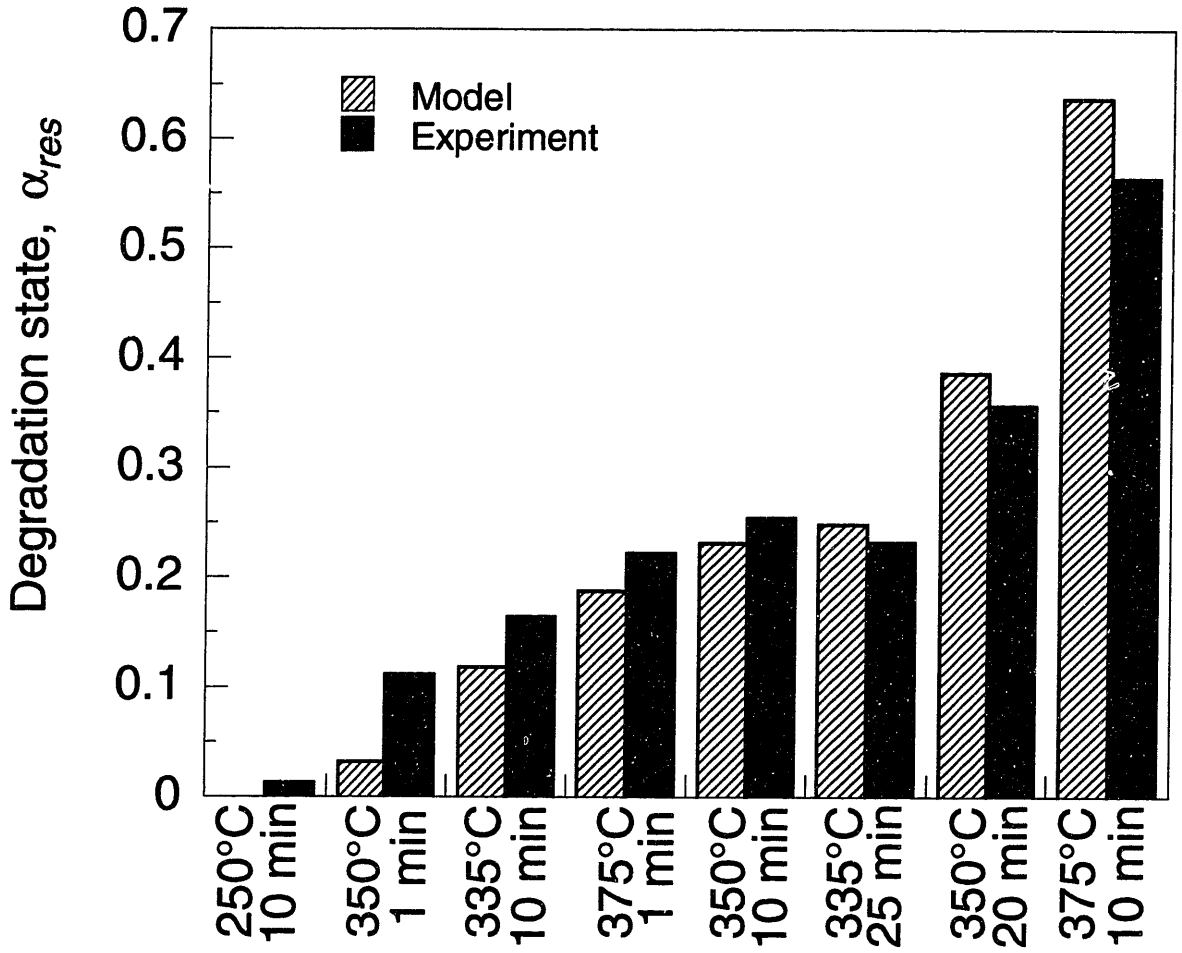

Figure 6.14 Comparison of experimentally measured residual degradation states and results predicted from degradation model (nominal exposure temperature indicated).

6.2.3 Degradation Assessment

After each verification test, the partially degraded sample was left in the thermogravimetric analyzer. The thermogravimetric analyzer was immediately programmed to perform a dynamic heating test in an inert nitrogen atmosphere from 25°C to 800°C at a heating rate of 10°C/min. At the end of the dynamic heating test, the sample was fully degraded and the only mass remaining was that of the nonreactive char. The final mass of each sample was recorded. All data is tabulated in Appendix B.

The ratio of the final mass of each sample to its mass after the verification test, i.e. the effective char yield of the partially degraded sample, was calculated using Equation 4.51. The results are tabulated in Table 6.4. In two cases, tests #2 and #4, the effective char yield was below the nominal char yield range of 0.21 to 0.25 observed in the initial series of dynamic heating tests. This was the result of experimental error. In these cases, the TGA sample pan was overfilled and a fraction of the nonreactive material spilled out as the sample degraded, resulting in an erroneously low final mass and effective char yield. The results of these two tests are therefore discounted.

The effective char yields calculated from the other tests were used to evaluate the usefulness of effective char yield as a metric for estimating the residual degradation state, α_{res}, of a partially degraded sample. A constant nominal char yield of 25%, which is within the range observed from the results of the initial series of dynamic heating tests, was assumed, and the estimated residual degradation state was calculated for each sample using Equation 4.52:

Table 6.4 Effective char yield from each sample

Test #	Effective char yield
1	0.305
2	0.039
3	0.312
4	0.150
5	0.426
6	0.309
7	0.296
8	0.295

Table 6.5 Estimated and actual residual degradation states

Test #	Estimated α_{res}	Actual α_{res}	Error from estimate (%)
1	0.241	0.232	3.9
3	0.264	0.356	-25.9
5	0.551	0.564	-2.4
6	0.253	0.254	-0.3
7	0.209	0.164	27.6
8	0.202	0.222	-9.0

$$\alpha_{res} = \frac{1 - \frac{nominal\ char\ yield}{effective\ char\ yield}}{nominal\ char\ yield} \tag{4.52}$$

The results are summarized, along with the measured residual degradation states reported in Section 6.2.2, in Table 6.5. In three of the cases, the effective char yield estimate of residual degradation state was within 4%, however other estimates were not as good. The actual and estimated degradation states differed by as much as 28%. Several sources of error may account for the poor estimates. Problems with accidental mass loss caused by overfilling the sample pan were already noted. The variability in nominal char yield from one sample to another is another source of error; while a nominal char yield of 25% was assumed, values measured from experiments varied from 21 to 26%.

6.3 MECHANICAL PROPERTY STUDIES

In this section, the results of a series of tensile tests are presented. These tests were performed on $[0]_4$ and $[90]_{12}$ coupons exposed to elevated temperatures inside a split cylinder furnace as described in Section 5.2. Stiffness and strength were measured following a 10-minute hold at the specified temperature. In some tests, measurements were taken while the coupons were loaded at the elevated temperature. In other tests, the coupons were cooled to room temperature before being loaded. The properties measured are compared to accepted values for the room temperature properties of AS4/3501-6 graphite/epoxy, cited in Table 6.6. The strength and stiffness results are correlated with the temperature and degradation state of the coupons, and models of the ply tensile stiffnesses and strengths as functions of temperature and degradation state are developed.

Table 6.6 AS4/3501-6 Graphite/Epoxy Ply Properties

Longitudinal Young's modulus[a]	E_L	GPa	124.8
Transverse Young's modulus[a]	E_T	GPa	8.41
Poisson's ratio[b]	ν_{LT}		0.3
Shear modulus[b]	G_{LT}	GPa	6.00
Longitudinal coefficient of thermal expansion[b]	α_L	/°C	-0.36
Transverse coefficient of thermal expansion[b]	α_T	/°C	28.8
Longitudinal tensile strength[a]	X^t	MPa	2000
Longitudinal compressive strength[b]	X^c	MPa	1468
Transverse tensile strength[a]	Y^t	MPa	55.2
Transverse compressive strength[b]	Y^c	MPa	186
Shear strength[b]	S	MPa	105

[a] From MIL-HDBK-17 [24]
[b] From TELAC standard material properties [11]

6.3.1 Stress-Strain Response

A typical stress-strain curve from a $[90]_{12}$ coupon is shown in Figure 6.15. All of the stress-strain data plots are cataloged in Appendix D. The results in Figure 6.15 are very linear, with the R-value for a linear fit of all the data up to the point of failure exceeding 0.999. The R-values for all of the other $[90]_{12}$ stress-strain results, tabulated in Appendix D, all exceeded 0.99. The transverse modulus at 300°C could not be measured because the extensometer caused the extremely delicate coupons to break. It should be noted that the strain when the load is applied is non-zero in Figure 6.15. This occurred in a number of cases. This is most likely caused by strain due to thermal expansion and/or drift of the extensometer from its zero point.

A typical stress-strain curve from a $[0]_4$ coupon is shown in Figure 6.16. All of the stress-strain plots are cataloged in Appendix D. The reduction in strain at the onset of loading was observed in a number of the "at-temperature" tests, in which the coupon was clamped while hot. The reason for these initial decreases in strain is unknown. Horizontal jumps in the stress-strain curve, such as that shown in Figure 6.16, were thought to be due to slippage of the extensometer tips. These discontinuities often corresponded with loud pops from the coupon. In tests conducted with the furnace open, when the loading process could be observed, it was noted that loud pops from the coupon were often associated with matrix splitting.

Slippage of the extensometer tips did not affect the extensometer calibration, so it was often possible to take multiple modulus measurements from such stress-strain curves. This is the case for the results in Figure 6.15. Two nearly identical modulus measurements were taken, each with a linear fit R-value greater than 0.985. Horizontal

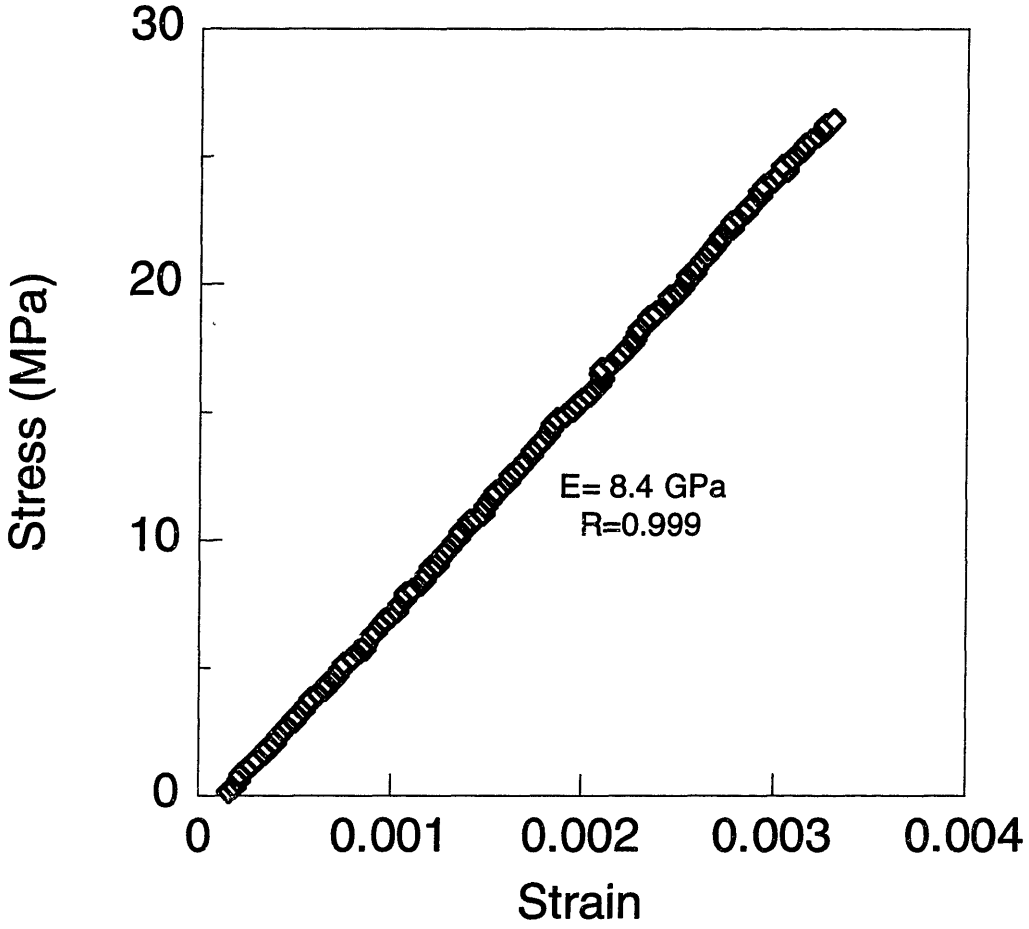

Figure 6.15 Typical stress-strain results for a $[90]_{12}$ coupon (residual test with exposure at 200°C).

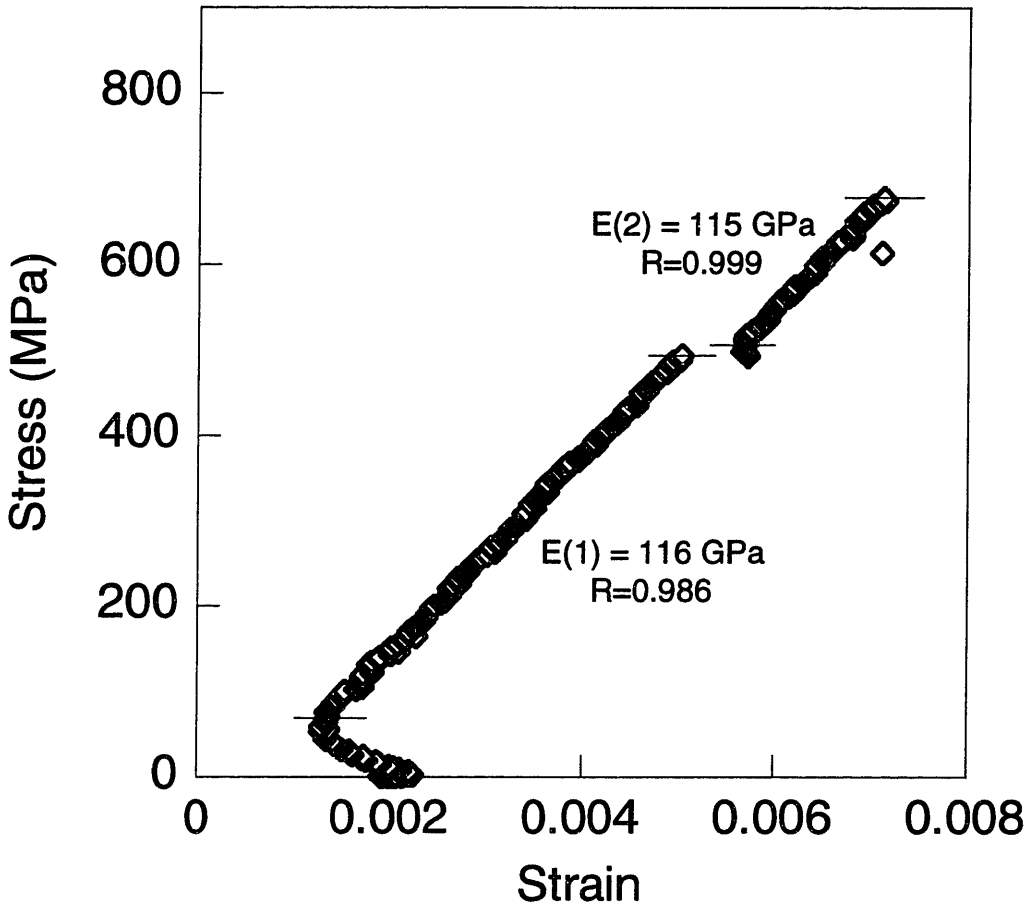

Figure 6.16 Typical stress-strain results for a $[0]_4$ coupon (at-temperature test with exposure at 200°C).

lines added to the stress-strain plot denote the points between which linear fits were applied to determine modulus. All of the modulus curve fits applied to data from other coupons (except for exposure temperatures of 350°C and above) also had R-values greater than 0.985. All of the modulus results are tabulated in Appendix D.

The at-temperature modulus of $[0]_4$ coupons exposed at 350°C and 400°C could not be measured because the extensometer lost contact with the coupons as the coupons became severely degraded. For the residual modulus tests, the extensometer was attached to the coupon after it had cooled down. However, the residual modulus of $[0]_4$ coupons heated to 350°C and 400°C could not be determined because the stress-strain results were very erratic. Typical stress-strain results for a $[0]_4$ coupon exposed at 400°C are plotted in Figure 6.17. Different sections of the plot produce widely different modulus measurements, and it is not clear that any one measurement is representative. The very low initial modulus of 17.4 GPa resulted from straightening of the fibers, which had puffed out as the matrix degraded. Once the fibers straightened and began to resist the load, the modulus of the coupon jumped to approximately 300 GPa. The transient response of the coupon makes it difficult to define the modulus.

The average at-temperature and residual transverse modulus data, as determined from the $[90]_{12}$ coupons, is reported as a function of exposure temperature in Tables 6.7 and 6.8, respectively. Usually three tests were performed at each temperature. However, sometimes additional tests were included to clarify trends in the data. The standard deviation and coefficient of variation of each set of data is also reported in the tables. Data from each individual test is compiled in Appendix D.

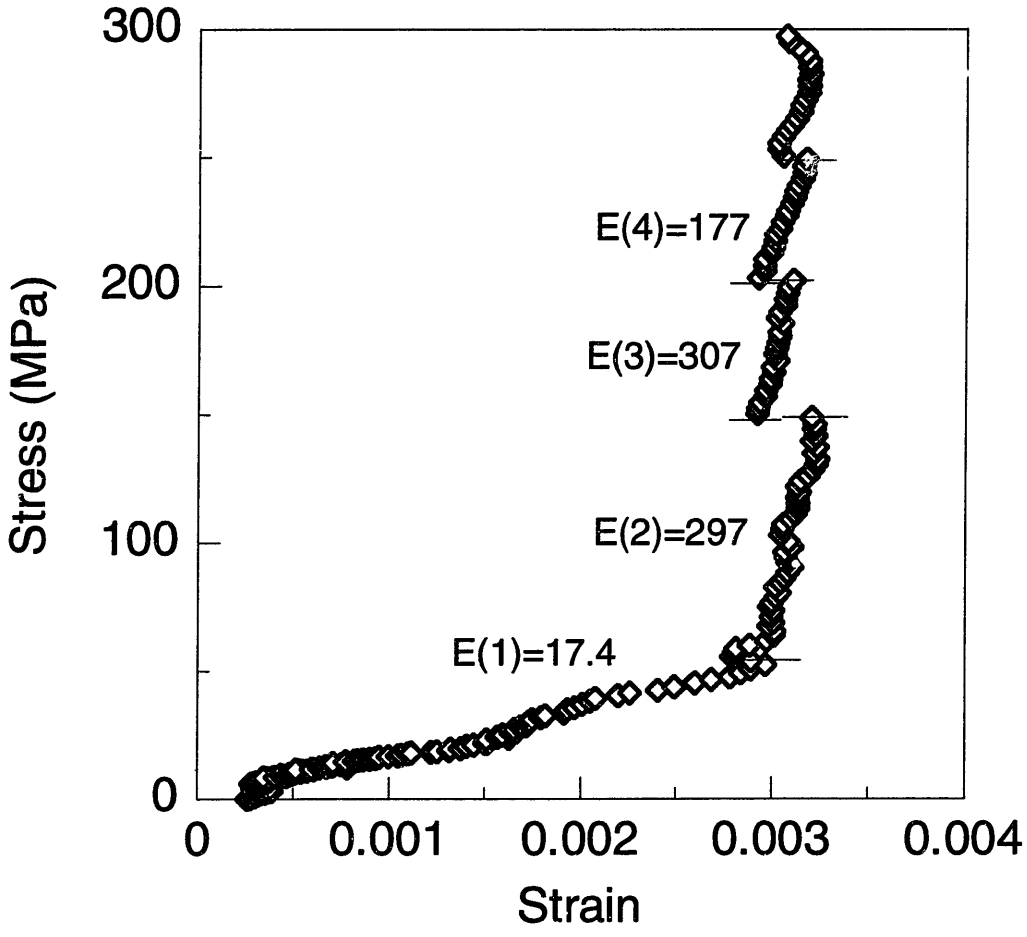

Figure 6.17 Typical stress-strain results for a $[0]_4$ coupon (residual test with exposure at 400°C).

Table 6.7 At-temperature transverse modulus data

Exposure Temperature (°C)	Average Modulus (GPa)	Standard Deviation (GPa)	Coefficient of Variation (%)
25	9.2	0.8	8.2
150	8.3	1.4	16.9
200	5.6	5.1	91.1
250	0.8	0.5	62.5
300	---	---	---

Table 6.8 Residual transverse modulus data

Exposure Temperature (°C)	Average Modulus (GPa)	Standard Deviation (GPa)	Coefficient of Variation (%)
150	8.9	0.7	7.9
200	9.5	0.9	9.5
250	8.0	0.6	7.5
300	5.9	0.3	5.1

The scatter in the values of the at-temperature transverse modulus is quite large, meaning that the modulus varied considerably from one test to the next. Due to the imperfect temperature control of the test furnace, the exact temperature of exposure varied from the nominal test temperature by a few degrees for each test. The variation in at-temperature modulus is thus most likely a reflection of the high sensitivity of the modulus to the ambient temperature. In contrast, the residual modulus data, which was all collected when the coupons were at room temperature, is very consistent. The coefficient of variation of each averaged data point is less than 10%.

At-temperature and residual transverse modulus are plotted as a function of nominal exposure temperature in Figures 6.18 and 6.19, respectively. Individual data points were plotted rather than average values to provide more information. The at-temperature modulus, shown in Figure 6.18, is approximately constant through 150°C. A large transition occurs around 200°C that causes the modulus to drop by an order of magnitude, from nearly 10 GPa at 150°C to less than 1 GPa at 250°C. The transition appears to occur at 200°C, at which nominal temperature there is a great deal of scatter in the data. As noted in Section 2.2, 200°C is the approximate glass transition temperature of epoxy, hence the large drop in modulus correlates with the glass transition. The large scatter in the data at 200°C most likely reflects the imperfect control of the furnace temperature. Coupons tested when the furnace was slightly below the glass transition temperature would have a much higher modulus than coupons tested when the furnace was slightly above the glass transition temperature.

The residual transverse modulus behavior is substantially different from the at-temperature behavior. The residual transverse modulus measured from the $[90]_{12}$

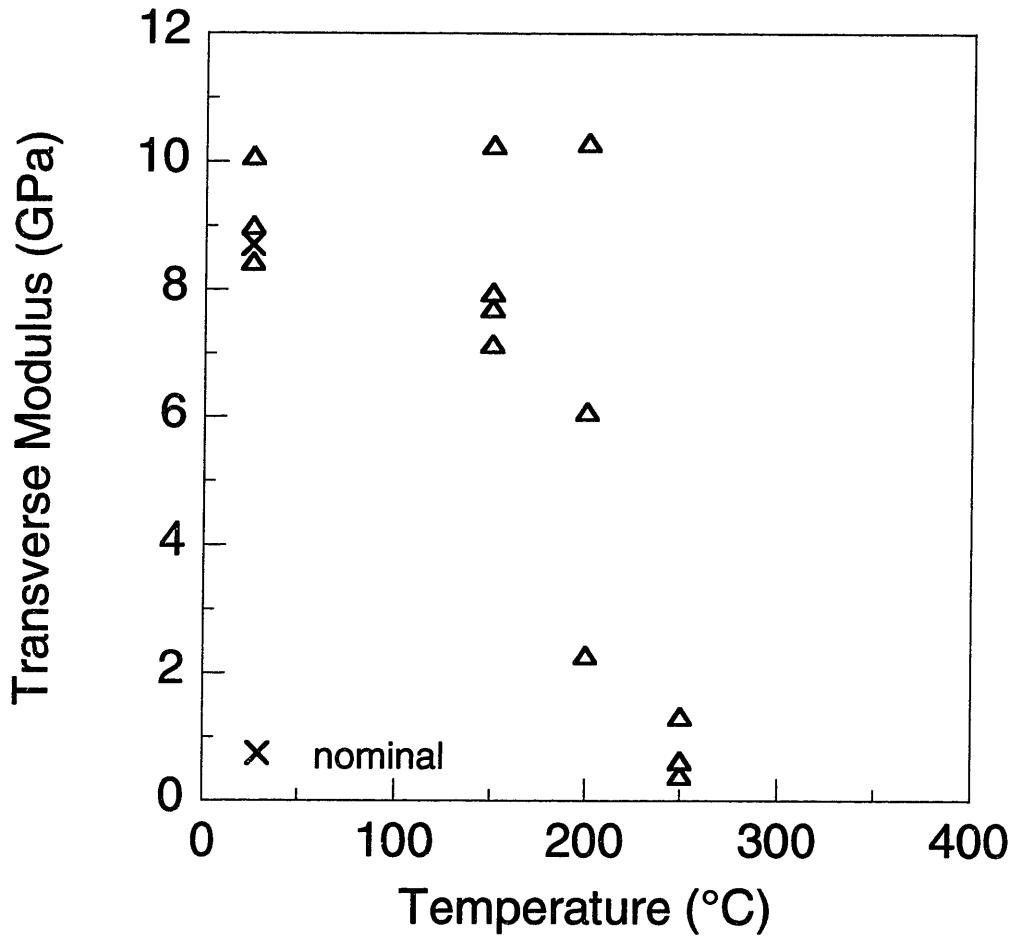

Figure 6.18 At-temperature modulus of $[90]_{12}$ coupons versus nominal test hold temperature.

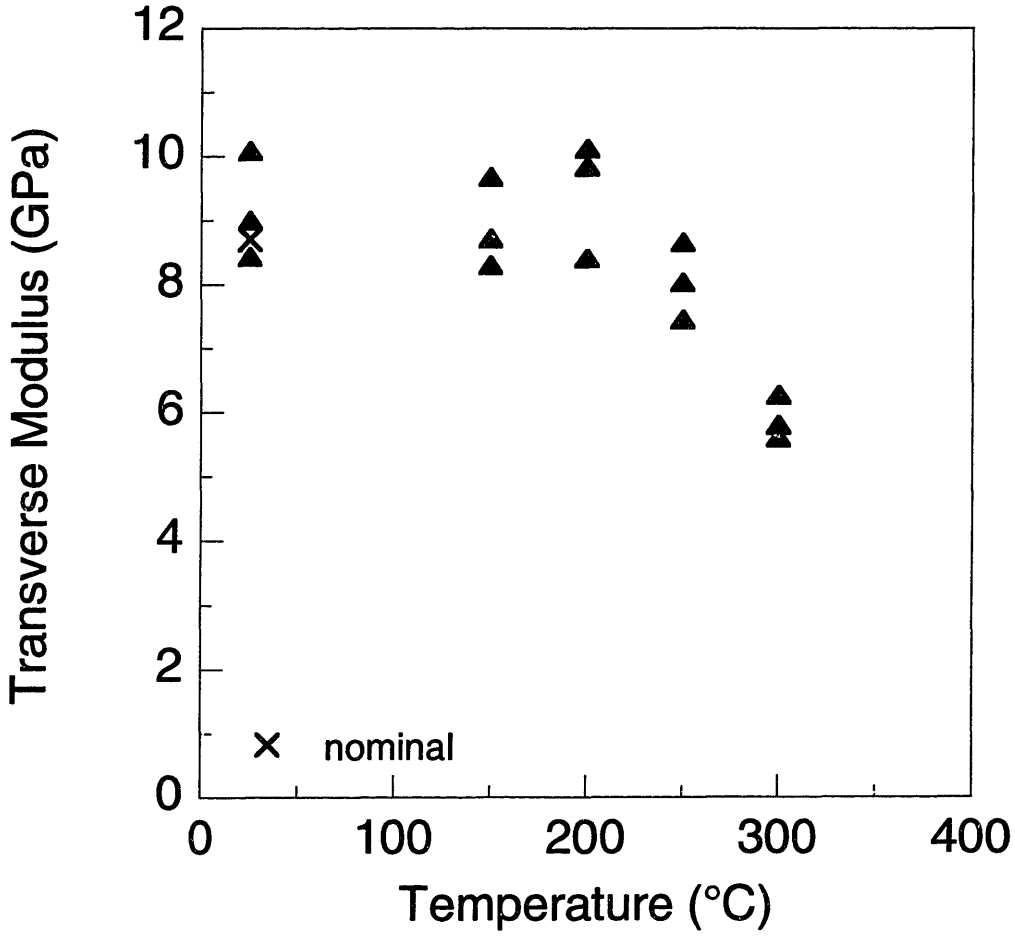

Figure 6.19 Residual modulus of $[90]_{12}$ coupons versus nominal test hold temperature.

coupons is plotted in Figure 6.19. The residual modulus is relatively unchanged up to 200°C. The modulus drops gradually following exposures to higher temperatures. However, even after exposures to 300°C, the coupons have a residual modulus that is more than 65% of the room temperature value. This rebound in modulus after the coupons cool is evidence that changes caused by the glass transition are reversible.

The average transverse modulus data for the AS4/3501-6 graphite/epoxy coupons tested in this work is normalized by dividing by the room temperature ("RT") transverse modulus value of 8.41 GPa cited in Table 6.6. This is then compared in Figure 6.20 with graphite/epoxy data from other investigations [31] that is normalized in each case by the reported room temperature value[32,33,34]. Except where noted, at-temperature modulus is plotted. The material system used in the experiments, when known, is cited on the plot. Different types of graphite/epoxy and testing arrangements are represented in this plot, but common trends are evident. The data in Figure 6.20 shows that while the temperature at which modulus loss begins varies somewhat, all the data shows a significant drop in modulus around 200°C and negligible properties at 250°C and above. The substantially higher residual modulus contrasts sharply with these trends.

Averaged at-temperature and residual longitudinal modulus data, measured from the $[0]_4$ coupons, is tabulated in Tables 6.9 and 6.10. Data from individual tests is in Appendix D. The at-temperature modulus data is very consistent, with the coefficient of variation of the data being low at most temperatures. The data with the most scatter was collected at 200°C, which is the approximate glass transition temperature of the epoxy matrix. The residual modulus data is also quite consistent. With the exception of the

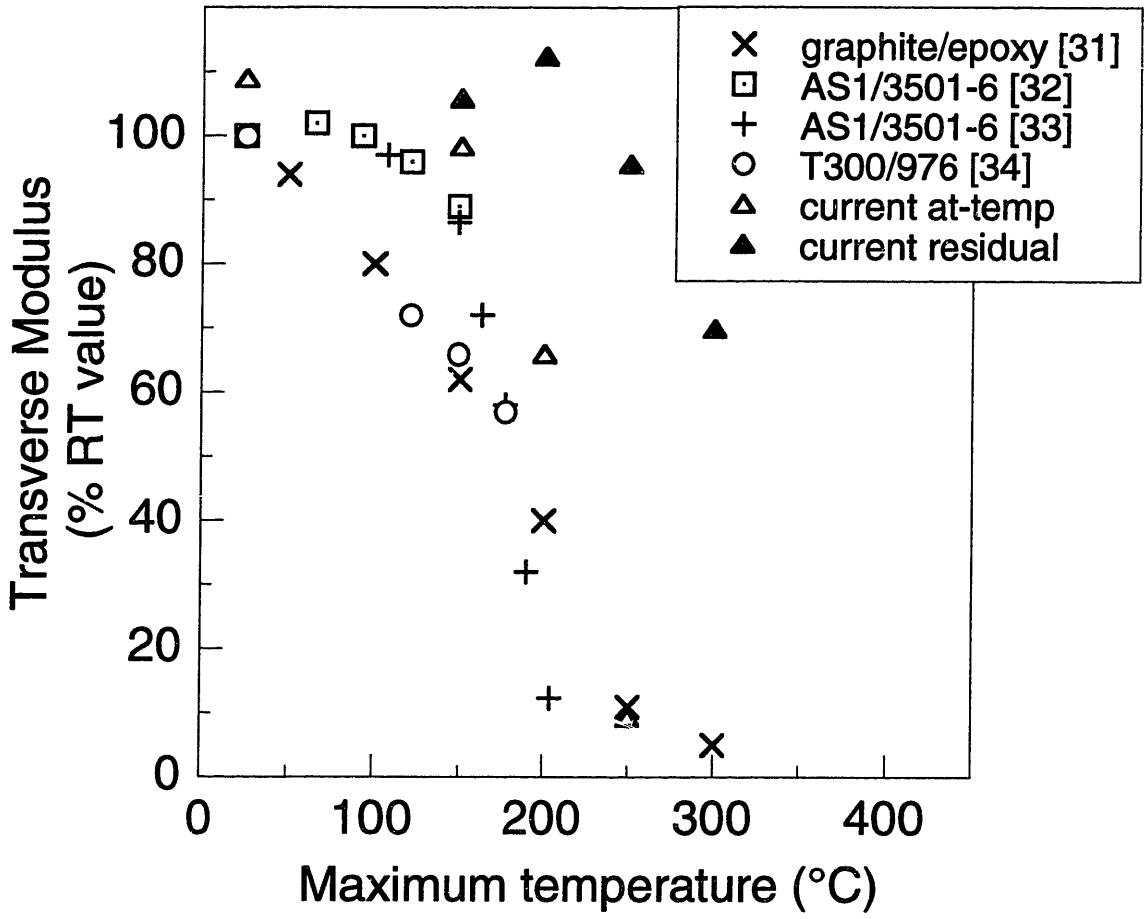

Figure 6.20 Plot of current normalized transverse modulus data and previously reported values versus maximum exposure temperature.

Table 6.9 At-temperature longitudinal modulus data

Exposure Temperature (°C)	Average Modulus (GPa)	Standard Deviation (GPa)	Coefficient of Variation (%)
25	121	8.9	7.4
150	124	8.5	6.9
200	134	41.7	31.1
250	120	4.1	3.4
300	115	23.8	20.7
350	---	---	---
400	---	---	---

Table 6.10 Residual longitudinal modulus data

Exposure Temperature (°C)	Average Modulus (GPa)	Standard Deviation (GPa)	Coefficient of Variation (%)
150	131	11.7	8.9
200	104	5.6	5.4
250	133	27.8	20.9
300	119	7.0	5.9
350	---	---	---
400	---	---	---

data from tests performed at 250°C, which has a coefficient of variation of 21%, all of the data vary by less than 10%.

The longitudinal modulus data is plotted versus temperature in Figures 6.21 and 6.22. Data points from individual tests are plotted. Both at-temperature modulus, in Figure 6.21, and residual modulus, in Figure 6.22, are approximately constant up to 300°C. There is some variation in the data, but no clear downward trend of modulus loss. Above 300°C, the modulus could not be measured because of the severe degradation of the coupons.

The data from the current investigation is normalized by the room temperature longitudinal modulus value of 124.8 GPa in Table 6.6 and compared to other normalized longitudinal modulus data [31,32,33,34] in Figure 6.23. Data from previous investigations is normalized by the reported room temperature modulus in each report. All of the data is in agreement in that longitudinal modulus is constant up to 300°C. Both at-temperature and residual moduli are constant, and there is no trend of higher residual properties. Only one data point is available above 300°C and it shows a drop of approximately 20% in at-temperature longitudinal modulus at 400°C.

6.3.2 Strength Response

Strength was determined for each coupon by dividing the highest load carried by the coupon by its thickness and width, measured before the coupon was heated. The maximum load data and dimensions of each specimen are tabulated in Appendix D. Cases in which unacceptable failure modes, such as transverse failure right at the end of

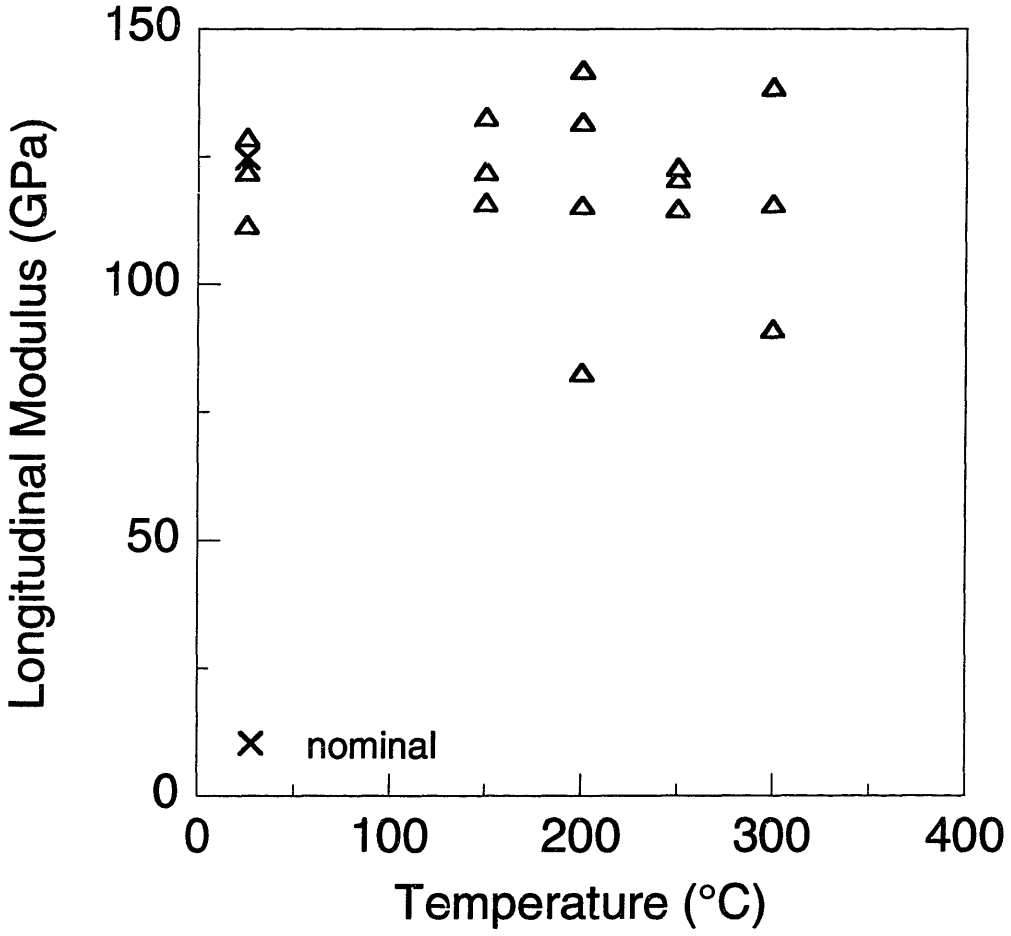

Figure 6.21 At-temperature modulus of $[0]_4$ coupons versus nominal test hold temperature.

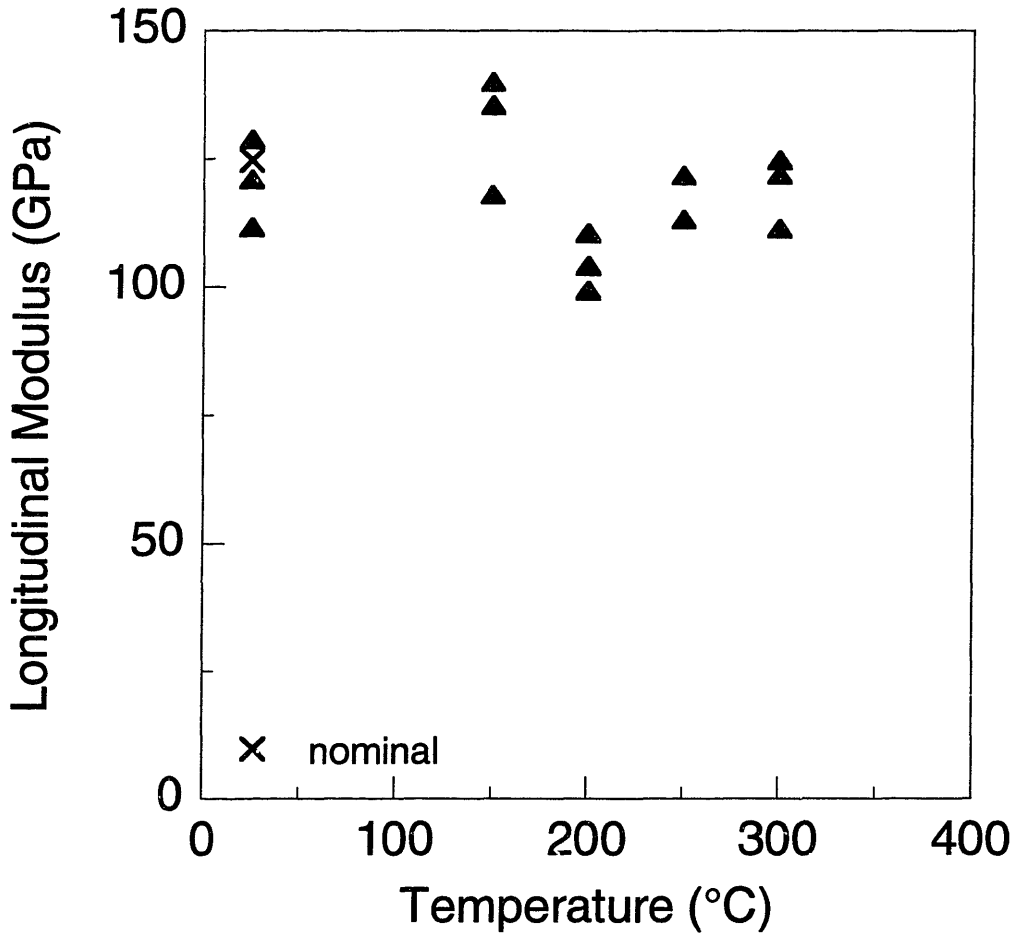

Figure 6.22 Residual modulus of $[0]_4$ coupons versus nominal test hold temperature.

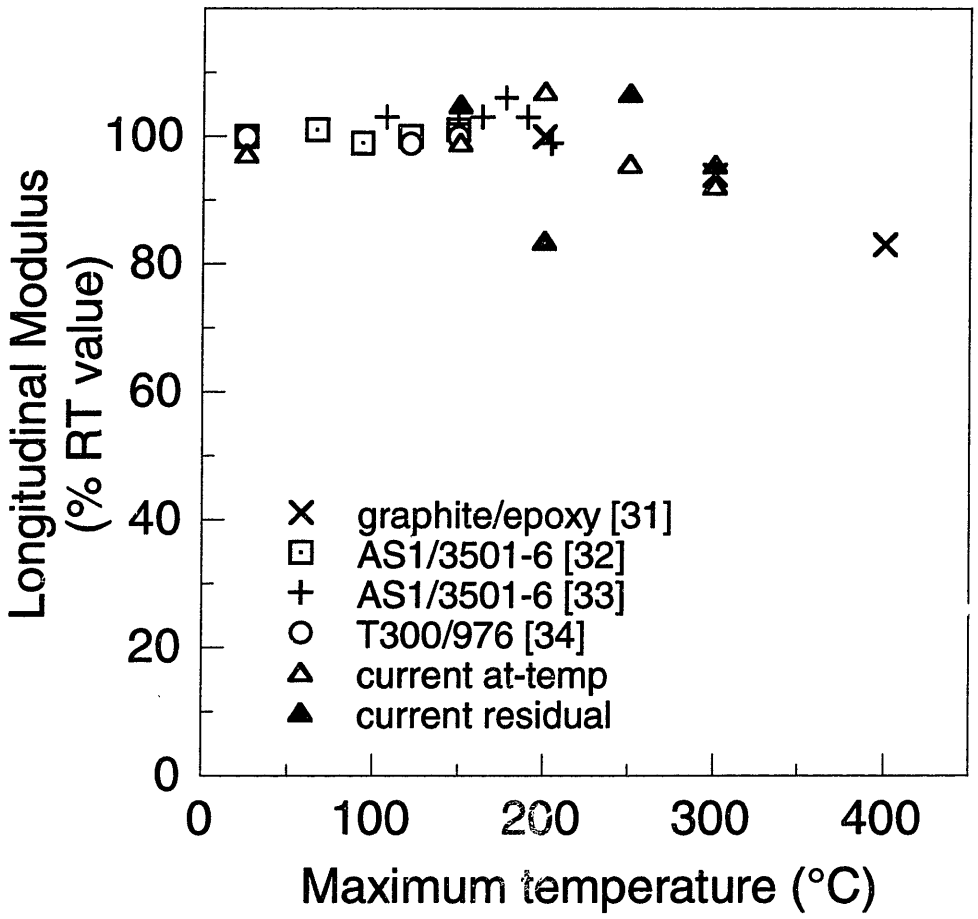

Figure 6.23 Plot of current normalized longitudinal modulus data and previously reported values versus nominal exposure temperature.

the loading tabs (referred to as "grip failures") or extensive longitudinal splitting, affected the measured strength are noted.

The $[90]_{12}$ coupons all exhibited brittle failure. A number of coupons failed at one or both of the grips. This was the case for at-temperature tests at room temperature and 150°C, and for residual property tests following exposures up to 250°C. At higher temperatures, the failures were clean breaks across the width of the coupon within the heated area. The $[90]_{12}$ coupons did not change in appearance with exposures up to 250°C. After being exposed at 300°C for ten minutes, the coupons had a shiny gloss and blisters on the surface.

Average at-temperature and residual transverse strength, as measured from $[90]_{12}$ coupons, is tabulated in Tables 6.11 and 6.12. Each data point is the average of data from three tests. All of the raw data, including data from coupons that failed at the grips, is included in these averages in order to show the measured trends. Data from each individual test is in Appendix D. The scatter in the at-temperature data is quite high. The coefficient of variation is above 27% for the specimens tested at room temperature, and the variation in the data increases as the testing temperature increases. The variation in the at-temperature strengths may be a reflection of variations in the actual test temperature. The residual transverse strength data is more consistent as the coefficient of variation, while consistently above 10%, is still much lower than that of the at-temperature strength data.

Transverse strength measurements from individual tests are plotted in Figures 6.24 and 6.25. Coupons that failed at the grips are denoted with a diamond data point; failures that occurred within the gage section of the coupons are denoted with a triangle

Table 6.11 At-temperature transverse strength data

Exposure Temperature (°C)	Average Strength (MPa)	Standard Deviation (MPa)	Coefficient of Variation (%)
25	28.1	7.8	27.8
150	24.2	8.8	36.4
200	13.0	6.9	53.1
250	1.9	1.1	57.9
300	0.4	0.3	75.0

Table 6.12 Residual transverse strength data

Exposure Temperature (°C)	Average Strength (MPa)	Standard Deviation (MPa)	Coefficient of Variation (%)
150	28.5	6.9	24.2
200	26.5	2.8	10.6
250	27.5	5.2	18.9
300	1.7	0.3	17.6

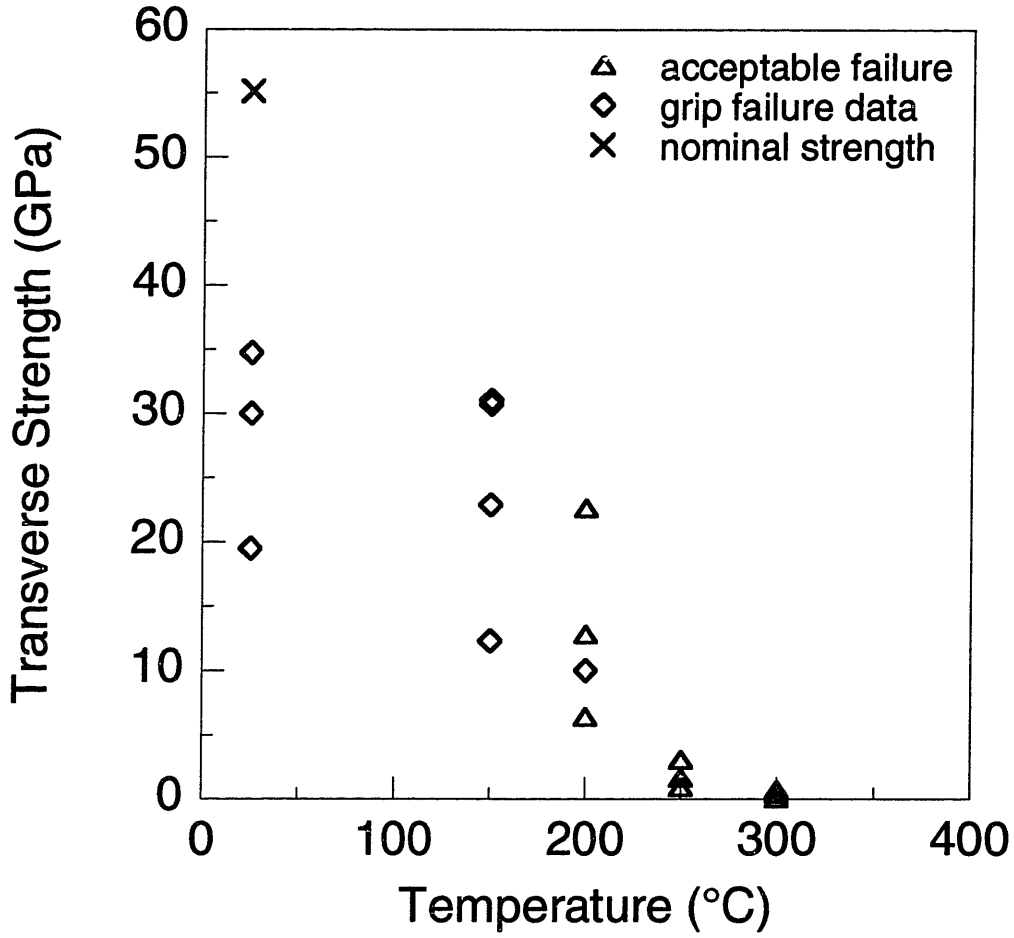

Figure 6.24 At-temperature strength of $[90]_{12}$ coupons versus nominal test hold temperature.

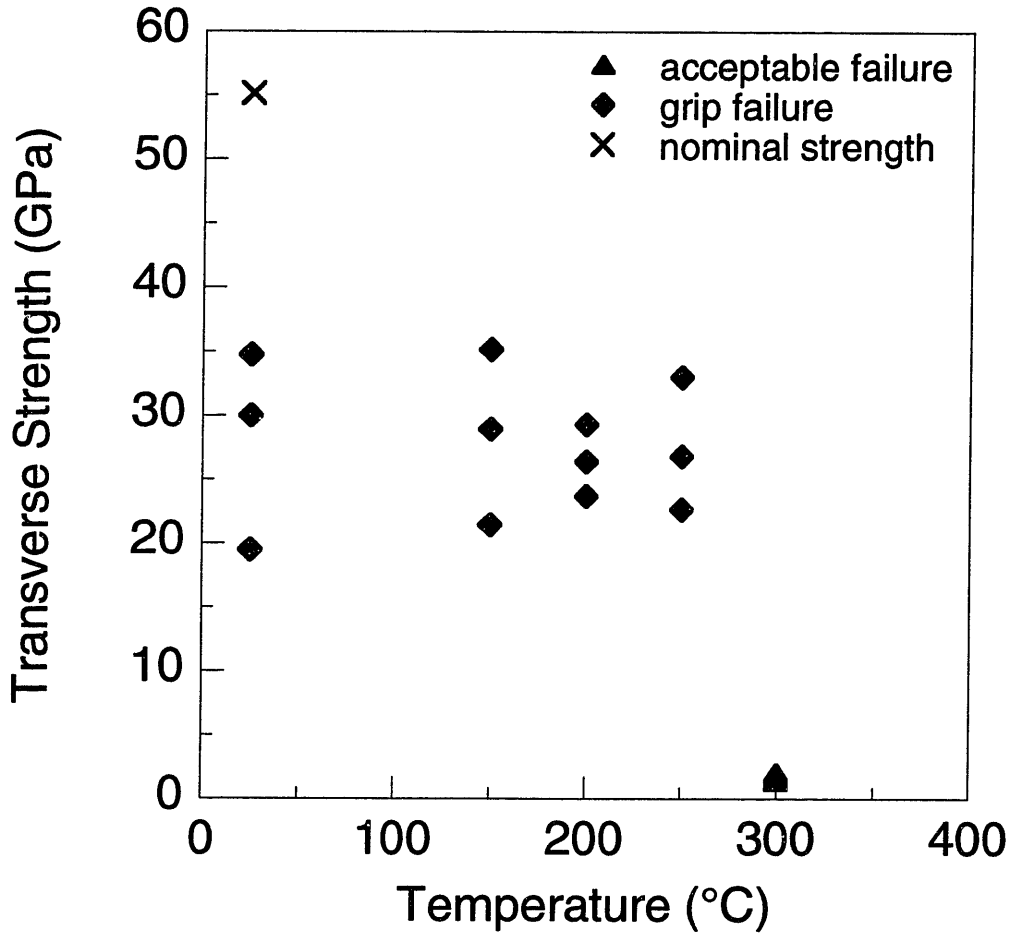

Figure 6.25 Residual strength of $[90]_{12}$ coupons versus nominal test hold temperature.

data point. Grip failures were observed in all of the at-temperature tests at 25°C and 150°C. Therefore, the strength measured in these cases may be artificially low. At 200°C, the average strength drops, by approximately 50% from the previous value, and by 250°C, the at-temperature strength is nearly zero. Most of the residual transverse strength data is compromised by grip failures. Up through 250°C, coupons failed at the grips, hence the measured strength may be artificially low. The measured strength from these coupons may be considered to be a lower bound to the actual material strength. The strength after an exposure to 300°C was minimal.

Transverse strength data was normalized by the nominal room temperature transverse strength of 55.2 MPa cited in Table 6.6. The data is compared in Figure 6.26 with data from previous investigations [31,32,33,34] that was normalized by the reported room temperature value from each report. Current data from at-temperature and residual tests at temperatures of 150°C and below were ignored because of the grip failures. However, data from tests at higher temperatures was retained to contrast the at-temperature and residual strength behavior. As with the stiffness data in Figure 6.17, the temperature at which property loss begins varies between investigations, but almost no strength loss is noted below 150°C, and there is a large drop in at-temperature strength around 200°C. Both at-temperature and residual strength approach zero at 300°C. The available residual transverse strength data, including the data that provides a lower bound to the material strength, indicates that the residual strength of coupons heated to a given temperature may be substantially higher than the at-temperature strength of coupons heated to the same temperature.

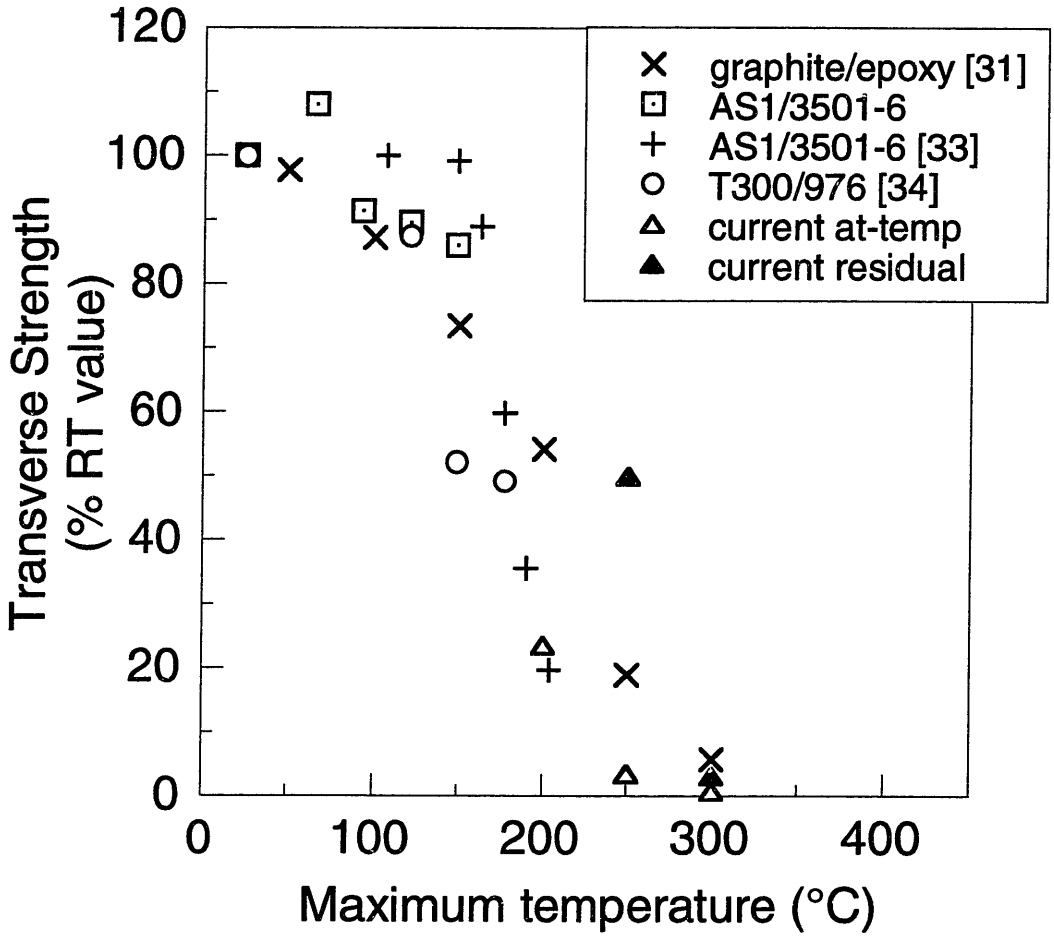

Figure 6.26 Plot of current normalized transverse strength data and previously reported values versus maximum exposure temperature.

Many of the $[0]_4$ coupons experienced extensive splitting before failure. Cracking and popping noises were heard during loading, and top-to-bottom splits in the coupons, parallel to the fibers, were observed. In many cases, the splitting caused portions of the coupons to break off before final failure, thereby reducing the cross-sectional area of the coupons, increasing the stress on the remaining part of the coupon. Since strength was calculated based on the initial dimensions of the coupon, strength data from these coupons with reduced cross-sectional area is invalid. As splits occurred, the load would often drop and then rise again. A sample plot of load data from a $[0]_4$ coupon is shown in Figure 6.27. Two load drops are apparent: a 400 N (1.3%) drop at 30.2 kN, and a 6000 N (16.4%) drop at 36.6 kN. Coupons tested at temperatures of 200°C and below failed explosively, as the coupon broke into tiny splinters. Splitting was less evident at higher temperatures. At exposure temperatures of 300°C and above, individual fibers were visible at failure. The fibers puffed out when they broke, and fewer splinters were produced than at lower exposure temperatures. At exposure temperatures of 350°C and above, a distinct ripping sound was heard when the fibers pulled apart at failure.

The $[0]_4$ coupons showed no change in appearance following exposures to temperatures below 300°C. After exposures at 300°C, coupons exhibited shininess and blistering. At higher temperatures, the degradation of the matrix gave the fibers a stringy, matted look. In addition, the flat surface of the composite became puffy and the thickness increased by approximately a factor of two, from 0.6 mm to well over 1 mm.

Longitudinal strength, as measured from the $[0]_4$ coupons, is tabulated as a function of exposure temperature in Tables 6.13 and 6.14. Each data point is the average of at least three measurements. All of the data is cataloged in Appendix D. The data is

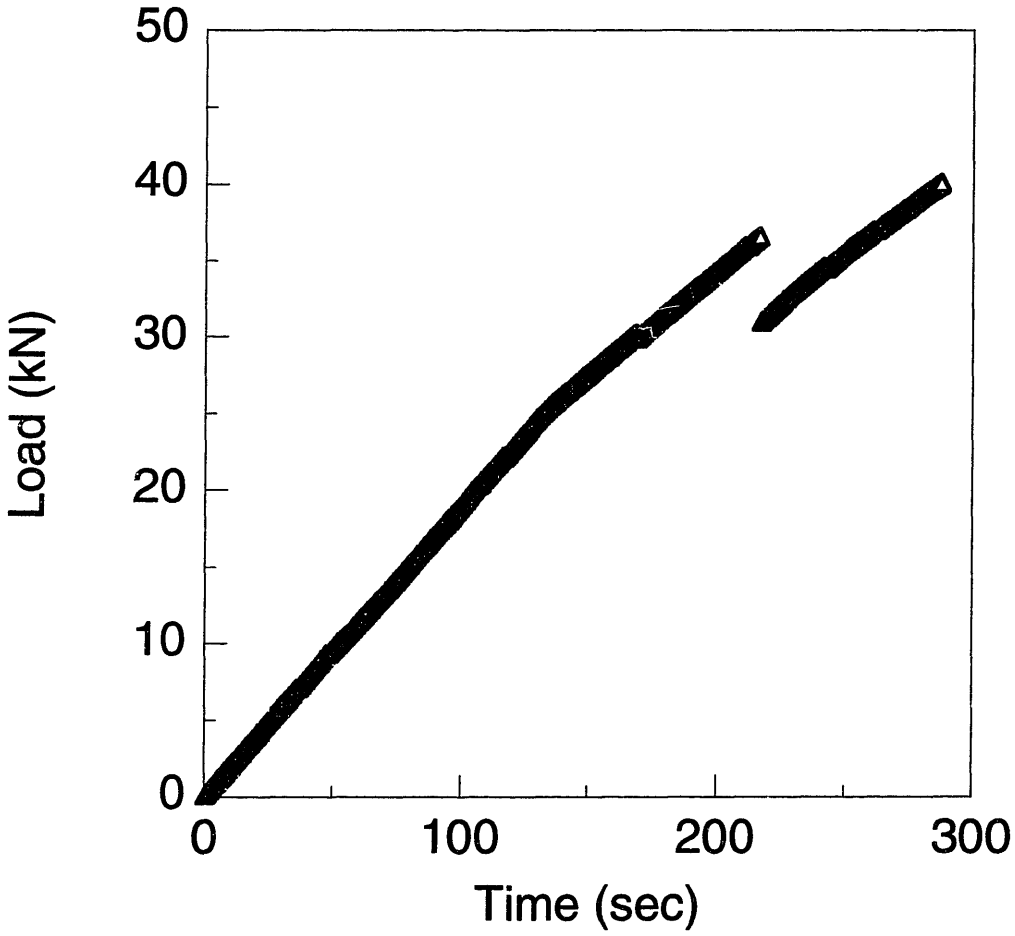

Figure 6.27 Typical load versus time data for a $[0]_4$ coupon tested at a temperature below 200°C.

Table 6.13 At-temperature longitudinal strength data

Exposure Temperature (°C)	Average Strength (MPa)	Standard Deviation (MPa)	Coefficient of Variation (%)
25	1227	250.7	20.4
150	1158	195.4	16.9
200	1117	178.5	16.0
250	1143	196.8	17.2
300	811	64.4	7.9
350	636	130.4	20.5
400	774	56.3	7.3

Table 6.14 Residual longitudinal strength data

Exposure Temperature (°C)	Average Strength (MPa)	Standard Deviation (MPa)	Coefficient of Variation (%)
150	1184	195	16.5
200	1283	49.8	3.9
250	1319	50.8	3.9
300	1177	288.8	24.5
350	952	13.4	1.4
400	876	90.7	10.4

reasonably consistent. The coefficient of variation for all of the at-temperature is less than or equal to 20%, and the residual strength data is even more consistent, as measured by the coefficient of variation.

Longitudinal strength data from individual tests is plotted as a function of nominal exposure temperature in Figures 6.28 and 6.29. None of the coupons approached the 2000 MPa nominal room temperature longitudinal ply strength of graphite/epoxy, as reported in MIL-HDBK-17 [24]. This is most likely due to extensive longitudinal splitting, which was most pronounced in coupons tested at 200°C and below. The coupons exposed at higher temperatures did not exhibit as much splitting, hence the strengths of these coupons may more closely approach the true material strength. The trends in both the at-temperature and residual strengths are similar: strength drops gradually between 300°C and 400°C, and even the coupons exposed at the highest temperature retain significant strength. When at-temperature and residual longitudinal strengths can be directly compared, the residual strength is slightly higher.

The plot in Figure 6.30 shows the longitudinal strength data normalized by the MIL-HDBK-17 value of 2000 MPa [24] from Table 6.6 for longitudinal strength. The data is supplemented with data from other investigations [31] that was normalized in each case by the reported room temperature value[32,33,34]. Data from tests in the current investigation involving exposures at 200°C and below were ignored because of the extensive splitting they exhibited. All of the data shows that longitudinal strength remains constant through exposures to 200°C. The only data available from higher exposure temperatures comes from the current investigation and Greszczuk [31]. Both sets of data show a gradual decrease in strength between 250°C and 400°C.

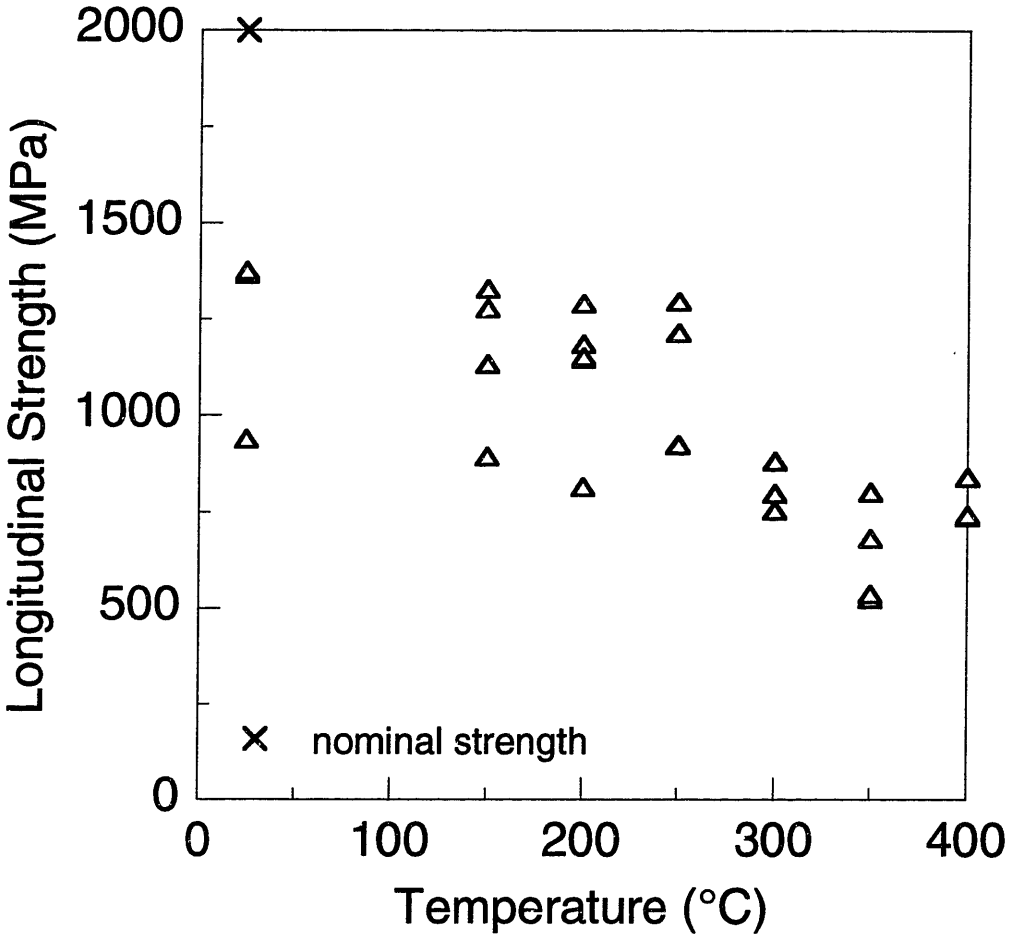

Figure 6.28 At-temperature strength of $[0]_4$ coupons versus nominal test hold temperature.

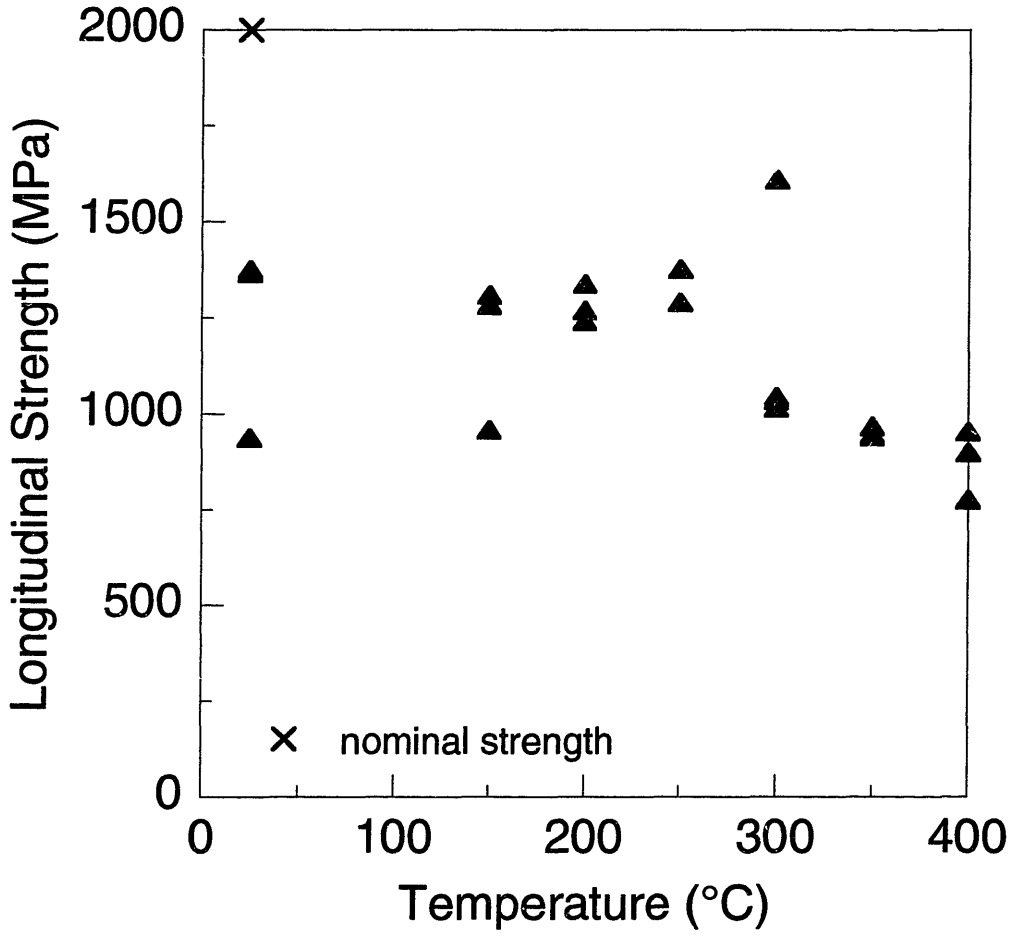

Figure 6.29 Residual strength of $[0]_4$ coupons versus nominal test hold temperature.

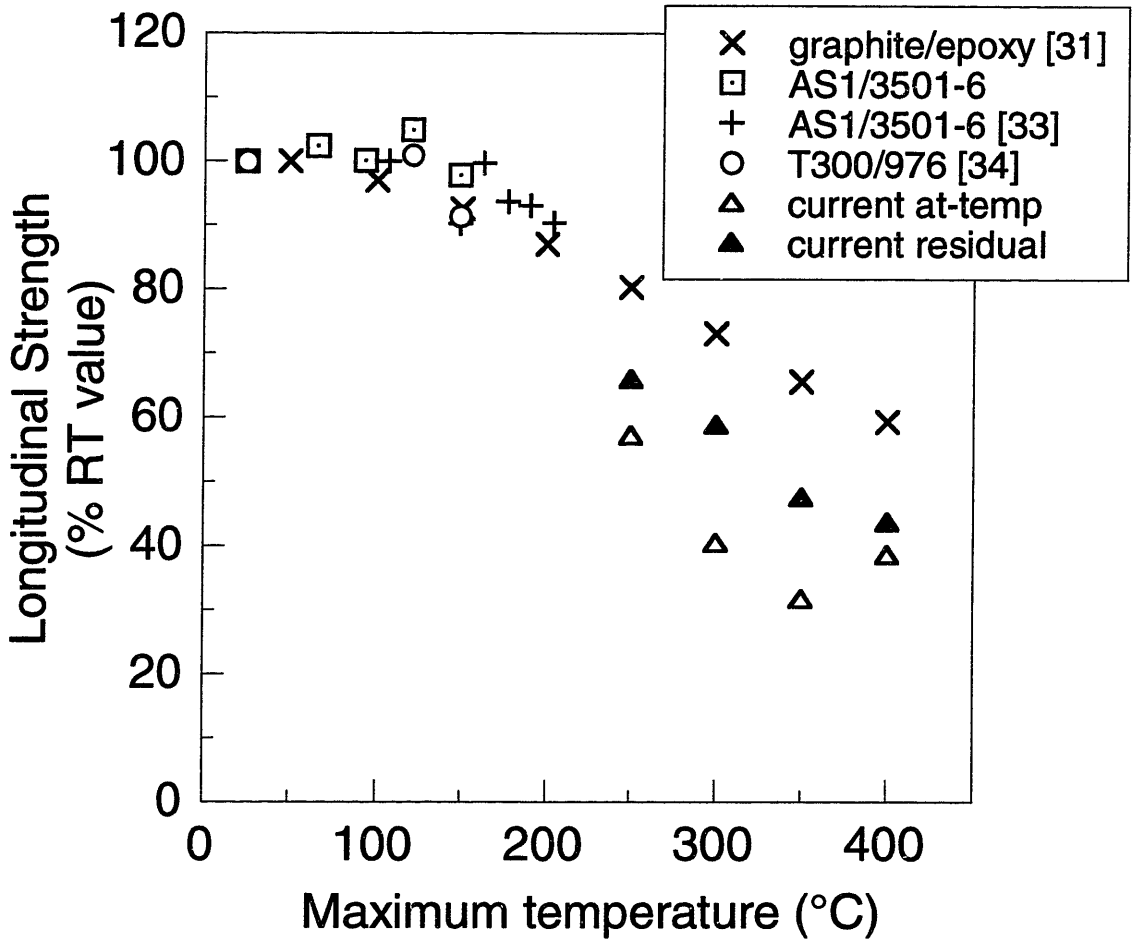

Figure 6.30 Plot of current normalized longitudinal strength data and previously reported values versus maximum exposure temperature.

Disagreement over the magnitude of the property loss may be a reflection of differences in testing conditions. While strength was measured in the current investigation following a 10-minute hold at temperature in a furnace, Greszczuk measured strength after a 4-second laser exposure. The longer exposure is associated with a larger strength loss.

6.3.3 Degradation State as a Property Metric

To evaluate the usefulness of degradation state as a metric from which to determine residual material properties, the degradation states of each coupon were calculated using averaged thermocouple data from the coupons and the degradation model described in Section 4.2. Residual modulus and strength were then plotted as functions of degradation state. Results from each test were plotted separately.

The transverse property data, reported in Tables 6.15 and 6.16, was supplemented with results from a series of tests designed to explore whether different exposure histories designed to yield the same degradation state of approximately 0.03 would produce equal material properties. The residual property results from 10-minute exposures at 300°C were compared to the results of exposures of less than 1-minute at 317°C and 55-minute exposures at 275°C. The degradation states calculated from the thermocouple data for these coupons with different types of exposures were all between 0.024 and 0.046.

In Figures 6.31 and 6.32, the transverse modulus and strength results are plotted versus degradation state. From Figure 6.31 it is clear that most of the exposures studied in the tensile test series produced very small degradation states. Degradation rate is exponential with temperature, hence low temperature exposures produce degradation very slowly. For coupons with very small degradation states, of α less than 0.001, there

Table 6.15 Transverse residual modulus data as a function of degradation state

Nominal test temp, duration of hold	Modulus (GPa)	% RT modulus	Calculated degradation state
25°C (10 min)	8.4	100	0
25°C (10 min)	10.1	120	0
25°C (10 min)	9.0	107	0
150°C (10 min)	9.7	115	3.92e-8
150°C (10 min)	8.7	104	3.19e-8
150°C (10 min)	8.3	99	3.25e-8
200°C (10 min)	9.8	117	1.13e-5
200°C (10 min)	10.1	120	12.0e-5
200°C (10 min)	8.4	100	6.73e-6
250°C (10 min)	8.7	103	7.89e-4
250°C (10 min)	8.0	96	6.92e-4
250°C (10 min)	7.4	89	7.06e-4
300°C (10 min)	5.8	69	0.0239
300°C (10 min)	6.3	74	0.0286
300°C (10 min)	5.6	67	0.0458
317°C (0.1 min)	6.7	80	0.0260
317°C (0.1 min)	5.3	63	0.0304
317°C (0.1 min)	4.5	54	0.0403
275°C (55 min)	4.9	58	0.0266
275°C (55 min)	6.9	82	0.0292
275°C (55 min)	6.2	73	0.0283

Table 6.16 Transverse residual strength data as a function of degradation state

Nominal test temp, duration of hold	Strength (MPa)	% RT strength	Calculated degradation state
300°C (10 min)	1.6	2.8	0.0292
300°C (10 min)	2.1	3.8	0.0239
300°C (10 min)	1.9	3.4	0.0286
300°C (10 min)	1.4	2.5	0.0458
317°C (0.1 min)	5.0	9.2	0.0260
317°C (0.1 min)	5.4	9.9	0.0304
317°C (0.1 min)	2.6	4.6	0.0403
275°C (55 min)	3.9	7.0	0.0266
275°C (55 min)	5.0	9.2	0.0292
275°C (55 min)	5.6	10.1	0.0283

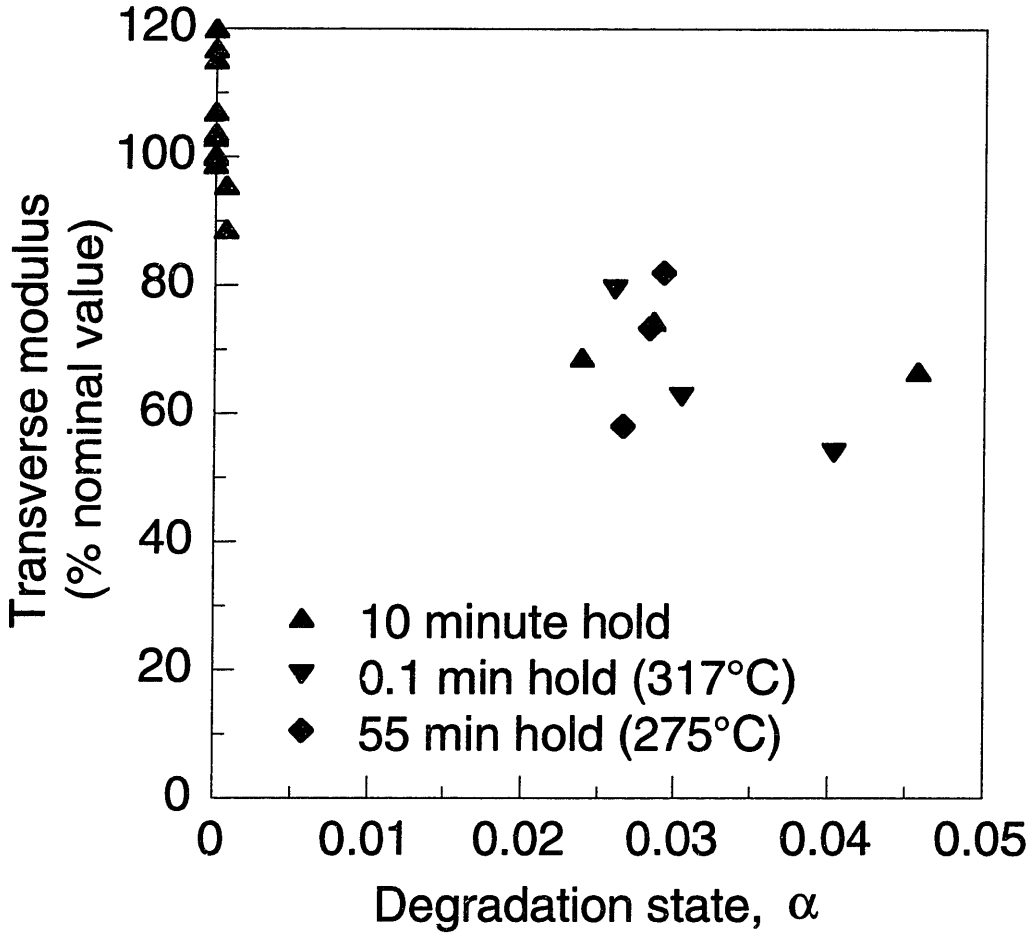

Figure 6.31 Residual modulus of $[90]_{12}$ coupons versus degradation state for different exposure cycles.

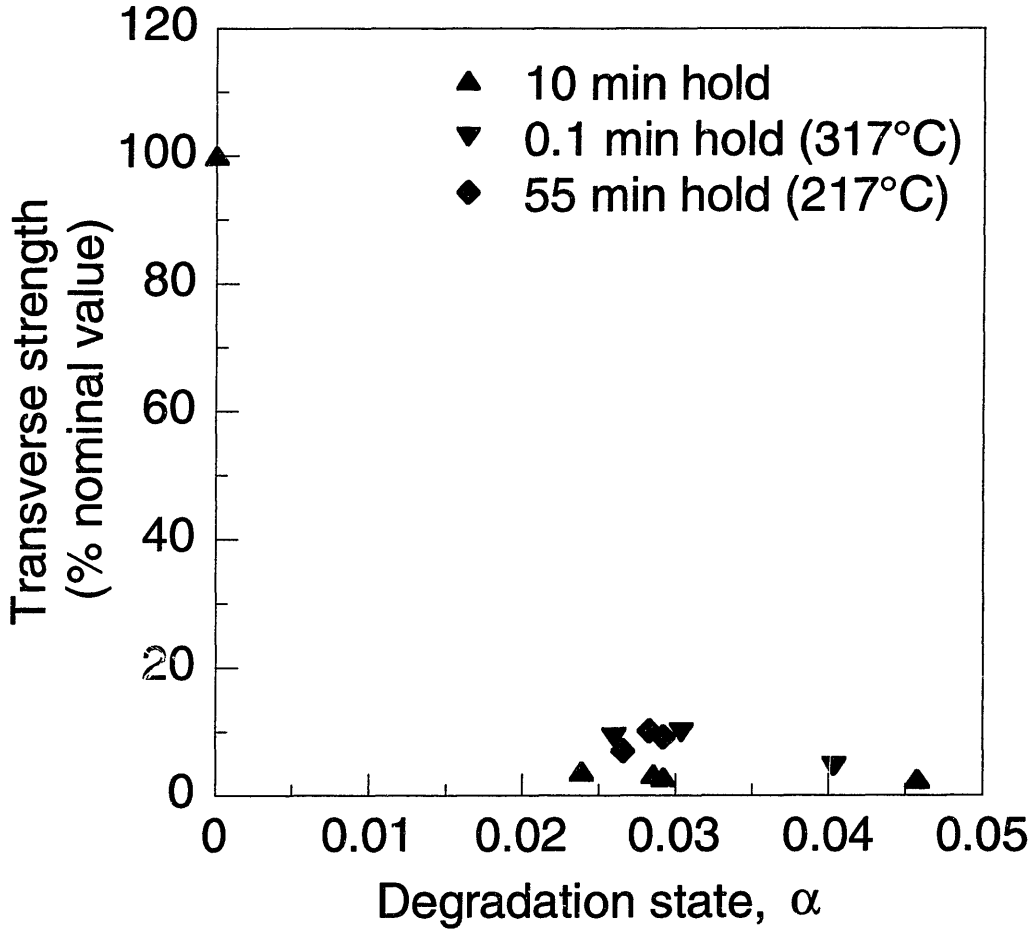

Figure 6.32 Residual strength of $[90]_{12}$ coupons versus degradation state for different exposure cycles.

is virtually no change in residual transverse modulus. A drop in modulus of approximately 30% occurs by the time a degradation state of 0.03 is reached. The data points in the degradation state range of 0.024 to 0.046, collected from coupons with different types of exposures, are grouped in a cluster. There is a lot of scatter in this data, but the cluster of data points supports the conclusion that residual transverse modulus is dependent upon degradation state, but independent of the type of exposure that produces the degradation.

The plot of residual transverse strength in Figure 6.32 tells a similar story. However, the magnitude of the drop in strength at a degradation state of 0.03 is much higher. Strength data from coupons with lower degradation states is omitted because the coupons experienced unacceptable grip failures. The coupons subjected to different types of exposures that produced degradation states between 0.024 and 0.046 had very similar residual strengths. The strength of these coupons was less than 10% of the nominal value. Because of the clustering of the data points from coupons with different types of exposures, residual transverse strength, like residual transverse modulus, appears to be dependent upon degradation state, but independent of the type of exposure that produces the degradation. Residual strength is much more sensitive than residual modulus to low values of degradation state, however.

Residual longitudinal modulus and strength data is tabulated with degradation state data from each test in Tables 6.17 and 6.18. Residual strength data from tests below with exposures below 250°C were omitted because of the extensive splitting shown by these coupons that caused the data to be unacceptable. Residual longitudinal modulus and strength are plotted against degradation state in Figures 6.33 and 6.34, respectively.

Table 6.17 Longitudinal residual modulus data as a function of degradation state

Nominal test temp (all exposed for 10 min)	Modulus (GPa)	% RT modulus	Calculated degradation state
25°C	124	99	0
25°C	112	89	0
25°C	129	103	0
150°C	140	112	2.61e-8
150°C	135	108	2.48e-8
150°C	118	94	3.14e-8
200°C	99	80	4.00e-6
200°C	104	83	9.38e-6
200°C	110	88	1.29e-5
250°C	165	132	1.62e-3
250°C	113	91	7.69e-4
250°C	122	98	6.20e-4
300°C	122	98	0.0266
300°C	111	89	0.0248
300°C	125	100	0.0300
350°C	---	---	0.502
350°C	---	---	0.534
350°C	---	---	0.493
400°C	---	---	1.0
400°C	---	---	1.0
400°C	---	---	1.0

Table 6.18 Longitudinal residual strength data as a function of degradation state

Nominal test temp (all exposed for 10 min)	Strength (MPa)	% RT strength	Calculated degradation state
250°C	1290	64	0.00162
250°C	1290	64	0.00077
250°C	1378	69	0.00062
300°C	1016	51	0.0552
300°C	1610	80	0.0266
300°C	1046	52	0.0248
300°C	1036	52	0.0300
350°C	967	48	0.502
350°C	942	47	0.534
350°C	947	47	0.493
400°C	899	45	1.0
400°C	776	39	1.0
400°C	953	48	1.0

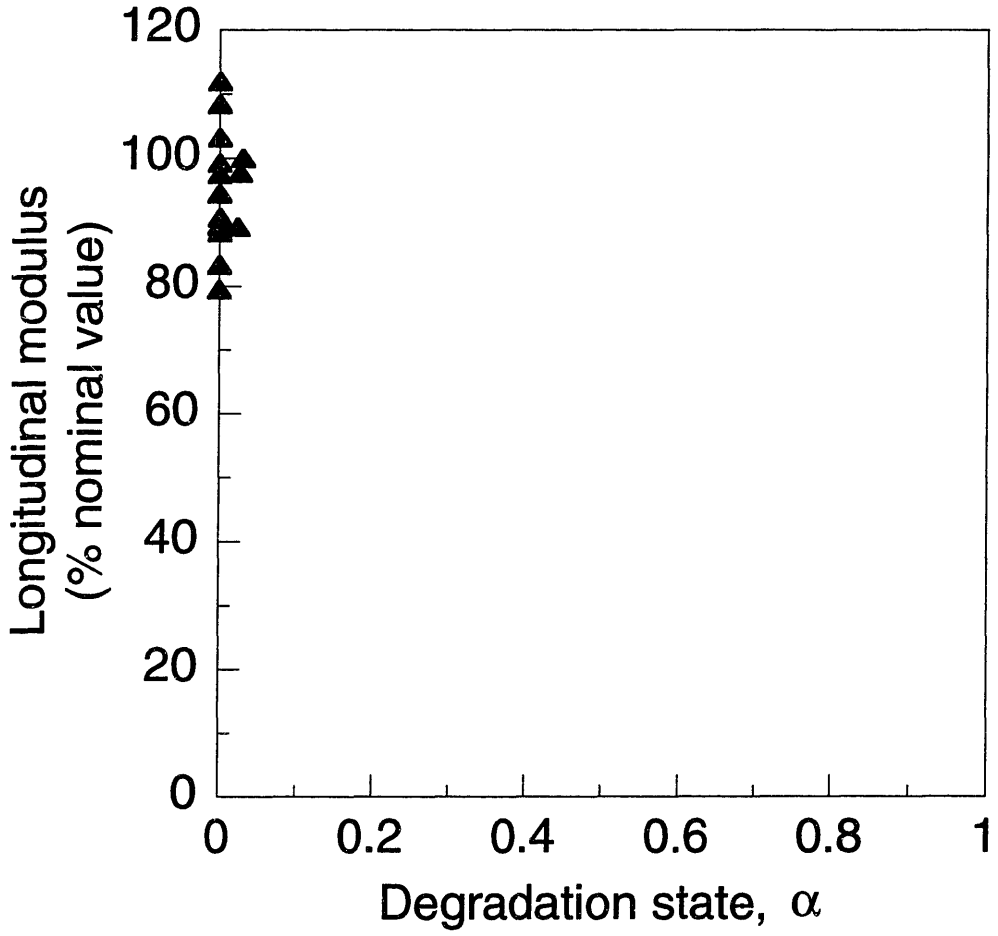

Figure 6.33 Residual modulus of $[0]_4$ coupons versus degradation state for different exposure cycles.

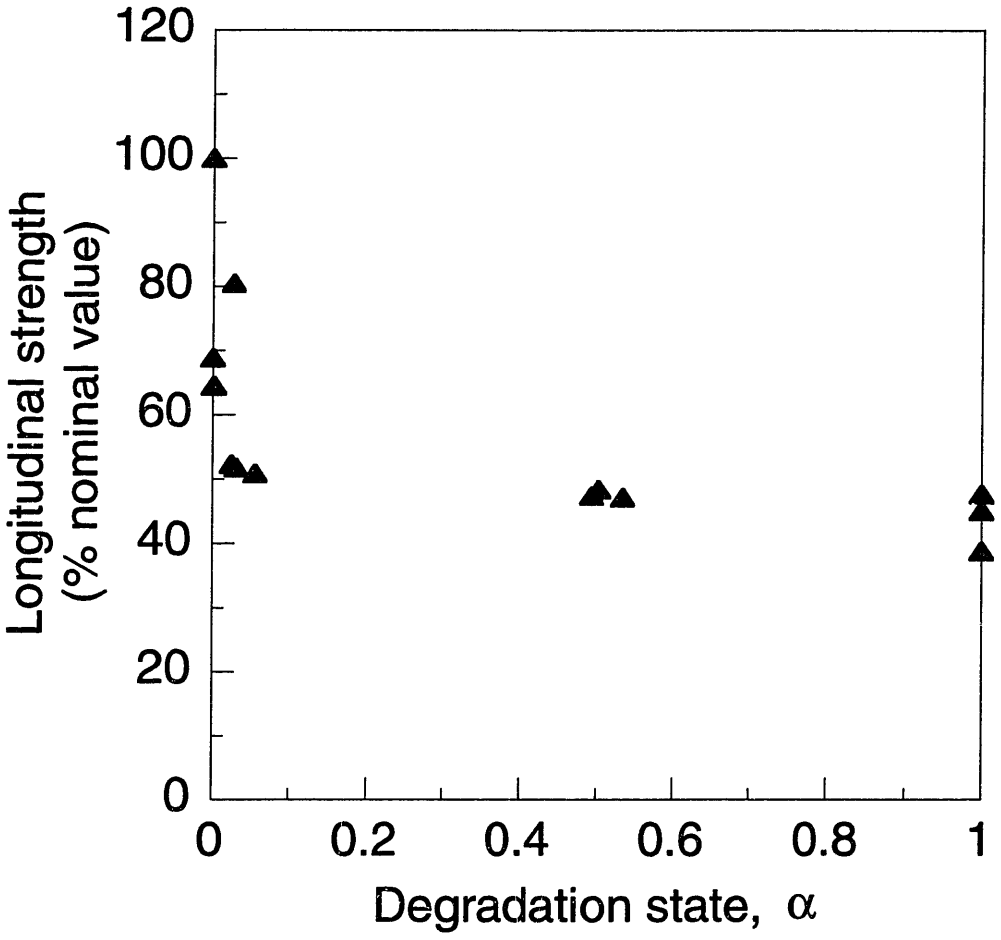

Figure 6.34 Residual strength of $[0]_4$ coupons versus degradation state for different exposure cycles.

It is difficult to draw conclusions from the plot of modulus data because there is no clear trend in the available modulus data, and no data was available from tests that produced higher degradation states. More can be said about the strength results. The residual longitudinal strength is quite sensitive to low degradation states, as nearly 50% of the strength has been lost by a degradation state of 0.03. The nature of the relationship between degradation state and strength for degradation states below 0.03 cannot be characterized because of the unacceptable failure modes of the coupons tested. Fully degraded coupons (with α equal to 1) retain over 40% of their nominal strength.

6.3.4 Material Property Models

The temperature and degradation dependence of the mechanical properties can be summarized via empirical property models that provide modulus and strength as functions of temperature and degradation state. From these models, transverse and longitudinal ply properties of graphite/epoxy can be determined for any temperature and degradation state. The models take the form of tabulated data, presented graphically in Figures 6.35, 6.36, 6.37, and 6.38 in 3-D surface plots, where the three axes are temperature, degradation state, and modulus or strength. The surfaces were generated by plotting experimentally measured data (denoted on the plots with black dots) and then filling in the volume based on observed trends in the data, as subsequently explained for each case. In the absence of data, surfaces were interpolated (and in some cases extrapolated) by assuming that the temperature and degradation dependencies of the properties could be separated, i.e. $f(T, \alpha) = f(T)*f(\alpha)$.

Models of transverse modulus and tensile strength are shown in Figures 6.35 and 6.36. Both properties are strongly dependent on temperature. The transverse strength drops to approximately zero at very small values of degradation state, whereas the transverse modulus is less sensitive to degradation. However, more modulus data is clearly needed between degradation states of 0.03 and 1 to determine the exact slope of the surface. Lacking this data, the simplest possible relationship of a linear drop in modulus with degradation state, is assumed between the degradation state values of 0.03 and 1.

Models of longitudinal modulus and tensile strength are shown in Figures 6.37 and 6.38. The data points shown all come from the current investigation. The only modulus data available above a degradation state of 0.03 is that of Greszczuk [31], which showed a 20% drop in modulus for coupons exposed at 400°C. The conditions under which Greszczuk conducted his tests were assumed to be severe enough to degrade the coupon to a degradation state of 1, based on a description of the testing environment [14]. Longitudinal modulus is assumed to be insensitive to temperature and to drop 20% when as the degradation state of the material approaches a value of 1. This is a reasonable assumption given the fact that longitudinal modulus is dominated by the modulus of the graphite fibers which are themselves insensitive to matrix degradation state and insensitive to temperature in this range. Longitudinal tensile strength drops significantly at small values of degradation state but then asymptotes at approximately 40% its nominal value. Longitudinal tensile strength measurements at relatively low degradation states show a slight dependence on temperature. This dependence is retained at higher degradation states.

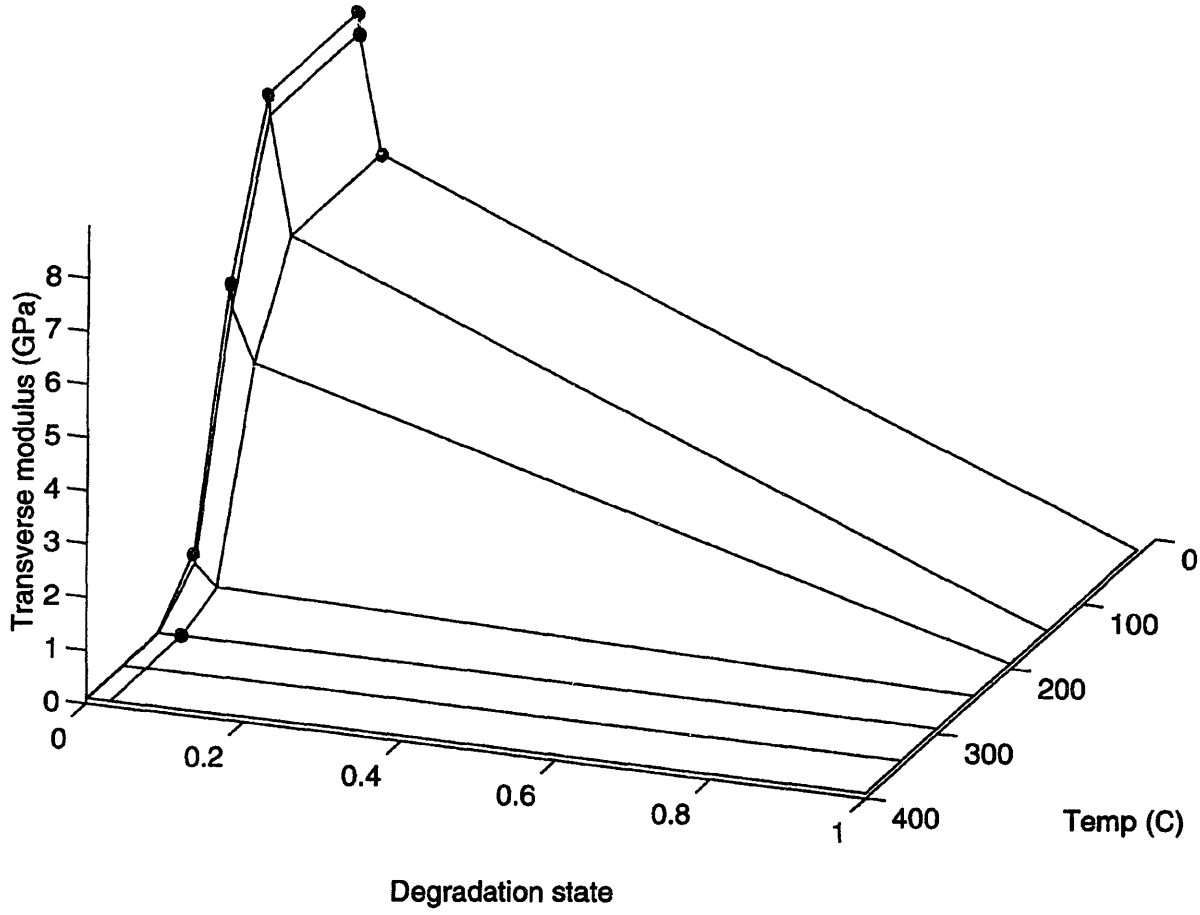

Figure 6.35 Transverse modulus model.

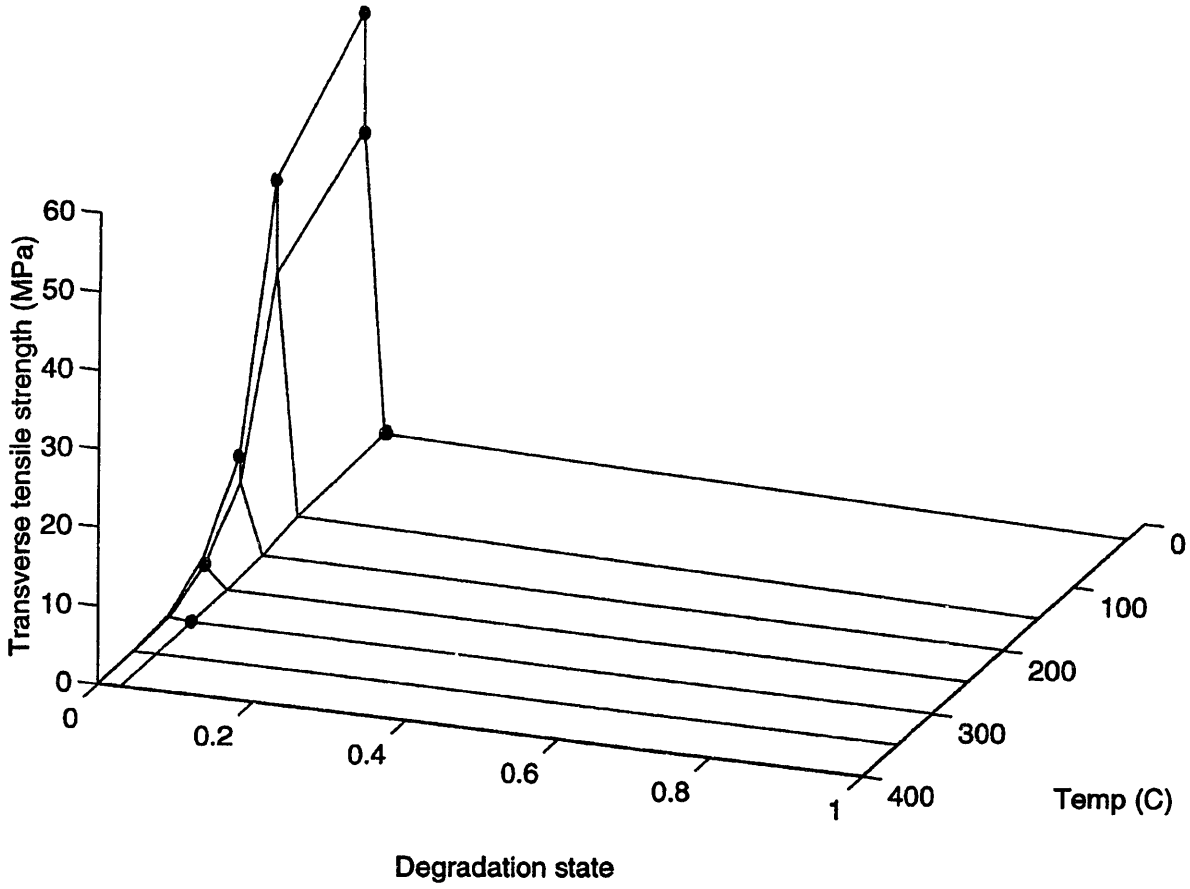

Figure 6.36 Transverse tensile strength model.

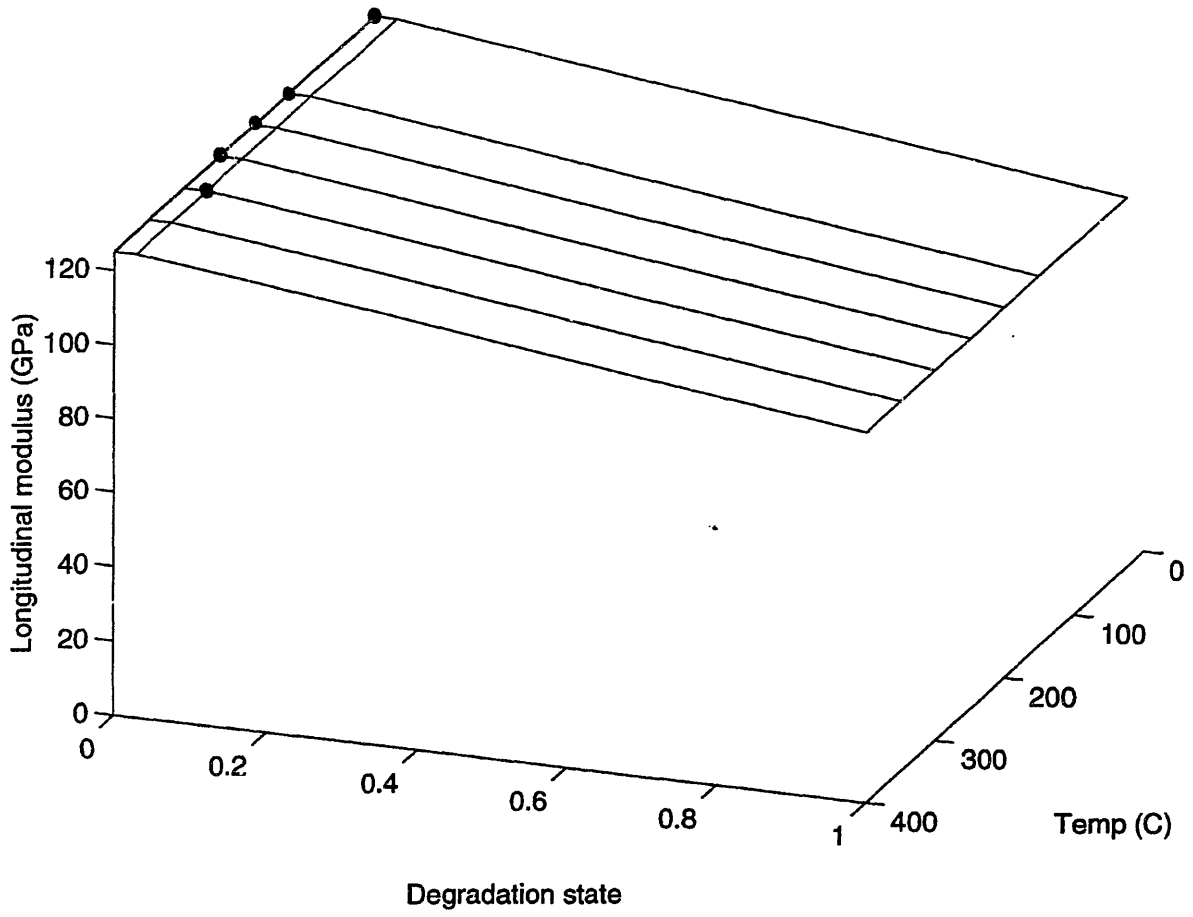

Figure 6.37 Longitudinal modulus model.

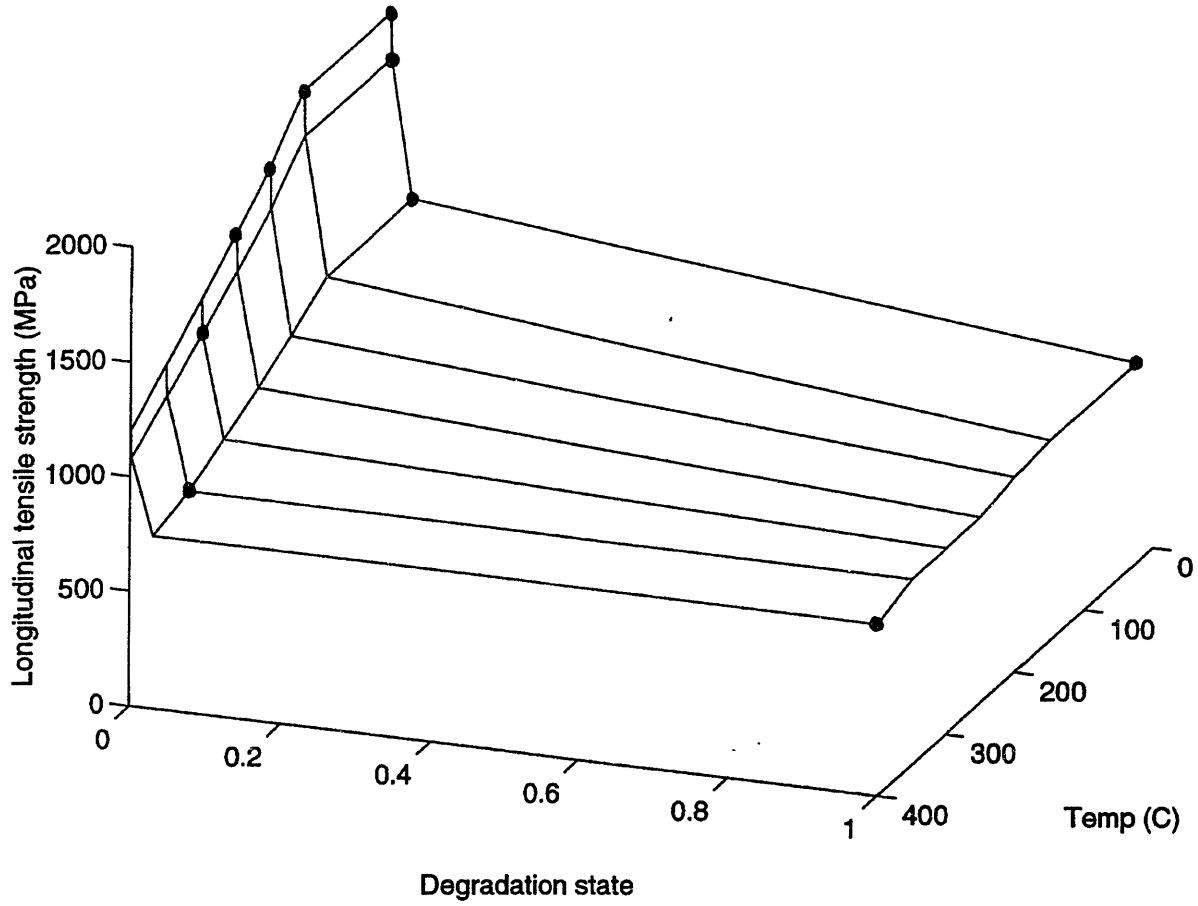

Figure 6.38 Longitudinal tensile strength model.

CHAPTER 7

INTEGRATED MODEL

An important application of the knowledge gained from studies of the thermal response, degradation chemistry, and material property response of graphite/epoxy laminates exposed to high temperature environments is the integration of the models of these mechanisms into a predictive code. Such a code has been developed. The name of the code is CHARplus and it is written in the FORTRAN programming language. The code implements an integrated model describing the response of a laminated plate exposed to the environment while being loaded mechanically. The knowledge developed in this work is utilized in developing the integrated model. The two major objectives of developing the code were to show the general capabilities of such an integrated model and to create a tool with predictive utility for AS4/3501-6 graphite/epoxy within a regime limited by the scope of this work.

The development and use of the CHARplus code are discussed in this chapter. The philosophy guiding the development of CHARplus is reviewed, and the assembly of a material property input file for AS4/3501-6 graphite/epoxy is described. The results of analytical verification tests designed to validate the output of CHARplus are presented, and CHARplus predictions are compared with experimental data from other investigators. Finally, the capabilities of such a code are illustrated through an example.

7.1 DEVELOPMENT OF INTEGRATED MODEL

In Chapter 3, the effects of simultaneous exposure to a high temperature environment and mechanical loading on a laminated composite were considered in terms of the mechanisms that affect the state of the laminate. These mechanisms are thermal response, degradation chemistry, thermomechanical response, and mechanical damage mechanisms. Models of the thermal response and degradation chemistry of graphite/epoxy were developed in this work, along with models of the changes in mechanical material properties of graphite/epoxy as functions of temperature and degradation state. A thermomechanical response model based on classical laminated plate theory is described in Appendix E. Models of mechanical damage mechanisms were not addressed.

In order to calculate a solution to the problem shown in Figure 3.1, that of a mechanically loaded laminate exposed on one surface to a flame, it is necessary to integrate the models of the mechanisms and implement them in a software package that will perform the calculations. An approach to integrating the models is depicted in Figure 7.1. This is a modification of a modeling approach first described by McManus, et al. [41]. The flowchart in Figure 7.1 is similar to the modeling approach shown in Figure 3.2, in that the boxes represent models of mechanisms and the arrows between the boxes represent information input to and output from the models. The difference is that Figure 3.2 shows a general philosophy for breaking down the problem illustrated in Figure 3.1 into the operative mechanisms while the flowchart in Figure 7.1 emphasizes how the pieces of the problem can be reassembled.

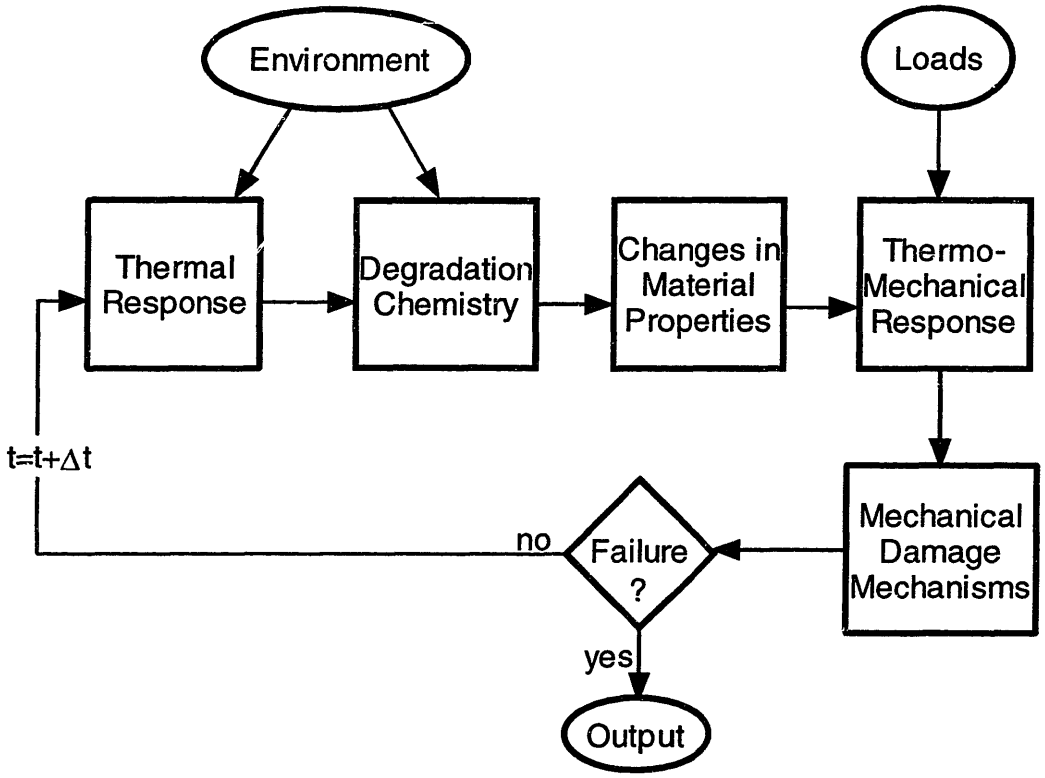

Figure 7.1 Illustration of model integration approach.

The approach shown in Figure 7.1 includes iterative calculations of the variables that constitute the state of the laminate. At each time step, temperatures are calculated using a thermal response model, based on information about the environment. From the temperatures, the degradation state is then calculated using a degradation chemistry model. Next, the material properties are evaluated based on information provided from the thermal response and degradation chemistry models. All of the output of the first three models serves as input to the thermomechanical response model, where stresses and strains are calculated. Finally, mechanical damage mechanisms are considered, and the occurrence of mechanical damage is determined. If the conditions are not sufficient for the laminate to fail, the process is repeated at the next time step. The laminate conditions at one time step serve as input for calculations at the next time step. The environmental conditions and loads may change with time.

The approach depicted in Figure 7.1 is implemented in the FORTRAN computer code entitled CHARplus. The code is a revised version of the CHAR code by McManus [13]. The FORTRAN source code and user's manual are given in a separate report [53]. CHARplus models a laminated plate of an orthotropic material that is exposed to the environment on one surface. The code predicts the temperature, degradation state, stress, strain, and strength fraction (defined in Appendix E) at all nodes in the laminate. Models of mechanical damage mechanisms and failure were not included.

A one-dimensional formulation of the finite difference thermal response model from Section 4.1.2 and the finite difference degradation chemistry model derived in Section 4.2.2 are integrated in the code. The thermomechanical response model uses a discretized formulation of classical laminated plate theory, which is derived in Appendix

E. The laminate is discretized through the thickness. Models of mechanical damage mechanisms and failure are not included, but such modules could be added at a later date. Material property models developed in Section 6.3.5 are not part of the main source code, but are included in the material property input file developed for AS4/3501-6.

An interactive preprocessor called PreCHARplus is used to generate the CHARplus input file. The user supplies details of the degradation model, the material properties as functions of temperature and degradation state, and the laminate geometry, including ply angles and thickness. Environmental conditions can be specified as a temperature, flux, or convection/radiation boundary condition, and mechanical loadings are specified as applied force and moment vectors, $\{\mathbf{N}\}$ and $\{\mathbf{M}\}$.

The code generates output files giving the temperature, degradation state, stresses, and strength fractions as functions of time and location. The history at particular nodes can be recorded, as well as "snapshots" of the entire response at particular times. The computation algorithm for CHARplus is shown in flowchart form in Figure 7.2.

7.2 SELECTION OF MATERIAL PROPERTIES

The CHARplus code requires an extensive material property input file for the material being modeled. Material property inputs include density, thermal conductivity, specific heat, coefficients of thermal expansion, elastic constants, and strengths. Many of these properties vary with temperature or degradation state (referred to as "char volume" in the CHARplus code.) These dependencies are captured in tables in which values of the material properties at different temperatures and degradation states are tabulated. The

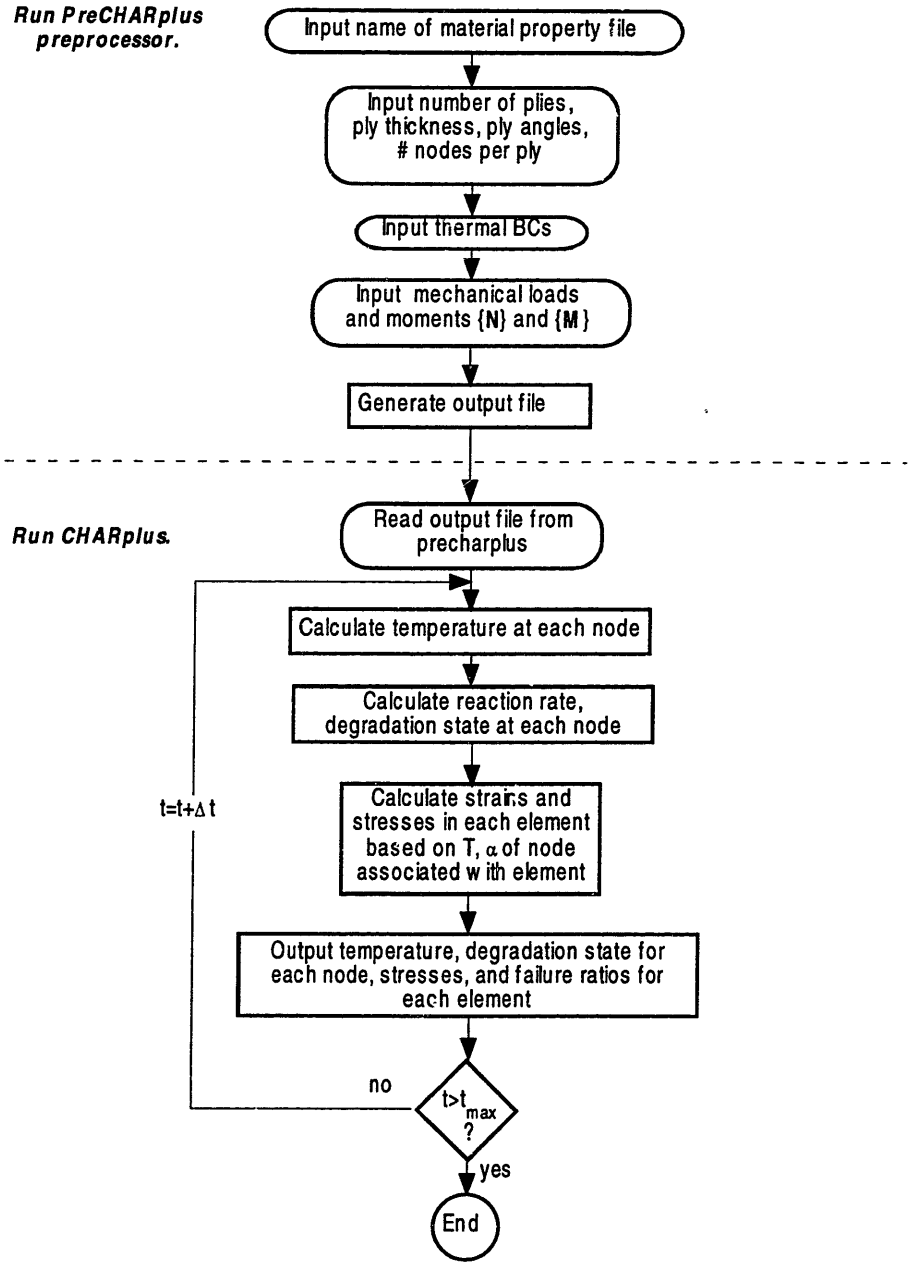

Figure 7.2 Flowchart for CHARplus code.

code uses the tables by first determining the temperature and degradation state at each node. Given the temperature and degradation state at each node, linear interpolation is used to determine the values of the material properties at the node from the property tables. A number of material properties are also required to use features of the code that are currently inactive. These include permeability, porosity, coefficient of moisture expansion, and properties of the volatiles released as a product of degradation reactions, including volatile specific heat, viscosity, and molecular weight.

An annotated listing of the AS4/3501-6 graphite/epoxy material property input file, called MAT.AS435016, appears in Appendix F. These properties were collected from a variety of sources. Some properties, including the reaction constants for the epoxy degradation reaction and ply moduli and strengths, were based on models developed in the current work. Reaction constants were determined from the current work, as discussed in Section 6.2.2, as were transverse and longitudinal modulus and tensile strength models, as discussed in Section 6.3.5. The development of models of shear modulus, shear strength, transverse compressive strength, and longitudinal compressive strength is discussed in Appendix G. Other properties, including thermal conductivity, density, specific heat, and latent heat of reaction, were based on values reported by other investigators [9,16] and discussed in Chapter 2.

Graphite/epoxy porosity and permeability values and volatile properties are unimportant in the current work. The calculations in which they are used, involving mass flow and pressure calculations, are inactive features retained from the original CHAR code. The calculations were not deleted from the revised code, but they are not part of the laminate temperature, degradation, or stress response calculations of CHARplus.

Values of the properties had to be included in the material property input file in order for the code to compile properly, so values from the FM/5055 carbon/phenolic material input file created for use with the original CHAR code [13] were adopted as placeholders. The mass flow and pressure calculation features could be reactivated at a future date to aid in calculation of through-thickness stresses, important for determination of delamination. In this case, it would be necessary to correctly determine values of the properties for AS4/3501-6.

Another inactive feature of the CHAR code is the calculation of strain due to moisture and char expansion and internal pressure. Consideration of strains induced by moisture, degradation, and pressure is beyond the scope of this work. However, rather than deleting the strain calculation features from the revised CHAR code, the parameters were nullified by setting the moisture and char expansion coefficients, pressure compliances, and pressure-stress coupling factors to zero or one, as needed.

The sources of the various properties in the AS4/3501-6 material property input file are summarized in Table 7.1. Properties in the y-direction and z-direction were set equal to each other because AS4/3501-6 is a transversely isotropic material.

7.3 ANALYTICAL VERIFICATION

A number of checks were performed to verify the integrity of the calculations performed in the CHARplus code. To examine the effects of spatial discretization, an analytical temperature solution was compared with code predictions made using different numbers of through-thickness nodes. To examine the effects of time discretization,

Table 7.1 Sources of AS4/3501-6 properties used in input file

Property	Source
Reaction type	Specified Arrhenius-type reaction based on results of current TGA studies
Activation energy	Curve fit to current TGA data for 3501-6 epoxy (see Sect. 6.2)
Rate constant	Curve fit to current TGA data for 3501-6 epoxy (see Sect. 6.2)
Order of reaction	Curve fit to current TGA data for 3501-6 epoxy (see Sect. 6.2)
Heat of reaction	From [10]
Density	Calculated from fiber and matrix properties via rule of mixtures [54]
Porosity	Inactive feature (value from properties of carbon-phenolic composites [13])
Absorptivity/Emissivity	Inactive feature (value from properties of carbon-phenolic composites [13])
Permeability	Inactive feature (value from properties of carbon-phenolic composites [13])
Thermal conductivity	x-direction conductivity from [8]; y- and z-direction conductivity averaged from [8,9,16,17,19,20]
Specific heat	From [9]
Young's modulus	x-direction modulus taken from Fig. 6.37. y- and z-direction modulus taken from Fig 6.35.
Poisson's ratio	From Table 6.6 [55]. Assumed constant with temperature and degradation state [32,33,34]
Shear modulus	From Fig. G.1
Coefficient of thermal expansion	From Table 6.6 [55]
Coefficient of moisture expansion	Inactive feature (set to zero)
Coefficient of char expansion	Inactive feature (set to zero)
Pressure compliance	Inactive feature (set to zero)
Pressure-stress coupling factor	Inactive feature (set to one)
Tensile strength	x-direction strengths from Fig. 6.38. y- and z-direction strengths from Fig 6.36.
Compressive strength	x-direction strengths from Fig. G.4. y- and z-direction strengths from Fig. G.3.
Shear strength	From Fig. G.2.
Volatile specific heat	Inactive feature (value from properties of carbon-phenolic composites [13])
Volatile viscosity	Inactive feature (value from properties of carbon-phenolic composites [13])
Volatile molecular wt.	Inactive feature (value from properties of carbon-phenolic composites [13])

degradation state predictions made using different sizes of time steps were compared. Also, degradation state and stress/strain calculations from the code were compared with hand calculations to verify that there were no programming errors in the code.

In the first verification test, the temperature distribution inside a one meter thick semi-infinite aluminum plate was calculated. The geometry of the plate is shown in Figure 7.3. One face of the plate (at z equal to zero) is insulated. Initially the plate is at a uniform temperature T_0 of 0°C. At time t greater than zero, the non-insulated face of the plate is held at a constant temperature of T_s = 100°C. The temperature distribution through the thickness (z-direction) of the plate can be calculated by an exact solution of the heat conduction equation [47]:

$$T(z,t) = T_0 + (T_s - T_0)\sum_{n=0}^{\infty}(-1)^n \frac{4}{\pi(2n+1)} cos\left[\frac{(2n+1)\pi z}{2L}\right] exp\left[-\frac{\pi^2}{4} Fo_z (2n+1)^2\right] \quad (7.1)$$

where the Fourier number, Fo_z, is calculated via:

$$Fo_z = \frac{k_z t}{\rho c L^2} \quad (7.2)$$

Constant material properties typical of aluminum were used in the calculations. The thermal conductivity, k_z, was set at 64 W/m·K; the density, ρ, at 2787 kg/m^3; and specific heat, c, at 833 J/kg·K. The temperature distributions were calculated by the CHARplus computer code and the temperature at the insulated surface (where z equals zero) was determined 5000 seconds into the simulation using different numbers of nodes through the thickness of the plate and a time step of 10 seconds. The exact solution,

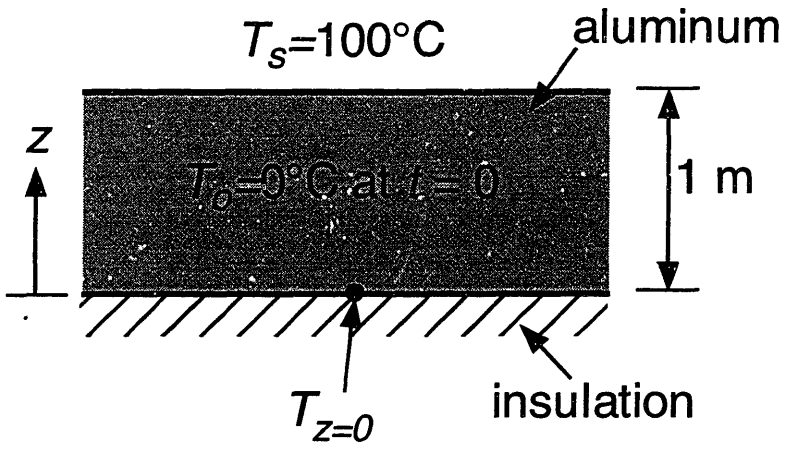

Figure 7.3 Geometry of a 1 m thick aluminum plate heated on one surface.

determined from Equation 7.1 using 8 modes, was 46.754°C. The magnitude of the eighth mode was on the order of 10^{-87}.

The results are compared in Figure 7.4a. The plot shows that when more than 20 nodes are used, the calculated temperatures agree with the analytical solution within 5%. Using 25 nodes, which produces an error of less than 5%, the temperature distributions through the thickness were then calculated at times of 500, 2000, and 5000 sec. The code results and exact solutions are compared in Figure 7.4b and, as expected, show excellent agreement.

The second test was used to examine the convergence of the degradation state calculations made by CHARplus. The problem involves a one cm-thick non-degraded graphite/epoxy laminated plate, initially at 350°C, and held at 350°C for one hour. A 0° laminate was modeled. However, the ply orientation is irrelevant in calculations of degradation state. The degradation state of the material (which is uniform through the thickness because the temperature is uniform) is determined as a function of time using time steps of 10 min, 1 min, and 0.1 min. The results are plotted in Figure 7.5. The plot shows that a time step of 10 minutes causes the code to overestimate the degradation state. If the time step is reduced to 1 minute, the degradation state solution converges to within 2.5% of the values calculated with an even smaller time step of 0.1 minutes. A time step of 0.1 minutes was therefore selected for future calculations using CHARplus.

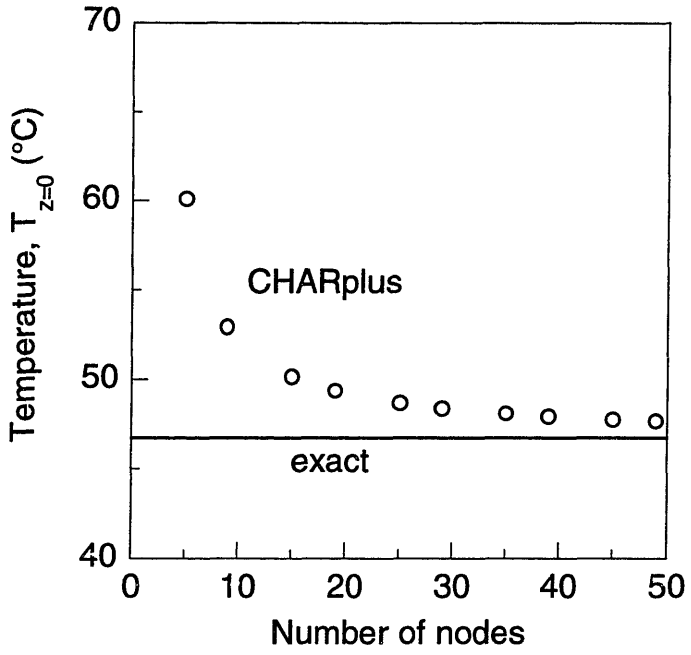

Figure 7.4a Comparison between exact solution (Equation 7.1) of the temperature of the bottom surface of an aluminum plate and the results of the CHARplus code at 5000 seconds.

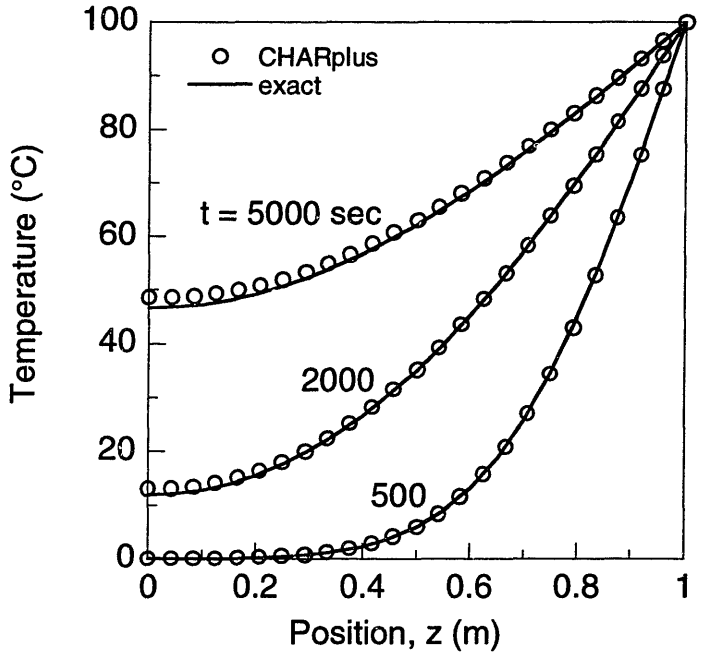

Figure 7.4b Temperature distributions from exact solutions (Equation 7.1) and CHARplus results for a 1 m thick aluminum block for different times.

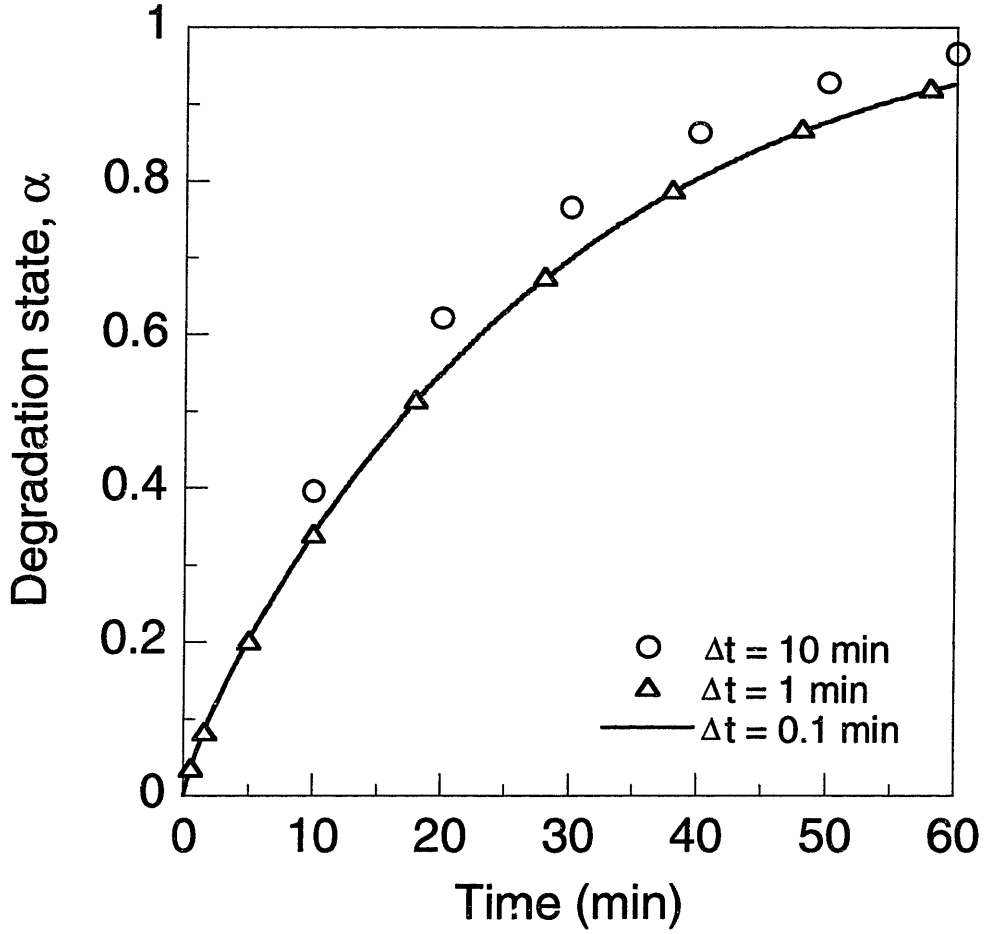

Figure 7.5 Degradation state predictions from CHARplus as a function of time step for a one-cm thick graphite/epoxy plate held at 350°C for one hour.

7.4 COMPARISON WITH EXPERIMENTAL DATA

Many assumptions were necessary to develop the material property database for AS4/3501-6. The models used in CHARplus are thus best-effort approximations. There is utility, however, in comparing the predictions from CHARplus with available experimental data. In addition to demonstrating some of the capabilities of the code, such an exercise serves to validate the modeling methodology and provide assurance that the models are fundamentally sound. The comparison with data also demonstrates the utility of the CHARplus code for predicting the behavior of AS4/3501-6 graphite epoxy within a limited regime.

The applicability of the CHARplus code is limited to the regime studied in this work, meaning environments with temperatures of 200°C and above, with exposure times of 25 minutes or less. While no experiments suitable for direct comparison with CHARplus predictions were carried out in the current investigation, other investigators conducted experiments testing AS4/3501-6 laminates in similar regimes. Ottaviano and Yeh [42] conducted experiments in which the modulus and strength of AS4/3501-6 graphite/epoxy coupons that had been exposed to temperatures as high as 350°C in an oven were measured. Coupons with a layup of $[\pm 45]_s$ and nominal thickness of 0.6 mm were heated to the test temperature, immediately cooled to room temperature without an at-temperature hold, and then loaded in tension to failure. The modulus data from these experiments is suitable for direct comparison with predictions from CHARplus. Furthermore, although CHARplus does not model failure, it is possible to estimate the reduction in tensile strength of the $[\pm 45]_s$ laminates studied by Ottaviano and Yeh.

The oven temperature as a function of time was specified as boundary condition input to the CHARplus code. The MAT.AS435016 input file was used to describe material properties. At the end of each simulation, CHARplus provided output files including the ply shear strength as a function of depth and the extensional stiffness of the $[\pm 45]_s$ laminate. The predicted laminate modulus is plotted along with the experimentally measured modulus as a function of exposure temperature in Figure 7.6.

The code predicts correctly that the modulus does not change following exposures to temperatures as high as 250°C. There is significant scatter in the data, particularly at higher exposure temperatures. While there is good agreement between data and model up to 250°C, more data is needed to assess the quality of the predictions at higher temperatures.

As noted previously, CHARplus does not model failure, but it is possible to estimate the reduction in tensile strength of the $[\pm 45]_s$ laminates. Past investigators have used changes in the tensile strength of $[\pm 45]_s$ coupons as an indicator of changes in ply shear strength [33], and ASTM D3518 [56] recognizes a method whereby inplane shear stress is determined from the load applied to a $[\pm 45]_s$ coupon. This relationship is turned around here: predicted percentage reductions in the ply shear strength predictions from CHARplus for various exposures are used to estimate percentage reductions in the tensile strength of $[\pm 45]_s$ coupons. It is assumed, for example, that an environment that induces degradation sufficient to cause a 20% loss in ply shear strength will cause a 20% loss in the tensile strength of a $[\pm 45]_s$ laminate.

Percentage reductions in the shear strength of the plies of the coupons heated in an oven by Ottaviano and Yeh were predicted by the CHARplus code using the same

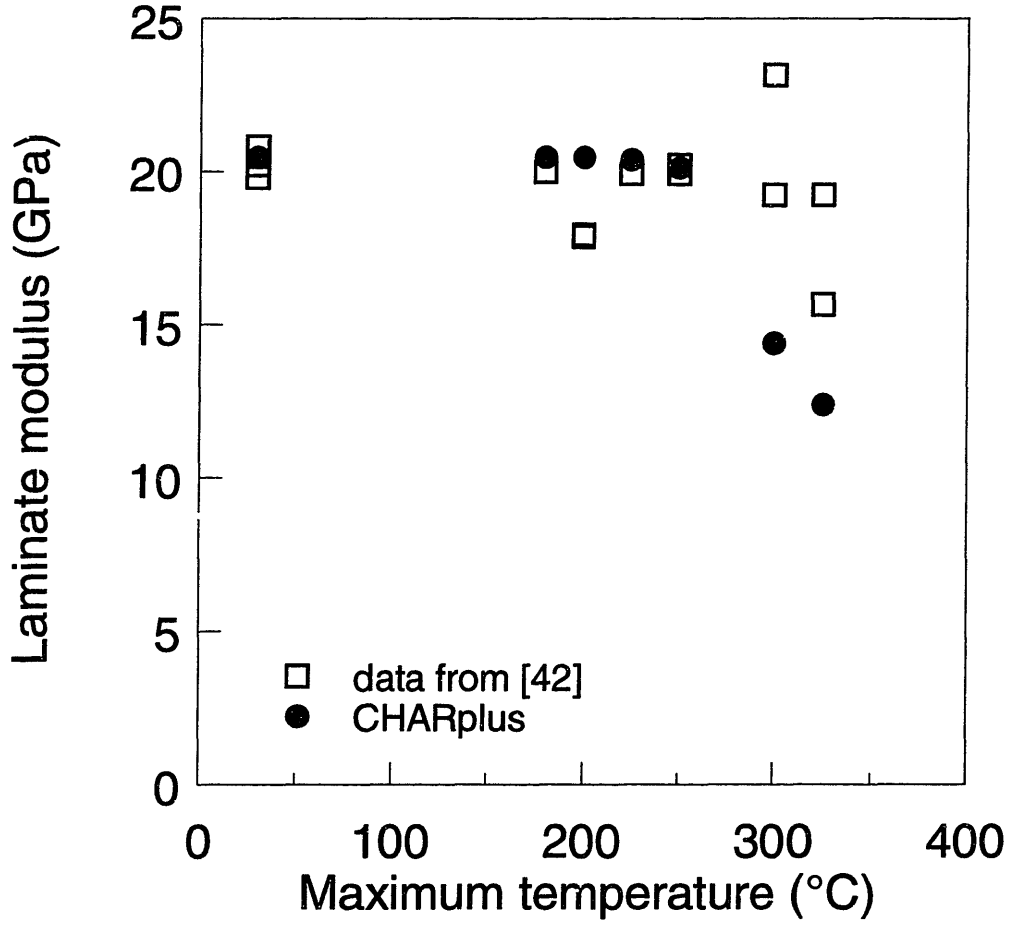

Figure 7.6 Predicted values and experimental results [42] of the longitudinal modulus of a $[\pm 45]_s$ graphite/epoxy laminate heated in an oven and cooled before loading as a function of exposure temperature.

boundary condition and set of material property inputs as were used to determine modulus loss in these coupons. Percentage reductions in laminated tensile strength were equated with the percentage reductions in ply shear strength. The results are plotted in Figure 7.7. CHARplus predicted that exposures to temperatures as high as 250°C would cause very little percentage loss in ply shear strength, and, by extension, little percentage tensile strength loss in a $[\pm 45]_s$ laminate. Strength rapidly drops at higher temperatures, and the material has almost no shear strength remaining after an exposure at 350°C. The strength reduction estimates from CHARplus compare well with the available experimentally measured strength reductions below 250°C and above 350°C. However, the strength data is limited and the amount of scatter in the data is unknown. More data is needed to make a better assessment of the accuracy of the CHARplus predictions.

Ottaviano and Yeh [42] also conducted experiments in which graphite/epoxy coupons with layup $[\pm 45]_{4s}$ were exposed on one surface to a diffused propane flame. Thermocouples embedded in the coupons provided measurements of the internal temperature. The placement of the thermocouples is illustrated in Figure 7.8. The exposure times ranged from 15 seconds up to 45 seconds. After being removed from the flame, the coupons were loaded in tension to failure. CHARplus was used to predict the internal temperature distribution during exposure. The code also provided estimates of the percentage reduction in the residual tensile strength of the degraded coupons based on the percentage reduction in ply shear strength, as before.

The $[\pm 45]_{4s}$ graphite/epoxy coupons were 2 mm thick and the heated region was 51 mm wide. The temperature distribution was calculated via CHARplus using the MAT.AS435016 material property input file and convection boundary conditions with an

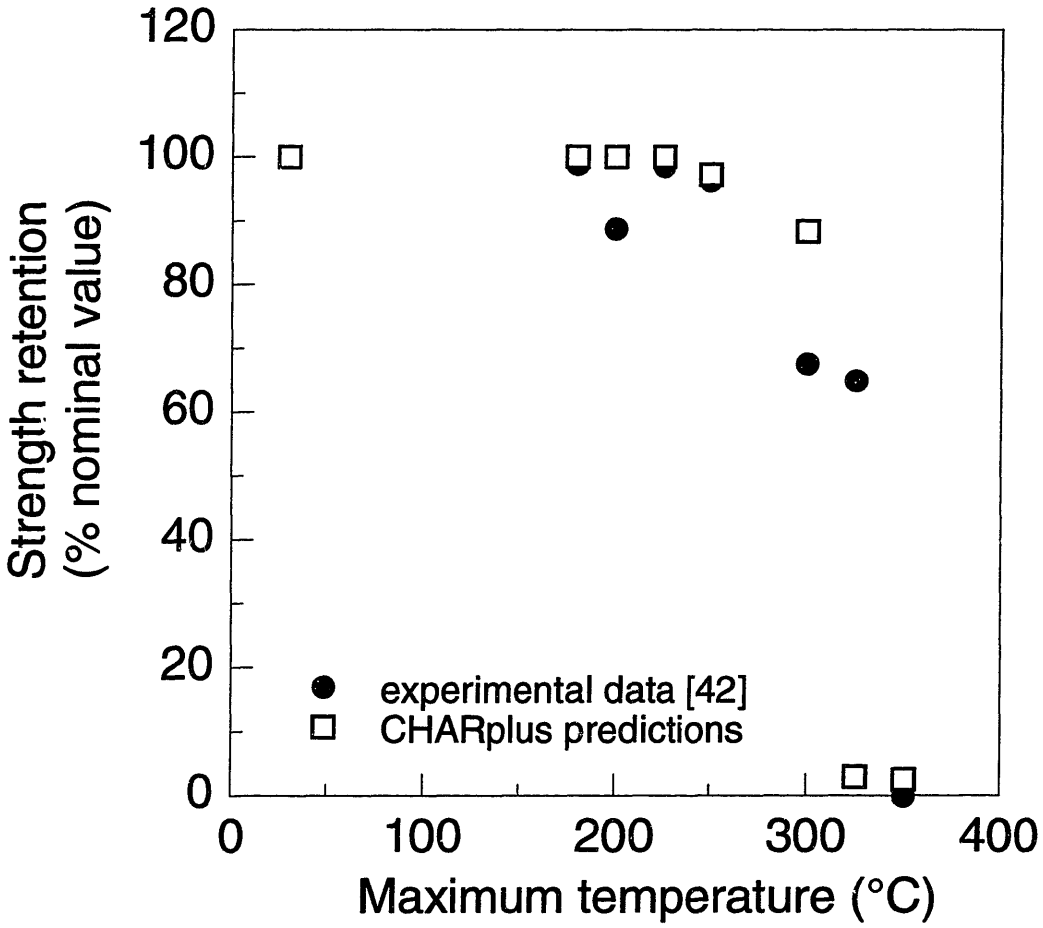

Figure 7.7 Tensile strength retention of $[\pm 45]_s$ graphite/epoxy laminates heated in an oven and cooled before loading, compared with CHARplus predictions of shear strength retention for individual plies within laminates in the same environment.

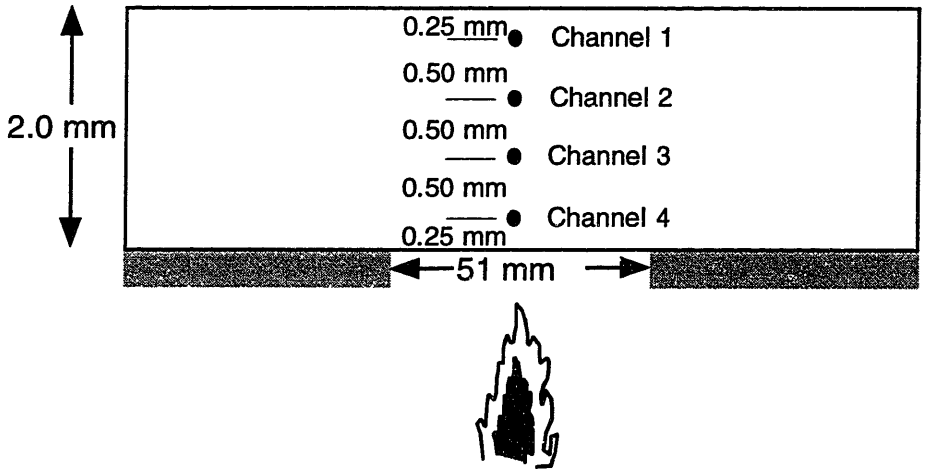

Figure 7.8 Placement of thermocouples inside a $[\pm 45]_{4s}$ laminate heated on the lower surface by a diffused propane flame in tests by [42].

effective flame temperature of 550°C and a heat transfer coefficient of 125 W/m^2·K. These boundary conditions were selected because they provided a good match with experimental data. The low effective flame temperature is reasonable due to the stagnation of the air next to the laminate. The match between predictions and thermocouple data is shown in Figure 7.9. The predictions capture the gradient in temperature from Channel 4, close to the flame, to Channel 1, near the back of the coupon. The predictions also show the steep initial increase in temperature, followed by a gradual asymptote to the effective flame temperature.

Since the laminate being modeled is heated over only a portion of the lower surface, it is important to verify that the CHARplus one-dimensional thermal model is appropriate. Given the geometry, a heat transfer coefficient of 125 W/m^{2}K, and thermal conductivities (from the file MAT.AS435016) of k_z equal to 0.7 W/m·K and k_x equal to 6.8 W/m·K, the geometry-orthotropy parameter and Biot number are calculated to be 16.6 and 0.36, respectively. From the contour plot in Figure 6.7, the maximum back face temperature that can be modeled with a one-dimensional model with less than 5% error is approximately a value of Θ of 0.3. For an initial temperature of 25°C and a flame temperature of 550°C, this non-dimensional temperature is equivalent to 390°C. As seen from the temperatures in Figure 7.9, the CHARplus model is sufficiently accurate for modeling exposures up to approximately 60 seconds. However, longer simulations will have error greater than 5%.

The same convection boundary conditions used to calculate the temperature distribution were used to simulate the exposure of coupons for 15, 30, and 45 seconds. At the beginning of each simulation, the boundary conditions were specified as values of

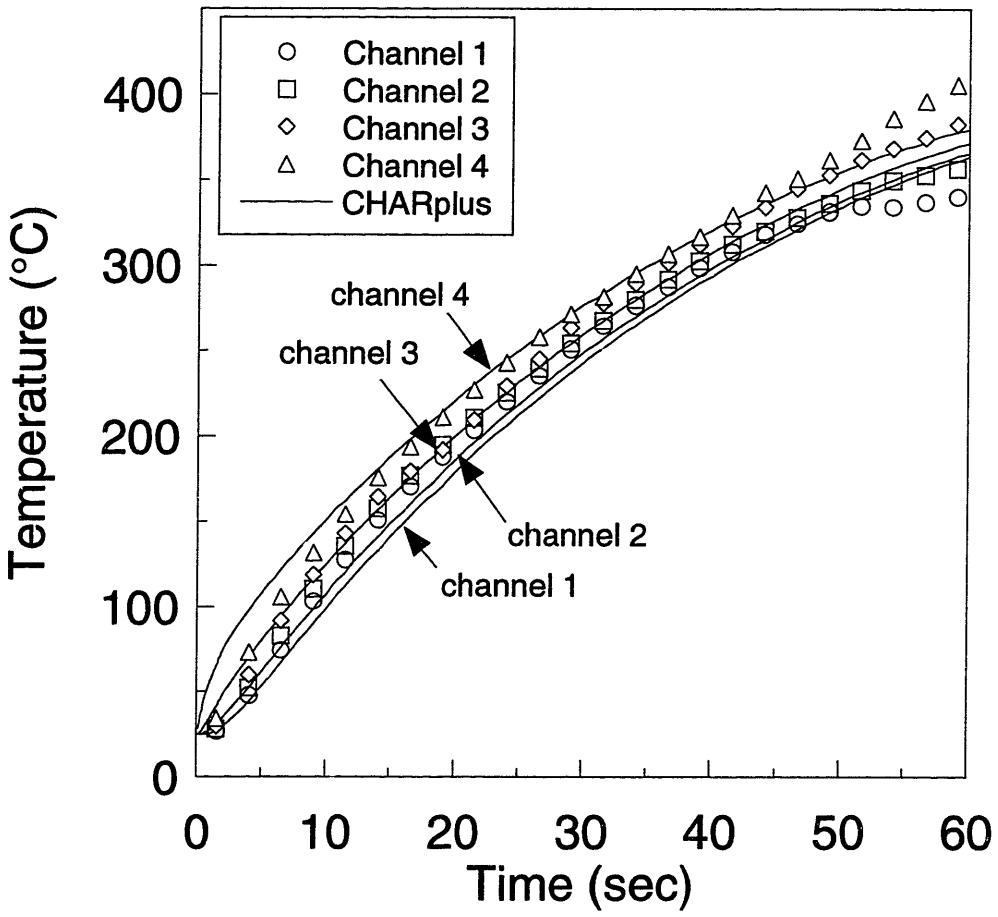

Figure 7.9 CHARplus temperature predictions compared with data from [42] for a $[\pm 45]_{4s}$ laminate heated on the lower surface by a diffused propane flame.

h_c of 125 W/m^2·K and T_∞ of 550°C. When the flame was removed at times of 15, 30, or 45 seconds, the boundary conditions were changed to values of h_c of 25 W/m^{2}K and T_∞ of 25°C. The coupons were held at this condition for five minutes, simulating a gradual cooldown to room temperature inside a fume hood with mildly agitated air. These are the approximate experimental conditions seen by the laminates being modeled. At the end of the cooldown, the code generated an output file, including the ply shear strength as a function of location through the thickness of the laminate. Ply shear strength is plotted in Figure 7.10a as a function of location. The front of the laminate (at *depth* = 0) experienced higher temperatures and more degradation, hence the loss in ply shear strength was greater at the front.

As shown in Figure 7.10a, the brief 15-second exposure caused a shear strength loss of only 4%. Therefore, using the same reasoning that was applied before, the tensile strength of the $[\pm 45]_{4s}$ coupon exposed for 15 seconds was estimated to be reduced by 4%. The 45-second exposure caused shear strength losses ranging from 40% for the material at the back of the coupon to 45% for the material exposed directly to the flame. The tensile strength of the $[\pm 45]_{4s}$ coupon exposed for 45 seconds was therefore estimated to be reduced by the same amount: 40 to 45%. These estimates of strength reduction as a function of exposure time are plotted along with actual tensile strength reduction data in Figure 7.10b. In the cases where the shear strength loss varied through the thickness, the range of strength loss is shown on the plot with bars around the average of the range.

The match between tensile strength data and CHARplus estimates is within 30%. The model is conservative, as it tends to overestimate the loss in strength caused by

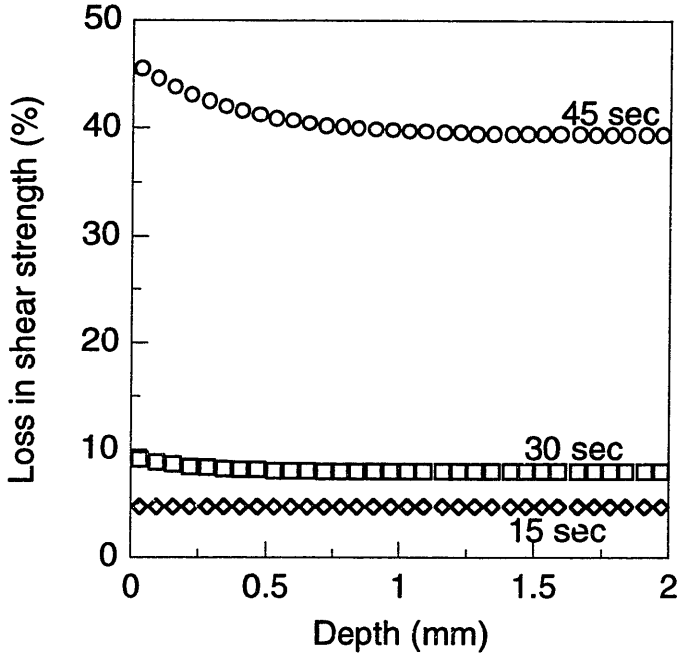

Figure 7.10a Predicted reduction in ply shear strength from a laminate exposed on a portion of one surface to a diffused propane flame.

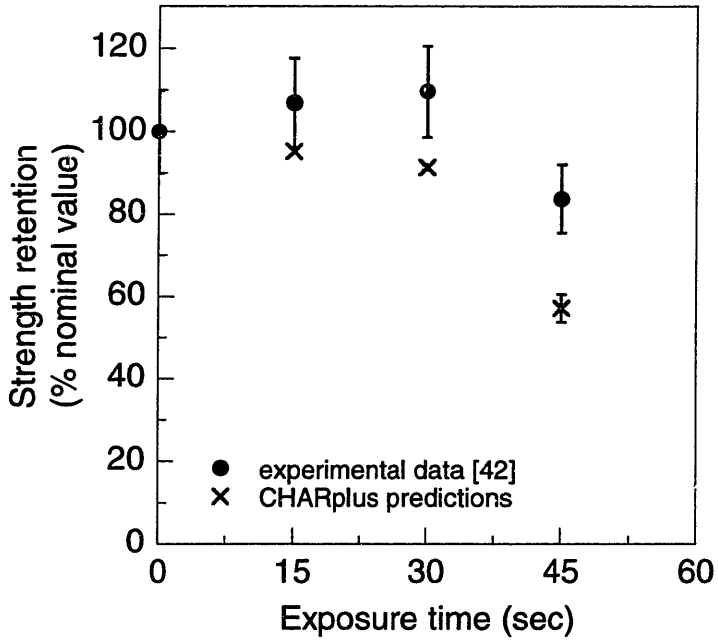

Figure 7.10b Tensile strength retention of $[\pm 45]_{4s}$ laminates exposed to a flame and cooled before loading compared with CHARplus predictions of shear strength retention of individual plies within laminates in the same environment.

longer exposures. There may be multiple reasons for the discrepancy between the CHARplus predictions and the experimental data. For one, the experimental data shows an initial increase in strength with exposure time. This is either indicative of experimental scatter in the data or a strength-increasing phenomenon that was not modeled. Furthermore, uncertainty in the temperature calculation, shear strength modeling, and estimation of $[\pm 45]_{4s}$ laminate tensile strength on the basis of ply shear strength compound to reduce the level of confidence in the CHARplus predictions. Nonetheless, the comparison between experimental data and model predictions demonstrates that the modeling approach is appropriate.

7.5 ILLUSTRATIVE EXAMPLE

In this final section, the capabilities of a code such as CHARplus are illustrated through an example. A case involving a laminate with plies of various orientation subjected to an environment that will produce gradients in temperature and degradation is selected because it involves multiple complicating factors that will highlight the extent of the predictive capability of such a code. The laminate selected is an AS4/3501-6 laminated graphite/epoxy plate with a layup of $[0_4/\pm 45_4/90_4]_s$, loaded mechanically with an axial load, N_x, of 500,000 N/m. Each of the plies is 0.125 mm thick, hence the laminate is 4 mm thick. The laminate, initially at 25°C, is exposed on one surface to a mild fire. The environmental conditions do not vary across the surface. The flame temperature is 600°C and the associated heat transfer coefficient is 100 $W/m^2 \cdot K$. The back surface of the plate is insulated. The fire is extinguished after three minutes, at

which time the plate is cooled by a gentle breeze at 25°C with a heat transfer coefficient of 25 $W/m^2 \cdot K$.

The temperature and degradation state distributions in the laminate are plotted as functions of time and depth in Figures 7.11a and 7.11b. The fire induces a substantial temperature gradient through the thickness of the laminate. After only one minute of exposure, the front of the laminate, which is directly exposed to the flame, is 85°C hotter than the insulated back surface of the laminate. The temperature gradient decreases gradually as the laminate approaches the flame temperature of 600°C. When the flame is removed after three minutes of exposure, the laminate gradually cools and exhibits only a slight temperature gradient. By the time the laminate has been cooling for one hour, the internal temperature has returned to room temperature.

The gradient in temperature causes a substantial gradient in degradation state through the thickness. After three minutes of exposure to the flame, the laminate is over 75% degraded at the exposed surface, but the material furthest away from the flame is less than 25% degraded. The degradation state of the material continues to increase for several minutes after the fire is extinguished because the laminate temperature is slow to decrease. After eight minutes of the simulation, which is five minutes after the flame is removed, the degradation model predicts that there will be no noticeable increase in degradation because the temperature has dropped to approximately 150°C everywhere in the laminate, at which temperature degradation occurs very slowly. Once the laminate has reached steady state, the material at the exposed surface has a degradation state of 0.80. The material at the insulated back surface has a final degradation state of 0.26.

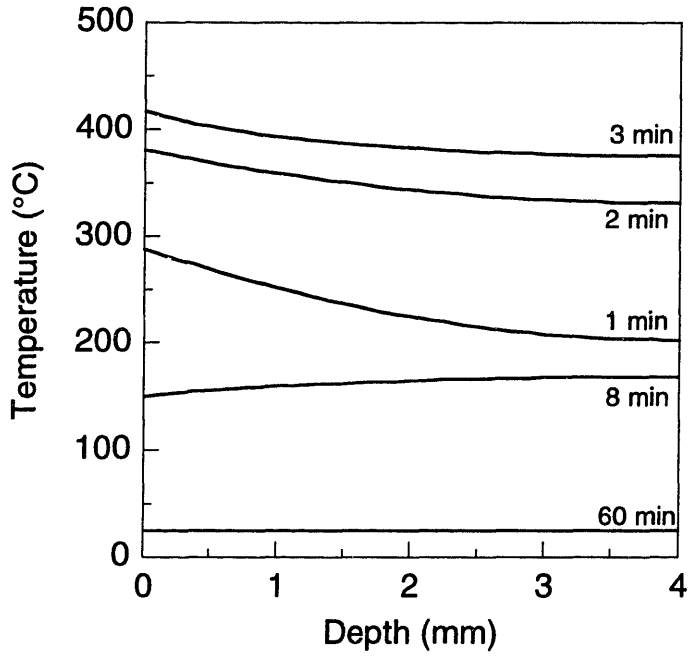

Figure 7.11a Through-thickness temperature distribution at various times in $[0_4/\pm45_4/90_4]_s$ laminate exposed for 3 minutes to 600°C flame with heat transfer coefficient of 100 W/m^2·K.

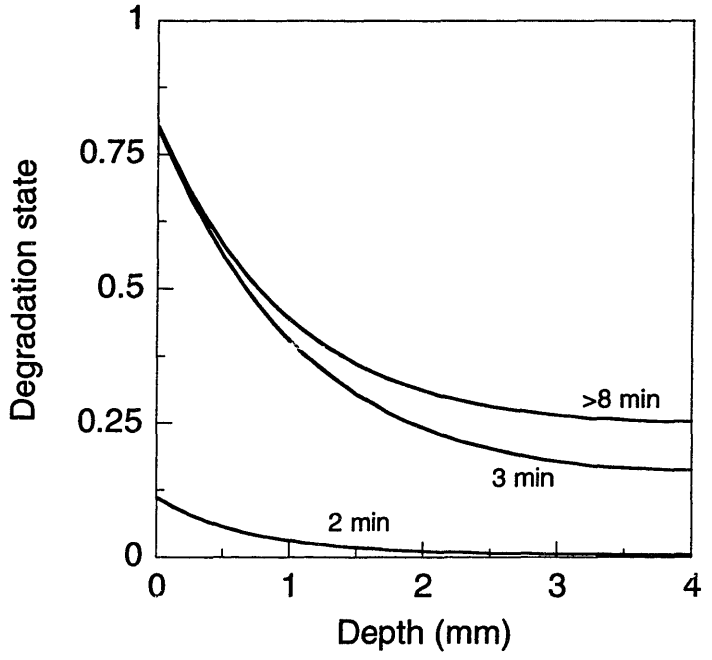

Figure 7.11b Degradation state at various times through thickness of $[0_4/\pm45_4/90_4]_s$ laminate exposed for 3 minutes to 600°C flame with heat transfer coefficient of 100 W/m^2·K.

The distribution of longitudinal stress through the thickness of the laminate is plotted as a function of time in Figures 7.12. The stress is defined in laminate coordinates and includes stresses induced by thermal effects from the cooldown of the laminate from the 180°C stress-free manufacturing temperature. The nominal stress distribution, defined as the stress distribution of a nondegraded laminate at room temperature, is shown with a thick solid line. Each group of plies with the same orientation can be considered as one 0.5 mm-thick ply. The evolution of the stress distribution during (1 min, 2 min, 3 min) and after (8 min, 60 min)the exposure to the flame is also plotted. The plot shows that as the laminate is heated, the distribution of stresses shifts. The changing distribution of thermally-induced stresses and loss of modulus in some of the plies causes the stress in the 0° and ±45° plies to increase while the stress in the 90° plies approaches zero. The slope in some of the stress curves shows the effect of the thermal and degradation gradients within the laminate. When the laminate cools down after the flame is removed, the stresses shift back toward their nominal levels. However, there is a permanent change in stress distribution. Comparing the distribution after 60 min, when the laminate has fully cooled to room temperature, to the nominal stress distribution, the stress in the 0° plies is slightly higher, and the stress in all of the other plies is slightly lower. This reflects the permanent change in the moduli of the different plies caused by matrix degradation.

The transverse stress in the laminate, expressed in laminate coordinates, is plotted in Figure 7.13. The nominal stresses in the 90° plies in the center of the laminate are large and compressive, due to the combined effects of Poisson contraction and thermally-induced stresses. The compressive stresses change slightly as the laminate heats up and

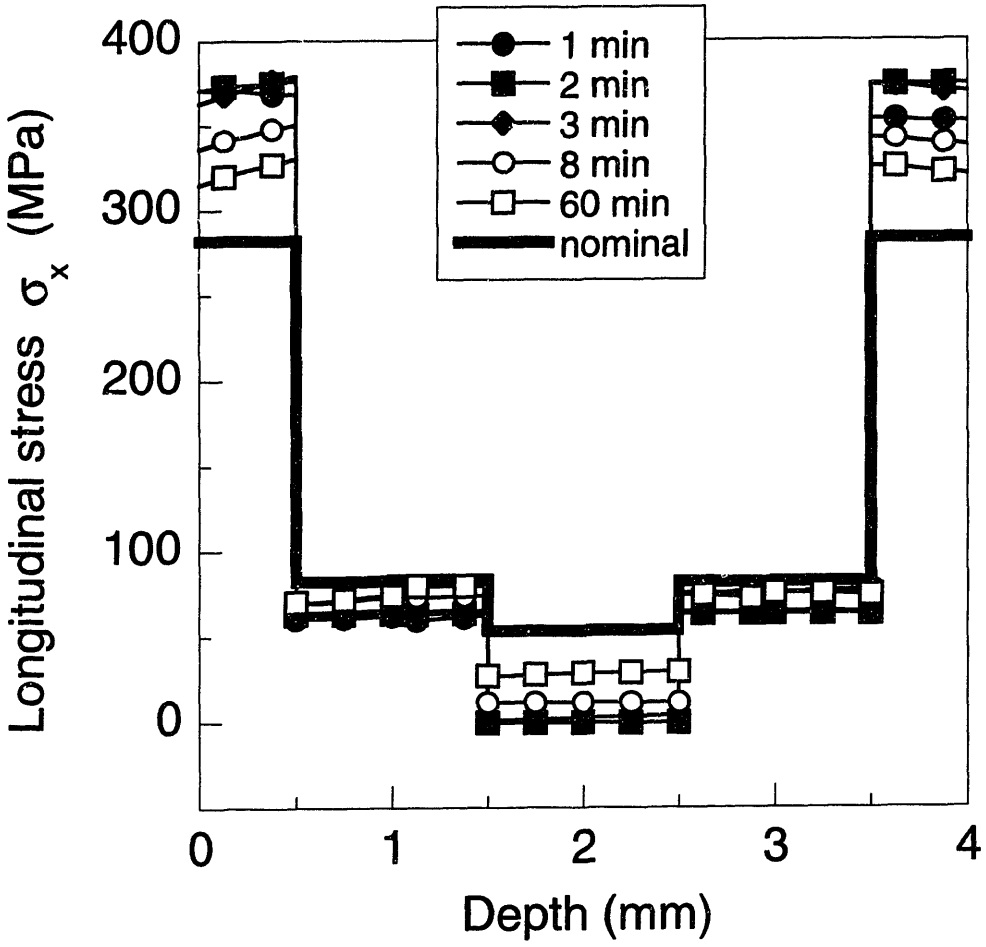

Figure 7.12 Longitudinal stress distribution at various times in $[0_4/\pm45_4/90_4]_s$ laminate exposed for 3 minutes to 600°C flame with heat transfer coefficient of 100 $W/m^2 \cdot K$ (in laminate coordinates).

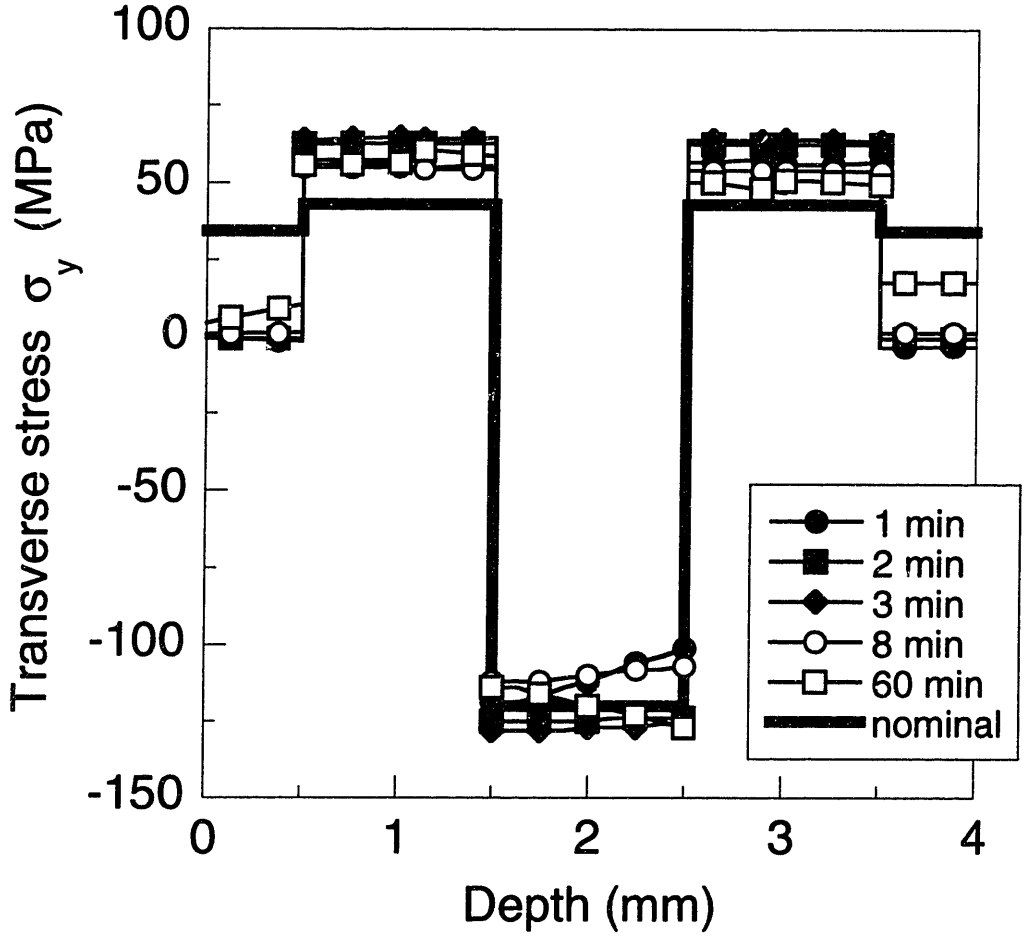

Figure 7.13 Transverse stress distribution at various times in $[0_4/\pm45_4/90_4]_s$ laminate exposed for 3 minutes to 600°C flame with heat transfer coefficient of 100 $W/m^2 \cdot K$ (in laminate coordinates).

then cools. The final post-cooldown stress distribution shows a permanent decrease in the transverse stress carried in the 0° plies and a permanent increase in the transverse stress carried in the ±45° plies. This is again due to the permanent changes in material properties induced by degradation.

Shear stress expressed in laminate coordinates is plotted in Figure 7.14. At no point do the 0° or 90° plies have any shear stresses. Such stresses occur only in the ±45° plies due to the orientation of the plies and the orthotropy of the material. The magnitude of the stress in the ±45° plies increases as the laminate heats up and shows a permanent increase once the laminate has cooled.

Although failure is not predicted by CHARplus, the first step towards that goal is taken by the calculation of the ratio between the stress and strength, defined in Appendix E as the strength fraction. The strength fraction provides a perspective on the severity of the stresses in the plies. A strength fraction greater than one indicates that the material strength of the ply has been exceeded, suggesting that the ply may fail. In order to calculate strength fractions, the stresses in each ply must be rotated from laminate coordinates into ply coordinates. The stresses expressed in ply coordinates are then compared to the ply strengths.

In Figure 7.15a, the longitudinal ply stresses in each ply, in ply coordinates, are plotted. These numbers are compared to strengths and plotted as longitudinal strength ratios in Figure 7.15b. Even though the tensile stresses in the 0° plies and 45° plies are quite large, the strength fractions in these plies are low because the plies retain substantial longitudinal tensile strength. The 90° plies are in longitudinal compression, however, and longitudinal compressive strength, as modeled in Appendix G, is very sensitive to

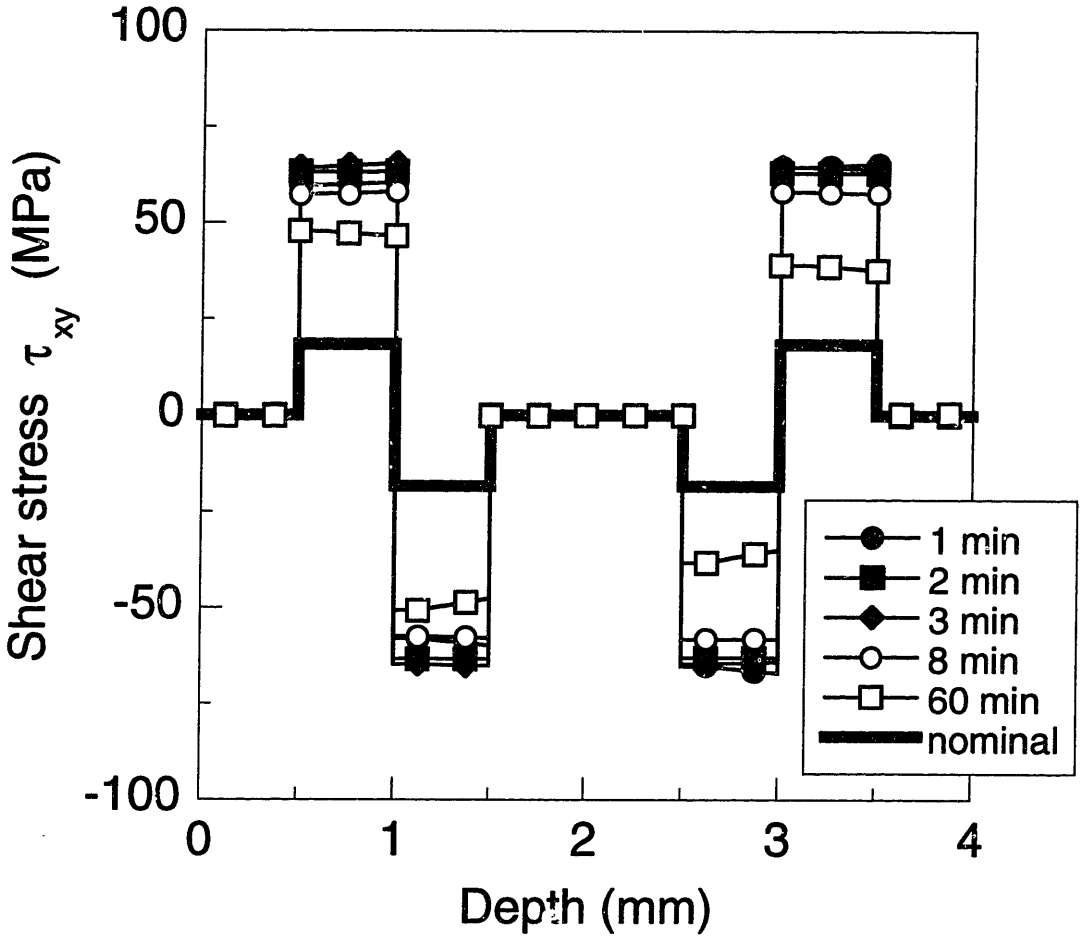

Figure 7.14 Shear stress distribution at various times in $[0_4/\pm45_4/90_4]_s$ laminate exposed for 3 minutes to 600°C flame with heat transfer coefficient of 100 W/m^2·K (in laminate coordinates).

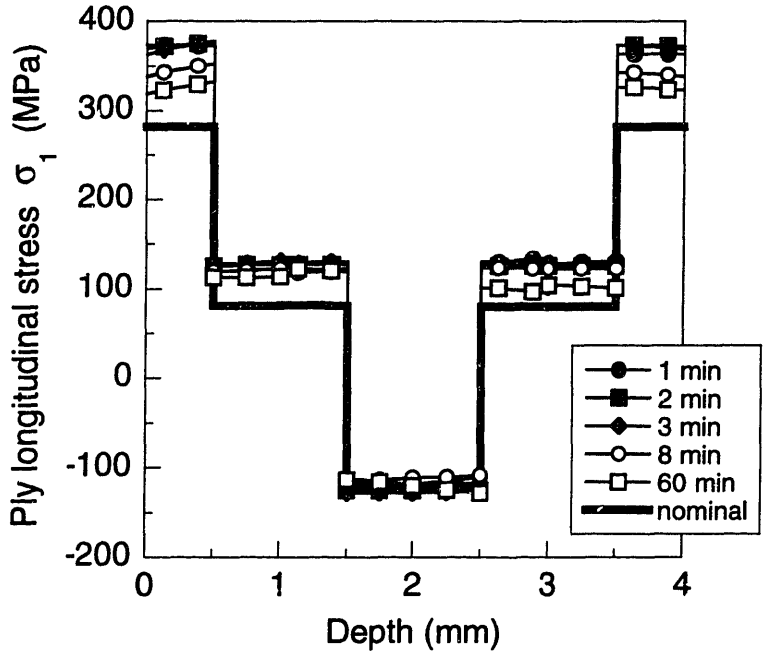

Figure 7.15a Longitudinal stress distribution at various times in $[0_4/\pm45_4/90_4]_s$ laminate exposed for 3 minutes to 600°C flame with heat transfer coefficient of 100 $W/m^2 \cdot K$ (in ply coordinates).

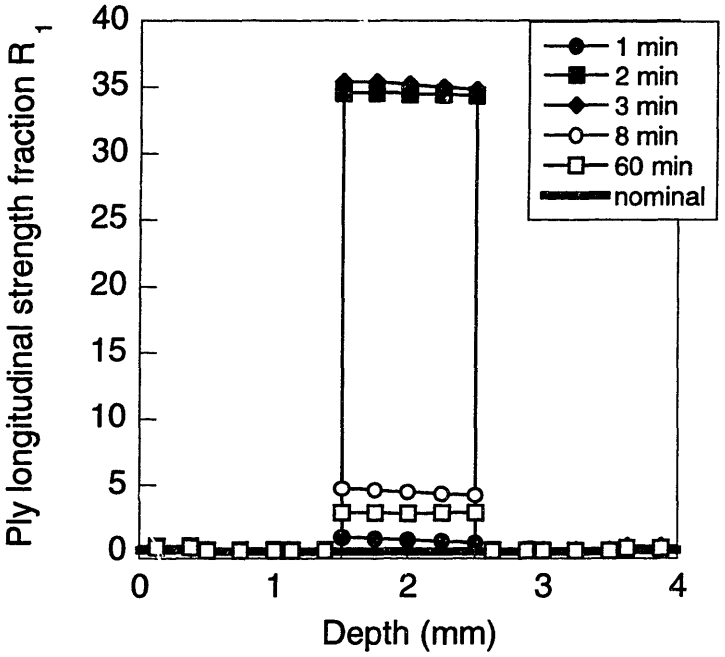

Figure 7.15b Longitudinal strength ratio distribution at various times in $[0_4/\pm45_4/90_4]_s$ laminate exposed for 3 minutes to 600°C flame with heat transfer coefficient of 100 $W/m^2 \cdot K$.

temperature and matrix degradation. The severe degradation of these plies causes severe strength loss, therefore the compressive stresses in the ply exceed the strength by a factor of nearly 35 at the height of the fire. As the laminate cools down, the thermally-induced stresses are reduced and compressive strength rebounds, hence the strength ratio decreases. This decrease in strength ratio may not benefit the laminate, however, because the plies may already be mechanically damaged at this point.

Transverse ply stresses, in ply coordinates, are plotted in Figure 7.16a. The strength fractions calculated from these stresses are plotted in Figure 7.16b. The plot in Figure 7.16b shows that the transverse strength of the plies throughout the laminate is exceeded by a wide margin. The situation actually becomes worse as the laminate cools down because stresses induced by thermal expansion become larger. At the steady state, after one hour, the transverse ply stresses in all of the plies exceed the transverse ply strength by a factor of more than 10.

Shear ply stresses, in ply coordinates, are plotted in Figure 7.17a. The 0° and 90° plies do not have such shear stresses. The magnitude of the shear stress in the ±45° plies decreases as the laminate is heated, and increases again as it cools. The permanent strength loss causes the strength fraction to grow as the laminate cools. The highest strength fraction, which indicates the situation most likely to cause failure, occurs slightly after the flame is removed, when the thermally-induced stresses are increasing, but before the ply has fully cooled and regained strength. This example and the transverse strength example raise the possibility that a structure may survive the conditions of a fire event, only to fail during cooldown after the event.

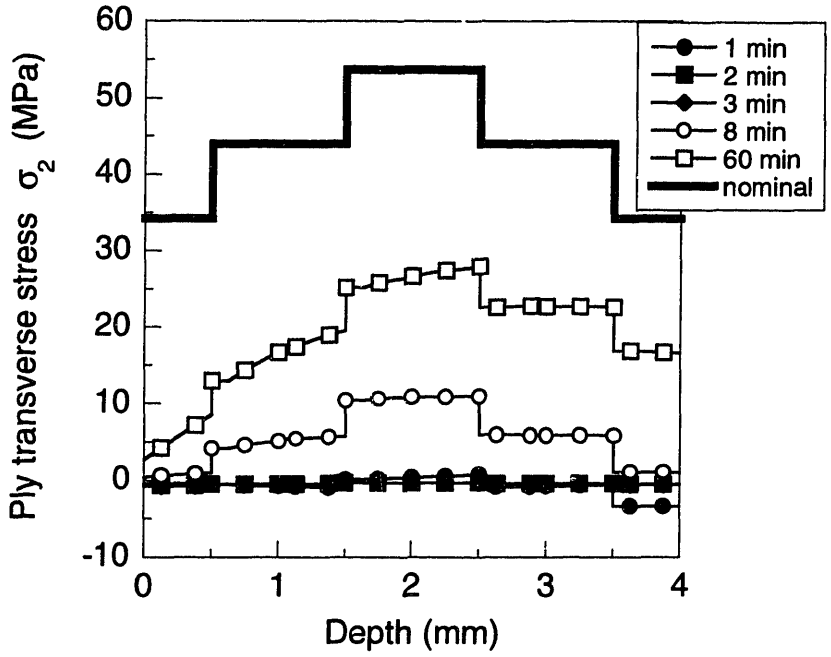

Figure 7.16a Transverse stress distribution at various times in $[0_4/\pm45_4/90_4]s$ exposed for 3 minutes to 600°C flame with heat transfer coefficient of 100 $W/m^2 \cdot K$ (in ply coordinates).

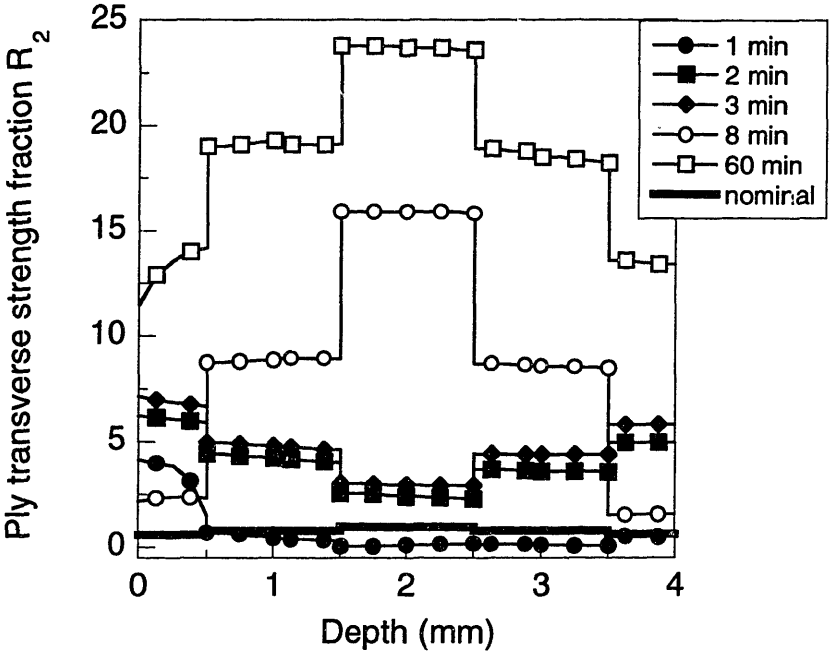

Figure 7.16b Transverse strength fraction distribution at various times in $[0_4/\pm45_4/90_4]s$ laminate exposed to 600°C flame with heat transfer coefficient of 100 $W/m^2 \cdot K$.

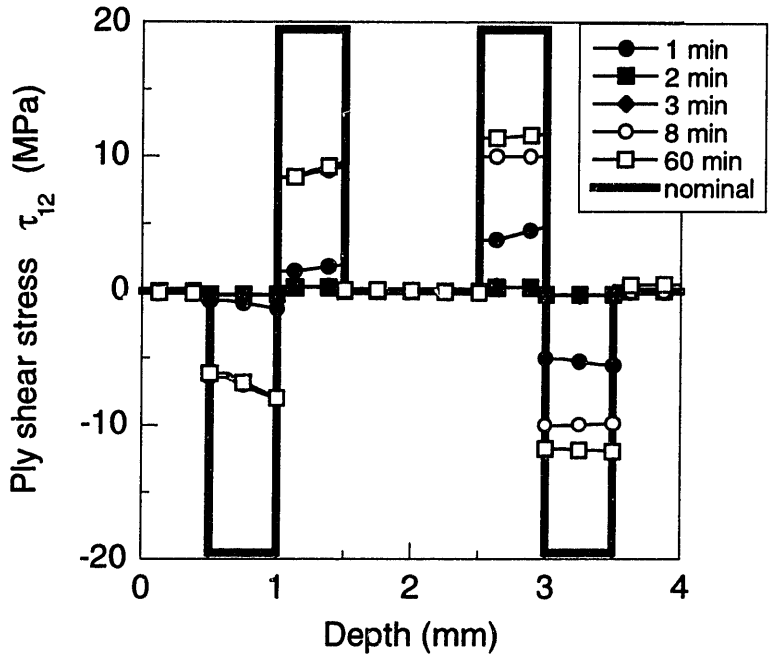

Figure 7.17a Shear stress distribution at various times in $[0_4/\pm45_4/90_4]s$ laminate exposed for 3 minutes to 600°C flame with heat transfer coefficient of 100 $W/m^2 \cdot K$ (in ply coordinates).

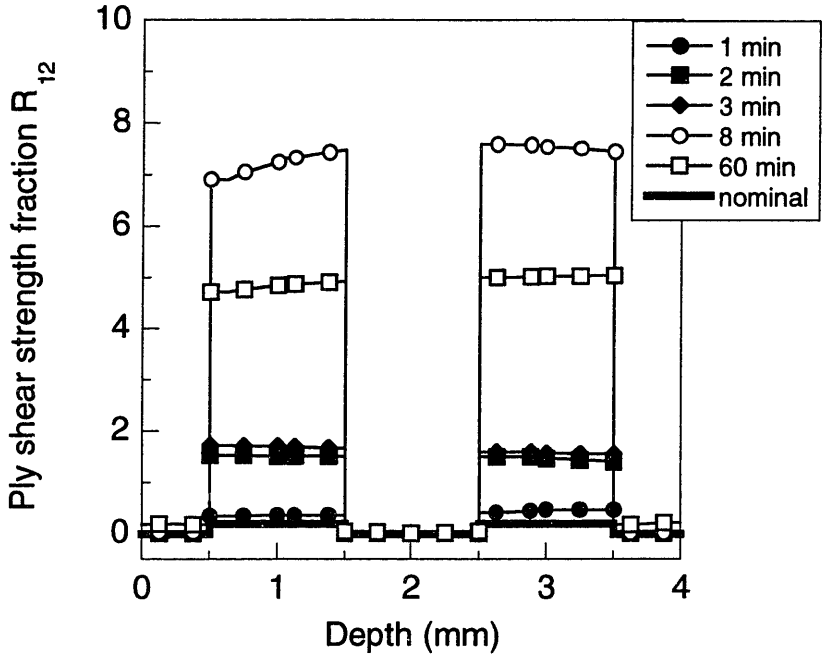

Figure 7.17b Shear strength fraction distribution at various times in $[0_4/\pm45_4/90_4]s$ laminate exposed for 3 minutes to 600°C flame with heat transfer coefficient of 100 $W/m^2 \cdot K$.

The temporary and permanent changes in material properties that are caused, respectively, by temperature changes and degradation can be nicely illustrated in a plot of the laminate modulus as a function of time. Laminate modulus is defined as the ratio of the axial strain of a laminate, loaded in axial tension only, to the axial stress applied. The plot in Figure 7.18 shows how the laminate modulus changes as the laminate is heated and then cools to room temperature. In the first minute of exposure, the laminate modulus drops about 15%. The temperature distribution plot in Figure 7.11a shows that after one minute of exposure, the temperature throughout the laminate is greater than the glass transition temperature of 200°C for the 3501-6 epoxy. The change in laminate modulus in the first minute of exposure is thus caused by the increased compliance of the matrix as the laminate approaches the glass transition temperature. After one minute, the laminate modulus briefly levels off because the modulus loss due to temperature effects has been fully realized. However, the epoxy matrix degrades quickly at these temperatures, and the laminate modulus drops further as the degradation progresses. When the flame is removed and the laminate gradually returns to room temperature, the laminate modulus increases slightly, demonstrating the reversible nature of effects due to temperature. There is a permanent laminate modulus decrease of approximately 15% once the laminate has cooled to room temperature, demonstrating the permanent effects of matrix degradation.

This example shows some of the ways in which an integrated model may be used. In addition to calculating the values of the temperature, degradation state, and stresses, the code offers insight into the behavior of the laminate, and can qualitatively determine how the laminate will respond to simultaneous heating and mechanical loading.

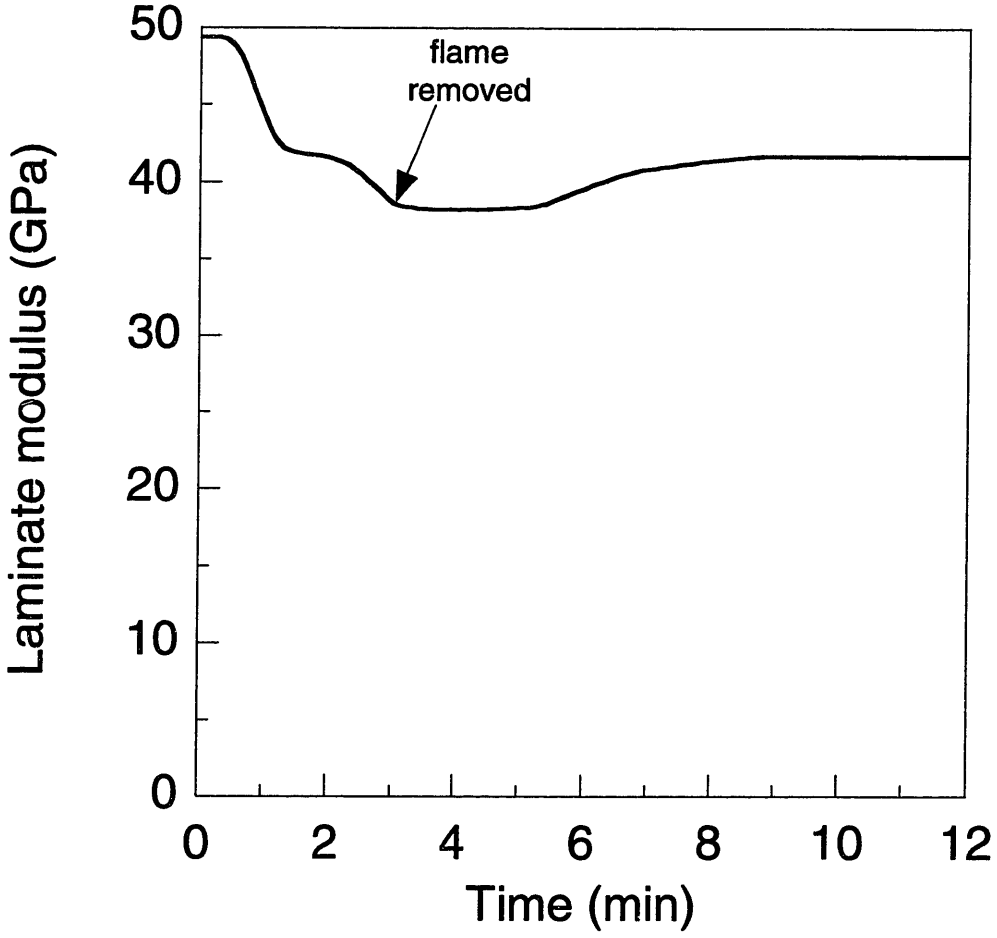

Figure 7.18 Laminate modulus versus time for $[0_4/\pm45_4/90_4]_s$ laminate exposed for 3 minutes to 600°C flame with heat transfer coefficient of 100 $W/m^2 \cdot K$.

CHAPTER 8

DISCUSSION

The experimental and analytical results and their significance are discussed in this chapter. In the first five sections, major findings are reviewed and applications of the knowledge are discussed. Caveats and limitations of the current work are discussed, followed by suggestions for how the limitations may be addressed. In the final section, an approach for applying the methodology developed here to other problems or materials is summarized.

8.1 THERMAL RESPONSE

Parametric studies of the thermal response of a plate heated on one side via convection demonstrated that the temperature distribution (e.g. the nondimensional temperature) inside the plate depends on several nondimensional parameters: the geometry-orthotropy parameter, the Biot number, and the Fourier number. For the case of a plate made of an orthotropic material heated by a flame on a portion of one surface, it was shown that increasing the geometry-orthotropy parameter, $\mathcal{L}_{xz}$, while holding other parameters constant makes the temperature distribution in the center of the plate more one-dimensional, meaning that heat flows mainly through the thickness of the plate and is not diverted into lateral heat flow. Reducing the Biot number, Bi_z, has no effect on the shape of the isotherms in the temperature distribution, but it does reduce the magnitude of

the temperatures. If two cases with equivalent temperatures are compared, then the case with the higher Biot number will have less lateral heat flow, and hence a more one-dimensional temperature distribution.

One of the objectives of the studies was to quantify, in terms of the nondimensional parameters, the accuracy of a one-dimensional approximation of the through-thickness temperature distribution in the center of the heated section of the plate. The metric selected to quantify accuracy was based on the time required for a specific point in the plate to reach a particular temperature. The approximation error was calculated by comparing the time required to reach the specified temperature using a one-dimensional model versus a two-dimensional model. The contour plot in Figure 6.7 describes, in terms of the geometry-orthotropy parameter, the Biot number, and nondimensional temperature, the conditions under which the approximation error is less than five percent.

The contour plot in Figure 6.7 describes the conditions under which a temperature field that varies in the x- and z-directions can be accurately approximated as varying in the z-direction only. The conditions under which this is possible also apply for approximating a field that varies in the y- and z-directions. The geometry-orthotropy parameter $\mathcal{L}_{xy}$ relates the geometry and material properties in the x- and y-directions. The same criteria that determine whether the parameter $\mathcal{L}_{xz}$ is sufficiently large to allow a one-dimensional approximation apply to $\mathcal{L}_{xy}$. If both geometry-orthotropy parameters are sufficiently large, then the through-thickness temperature distribution in the center of a three-dimensional structure, with a three-dimensional temperature field that varies in the

x-, y-, and z-directions, can be approximated using a one-dimensional model in which temperature varies only in the z-direction.

For an example of the use of the nondimensional parameters, consider the case of a composite aircraft wing skin exposed to a hot air plume off of a small fire, as might occur on the deck of an aircraft carrier. It is necessary to determine when a one-dimensional modeling approximation is appropriate. The wing skin is 7 mm thick and has material properties typical of graphite/epoxy (i.e. a through-thickness thermal conductivity of 0.7 W/m·K and a lateral thermal conductivity of 7 W/m·K.) The convection heat transfer coefficient is relatively mild, 50 $W/m^2 \cdot K$. The Biot number for this case is thus 0.5. The temperature response is to be modeled to calculate how much time can elapse before the temperature inside the wing reaches a critical temperature that might damage the interior structure. This critical temperature is one-half the plume temperature, giving a nondimensional temperature, Θ, of 0.5.

From Figure 6.7 it can be determined that the minimum geometry-orthotropy parameter for which a one-dimensional model could be used to calculate the time required for the structure to reach the critical temperature within 5% is 7.5. This applies to both $\mathcal{L}_{xz}$ and $\mathcal{L}_{yz}$. These geometry-orthotropy parameters are achieved if the heated area of the structure measures at least 1.2 cm by 1.2 cm. The 5% approximation error from eliminating x-direction heat flow and the 5% approximation error from eliminating y-direction heat flow are compounded. The required minimum dimensions are very small compared to the scale of the wing structure, and point out the importance of scale in modeling. Laminates with small geometry-orthotropy parameters, and the associated one-dimensional modeling inaccuracies, are typical in the small-scale coupons used in

laboratory studies but are rare in real cases. One-dimensional modeling of the thermal response would thus be appropriate in the heated wing example considered and in a wide variety of other real-world cases.

Even if the geometry, material properties, boundary conditions, or critical temperature are not known exactly, the contour plot in Figure 6.7 is useful for making estimates and performing sensitivity studies. It could be easily determined, for example, what effect increasing the thickness of the plate or widening the heat-exposed area would have on the modeling approach needed.

These findings regarding the nondimensional parameters controlling heat transfer arise directly from the fundamental equations of heat transfer. Material properties were assumed to be constant in the series of parametric studies. If the material properties were variable, the nondimensional parameters of the plate would not necessarily be single-valued, hence they could not be used to determine the temperature distribution. It would be necessary in such a case to calculate the internal temperature distribution using, for example, a finite difference code incorporating variable material properties. The decision as to whether or not a one-dimensional model is appropriate would have to be made on a case-by-case basis.

To improve the modeling of the thermal response of graphite/epoxy laminates, whether one-dimensional or multi-dimensional, thermal properties of the material must be better quantified. Techniques by which these properties can be measured are well established [17,20]. However, as noted in Chapter 2, many of the thermal material properties, such as thermal conductivity and specific heat, are not currently agreed upon. A series of tests focused on quantifying the thermal properties of graphite/epoxy,

particularly of AS4/3501-6, is needed. In particular, the variation of these properties with temperature and degradation needs to be quantified.

8.2 DEGRADATION CHEMISTRY

The degradation behavior of graphite/epoxy was studied by examining the chemistry of the epoxy matrix in isolation. This decoupling was possible because of the heat-resistance of graphite fibers [29], which are unaffected by exposure in the temperature range considered. In the case of graphite/epoxy in the environment considered, thermal degradation of the composite is assumed to be equivalent to thermal degradation of the matrix.

Thermogravimetric analysis (TGA) tests conducted at different heating rates provided data to determine appropriate reaction constants for a model of the thermal degradation of epoxy based on a single Arrhenius rate equation. The experimentally determined activation energy of 185 kJ/mol for the single degradation reaction modeled was within the range of other published values, 162 to 213 kJ/mol [4,25]. A second series of tests was performed to verify the predictions of the degradation model. The match between model and experimental data was good across a wide range of degradation states, as shown in Chapter 6, although the degradation rate at low levels of degradation was overestimated and the degradation rate at higher levels of degradation was underestimated. The single Arrhenius reaction model masks a multitude of complex degradation reactions.

The primary limitation of the degradation model is the cases to which it can be applied. It was designed to model relatively severe environments. Exposure environments of 300°C and above, in which complete degradation occurs within hours or minutes, are better modeled than environments in which degradation accumulates slowly. For example, the model predicts that an epoxy sample held at 200°C would take more than ten years to fully degrade. Given the inaccuracies of the model at low degradation states, estimates of the degradation state progression of the sample at 200°C could be off by several orders of magnitude. In contrast, the model predicts that a sample at 300°C would fully degrade in one day. Because this environment is more severe, predictions from the degradation model would be more accurate.

Furthermore, oxidative degradation was not considered in these studies. This was reasonable because in the high temperature environments considered, degradation occurred much faster than oxygen could diffuse into the laminate, meaning that oxidative degradation would only be a factor at the very surface of the laminate. For long-term degradation studies (on the order of days or months) or for cases involving extreme temperatures (above 450°C) in which oxygen concentration is sufficient to make the degradation of the graphite fibers an issue, oxidation must be included in the degradation model.

The accuracy of the degradation model in predicting response to these other environments can be improved through further thermogravimetric testing. Extended isothermal exposures of 3501-6 epoxy resin at low temperatures, for example exposures on the order of weeks at temperatures of 200°C or below, would provide mass loss data that could be used to improve the model for long-term degradation prediction. Additional

Arrhenius rate equations could be superimposed on the current degradation model, or another type of degradation model could be used. Work by Patekar [57] on the modeling of the long-term degradation of PMR-15 resin may serve as a useful reference.

The effects of oxygen concentration on oxidative degradation of 3501-6 epoxy resin can be determined through thermogravimetric testing in air and pure oxygen. From the TGA data, a model of oxidative degradation can be developed and superimposed on the existing model of thermal degradation, to characterize how the material degrades in an environment in which both thermal and oxidative degradation occur [30].

Furthermore, the possible degradation of the material used to coat the graphite fibers can be explored, also through thermogravimetric testing. While the fibers themselves are insensitive to temperature, the coating, or "sizing," on the fiber may thermally or oxidatively degrade. This mechanism was not considered in this work.

In its current state, the degradation model for 3501-6 epoxy is useful in a number of regimes such as the harsh high-temperature environments considered herein. Furthermore, it is particularly useful in parametric studies of the effects of temperature and exposure time on degradation. This capability is useful in the design of test matrices to evaluate the effects of degradation on, for example, material properties.

8.3 CHANGES IN MATERIAL PROPERTIES

A database of the tensile stiffnesses and strengths of the graphite/epoxy ply as functions of temperature and degradation state was developed experimentally. A number of previous investigators had studied the effects of temperature on these properties, but

properties were always measured at the exposure temperature. The current investigation provided, for the first time, a direct comparison between at-temperature and residual ply properties. That is, the response of the laminate while it is exposed to the environment can be compared to its response after it has been removed from the environment.

The observed trends in at-temperature stiffness and strength agreed with previous studies. The at-temperature transverse ply properties are very sensitive to temperatures exceeding the glass transition of epoxy. Transverse stiffness and strength remain fairly constant up until 200°C, at which temperature they rapidly approach zero. This temperature has been cited as the glass transition temperature of 3501-6 epoxy [24].

A significant difference was noted between the at-temperature and residual transverse properties. For example, the at-temperature transverse modulus at 250°C was less than 10% of the room-temperature value. However, when coupons exposed to 250°C were allowed to cool back to room temperature, the residual modulus increased to over 95% of the nominal value. The comparable values for exposures to 300°C are 5% and 70%, respectively. Residual strengths were also found to be higher than at-temperature strengths.

The substantial difference in at-temperature and residual transverse properties indicates that the transition from glassy to rubbery behavior and back is largely reversible. When laminates exceed the glass transition temperature, their transverse properties change significantly. However, exposures of only ten minutes at 200 to 250°C cause minimal irreversible thermal degradation, hence the properties rebound when the laminate cools. This has positive implications for composites used in applications where they may be exposed to fires, for it indicates that structural performance will not

necessarily be degraded if the fire is extinguished quickly. The degradation rate increases exponentially, however, and transverse properties are very sensitive to degradation states of less than 0.03. Therefore, it is unlikely that there will be a significant rebound in properties for laminates exposed to severe temperatures. The importance of both time and temperature of exposure in determining degradation state also implies that it is important to control the time of exposure when measuring at-temperature material properties. Prolonged exposures, even at temperatures of 200°C to 250°C, can cause degradation, thereby confounding the temperature-induced effects on material properties with degradation-induced effects. If the time of exposure is inconsistent from one test to the next, there could be high scatter in the data.

Longitudinal properties are much more stable than transverse properties at elevated temperatures. Both at-temperature and residual longitudinal stiffness are nearly constant through 300°C and strength decreases slowly between 200°C and 400°C. After exposures at 400°C severe enough to completely degrade the epoxy matrix, the coupons retained over 40% of their nominal strength. This illustrates clearly the importance of the heat-resistant graphite fibers in determining longitudinal properties.

Correlations between mechanical properties and degradation state indicate that degradation state may be an effective metric by which mechanical properties can be quantified. Transverse coupons subjected to different types of high temperature environments that produced equivalent levels of degradation all yielded similar modulus and strength data, albeit within a large scatter band. The results are not conclusive, however, and the relationships between degradation state and property loss can only be estimated.

The current best-effort correlations between temperature, degradation state, and transverse and longitudinal tensile ply properties are summarized in the material property models plotted in Figures 6.35 through 6.38. These models are based on the data collected and observed trends. Using these models, it is possible to estimate the ply properties of AS4/3501-6 graphite/epoxy for different environmental exposures with temperatures between 25°C and 400°C and degradation states between 0 and 1. However, it is important to note that the measured ply property data did not cover the entire range of temperatures and degradation states included in the property models. Thus, a great deal of estimation was needed to develop complete property models. The fidelity of the models is therefore limited. The most reliable model predictions are those based directly on data.

There are several areas in which the understanding of the changes in material properties can be improved. The relationship between degradation state and property loss should be explored further through a carefully designed series of experiments. Tests similar to the $[90]_{12}$ coupon tests involving different types of exposures that produce equivalent degradation states should be expanded to verify or disprove the hypothesis that properties depend on degradation state but are independent of the type of environment that causes the degradation. Since achieving a particular degradation state was difficult in the current work due to the variability of the test furnace, the number of coupons per testing condition should be increased, or a furnace with more accurate temperature control should be used.

The fidelity of the property models will be improved through further testing. Gaps in the current property data should be filled by investigating the modulus and

strength of transverse and longitudinal coupons with degradation states between 0.005 and 0.02, and residual modulus data from coupons with degradation states above 0.04. Also, a full series of tests to quantify the shear behavior and compressive response of graphite/epoxy plies is needed. While preliminary models of these properties are developed in Appendix G, they were supported by very little data, none of which came from the current investigation. To measure these properties, a new experimental setup must be devised. Compression and shear testing were impossible with the experimental setup employed in this investigation. Other limitations of the experimental setup were the inability to evaluate the longitudinal modulus of severely degraded coupons and the inability to measure transverse strain and thereby determine Poisson's ratio. Furthermore, the high frequency of grip failures in the transverse coupons and extensive splitting in the longitudinal coupons compromised much of the strength data. Longitudinal modulus and Poisson's ratio should be measured, and better strength data should be collected. The more data that is available, the better the models of material properties as functions of temperature and degradation state will become.

A separate area of study that may contribute to the understanding of the effects of temperature and degradation on mechanical material properties is the field of micromechanics. Work by Chamis [58] may serve as a useful reference. An established body of knowledge links the properties of composite constituents and interface properties with the properties of the composite plies. This area should be explored to identify and model the mechanisms by which temperature and matrix degradation (and possibly the degradation of fiber coatings) reduce mechanical ply properties. This will help to

improve the understanding of the mechanisms behind the observed effects and may reduce the need for extensive experimental studies.

8.4 INSPECTION OF THERMALLY DEGRADED COMPOSITES

In this work, a method was developed to assess the residual degradation state of epoxy-based composites. The envisioned procedure for estimating the residual degradation state of a sample of neat epoxy resin or graphite-reinforced epoxy composite exposed to a high temperature environment, as investigated herein, is based on effective char yield. A small quantity of the material to be inspected is first removed. The mass, m_{ro}, of the sample is precisely measured and the sample is then completely thermally degraded by exposing it to high temperatures in a furnace with an inert atmosphere. The mass, m_{rf}, of the fully degraded sample is then measured. If the sample tested is made of pure epoxy, the effective char yield is calculated by taking the ratio of masses before and after the test, using Equation 4.51. If the sample is a fiber-reinforced composite, the effective char/fiber yield is calculated using Equation 4.53. The residual degradation state is calculated by comparing the effective char (or char/fiber) yield with the nominal char (or char/fiber) yield using Equation 4.52 or 4.55, respectively. The nominal char yield can be measured from virgin material if it is unknown. A thermogravimetric analyzer is useful for conducting the assessment test because it takes very precise mass measurements, uses a very small sample, and has a controlled furnace atmosphere. Other types of furnaces could be used, however.

This method has the potential to be a very simple, efficient way of evaluating the integrity of heat-exposed composites. The test is not non-destructive in nature, but the size of the sample that must be removed is limited only by the precision with which its mass can be measured.

Experiments were performed in this investigation to evaluate the usefulness of this degradation assessment technique. Analysis of the results showed that in some cases, the estimate of residual degradation state based on effective char yield was within 4%. However, other estimates were not as good, with the actual and estimated degradation states differing by as much as 28%. The success of these tests was therefore limited. However, the fact that this technique is theoretically capable of detecting low degradation levels associated with the onset of material property loss warrants further pursuit of the technique.

The analytical derivation of the equations from which residual degradation state is calculated using this method indicates that there should be a perfect match between the estimated residual degradation state and the actual residual degradation state. The results presented in Section 6.2.3 indicate, however, that there are multiple sources of error that may compromise the accuracy of the estimates. One source of error is the fact that the technique is founded upon the assumption that the nominal char yield from a particular epoxy, or from a composite with a particular fiber volume fraction, is constant. If the nominal value is, in fact, variable, then there will be error in the estimate. To evaluate whether the nominal char yield of the epoxy is constant, multiple samples of virgin epoxy should be fully degraded and their char yields measured and compared. There is also potential for experimental error. Care must be taken to carefully extract the sample to be

tested, to precisely measure its mass before and after it is fully degraded, and to avoid losing fractions of the non-reactive mass, as happened in two of the assessment tests conducted in this investigation.

Further tests are needed to determine whether the theoretical accuracy of the assessment technique can be practically achieved. To begin, thermogravimetric tests on partially degraded neat epoxy resin, such as were conducted in this work, should be continued. Identified sources of experimental error should be eliminated, and the degree to which the char yield of 3501-6 epoxy is constant should be evaluated. If carefully controlled tests such as these produce accurate estimates of degradation state, then they should be followed by similar thermogravimetric tests on samples of partially degraded graphite/epoxy composites. If the degradation state estimates from these tests prove satisfactory, then tests on composites in less carefully controlled, non-laboratory conditions can begin. If these final tests are successful, then the technique may be considered for general diagnostic use.

Should the method prove viable, this would be a valuable way of assessing the integrity of a structure with an unknown exposure history. Given reliable models of material properties as functions of temperature and degradation state, the results of the assessment could be used to evaluate residual material properties and determine whether repair is needed.

8.5 USE OF THE INTEGRATED MODEL

The models of thermal response, degradation, and material property response were unified along with classical laminated plate theory in an integrated model. The model was implemented in a one-dimensional code entitled CHARplus. The code is capable of predicting temperature, degradation state, and ply strains and stresses for a loaded plate exposed to the environment. As demonstrated in Chapter 7, the code can be used to predict response in both isothermal environments and environments involving gradients in temperature and degradation. Both at-temperature and residual behavior can be evaluated. Temperature, degradation state, material properties, and stresses can be quantified at various points through the thickness, and laminate properties, such as laminate extensional modulus, can be determined. Such a code is especially useful for qualitatively determining the severity and extent of degradation caused by different environmental exposures and the effects of the degradation on the structural performance of the laminate.

The integrated model implemented in the CHARplus code combines the limitations of each of the component models from which it is assembled. Since the thermal model is one-dimensional, the cases that may be studied using the code are subject to the limitations discussed in Section 7.1 regarding the geometry-orthotropy parameter, Biot number, and maximum back face temperature. Additionally, the accuracy of the thermal model is limited by the accuracy of material properties such as thermal conductivity and specific heat. The degradation model is limited by the accuracy of the results of the thermal model and by the limited accuracy of the simple Arrhenius

model used to simulate complex polymeric reactions. The mechanical response model is limited by the accuracy of the material property database. As discussed earlier, the transverse and longitudinal property models, while based directly on experimental data, had to be supplemented with extrapolated values. The shear property models and compressive property models were designed using the same temperature and degradation trends as the transverse property models, however they were not fully corroborated by experimental data.

Furthermore, the application of such a code will be limited to modeling environments similar to the ones from which the material property database was constructed. The limitations of the degradation model in predicting response to environments at temperatures below 200°C have already been noted. Other environments may introduce mechanisms not included in the current model. For example, rocket nozzle or laser environments involving extreme temperatures and heating rates may cause spalling and/or ablation of the material. Oxidizing environments may change the degradation behavior and material property response. Existing models must be improved and expanded if the integrated model is to be used to predict response in these regimes.

Nevertheless, the models integrated in CHARplus and the integration methodology are the foundation upon which more sophisticated models may be built, in order to fully describe all aspects of the response of composite laminates to fire and other high temperature environments. There are a number of ways in which the model can be built upon. One is to pursue improvements in the existing models. Suggestions for addressing the limitations of the thermal response model, degradation chemistry model, and material property models have already been discussed. Another is to expand the

scope of the existing model. Models of mechanical damage mechanisms and failure can be added. Established models for these mechanisms do not currently exist for nondegraded composite laminates, so developing models for degrading composites is clearly a difficult step. However, the absence of damage and failure models is currently a significant limitation of the existing model.

Finally, the integrated model should be verified through a series of experiments designed to quantify laminate response to high temperature exposure. A useful approach to such testing is to gradually add levels of complexity to the cases tested. First, tensile tests on laminates with plies of different orientation in isothermal environments should be conducted. The experimental setup used to measure properties of unidirectional coupons in the current investigation may be used for these tests. By evaluating the modulus and strength of these coupons, the usefulness of classical laminated plate theory for determining the response of laminates based on ply properties and ply orientation can be verified.

Tensile tests on unidirectional laminates with temperature gradients should also be conducted. By comparing data from thermocouples embedded in the laminates and predictions from the thermal response model, the model can be verified. Predictions of laminate modulus can be compared with experimental data. Furthermore, such coupons are useful for beginning to explore the mechanisms by which stress is transferred from degraded material to nondegraded material.

The complexity of each test can gradually be increased. Eventually the predictions of the code should be validated through comparisons with results from tests on laminates with general layups and temperature and degradation gradients, subject to

multiple forces and moments, such as the laminate shown in the problem statement illustration in Figure 3.1.

8.6 APPLICATION OF METHODOLOGY

This work has focused on evaluating the behavior of AS4/3501-6 graphite/epoxy composites exposed to high temperature environments. However, the modeling framework presented in Figure 3.2 is not specific to this material system, or even to graphite/epoxy. The framework can hence be used in the modeling of other materials, and many of the particular models used can be applied to other composite material systems. It is instructive to consider how one would go about applying the techniques developed here to other composites. As in the current work, different aspects of the problems can be studied and modeled in isolation, and then the models reassembled into a single integrated model of structural response.

The first consideration is the thermal behavior. The heat transfer theory used to model the thermal response is not material-specific, although a number of material properties must be determined. The through-thickness axial conductivity, specific heat, and density of the material must be measured as functions of temperature and degradation. If the degradation reaction is exothermic, as is the case for graphite/epoxy, the latent heat of reaction must be measured. If a one-dimensional thermal model is to be used, the geometry-orthotropy parameter and Biot number must be quantified through consideration of the geometry, material properties, and boundary conditions of the structure to determine when a one-dimensional model is appropriate.

To model the degradation chemistry, it must first be established whether or not the fibers degrade. Graphite fibers are unaffected by temperature in the regime studied, so degradation of the composite was equated with degradation of the epoxy matrix. If polymeric fibers are used, fiber degradation must also be modeled. Degradation of the fiber coating material may also be important. If the degradation of more than one constituent is to be modeled, each constituent should be tested in isolation. Thermogravimetric analysis provides insights into polymer degradation. The results of a series of TGA tests conducted at different heating rates will indicate what type of degradation model is appropriate for describing the degradation reaction. If an Arrhenius-type reaction model is suitable, the TGA test results can be used to determine an appropriate set of reaction constants. While 3501-6 epoxy could be modeled with reasonable accuracy using a single Arrhenius equation, this will not necessarily be true of other materials. Similar studies on other matrix materials used in graphite fiber composites, such as PMR-15, a high-temperature polyimide, found that multiple Arrhenius-type reactions with different reaction constants had to be superimposed in order to accurately model the degradation chemistry [30].

Once determined, the degradation model should be used to design a test matrix for evaluating mechanical properties. The test matrix should include measurements of both residual and at-temperature properties. Through comparison of the results, reversible effects due to elevated temperature and irreversible effects due to degradation can be separated. It was noted in the current investigation that transverse properties are very sensitive to small degradation states, so a test matrix design for another material should initially focus on how properties change at the onset of degradation. The test matrix

should also investigate material properties above and below the glass transition temperature of the matrix. If other variables, such as oxygen concentration, contribute to the changes in material properties, they should be included in the test matrix. Judicious selection of testing conditions can demonstrate the major features of material property behavior in a minimal number of tests. In designing and performing the tests, it should be kept in mind that the results of at-temperature tests may confound the effects of temperature and degradation, especially at temperatures at which degradation occurs quickly.

With a database of mechanical material properties, reaction constants and thermal material properties, one can assemble the models into a single integrated model. The CHARplus code is an example of such a model. From the integrated model, analyses of the structure can be performed to determine structural response, including the temperature distribution, degradation, stresses, and strains. Eventually, through the inclusion of the necessary models, the occurrence of mechanical damage and failure can also be determined.

CHAPTER 9

CONCLUSIONS AND RECOMMENDATIONS

The effects of high temperature exposure on the structural response of composite laminates were investigated. A framework for breaking this complex problem down into its basic physical mechanisms was proposed. The four primary mechanisms were identified as the thermal response, degradation chemistry, thermomechanical response, and mechanical damage. The methodology developed was applied to study the behavior of graphite/epoxy. However, this approach is also suitable for the study of other material systems.

In the investigation of the thermal response, the nondimensional parameters that govern transient heat transfer in a plate made of an orthotropic material were identified. Some of these parameters, including the Biot number and Fourier number, are well known in heat transfer literature. A new parameter, called the geometry-orthotropy parameter, which combines a ratio of the dimensions of the plate and a ratio of the lateral and through-thickness thermal conductivities of the orthotropic material, was introduced. The ratio of the dimensions is squared in the geometry-orthotropy parameter while the ratio of conductivities is not, hence geometry has a larger relative effect on the thermal response than orthotropy of material properties.

Depending on the values of the nondimensional parameters, the relative importance of lateral heat flow in the plate compared to through-thickness heat flow changes. In cases in which through-thickness heat flow is dominant, it may be possible

to approximate the through-thickness temperature distribution in the plate using a one-dimensional thermal model. The accuracy of an approximation of the through-thickness temperature distribution of a plate with a multi-dimensional temperature field using a one-dimensional analysis was quantified as a function of the identified nondimensional parameters. Parametric studies involving the nondimensional parameters indicate that the cases most appropriate for a one-dimensional modeling approximation involve structures made of material with low ratio of axial to through-thickness conductivity, heated by an intense heat source across a region that is much wider than the thickness of the structure. Furthermore, the accuracy of approximations of the temperature distribution decreases as the duration of the simulation increases and thermal equilibrium is approached.

The parametric studies focused on determining when a two-dimensional temperature field that varies in the x- and z-directions can be accurately approximated as varying in the z-direction only. The conditions under which this is possible also apply for approximating a temperature field that varies in the y- and z-directions. If both sets of conditions are met, then a three-dimensional temperature field that varies in the x-, y-, and z-directions can be accurately approximated with a one-dimensional model. However, it should be noted that the error associated with each dimensional reduction compounds.

Experimental studies of the degradation chemistry of 3501-6 epoxy demonstrated that the thermal degradation of this epoxy is dependent on both temperature and time. An Arrhenius rate equation was applied to model the degradation. Although the degradation of epoxy is a complex process, a reaction model based on a single Arrhenius rate equation was shown to describe the degradation behavior under the conditions studied.

These conditions were exposures of up at 25 minutes to temperatures as high as 375°C. A single set of Arrhenius reaction constants was determined based on experimental data. The constants are a reaction constant of 2.338×10^{14} /min, a reaction order of 1, and an activation energy of 184.9 kJ/mol. The activation energy was within the range of values found by other investigators. The model was verified through a separate series of experiments. The match between model predictions and experimental data was considered satisfactory for modeling the effects of the environments considered. However, the model is inappropriate for determining degradation in other regimes including long-term (on the order of days or months) degradation behavior of epoxy at temperatures of 200°C and below, or cases in which oxidative degradation is important. The combined dependence on temperature and time indicates that in order to determine the degradation state of a composite structure, the entire thermal history must be considered.

An adjunct area of study derived from the investigation of degradation behavior was the proposal and evaluation of a method for estimating the residual degradation state of partially degraded epoxy-based composites. The method is based on the effective char yield of a sample of material. The procedure involves removing a small sample of the material to be inspected, fully degrading the sample, calculating the char yield, and comparing it with the nominal char yield of the material to assess its residual degradation state. While the analytical derivation of the equations used in the calculations of char yield and residual degradation state indicate that the match between estimated degradation state and the actual degradation state should be exact, experiments showed estimation errors between 4% and 28%. Further tests are warranted to fully evaluate

whether the technique is practical for assessing the degradation state of composites exposed to real environments.

A series of elevated temperature tensile tests on AS4/3501-6 graphite/epoxy provided a database of longitudinal and transverse ply properties, both at-temperature and after cooldown from a high temperature exposure. Temperature and degradation state were identified as appropriate metrics for determining mechanical properties, and models of longitudinal and transverse tensile properties as functions of temperature and degradation were developed from the experimental database. Transverse properties are very sensitive to temperature. Both transverse modulus and strength drop by an order of magnitude when the material exceeds the glass transition temperature of approximately 200°C. This property loss observed in the coupons exposed at 200°C was solely due to temperature effects because the degradation state of such coupons was negligible. Property losses associated with temperature effects are largely recoverable, if the specimen is allowed to cool. Property losses due to degradation effects are not reversible. Transverse properties are very sensitive to small levels of degradation (a degradation state less than 0.03). At temperatures of 300°C and above, a degradation state of 0.03 can be reached in ten minutes or less.

Longitudinal ply properties have a much different behavior. The graphite fibers, which are relatively insensitive to temperature and degradation, dominate the property response. No longitudinal strength or modulus loss was observed in coupons exposed at temperatures below 300°C. Property loss at higher temperatures is likely dominated by degradation effects, but may be exacerbated by temperature effects. However, plies can

retain large fractions of their nominal longitudinal properties even when the epoxy matrix is completely degraded.

A methodology for integrating models of the different mechanisms was presented. The mechanisms into which the general problem of structural response were broken down were assembled into an iterative flowchart. An example of such an integrated model was developed. The models of thermal response, degradation, and material property response developed in this work were integrated with a thermomechanical response model based on classical laminated plate theory and implemented in a predictive FORTRAN code entitled CHARplus. The state of a laminate exposed to a high temperature environment while mechanically loaded can be quite complex, involving gradients and changing material properties, and such a code is a useful tool for making the calculations necessary to evaluate temperature, degradation state, ply material properties, and stresses and strains in such a laminate. The integrated model is preliminary in many respects, but comparisons of predictions with available experimental data demonstrate that the code captures experimentally observed trends, lending credence to both the modeling approach and the models themselves. Exploratory analysis using such a code can demonstrate major features of the response of laminates to high temperature environments.

As previously noted, the analysis methodology developed to break down the general problem is not specific to graphite/epoxy, but may be applied to other polymer-matrix composite material systems. The approach by which this may be done was outlined.

This work provides a foundation upon which to build a complete mechanism-based model of the high temperature structural response of composite laminates. Recommendations for further work can be divided into three categories: improvement of existing models, addition of models, and verification/application of the integrated model.

To improve the modeling of the temperature distribution and other effects that depend on it, the thermal properties of graphite/epoxy should be accurately measured. Well-established techniques for the measurement of properties such as thermal conductivity, specific heat, and density are available. However, there is currently disagreement over the values of these properties for graphite/epoxy. For the current application, the properties should be quantified as functions of temperature and degradation state.

To improve the degradation model, its limitations should be addressed so that it will be applicable to a wider range of exposure environments. Toward this end, further thermogravimetric testing is warranted. Long-term exposures (on the order of days to months) at temperatures of 200°C or below should be studied. Mass loss data from these tests can be used to develop better models of degradation. For example, additional Arrhenius rate equations providing a more accurate model of degradation at these lower temperatures could be superimposed on the current degradation model. The effects of oxidative environments on the degradation of epoxy should also be quantified through TGA experiments on neat epoxy resin conducted in air and pure oxygen, and the results used to develop a model of oxidative degradation. This oxidative degradation model can then be combined with the thermal degradation model. Additionally, although it has been established that the graphite fibers do not degrade in the regimes studied, the potential

degradation of the fiber sizing should be investigated, possibly through thermogravimetric testing of neat sizing material.

Mechanical material property tests should be expanded to address some of the gaps in the current database. The relationship between degradation state and the residual strength and modulus of AS4/3501-6 graphite/epoxy plies should be explored further through a series of experiments similar to the tests conducted on $[90]_{12}$ coupons in this work, in which the effects of different types of exposures that produce the same degradation state were quantified. Tests of this nature should be conducted on both transverse and longitudinal unidirectional coupons, for a variety of degradation states. In particular, data is needed to describe the properties of coupons with degradation states between 0.005 and 0.02, and above 0.04. In conducting these tests, a new experimental setup should be devised to overcome the limitations of the current setup. A furnace with more precise temperature control should be used and the setup should allow for measurement of shear and compressive properties. Poisson's ratio should be quantified as a function of temperature and degradation state. Better strength data from coupons free of grip failures and excessive longitudinal splitting should also be collected.

The second major area in which improvements can be made is in the addition of new models. Two particular areas should be considered. First, the established micromechanics body of knowledge that links constituent properties, interface properties, and composite properties should be explored to identify and model the mechanisms by which matrix degradation reduces composite properties. Mechanism-based models of the relationship between degradation and material property loss can help to improve the understanding of the effects of high temperature environments on structural response and

may reduce the need for extensive experimental studies. Second, mechanical damage and failure should be modeled and these models included in the integrated model. Models of these mechanisms are not well-established. However, an integrated model of structural behavior in response to high temperature environments and mechanical loading will not be complete without them.

Finally, two series of verification experiments are proposed. The first involves the verification of the proposed degradation assessment technique. Thermogravimetric tests on partially degraded neat epoxy resin, such as were conducted in this work, should be continued. Identified sources of experimental error should be eliminated, and the degree to which the char yield of 3501-6 epoxy is constant should be evaluated. If the tests indicate that the theoretical accuracy of the assessment technique can be approached through carefully controlled tests on neat epoxy, then similar thermogravimetric tests on partially degraded graphite/epoxy composites should be conducted. If these also produce accurate estimates of degradation state, then the verification tests should be expanded to include coupons degraded under non-laboratory conditions.

Another series of tests should be undertaken to verify the predictions of the integrated model. Experiments should be designed to quantify laminate response to high temperature exposure. A useful approach to this verification testing is to gradually add levels of complexity to the cases tested. Laminates with plies of different orientations in isothermal environments should be studied, followed by unidirectional laminates in environments with temperature and degradation gradients. Tests of limited complexity will allow different aspects of the integrated model to be validated separately.

Eventually, laminates with plies of various orientations in gradient environments, loaded by multiple forces and moments, should be tested.

Once verified, the integrated model can be used in structural analysis and design. Databases and models developed for other polymer-based composite materials will allow other the response of other material systems to be modeled, as well. To extend this work to the modeling of other composite material systems, the various mechanisms must be addressed one by one. To address the thermal response, the thermal material properties of the material, including thermal conductivities, specific heat, and density, should be quantified as functions of temperature and degradation state. If the reaction by which the matrix material degrades is exothermic or endothermic, then the latent heat of reaction must be quantified. To quantify and model the degradation behavior of the material, thermogravimetric analysis experiments should be performed. Such experiments are quick and inexpensive and offer insight into the degradation response. If the reinforcing fibers of the composite and/or the fiber sizing material are sensitive to degradation, then the degradation behavior of these various constituents should be investigated separately, and degradation models for each constituent developed independently. Lessons learned about the degradation behavior of the material should serve as a guide in the development of a test matrix for the evaluation of mechanical material properties. Both at-temperature and residual ply properties should be measured, and the results compared to separate reversible effects due to temperature from irreversible effects due to degradation. Initial test matrices should focus on regimes in which major changes occur, such as the matrix glass transition temperature and the onset of non-trivial degradation (for graphite/epoxy, this meant a degradation state between 0.001 and 0.03.) With a database of mechanical

material properties, degradation reaction constants, and thermal material properties, the mechanism models can be assembled into a single integrated code, such as was developed for graphite/epoxy.

REFERENCES

1. Sorathia, Usman, T. Dapp, and C. Beck. "Fire Performance of Composites." Materials Engineering (1992): 10-12.

2. Mehrkam, Paul A., Eileen Armstrong-Carroll, and Roland Cochran. Fire Damage Assessment of A-6 Composite Wing BUNO 152951. Warminster, PA: Naval Air Warfare Center, 1993. NAWCADWAR-93058-60.

3. Kistner, Mark D., Ronald J. Kuhbander, and Daniel B. McCray. The Evaluation of Thermally Induced Damage in Polymer Matrix Composites Via a Design of Experiments Approach. Wright-Patterson Air Force Base, OH: Wright Laboratory Materials Directorate, 1997. WL-TR-97-4017.

4. Madorsky, S. L., and S. Straus. "Stability of Thermoset Plastics at High Temperatures." Modern Plastics 38.6 (1961): 134-210.

5. Morgan, Roger J., Fung-Ming Kong, and Jay K. Lepper. "Laser-Induced Damage Mechanisms of Kevlar 49-Epoxy Composites." Journal of Composite Materials 22 (1988): 1026-44.

6. Springer, George S., ed. Environmental Effects on Composite Materials. Westport, CT: Technomic Publishing, 1981.

7. Dasgupta, A., R. K. Agarwal, and S. M. Bhandarkar. "Three-Dimensional Modeling of Woven-Fabric Composites for Effective Thermo-Mechanical and Thermal Properties." Composites Science and Technology 56 (1996): 209-23.

8. Han, L. S., W. F. Boyee, and L. Glower. "Directional Thermal Conductivities of Graphite/Epoxy Composites: 0/90 and 0/±45/90." AIAA 20th Thermophysics Conference.

9. Menousik, J. F., and D. L. Monin. Laser Thermal Modeling of Graphite Epoxy. China Lake, CA: Naval Weapons Center, 1979. NWC Technical Memorandum 3834.

10. Griffis, C. A., R. A. Masumura, and C. I. Chang. "Thermal Response of Graphite Epoxy Composite Subjected to Rapid Heating." Journal of Composite Materials 15 (1981): 427-42.

11. Pering, Gregory A., Patrick V. Farrell, and George S. Springer. "Degradation of Tensile and Shear Properties of Composites Exposed to Fire or High Temperature." Environmental Effects on Composite Materials. Ed George S. Springer. Westport, CT: Technomic Publishing, 1981. 145-59.

12. Henderson, J. B., and T. E. Wiecek. "A Mathematical Model to Predict the Thermal Response of Decomposing, Expanding Polymer Composites." Journal of

Composite Materials 21 (1987): 373-93.

13. McManus, Hugh L. N. "High Temperature Thermomechanical Behavior of Carbon-Phenolic and Carbon-Carbon Composites.". Stanford University, 1990.

14. Griffis, C. A., et al. "Degradation in Strength of Laminated Composites Subjected to Intense Heating and Mechanical Loading." Journal of Composite Materials 20 (1986): 216-35.

15. Milke, James A., and Anthony J. Vizzini. "Thermal Response of Fire-Exposed Composites." Journal of Composites Technology and Research 13.3 (1991): 145-51.

16. Fanucci, Jerome Paul. "Thermal Response of Radiantly Heated Kevlar and Graphite/Epoxy Composites." Journal of Composite Materials 21 (1987): 129-39.

17. Farmer, Jeffrey D., and Eugene E. Covert. "Transverse Thermal Conductance of Thermosetting Composite Materials During Their Cure." Journal of Thermophysics and Heat Transfer 8.2 (1994): 358-65.

18. Sigur, W. A. "Ablation Characteristics of Graphite/Epoxy." SAMPE Quarterly 17.2 (1986): 25-33.

19. Berlin, P., O. Dickman, and F. Larsson. "Effects of Heat Radiation on Carbon/PEEK, Carbon/Epoxy and Glass/Epoxy Composites." Composites 23.4 (1992): 235-43.

20. Scott, Elaine P., and James V. Beck. "Estimation of Thermal Properties in Epoxy Matrix/Carbon Fiber Composite Materials." Journal of Composite Materials 26.1 (1992): 132-49.

21. Morgan, Roger J., and Eleno T. Mones. "The Cure Reactions, Network Structure, and Mechanical Response of Diaminodiphenyl Sufone-Cured Tetraglycidyl 4,4' Diaminodiphenyl Methane Epoxies." Journal of Applied Polymer Science 33 (1987): 999-1020.

22. Stevens, Malcolm P. Polymer Chemistry, An Introduction. Reading, MA: Addison-Wesley, 1975.

23. Morgan, Roger J. "Thermal Characterization of Composites." Thermal Characterization of Polymeric Materials. 2nd ed. Academic Press, 1997. 2091-261.

24. Composites Materials Handbook MIL-HDBK-17. Web Page. URL: www.ccm.udel.edu/army. 1 April 1998.

25. Strauss, E. L. "Polymer Degradation Processes in Ablation." Aspects of

Degradation and Stabilization of Polymers . ed. H. H. G. Jellinek. New York: Elsevier Scientific Publishing, 1978.

26. Bishop, D. P., and D. A. Smith. "Combined Pyrolysis and Radiochemical Gas Chromatography for Studying the Thermal Degradation of Epoxy Resins and Polyimides. I. The Degradation of Epoxy Resins in Nitrogen Between 400C and 700C." Journal of Applied Polymer Science 14 (1970): 205-23.

27. Lee, Lieng-Huang. "Mechanisms of Thermal Degradation of Phenolic Condensation Polymers. II. Thermal Stability and Degradation Schemes of Epoxy Resins." Journal of Polymer Science: Part A 3 (1965): 859-82.

28. Bowen, D. O. "Thermal Degradation of Epoxy Resins." Modern Plastics 44.12 (1967).

29. de Pruneda, J. A. H., and R. J. Morgan. "The Effects of Thermal Exposure on the Structural and Mechanical Integrity of Carbon Fibers." Journal of Materials Science 25 (1990): 4776-81.

30. Cunningham, Ronan A. "High Temperature Degradation Mechanisms in Polymer Matrix Composites." Master's Thesis. Massachusetts Institute of Technology, 1996.

31. Greszczuk, L. B. Washington, DC: Naval Research Laboratory, 1984. Final Report, NRL Contract No. N00014-83-C-2330.

32. Weems, Douglas B., and Linda S. Rini. Tensile Behavior of Graphite/Epoxy at Elevated Temperatures. Cambridge, MA: Technology Laboratory for Advanced Composites, Massachusetts Institute of Technology, 1984. TELAC Report 84-11.

33. Hinger, J. "High Temperature Effects on Graphite/Epoxy." Master's Thesis. Massachusetts Institute of Technology, 1985.

34. Ha, Sung K., and George S. Springer. "Mechanical Properties of Graphite Epoxy Composites at Elevated Temperatures." 6th International Conference on Composite Materials and 2nd European Conference on Composite Materials: 1987. 4.422-4.430.

35. Barker, A. J., and H. Vangerko. "Temperature Dependence of Elastic Constants of CFRP." Composites (1983): 52-56.

36. Frame, B. J., et al. Oak Ridge, TN: Oak Ridge National Laboratory, 1990. ORNL/ATD-33.

37. Grimsley, Frank M., and C. E. Michaels. 1994. AIAA-94-1432-CP.

38. Chen, J. K., C. T. Sun, and C. I. Chang. "Failure Analysis of a Graphite/Epoxy

Laminate Subjected to a Combined Thermal and Mechanical Loading." Journal of Composite Materials 19 (1985): 408-23.

39. Hahn, H. T., and S. W. Tsai. Introduction to Composite Materials. Lancaster, PA: Technomic, 1980.

40. Springer, George S. "Model for Predicting the Mechanical Properties of Composites at Elevated Temperatures." Journal of Reinforced Plastics and Composites 3 (1984): 85-95.

41. McManus, H. L., B. J. Foch, and R. A. Cunningham. "Mechanism-Based Modeling of Long-Term Degradation." Journal of Composites Technology and Research .

42. Ottaviano, Marcus J., and Jimmy L. Yeh. "Fire Damage to Composite Structures." 16.622 Final Report. Department of Aeronautics and Astronautics, Massachusetts Institute of Technology, 1996.

43. Askins, D. Robert. "A Study of Overheat Damage to Structural Composites." 24th International SAMPE Technical Conference: 1992. T806-T820.

44. Smith, Elizabeth T., and Daniel Schwartz. "Fire Damage to Composite Structures." 16.622 Final Report. Massachusetts Institute of Technology, 1992.

45. Kucner, Lauren K. "Experimental Investigation of Fire Damage to Composite Materials." Master's Thesis. Massachusetts Institute of Technology, 1995.

46. Gedemer, Thomas J. "The Use of Thermogravimetry to Estimate Degree of Thermal Degradation." Polymer Characterization by Thermal Methods of Analysis. ed. Jen Chiu. New York: Marcel Dekker, Inc., 1974.

47. Mills, Anthony F. Basic Heat and Mass Transfer. Boston: Richard D. Irwin, Inc., 1995.

48. Kreith, Frank, and Mark S. Bohn. Principles of Heat Transfer. 1958. Fifth ed. New York: West Publishing Company, 1993.

49. Kissinger, Homer E. "Reaction Kinetics in Differential Thermal Analysis." Analytical Chemistry 29.11 (1957): 1702-06.

50. Lagace, Paul A., et al. 1991. TELAC Report 88-4b.

51. Kissinger, Homer E. "Variation of Peak Temperature With Heating Rate in Differential Thermal Analysis." Journal of Research of the National Bureau of Standards 57.4 (1956): 217-21.

52. "General Curve Fits." Kaleidagraph Learning Guide. Fourth ed. Reading, PA: Synergy Software. 543.

53. Crews, Lauren K., and Hugh L. McManus. CHARplus User Manual. Cambridge, MA: Technology Laboratory for Advanced Composites, Massachusetts Institute of Technology, 1998. TELAC Report 98-xx.

54. Tsai, Steven W. Composites Design. 4th ed. Dayton, OH: Think Composites, 1988.

55. Maddocks, Jason R. "Microcracking in Composite Laminates Under Thermal and Mechanical Loading." Master's Thesis. Massachusetts Institute of Technology, 1995.

56. "ASTM D3518: Standard Test Method for In-Plane Shear Response of Polymer Matrix Composite Materials by Tensile Test of a +-45 Laminate." Annual Book of ASTM Standards. Vol. 15.03. Philadelphia, PA: American Society for Testing and Materials, 1997.

57. Patekar, Kaustubh. "Long Term Degradation of Resin for High Temperature Composites." Master's Thesis. Massachusetts Institute of Technology, 1998.

58. Chamis, Christos C. "Simplified Composite Micromechanics Equations for Hygral, Thermal, and Mechanical Properties." SAMPE Quarterly (1984): 14-23.

59. Jones, Robert M. Mechanics of Composite Materials: Taylor and Francis, 1975.

GLOSSARY

at-temperature properties	properties of a material while it is at an elevated temperature
char	carbonaceous residue formed as a product of charring [4]
charring	pyrolysis of a polymer that results in the loss of gaseous reaction products
char yield	the fraction of inert mass remaining when a polymeric material has been completely pyrolyzed
damage	permanent mechanical changes in a laminate, including matrix cracking, delamination, or fiber breakage
degradation	a permanent change in a polymeric material that alters its material properties
degradation state	a quantitative description of the degree to which the material has charred, from a minimum of zero to a maximum of one, denoted $\alpha(x,y,z)$
exposure history	a general term for parameters describing the environment at the surface as a function of time, such as ambient temperature, $T_\infty(x,y,z,t)$, heat flux, $q''(x,y,z,t)$, or heat transfer coefficient, $h_c(x,y,z,t)$
failure	the point at which degradation and/or damage becomes extensive enough that the structure no longer meets its design requirements
mechanical material properties	properties of the composite material that describe its response to mechanical loading, including strength, stiffness, and other properties directly related to the structural response
residual properties	the properties of a material that has returned to ambient conditions following exposure at an elevated temperature
thermal history	the temperature distribution within the laminate up to the time of interest, τ, denoted $T(x,y,z,0<t\leq\tau)$

thermal state	the internal temperature distribution as a function of position, denoted $T(x,y,z)$
thermo-mechanical response	the stress/strain behavior of a structure, in response to mechanical loading and/or thermally-induced loading

APPENDIX A

TEMPER SOURCE CODE

The code listed below is named Temper. The code calculates the temperature distribution in a plate heated by convection over a portion of one surface. The code is self-contained and does not require a separate input file.

```
C*****************************************************************
C                            T E M P E R
C
C                     CODE FOR THE PREDICTION OF
C    TWO-DIMENSIONAL TEMPERATURE DISTRIBUTION IN PLATE CROSS-SECTION
C
C                      © 1998 Lauren K. Crews
C                Massachusetts Institute of Technology
C                Room 41-317, 77 Massachusetts Avenue
C             Cambridge, MA  02139    lkcrews@alum.mit.edu
C
C*****************************************************************
C
C  Version 1.0  7/98
C
C  Written in FORTRAN 77 for use on a Sun UNIX platform
C
C*****************************************************************
C Permission to use, copy, and modify this software for internal
C purpose only without fee is hereby granted provided that the above
C copyright notice and this permission appear on all copies of the
C code.  For any use of this software, in original or modified form,
C including, but not limited to, adaptation as the basis of a
C commercial software or hardware product, or distribution in whole or
C part, specific prior permission and/or the appropriate license must
C be obtained from MIT.  This software is provided "as is" without any
C warranties whatsoever, either expressed or implied, including but not
C limited to the implied warranties of merchantability and fitness for
C a particular purpose.  This software is a research program and MIT
C does not represent that it is free of error or bugs or suitable for
C any particular task.
C*****************************************************************
C
C     Define arrays, variables
      double precision Told(61,11)
      double precision Tnew(61,11)
      double precision deltT(61,11)
      real Lxz, Biot, Fourier
      double precision thickness,width,dt,dx,dz,kx,hf,hb,kz,hfront
```

```
      double precision left,down,right,up,Tflame,maxtemp
      double precision duration,t
      integer N,M,i,k,widthflame,aaa

C     Thickness (m)
      thickness=0.01

C     Width (m)
      width=.500

C     Number of through-thickness nodes
      N=11

C     Number of horizontal nodes
      M=61

C     Location of last heated node (node #)
      widthflame=13

C     Duration of simulation (sec)
      duration =60

C     Maximum back face temp (used as end condition)
      maxtemp=250

C     Timestep (sec)
      dt=0.005

C     Thickness length increment (m)
      dz=thickness/(N-1)

C     Horizontal length increment (m)
      dx=width/(M-1)

C     Set initial temperature condition
      do 10 i=1,M
       do 10 j=1,N
        Told(i,j)=0
        deltT(i,j)=0
 10   continue

C     Set material properties
C
C     Density (kg/m3)
      rho=1000
C
C     Specific heat (J/kgK)
      c=1000
C
C     Through-thickness thermal conductivity (W/mK)
      kz=1
C
C     Axial thermal conductivity (W/mK)
      kx=10
C
C     Set boundary conditions
C     Front and back heat transfer coefficients (W/m^2K)
```

```
      hfront=50
      hb=0

C     Flame temperature (C)
      Tflame=1000

      open(12,file='temp')

C     ---------------------------------------------------------------
      aaa=0
      t=0
      Lxz=(width*(widthflame-1)/(M-1))**2/thickness**2*1/kx
      Biot=hfront*thickness/1
      write(*,*) 'Starting Temper...'
      write(*,*) 'Lxz = ',Lxz,'   Biz = ',Biot,'
c      do while (t.lt.duration)
      do while (Told(1,N).lt.maxtemp)

C Calculate block (1,1) temperature
      left= 0
      down= hfront*dx/2*(Tflame-Told(1,1))
      right=kx*dz/2/dx*(Told(1,1)-Told(2,1))
      up =  kz*dx/2/dz*(Told(1,1)-Told(1,2))
      vol=dx*dz/4
      deltT(1,1)=dt/(rho*c*vol)*(left+down-right-up)
      Tnew(1,1)=Told(1,1)+deltT(1,1)
C
C Calculate block (1,N) temperature
      left= 0
      down= kz*dx/2/dz*(Told(1,N-1)-Told(1,N))
      right= kx*dz/2/dx*(Told(1,N)-Told(2,N))
      up =  hb*dx/2*(Told(1,N)-25)
      vol=dx*dz/4
      deltT(1,N)=dt/(rho*c*vol)*(left+down-right-up)
      Tnew(1,N)=Told(1,N)+deltT(1,N)
C
C Calculate temps in column 1
      do 30 k=2,N-1
         left= 0
         down = kz*dx/2/dz*(Told(1,k-1)-Told(1,k))
         right=kx*dz/dx*(Told(1,k)-Told(2,k))
         up =kz*dx/2/dz*(Told(1,k)-Told(1,k+1))
         vol=dx*dz/2
         deltT(1,k)=dt/(rho*c*vol)*(left+down-right-up)
         Tnew(1,k)=Told(1,k)+deltT(1,k)
 30   continue

C Vary i to calculate central columns
      do 40 i=2,M-1
       if (i.le.widthflame) then
          hf=hfront
       else
          hf=0
       endif

C Calculate row 1 temps from (2,1) to (M-1,1)
       left= kx*dz/2/dx*(Told(i-1,1)-Told(i,1))
```

```
          down= hf*dx*(Tflame-Told(i,1))
          right=kx*dz/2/dx*(Told(i,1)-Told(i+1,1))
          up =  kz*dx/dz*(Told(i,1)-Told(i,2))
        vol=  dx*dz/2
          deltT(i,1)=dt/(rho*c*vol)*(left+down-right-up)
        Tnew(i,1)=Told(i,1)+deltT(i,1)
C
C Calculate row N temps from (2,N) to (M-1,N)
      left= kx*dz/2/dx*(Told(i-1,N)-Told(i,N))
      down= kz*dx/dz*(Told(i,N-1)-Told(i,N))
      right=kx*dz/2/dx*(Told(i,N)-Told(i+1,N))
      up = hb*dx*(Told(i,N)-25)
      vol=dx*dz/2
        deltT(i,N)=dt/(rho*c*vol)*(left+down-right-up)
        Tnew(i,N)=Told(i,N)+deltT(i,N)

C Calculate temps for central rows in insulated area
      do 50 k=2,N-1
      left= kx*dz/dx*(Told(i-1,k)-Told(i,k))
      down= kz*dx/dz*(Told(i,k-1)-Told(i,k))
      right=kx*dz/dx*(Told(i,k)-Told(i+1,k))
      up =  kz*dx/dz*(Told(i,k)-Told(i,k+1))
        vol=dx*dz
        deltT(i,k)=dt/(rho*c*vol)*(left+down-right-up)
      Tnew(i,k)=Told(i,k)+deltT(i,k)
 50   continue
 40   continue

C Calculate node (M,1) temp
      left= kx*dz/2/dx*(Told(M-1,1)-Told(M,1))
      down=0
      right=0
      up =  kz*dx/2/dz*(Told(M,1)-Told(M,2))
      vol=dx*dz/4
      deltT(M,1)=dt/(rho*c*vol)*(left+down-right-up)
      Tnew(M,1)=Told(M,1)+deltT(M,1)
C
C Calculate temps in column M
      do 70 k=2,N-1
      left= kx*dz/dx*(Told(M-1,k)-Told(M,k))
      down= kz*dx/2/dz*(Told(M,k-1)-Told(M,k))
      right=0
      up =  kz*dx/2/dz*(Told(M,k)-Told(M,k+1))
      vol=dx*dz/2
        deltT(M,k)=dt/(rho*c*vol)*(left+down-right-up)
      Tnew(M,k)=Told(M,k)+deltT(M,k)
70    continue

C Calculate node (M,N) temp
      left= kx*dz/2/dx*(Told(M-1,N)-Told(M,N))
      down= kz*dx/2/dz*(Told(M,N-1)-Told(M,N))
      right=0
      up =  hb*dx/2*(Told(M,N)-25)
      vol=dx*dz/4
      deltT(M,N)=dt/(rho*c*vol)*(left+down-right-up)
      Tnew(M,N)=Told(M,N)+deltT(M,N)
```

```
 999   format (26(f8.2,' '))
 998   format (26(1PE12.3,' '))

C     Update old values
        do 100 i=1,M
          do 110 k=1,N
              Told(i,k)=Tnew(i,k)
 110       continue
 100    continue

        aaa=aaa+1
        if (aaa.eq.500) then
           write(*,*) t,Tnew(1,N)
           aaa=0
        endif

        t=t+dt

        end do

        write(12,*) 'hc = ',hfront
        write(12,*) 'flame = ',Tflame
        write(12,*) 'heated width = ',width*(widthflame-1)/(M-1)
        write(12,*) 'thickness = ',thickness
        write(12,*) 'initial temp = ',0
        write(12,*) 'time = ',t-dt
        Fourier=(t-dt)*kz/rho/c/thickness**2
        write(12,*) 'Lxz = ',Lxz,'  Biz = ',Biot,'  Foz = ',Fourier
        do 171 kkk=1,N
        write(*,999) (tnew(ii,kkk),ii=1,26)
        write(12,999) (tnew(jj,kkk),jj=1,26)
 171    continue

      close(12)

      end
```

APPENDIX B

THERMOGRAVIMETRIC ANALYSIS DATA

B.1 RESULTS FROM DYNAMIC TGA TESTS

Table B.1 Mass loss data from dynamic heating TGA tests conducted at different heating rates

Heating rate (°C/min)	Initial mass (μg)	Mass of nonreactive fraction (μg)
5	6420	1460
10 (#1)	4670	1000
10 (#2)	3530	986
10 (#3)	5750	1270
15	5490	1360

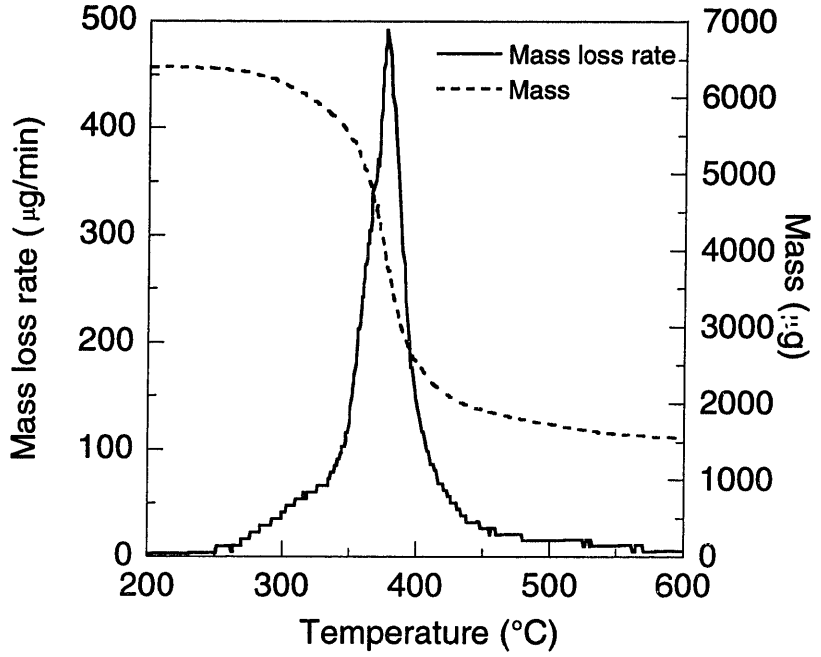

Figure B.1 Mass loss rate and mass data from dynamic heating test at 5°C/min

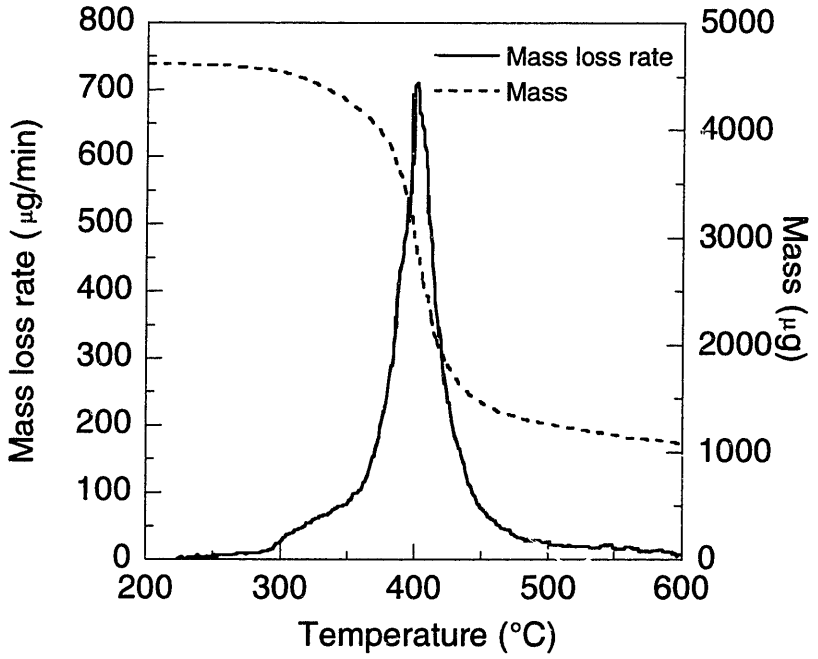

Figure B.2 Mass loss rate and mass data from dynamic heating test at 10°C/min (Trial #1)

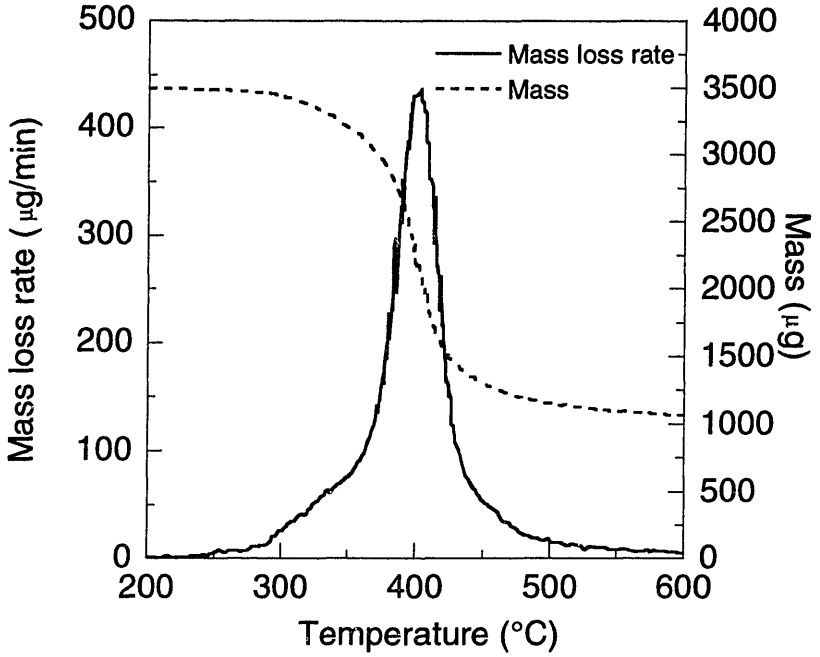

Figure B.3 Mass loss rate and mass data from dynamic heating test at 10°C/min (Trial #2)

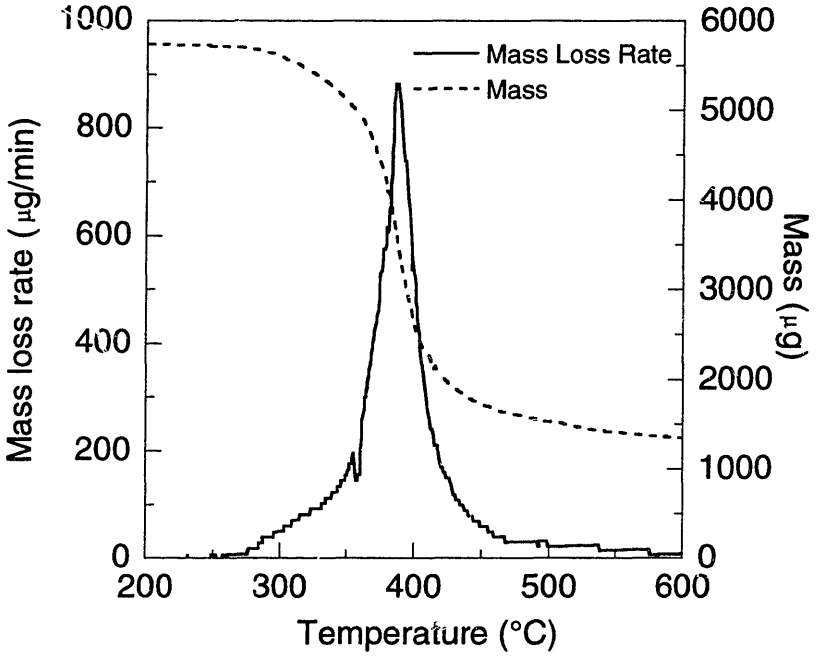

Figure B.4 Mass loss rate and mass data from dynamic heating test at 10°C/min (Trial #3)

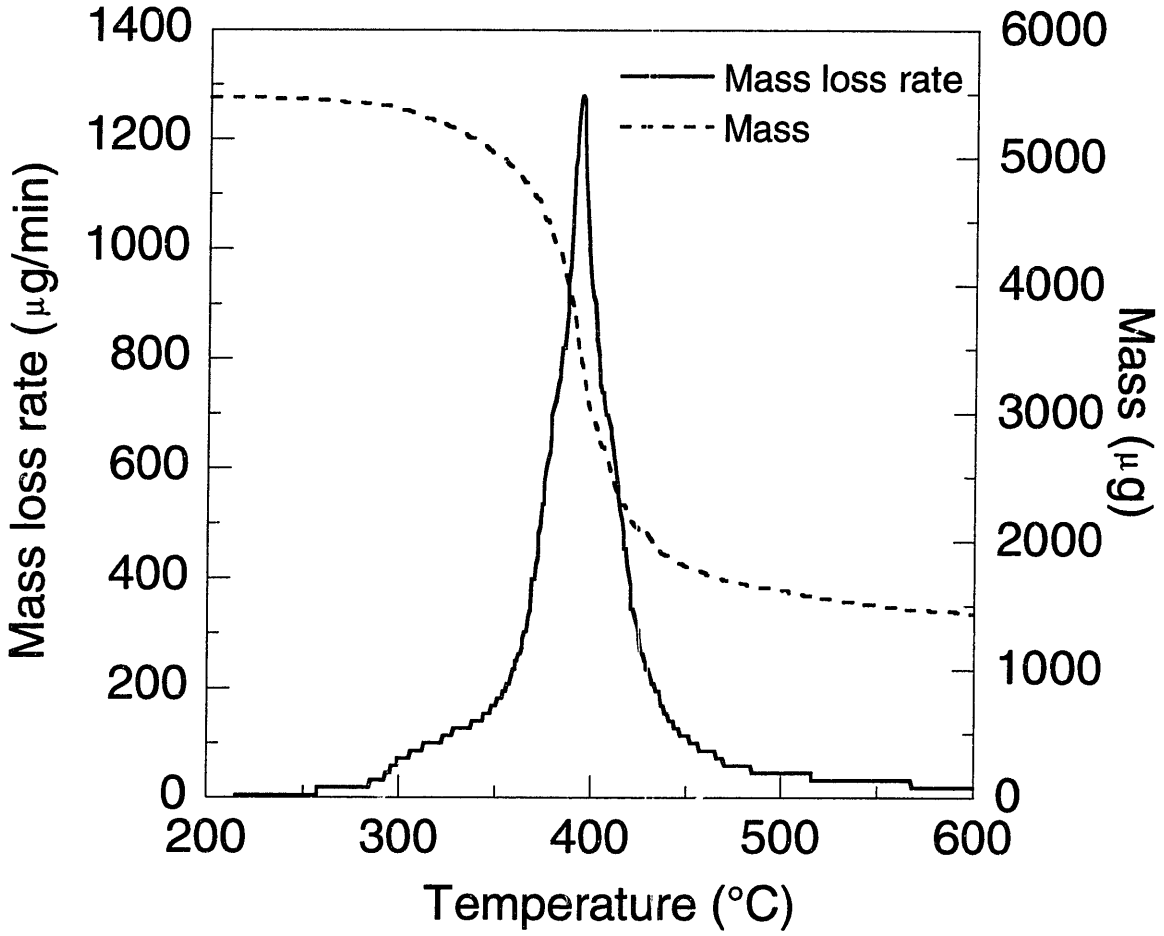

Figure B.5 Mass loss rate and mass data from dynamic heating test at 15°C/min

B.2 RESULTS FROM MODEL VERIFICATION TESTS

Table B.2 Mass loss data from degradation model verification tests and subsequent dynamic heating tests conducted at 10°C/min

Test #	Nominal exposure temperature (°C)	Exposure duration (min)	Initial mass (μg)	Mass after exposure (μg)	Mass of nonreactive fraction (μg)
1	350	10	6462	5340	1630
2	250	10	5763	5692	222.7
3	350	20	6362	4608	1436
4	350	1	5188	4691	703
5	375	10	6358	3646	1553
6	335	25	4239	3432	1059
7	335	10	4759	4183	1240
8	375	1	4472	3724	1097

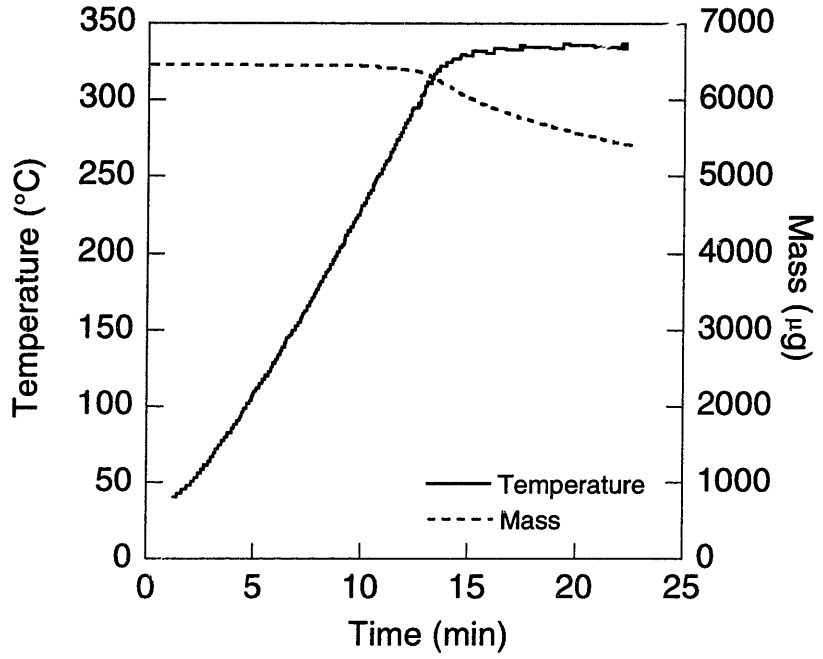

Figure B.6 Temperature and mass data from verification test #1 -- nominal exposure 10 minutes at 350°C

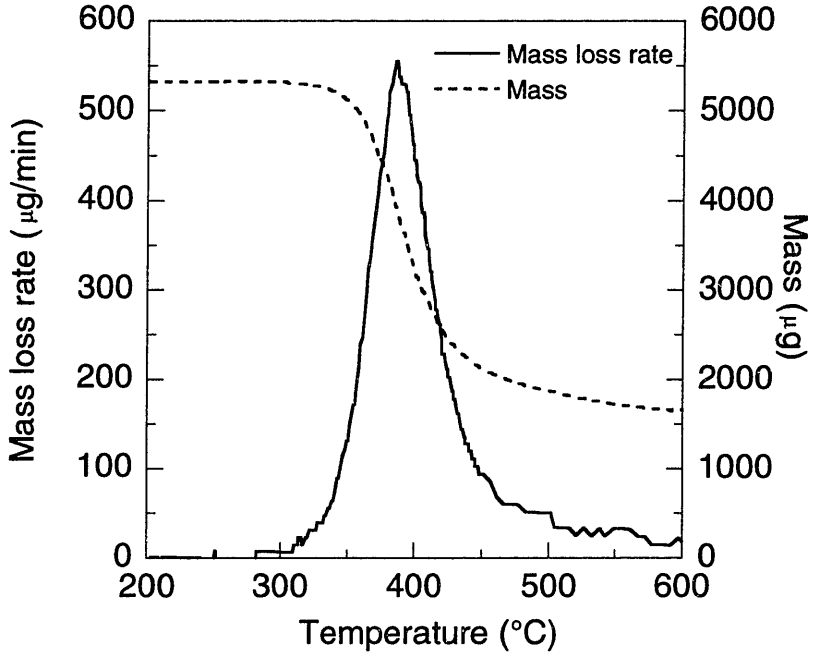

Figure B.7 Mass loss rate and mass data from dynamic heating at 10°C/min following verification test #1

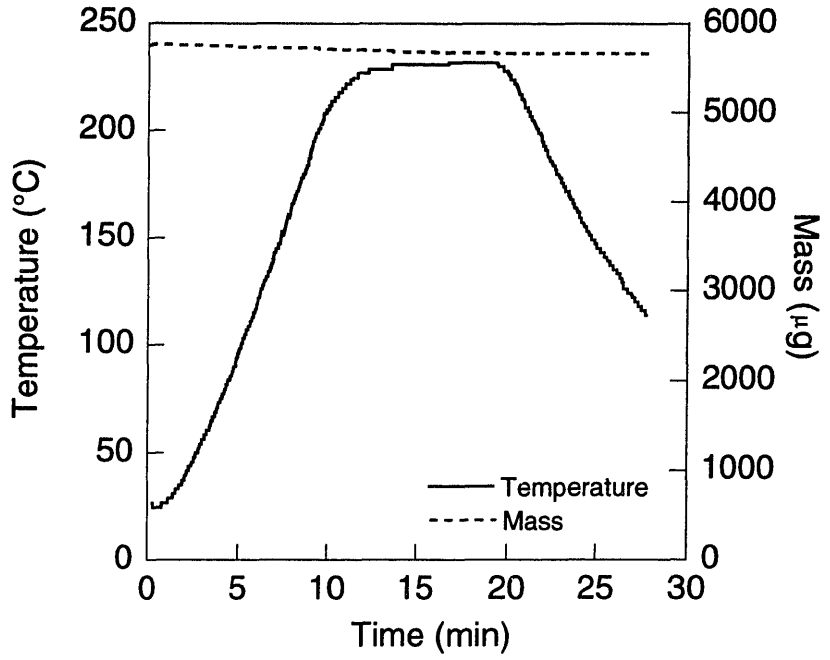

Figure B.8 Temperature and mass data from verification test #2 – nominal exposure 10 minutes at 250°C

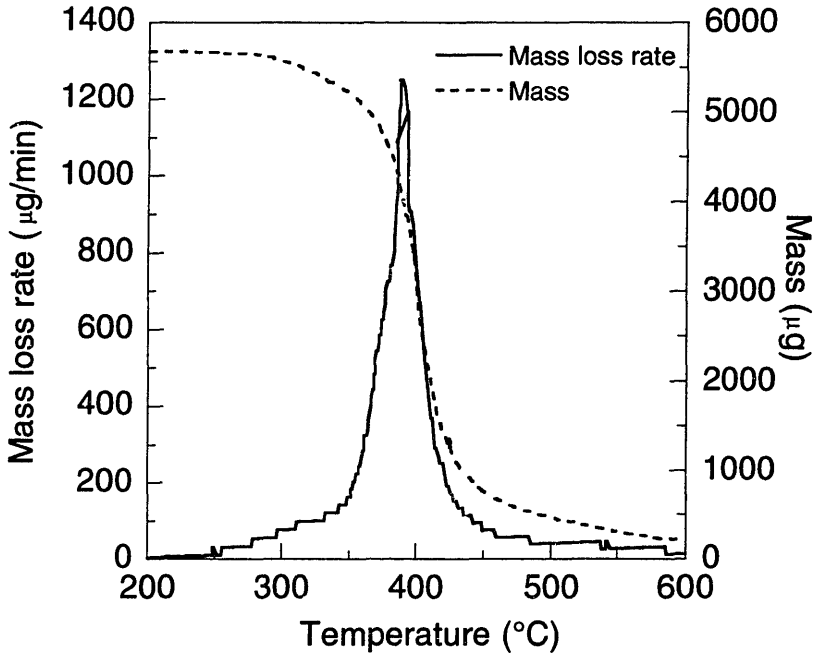

Figure B.9 Mass loss rate and mass data from dynamic heating at 10°C/min following verification test #2

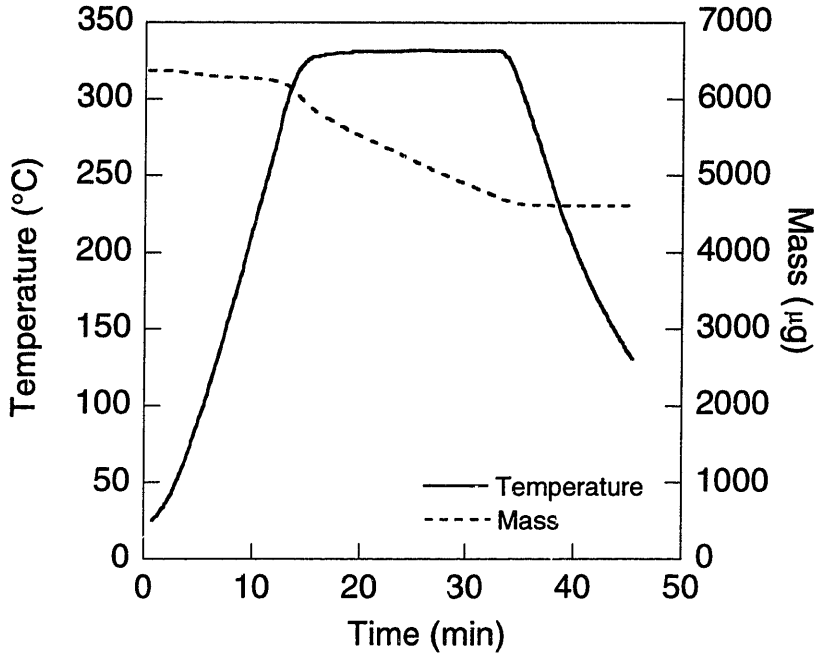

Figure B.10 Temperature and mass data from verification test #3 – nominal exposure 20 minutes at 350°C

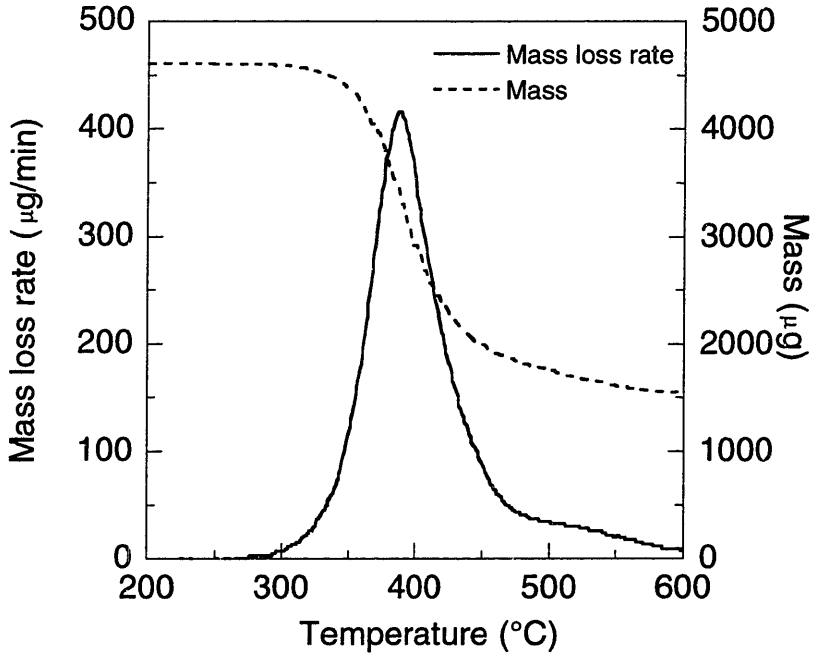

Figure B.11 Mass loss rate and mass data from dynamic heating at 10°C/min following verification test #3

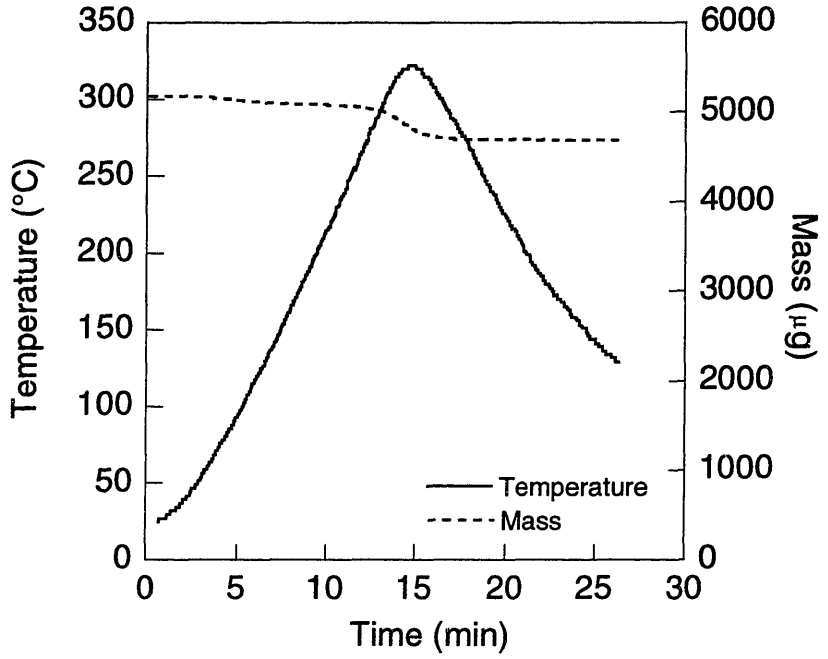

Figure B.12 Temperature and mass data from verification test #4 – nominal exposure 1 minute at 350°C

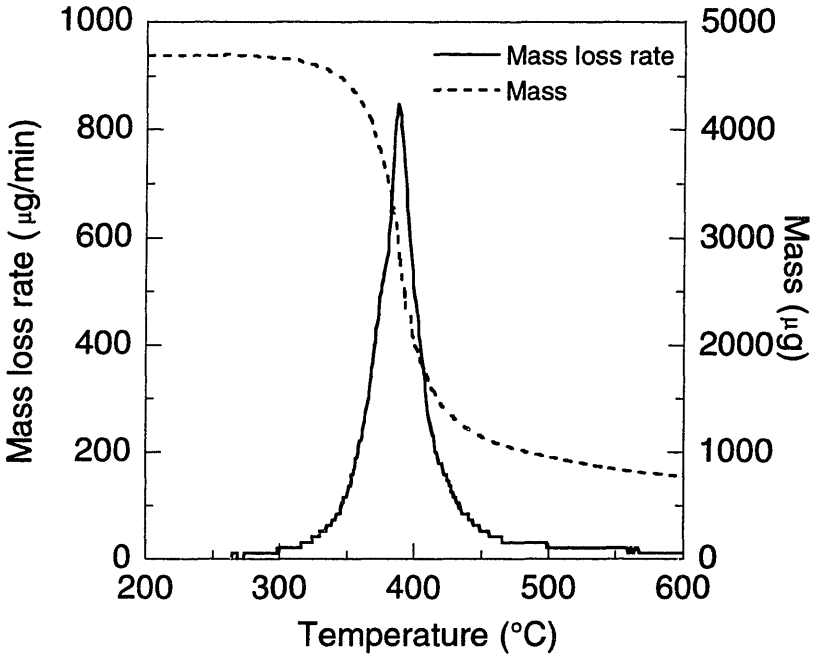

Figure B.13 Mass loss rate and mass data from dynamic heating at 10°C/min following verification test #4

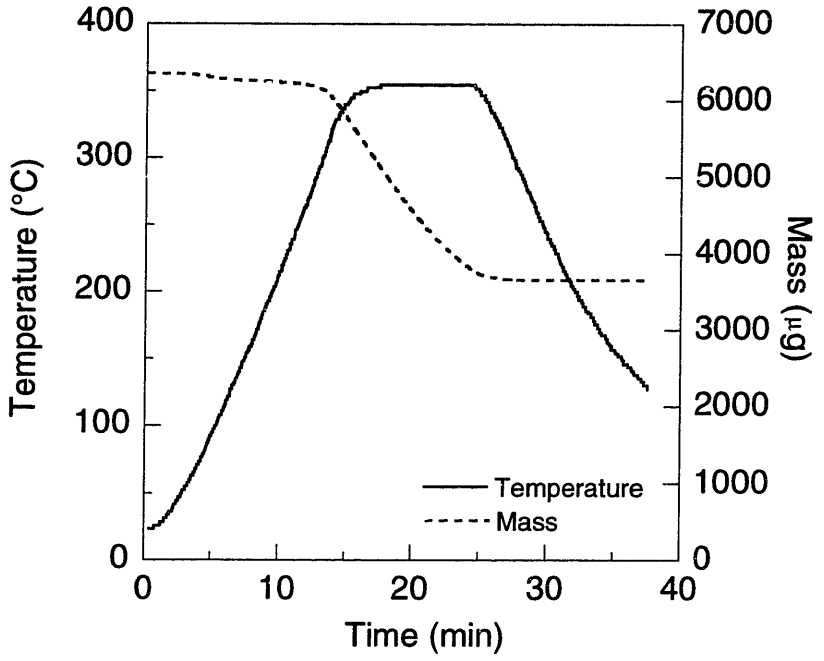

Figure B.14 Temperature and mass data from verification test #5 – nominal exposure 10 minutes at 375°C

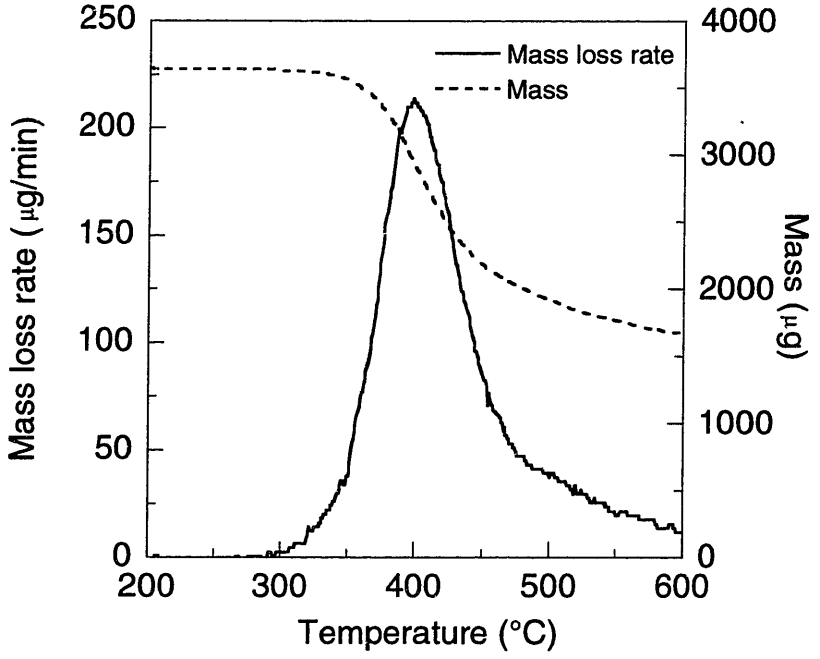

Figure B.15 Mass loss rate and mass data from dynamic heating at 10°C/min following verification test #5

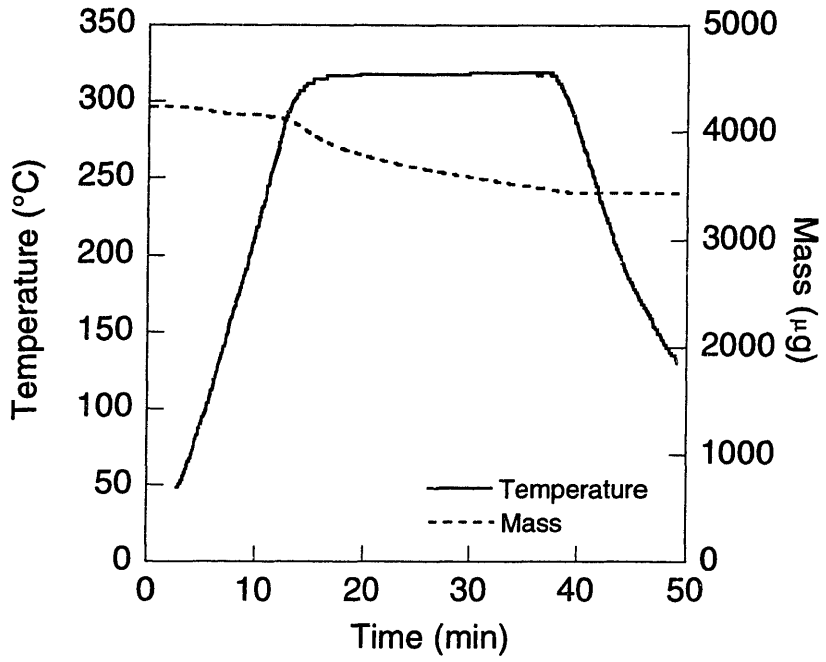

Figure B.16 Temperature and mass data from verification test #6 – nominal exposure 25 minutes at 335°C

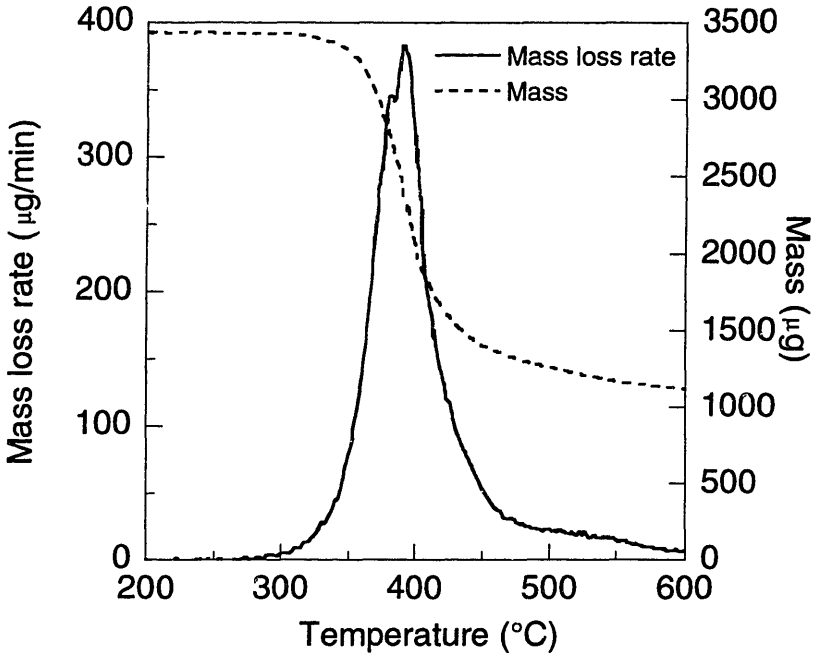

Figure B.17 Mass loss rate and mass data from dynamic heating at 10°C/min following verification test #6

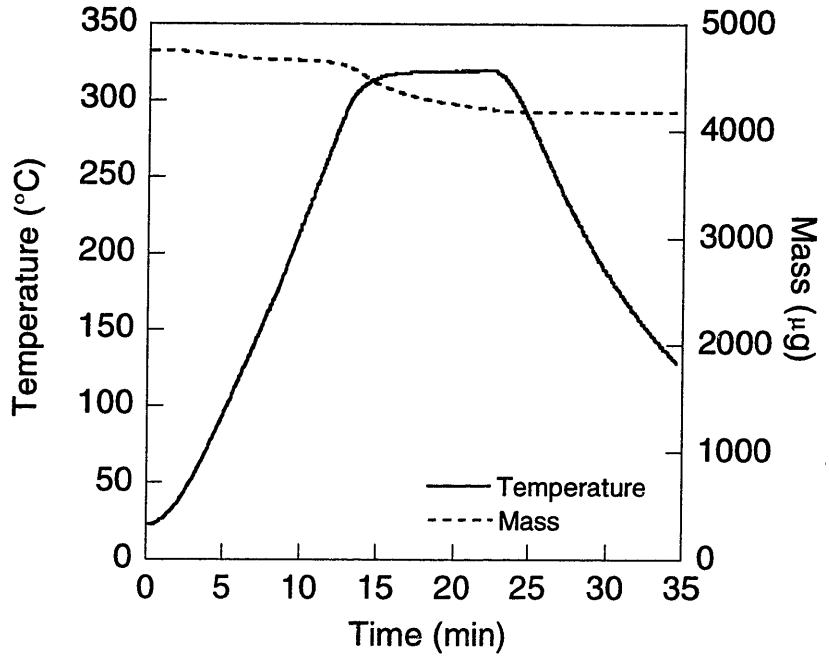

Figure B.18 Temperature and mass data from verification test #7 – nominal exposure 10 minutes at 335°C

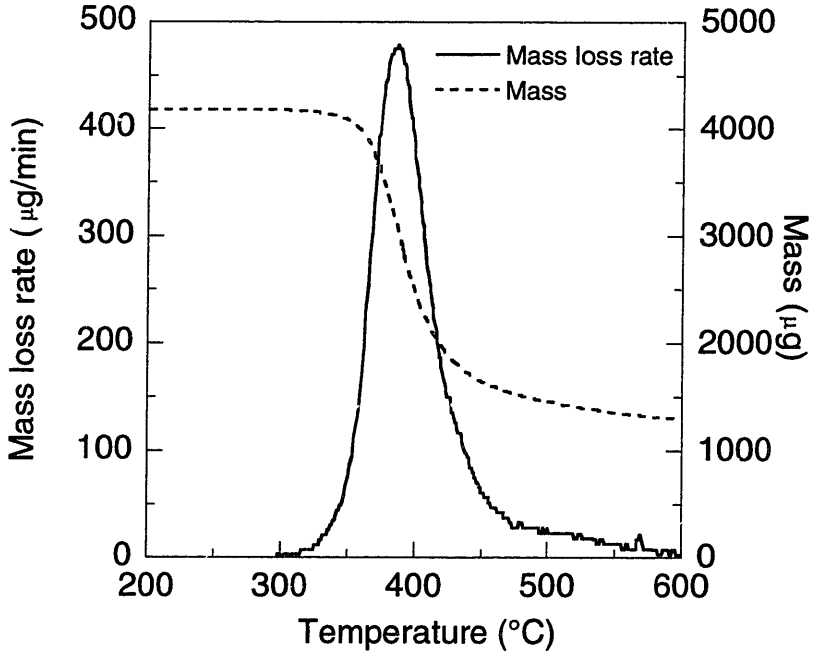

Figure B.19 Mass loss rate and mass data from dynamic heating at 10°C/min following verification test #7

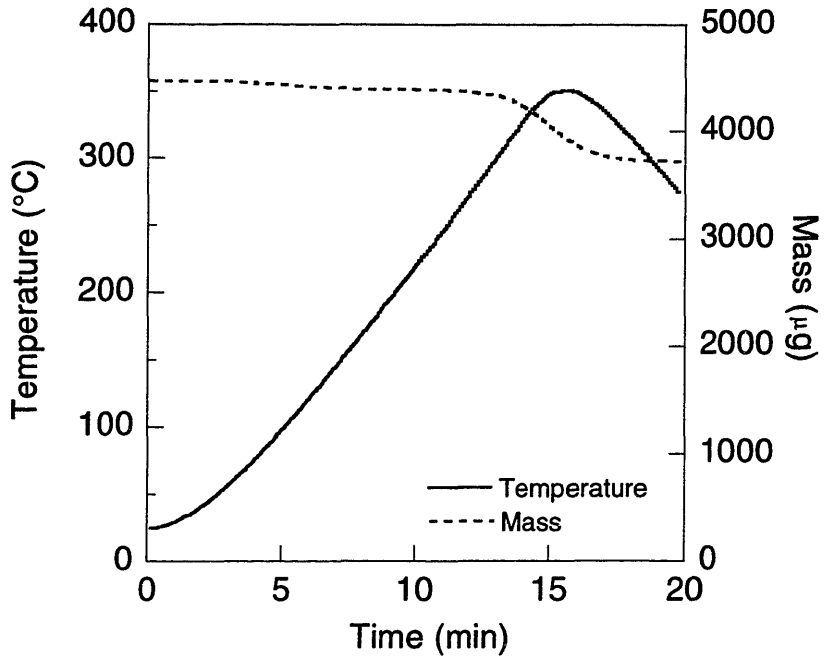

Figure B.20 Temperature and mass data from verification test #8 – nominal exposure 1 minute at 375°C

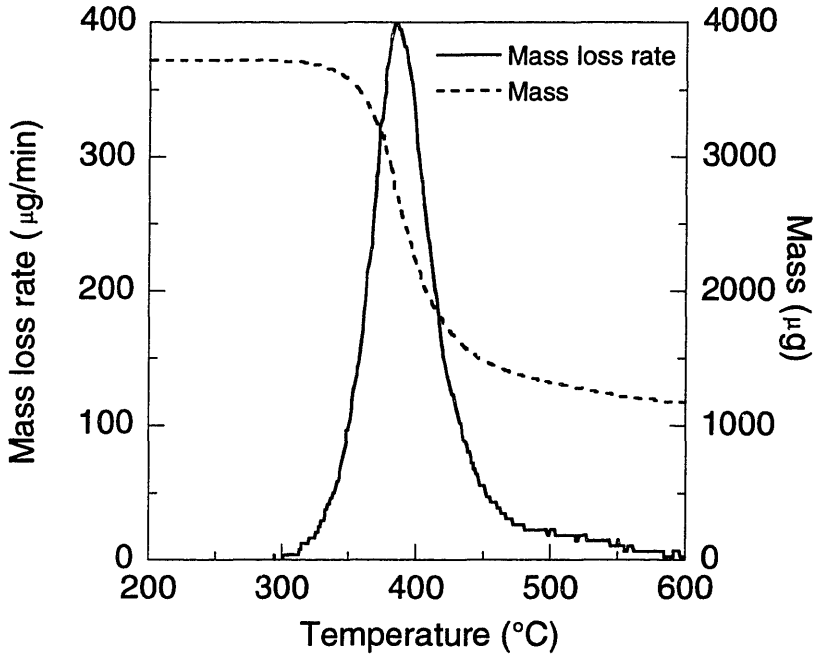

Figure B.21 Mass loss rate and mass data from dynamic heating at 10°C/min following verification test #8

APPENDIX C

METHOD FOR DETERMINING PEARSON'S R

Pearson's R is a metric for evaluating the quality of a fit between data and a model. The following equation is used to calculate Pearson's R [52]:

$$R = \frac{\sum_{i}^{N}(x_i - \bar{x})(y_i - \bar{y})}{\sqrt{\sum_{i}^{N}(x_i - \bar{x})^2}\sqrt{\sum_{i}^{N}(y_i - \bar{y})^2}} \quad \text{(C.1)}$$

where x_I and y_I are the discrete data and model values, respectively. The products are summed across all discrete data values, N. The closer R is to one, the better the fit between model and data.

APPENDIX D

RESULTS FROM TENSILE TESTS

D.1 STRESS-STRAIN RESPONSE

Table D.1 Modulus and R-value data from at-temperature tensile tests on $[90]_{12}$ coupons

Test temperature (°C)	Test date	Modulus (GPa)	R-value of curve fit
25	8/8/97	8.4	0.9997
25	9/15/97	10.1	0.9997
25	9/22/97	9.0	0.9995
150	8/11/97	8.0	0.9980
150	9/21/97	7.7	0.9972
150	10/24/97	7.1	0.9980
150	10/30/97	10.1	0.9991
200	8/28/97	2.3	0.9988
200	10/26/97	6.1	0.9966
200	10/27/97	10.3	0.9967
250	8/22/97	1.3	0.9969
250	9/11/97	0.4	0.9866
250	9/19/97	0.6	0.9924
300	8/26/97	0.04	0.8514

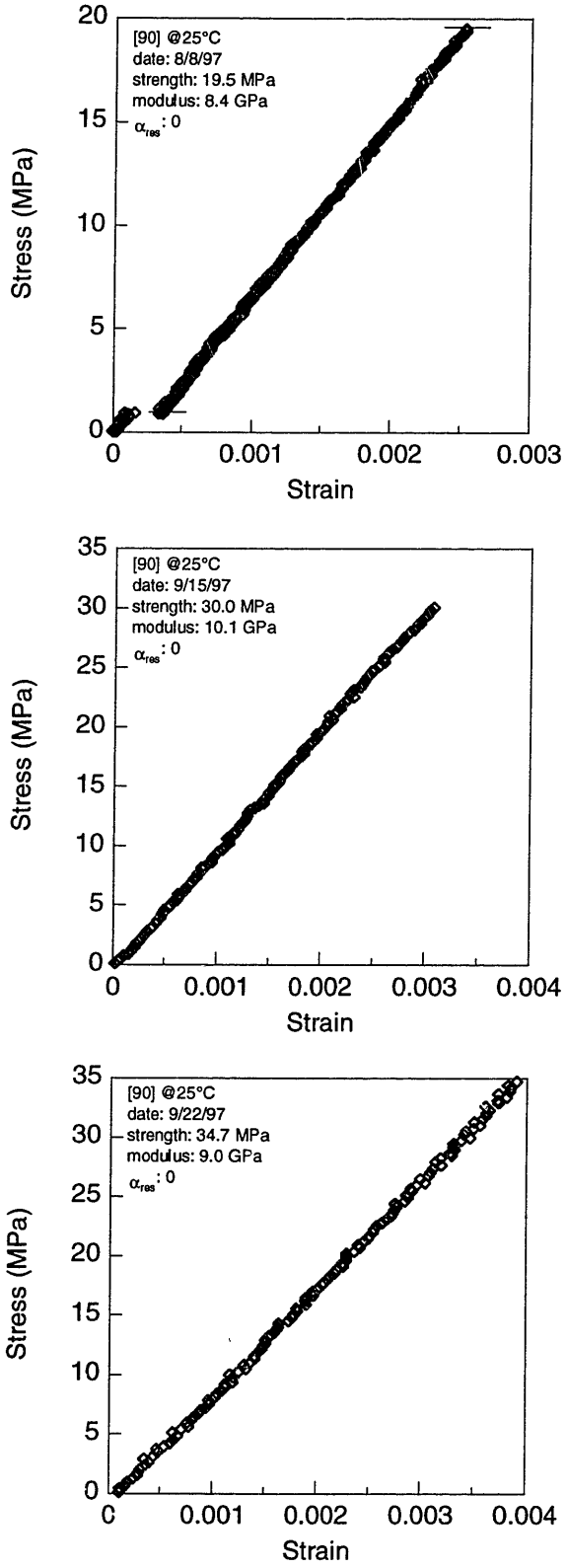

Figure D.1 Stress-strain data from at-temperature tests on $[90]_{12}$ coupons – nominal test temperature of 25°C.

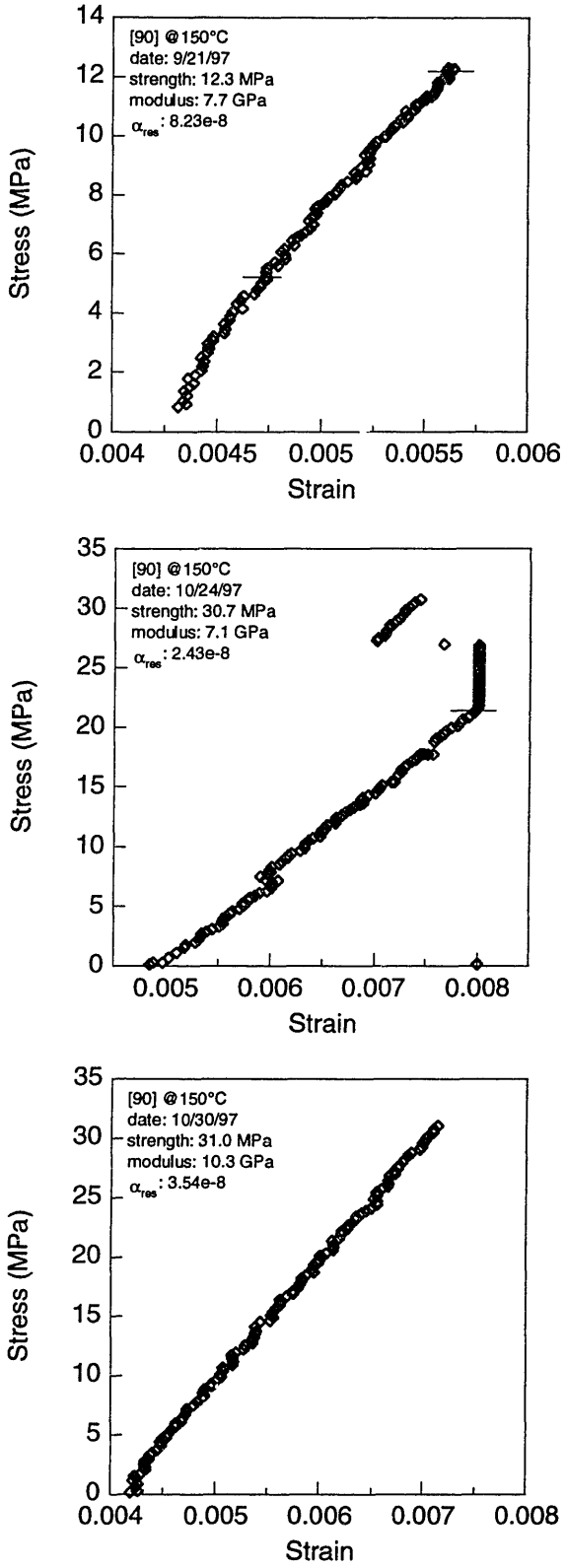

Figure D.2 Stress-strain data from at-temperature tests on $[90]_{12}$ coupons – nominal test temperature of 150°C.

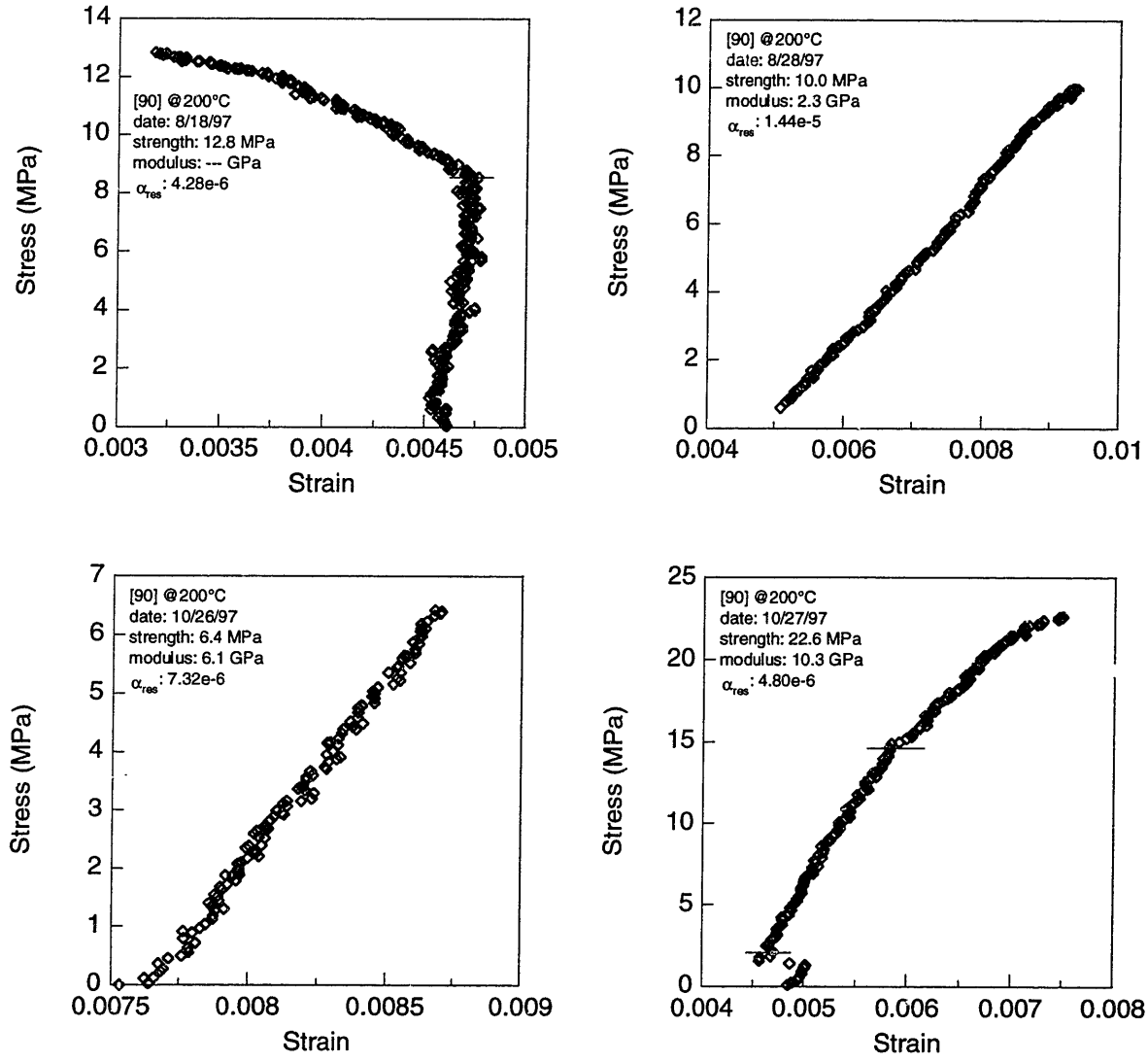

Figure D.3 Stress-strain data from at-temperature tests on $[90]_{12}$ coupons – nominal test temperature of 200°C.

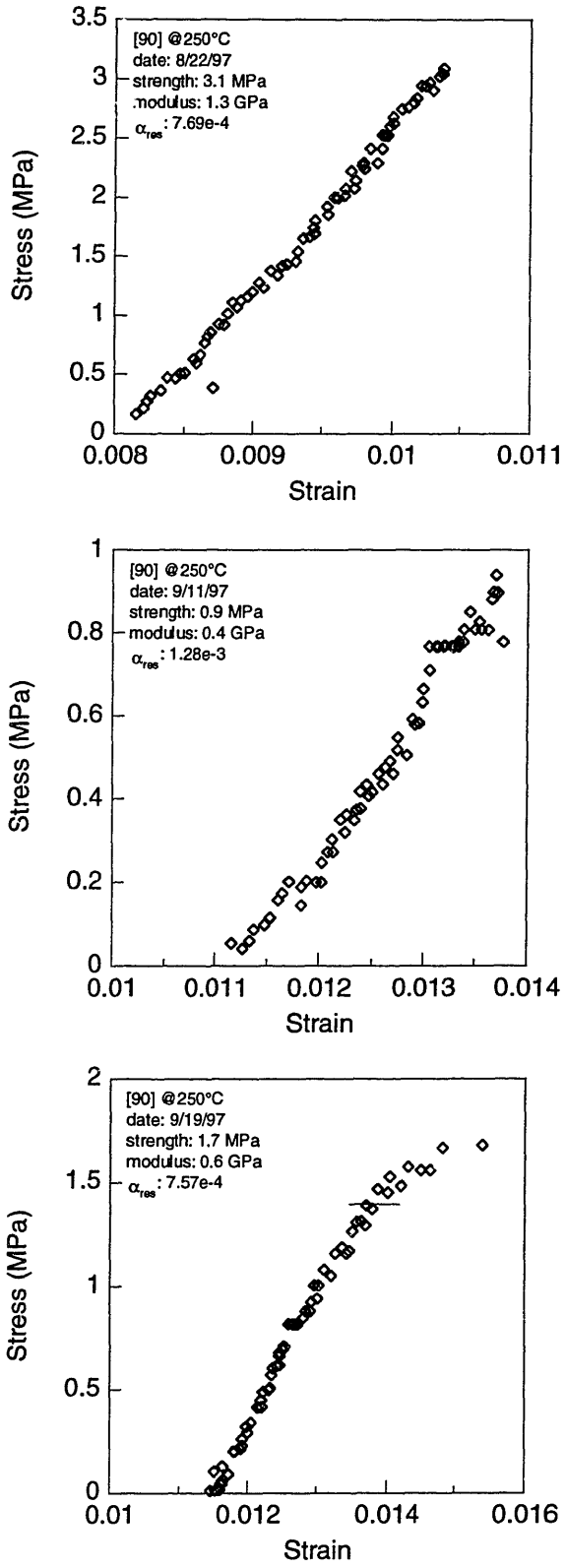

Figure D.4 Stress-strain data from at-temperature tests on $[90]_{12}$ coupons – nominal test temperature of 250°C.

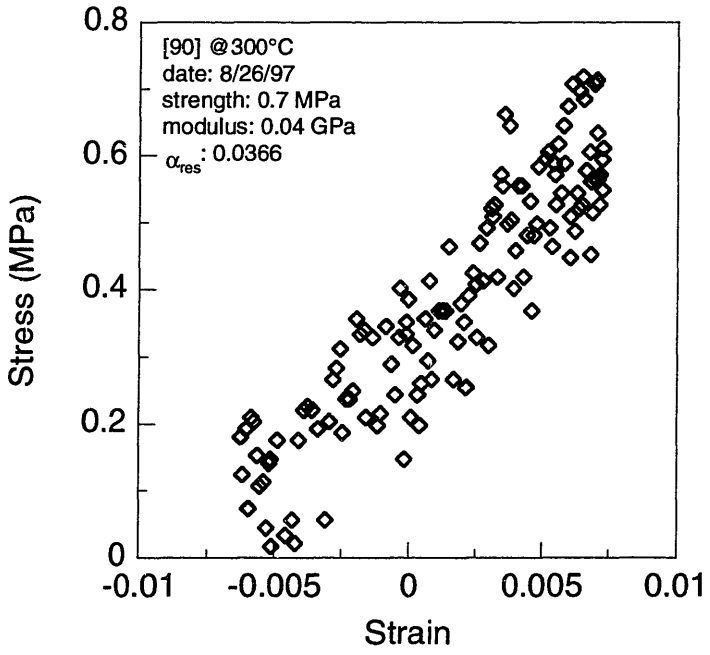

Figure D.5 Stress-strain data from at-temperature test on $[90]_{12}$ coupons – nominal test temperature of 300°C.

Table D.2 Modulus and R-value data from residual tensile tests on $[90]_{12}$ coupons

Test temperature (°C)	Test date	Modulus (GPa)	R-value of curve fit
150	8/29/97	9.7	0.9999
150	9/17/97	8.7	0.9994
150	10/26/97	8.3	0.9991
200	8/26/97	9.8	0.9987
200	9/10/97	10.1	0.9997
200	9/22/97	8.4	0.9998
250	8/19/97	8.7	0.9996
250	9/21/97	8.0	0.9991
250	10/26/97	7.5	0.9993
300	9/17/97	5.8	0.9934
300	9/19/97	6.3	0.9989
300	10/27/97	5.6	0.9956
275 (55 min hold)	12/21/97 #1	4.9	0.9977
275 (55 min hold)	12/21/97 #2	6.9	0.9982
275 (55 min hold)	12/21/97 #3	6.2	0.9981
317 (0.1 min hold)	12/20/97	6.7	0.9991
317 (0.1 min hold)	12/22/97 #1	5.3	0.9979
317 (0.1 min hold)	12/22/97 #2	4.5	0.9981

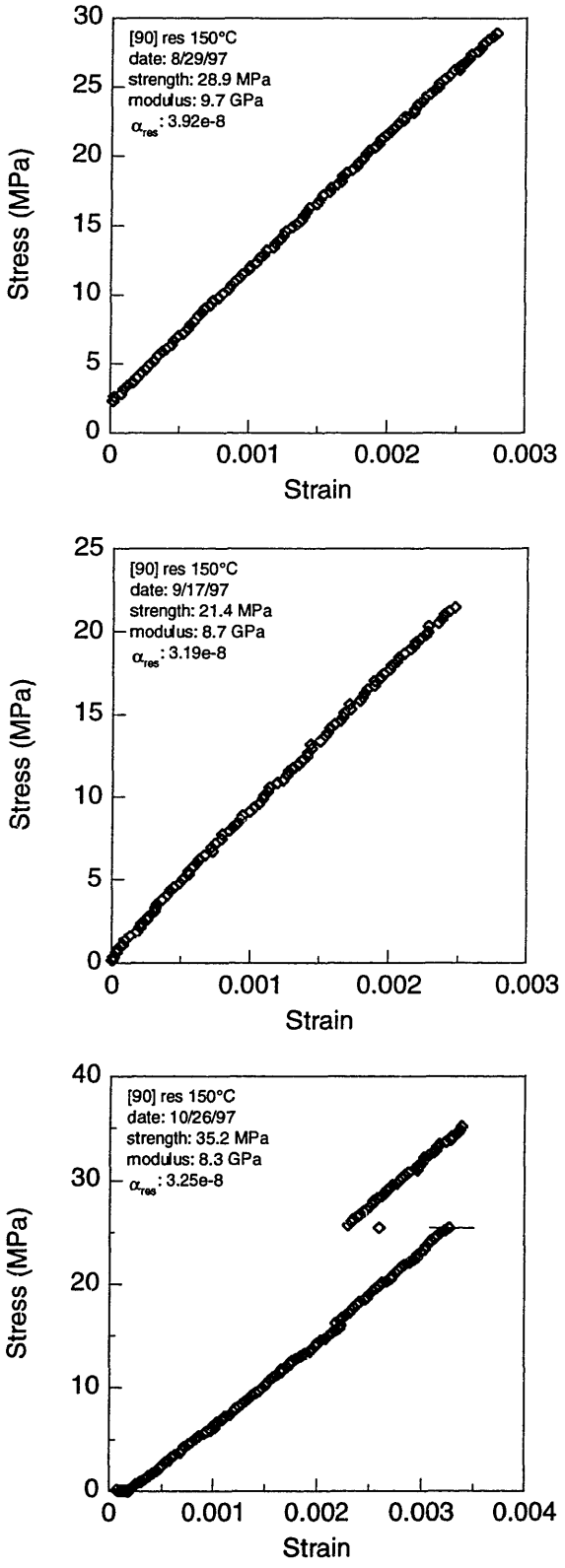

Figure D.6 Stress-strain data from residual tests on $[90]_{12}$ coupons – nominal test temperature of 150°C.

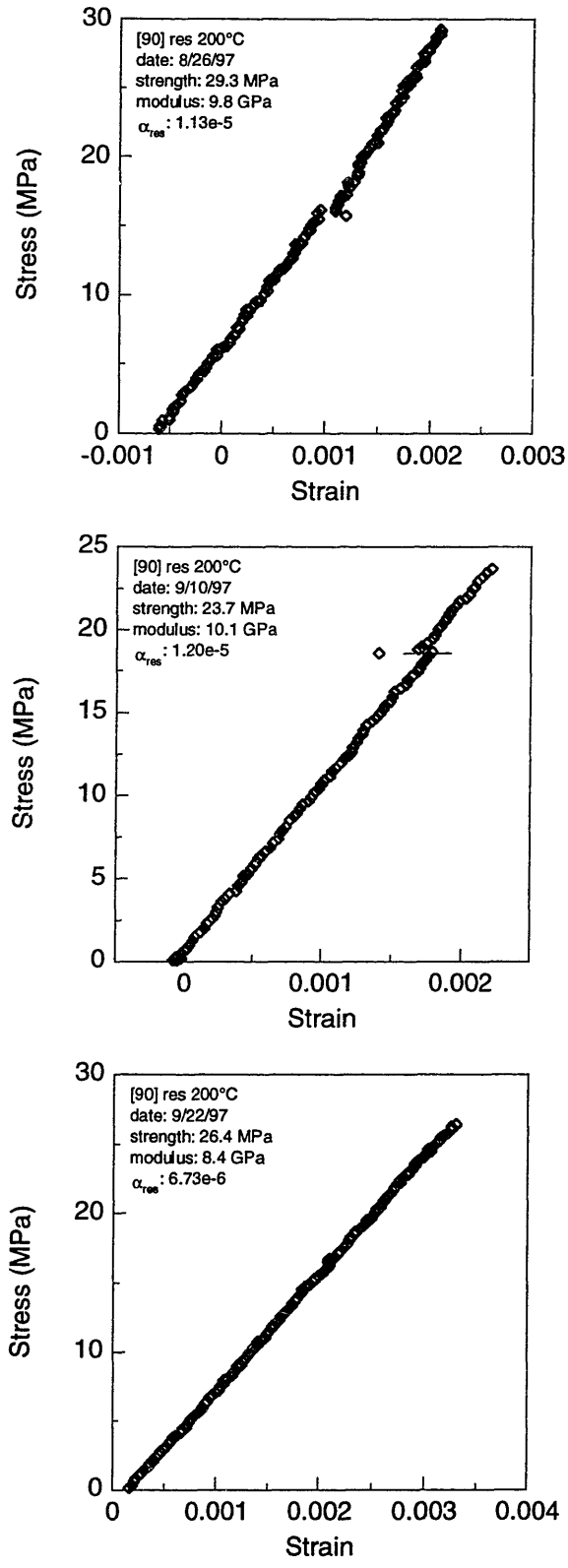

Figure D.7 Stress-strain data from residual tests on $[90]_{12}$ coupons – nominal test temperature of 200°C.

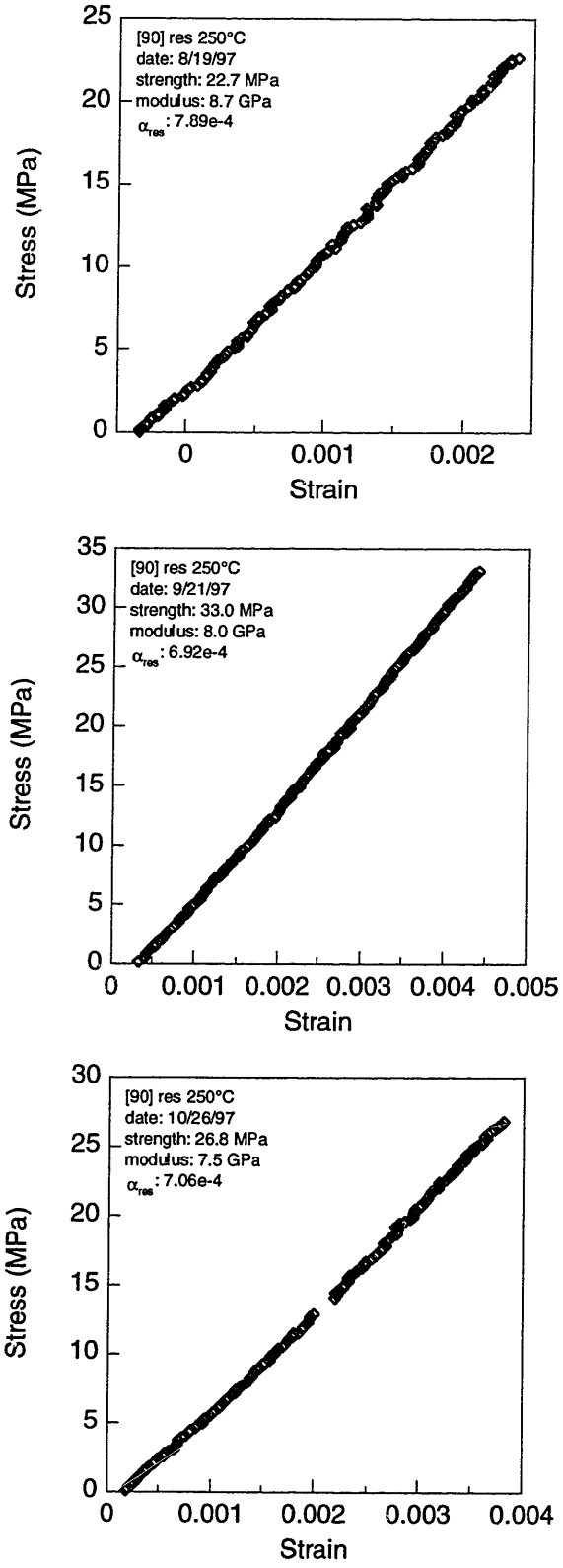

Figure D.8 Stress-strain data from residual tests on $[90]_{12}$ coupons – nominal test temperature of 250°C.

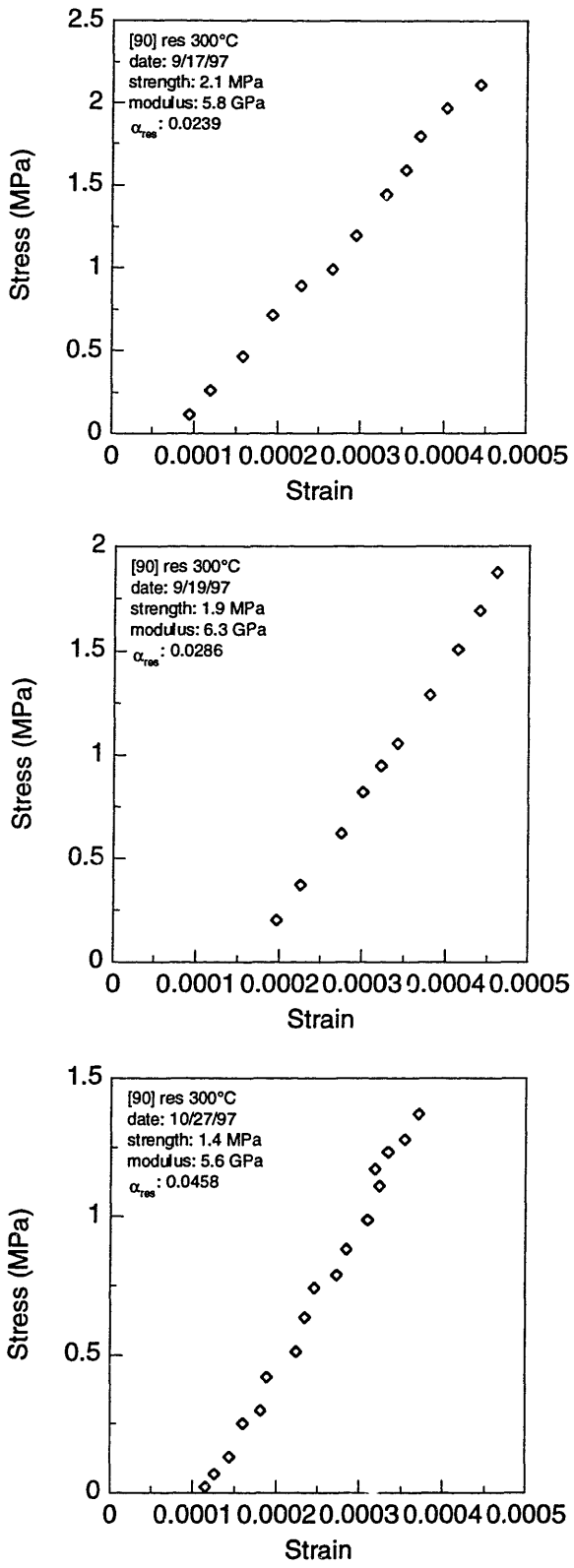

Figure D.9 Stress-strain data from residual tests on $[90]_{12}$ coupons – nominal test temperature of 300°C.

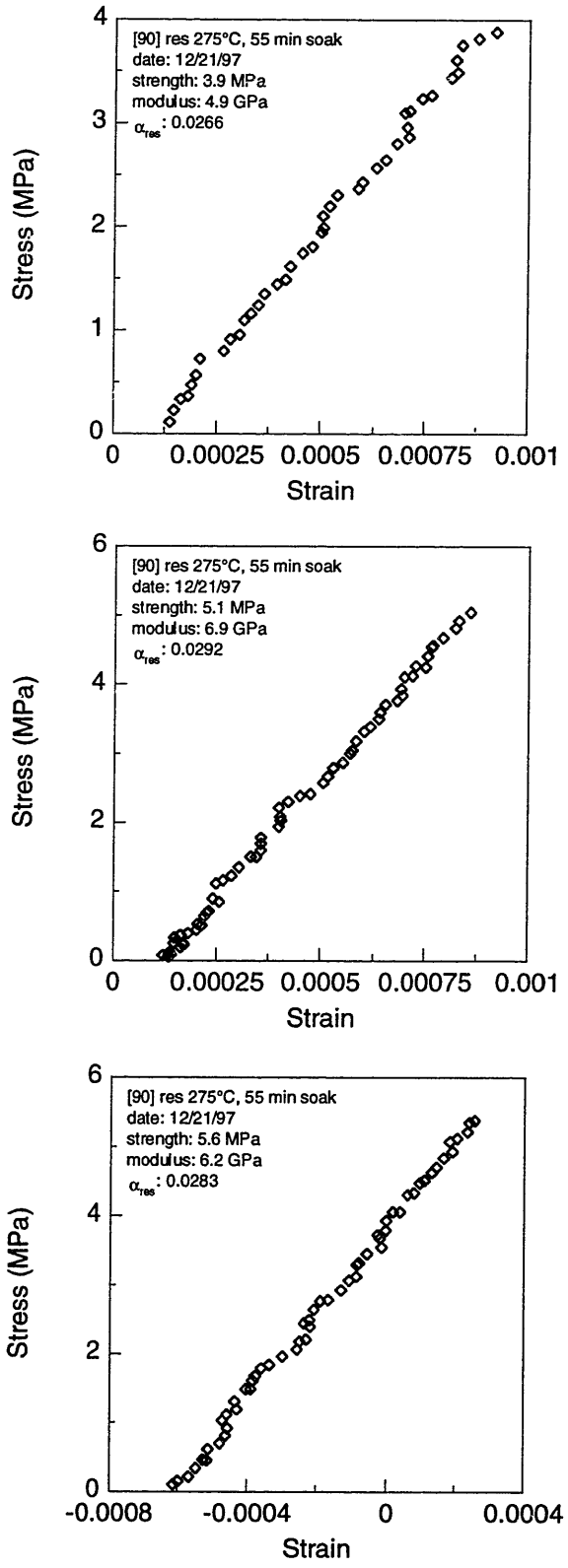

Figure D.10 Stress-strain data from residual tests on $[90]_{12}$ coupons – nominal test temperature of 275°C, 55 minute hold.

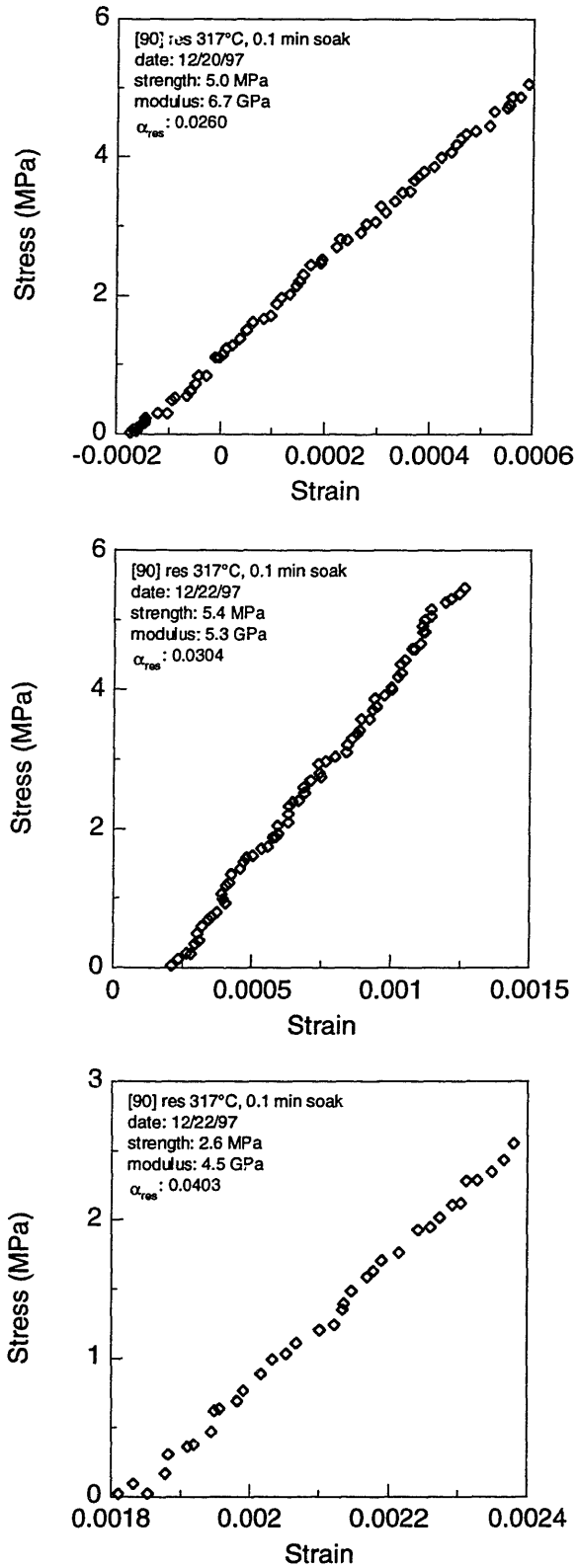

Figure D.11 Stress-strain data from residual tests on $[90]_{12}$ coupons – nominal test temperature of 317°C (0.1 minute hold).

Table D.3 Modulus and R-value data from at-temperature tensile tests on $[0]_4$ coupons

Test Temperature (°C)	Test date	Modulus (GPa)	R-value of curve fit
25	9/10/97	124 125	0.9997 0.9991
25	9/21/97	112	0.9996
25	9/22/97	125 133	0.9998 0.9996
150	8/27/97	133	0.9986
150	10/29/97 #1	122	0.9996
150	10/29/97 #2	116 116	0.9984 0.9987
200	8/20/97	83	0.9980
200	8/28/97	196	0.9889
200	9/10/97	130 134	0.9989 0.9989
200	10/22/97	142	0.9991
200	10/30/97	116 115	0.9993 0.9865
250	8/19/97	121	0.9970
250	9/15/97	115	0.9992
250	9/18/97	123	0.9995
300	8/18/97	116	0.9988
300	9/16/97	91	0.9961
300	10/29/97	139	0.9979

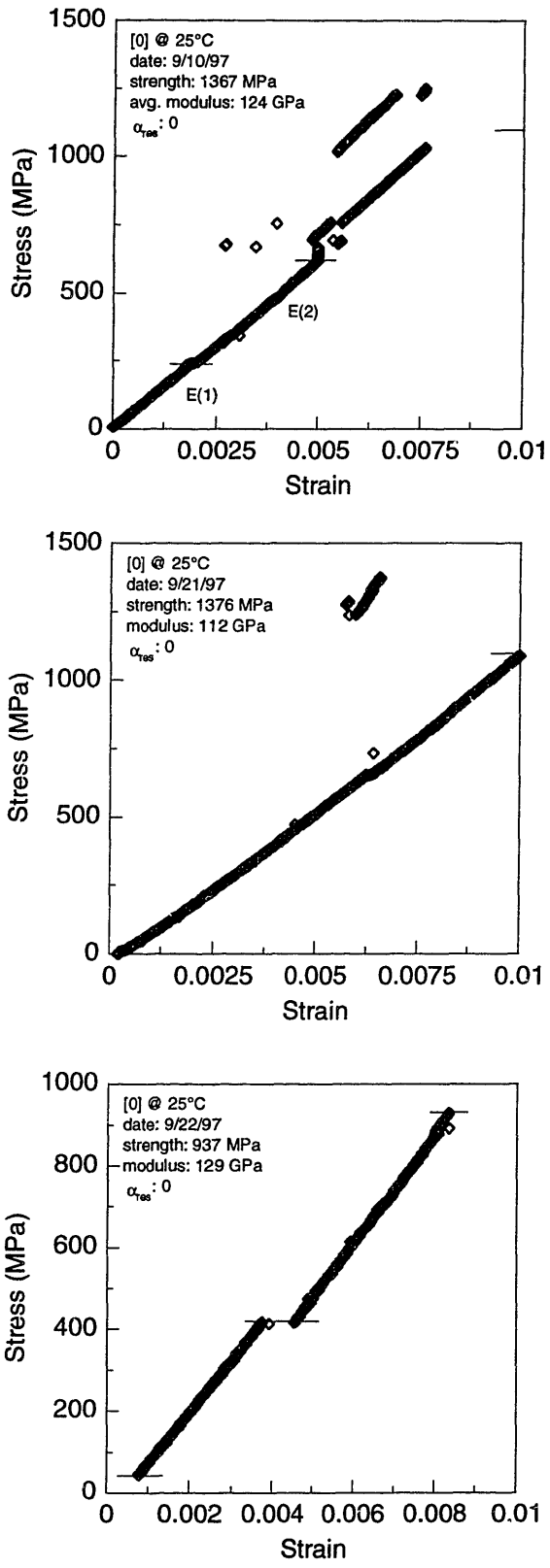

Figure D.12 Stress-strain data from at-temperature tests on $[0]_4$ coupons – nominal test temperature of 25°C.

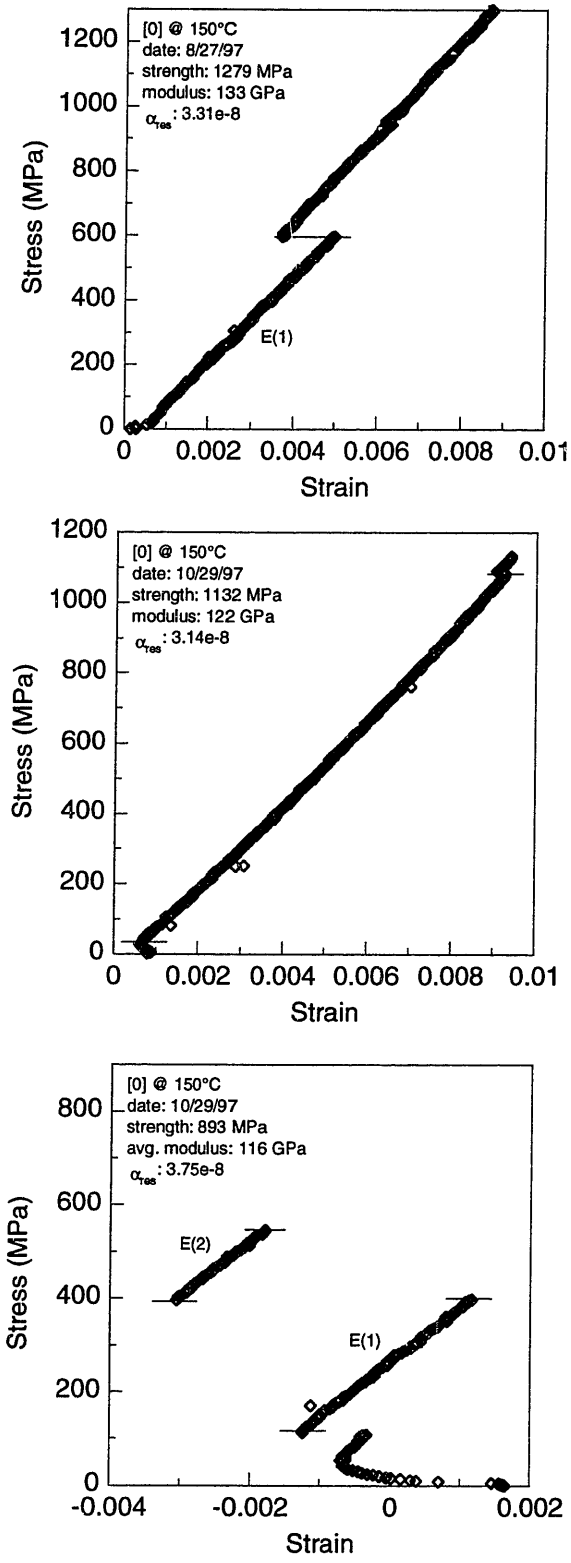

Figure D.13 Stress-strain data from at-temperature tests on $[0]_4$ coupons – nominal test temperature of 150°C.

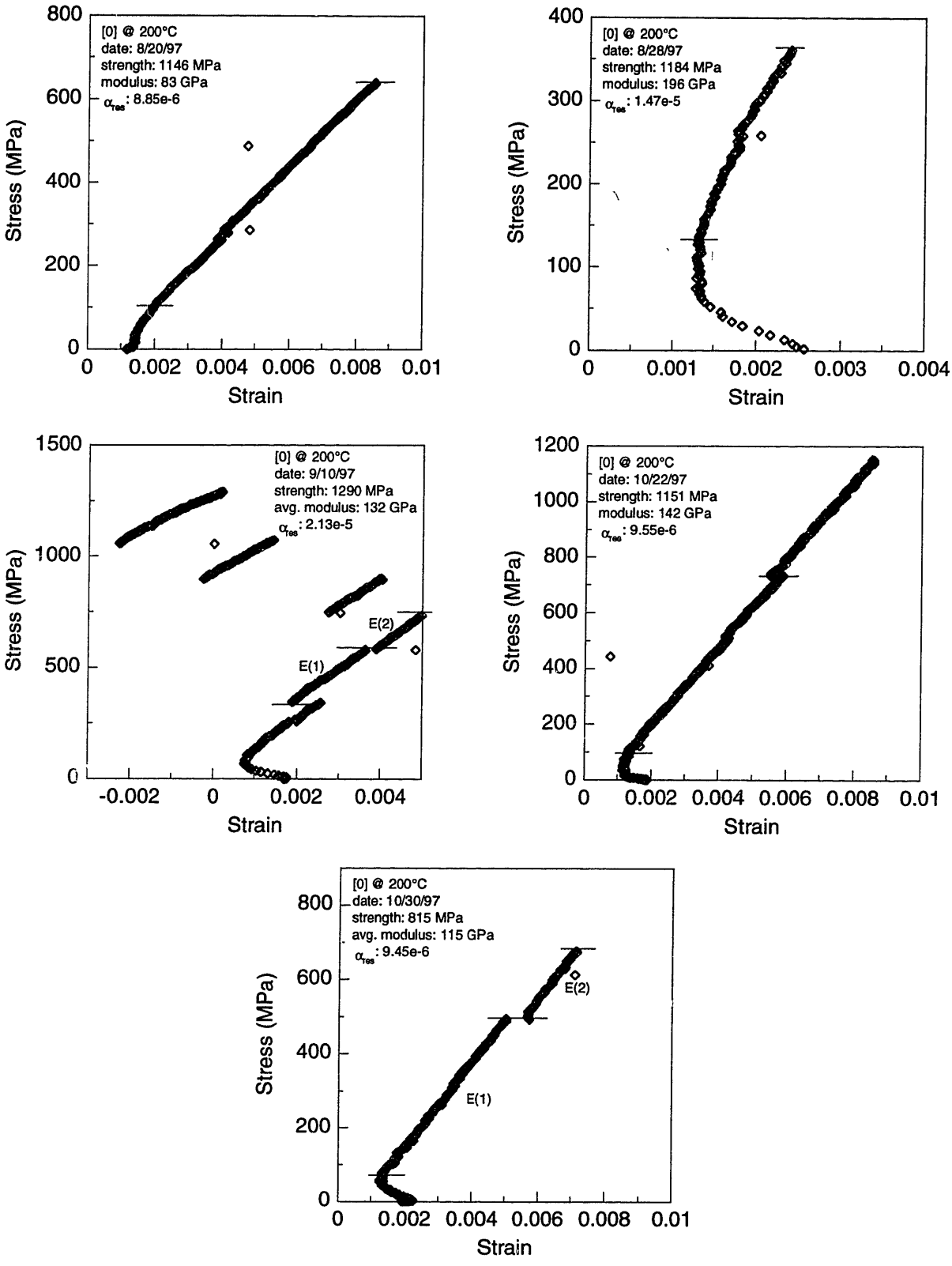

Figure D.14 Stress-strain data from at-temperature tests on $[0]_4$ coupons – nominal test temperature of 200°C.

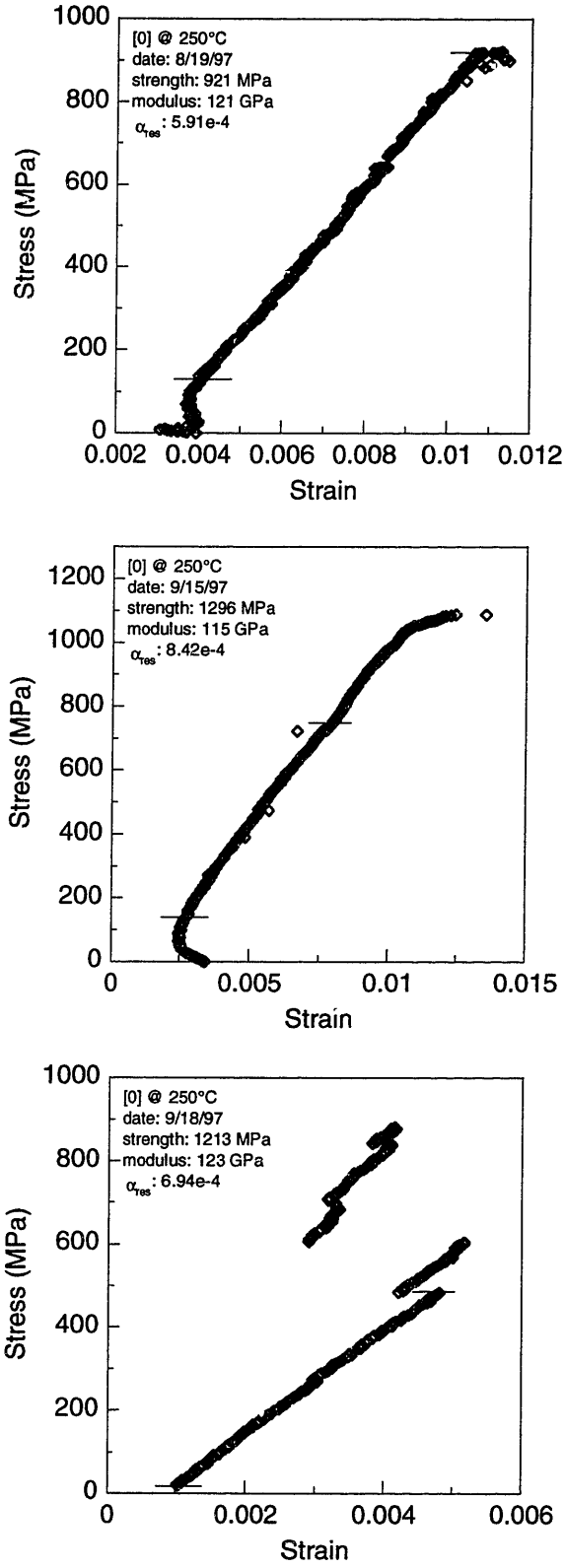

Figure D.15 Stress-strain data from at-temperature tests on $[0]_4$ coupons – nominal test temperature of 250°C.

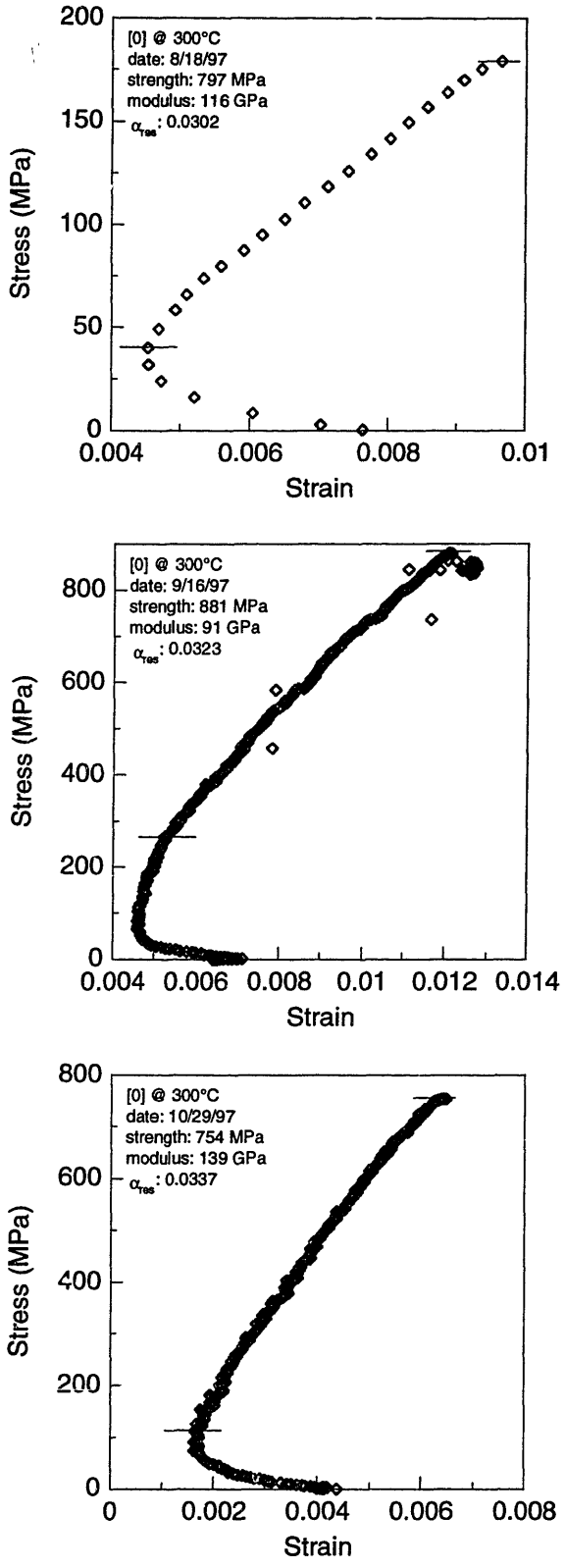

Figure D.16 Stress-strain data from at-temperature tests on $[0]_4$ coupons – nominal test temperature of 300°C.

Table D.4 Modulus and R-value data from residual tensile tests on $[0]_4$ coupons

Test Temperature (°C)	Test date	Modulus (GPa)	R-value of curve fit
150	8/27/97	140 141	0.9982 0.9997
150	9/22/97	135	0.9997
150	10/29/97	118	0.9999
200	8/29/97	99	0.9997
200	9/17/97	99 111	0.9997 0.9997
200	10/21/97	110	0.9998
250	8/25/97	168 165	0.9975 0.9994
250	8/28/97	113	0.9992
250	10/26/97	122	0.9994
300	9/15/97	122	0.9996
300	9/22/97	117 123	0.9989 0.9995
300	10/30/97	125	0.9995
350	9/20/97	77 94	0.9971 0.9983

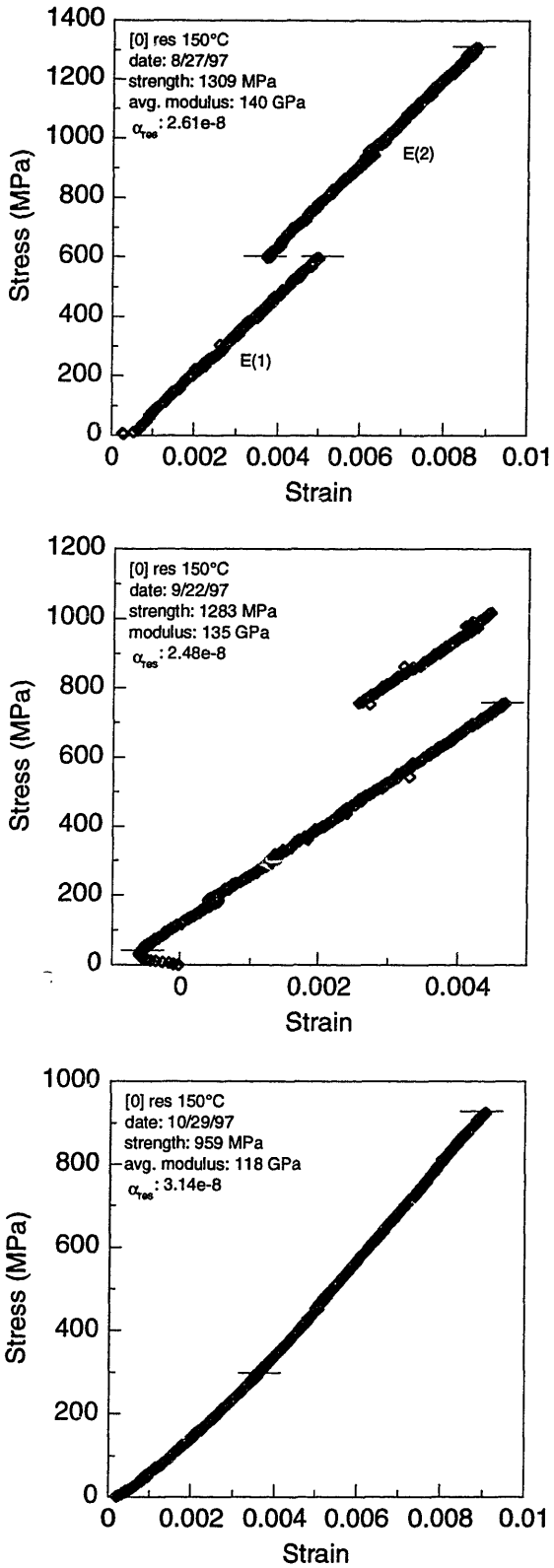

Figure D.17 Stress-strain data from residual tests on $[0]_4$ coupons – nominal test temperature of 150°C.

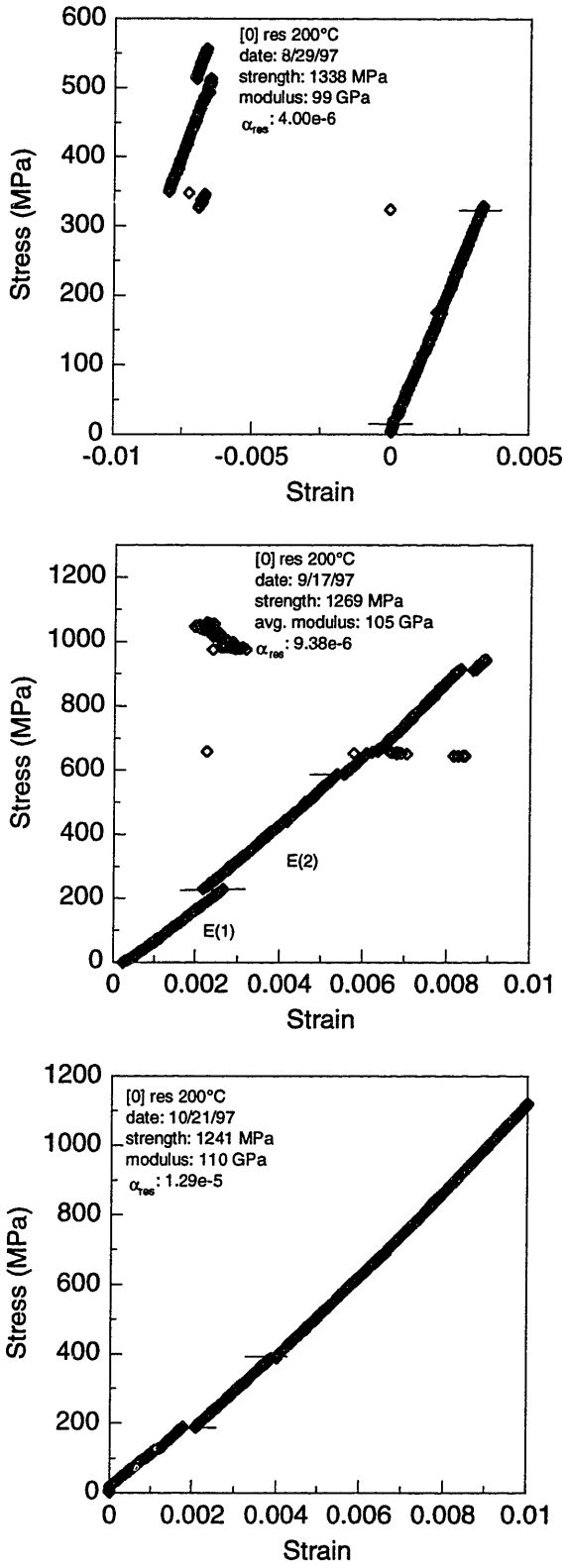

Figure D.18 Stress-strain data from residual tests on $[0]_4$ coupons – nominal test temperature of 200°C.

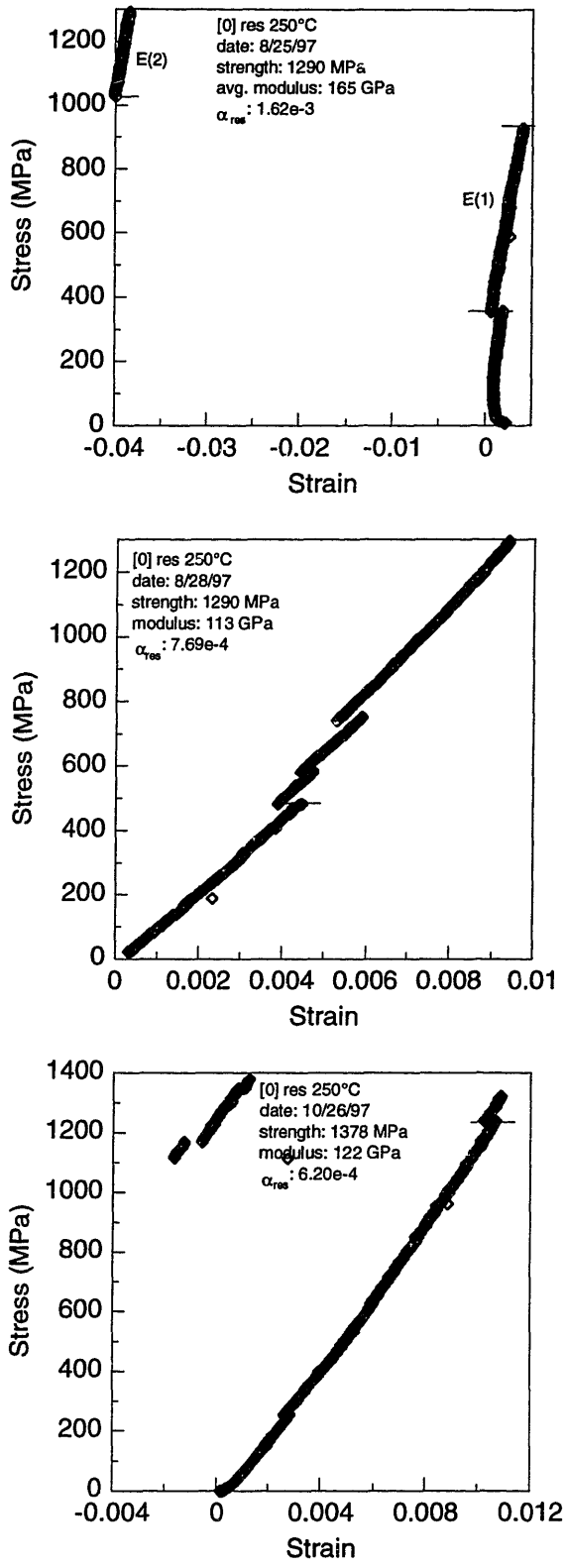

Figure D.19 Stress-strain data from residual tests on $[0]_4$ coupons – nominal test temperature of 250°C.

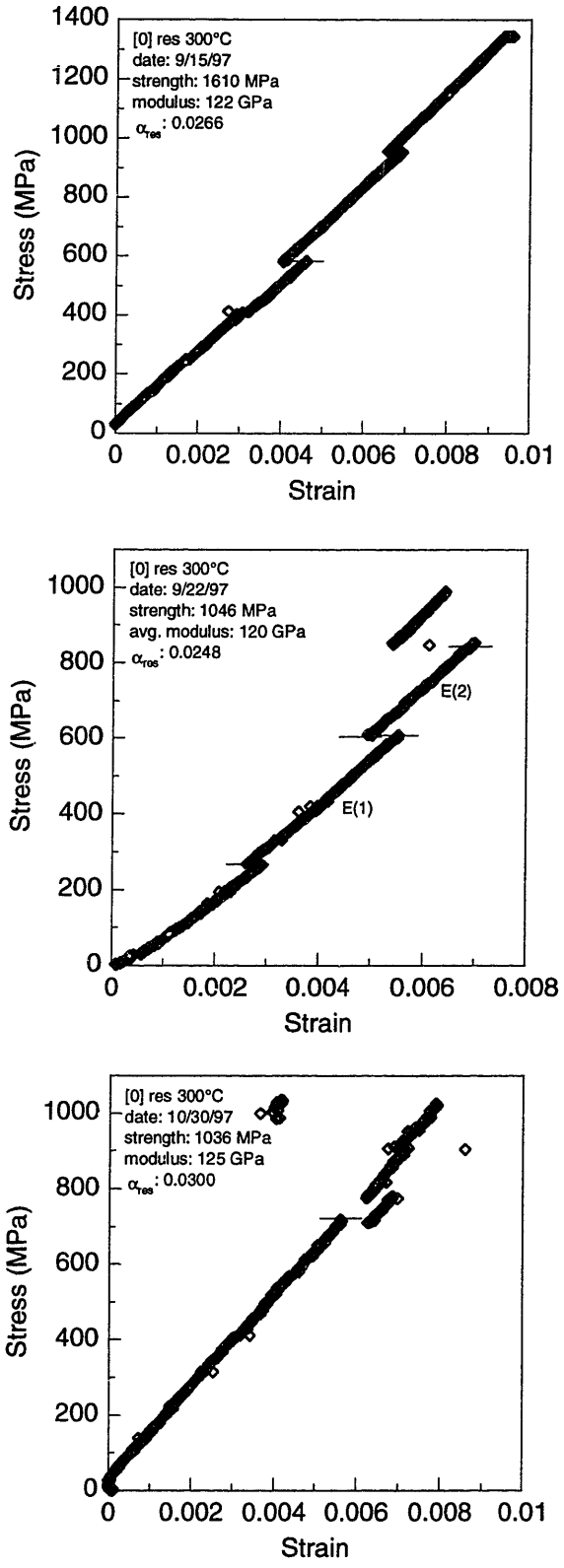

Figure D.20 Stress-strain data from residual tests on $[0]_4$ coupons – nominal test temperature of 300°C.

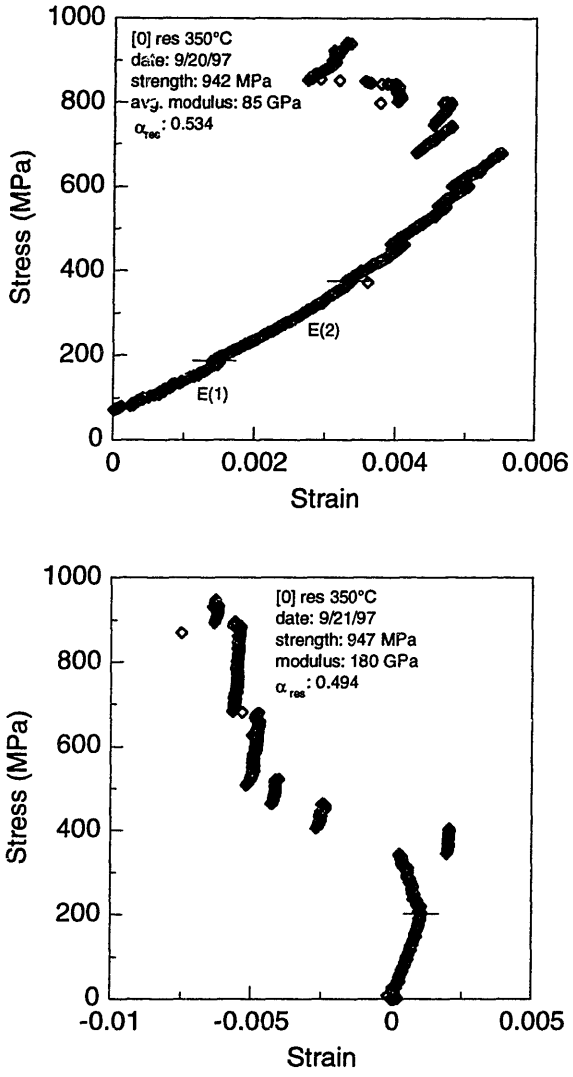

Figure D.21 Stress-strain data from residual tests on $[0]_4$ coupons – nominal test temperature of 350°C.

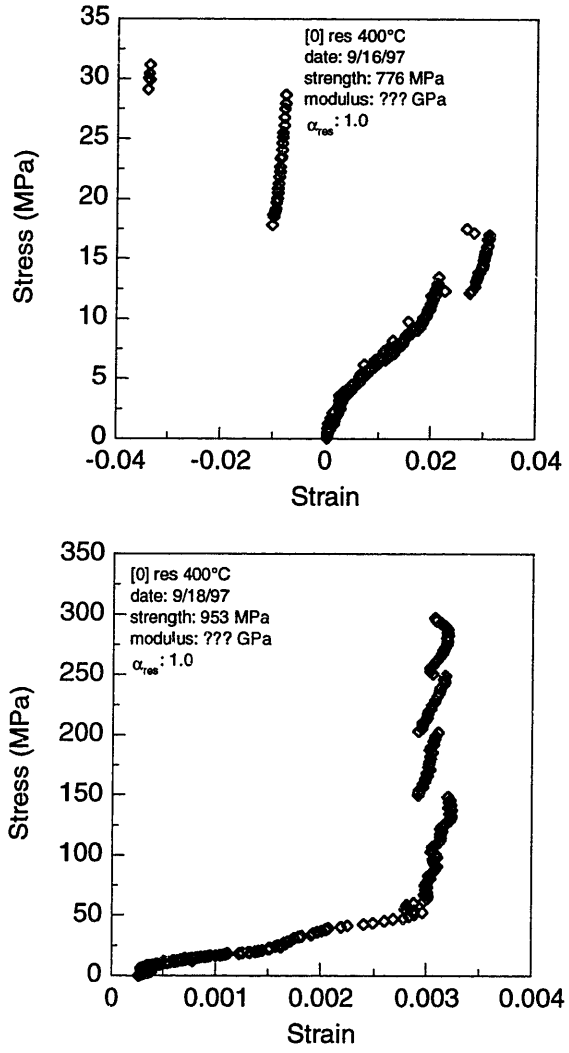

Figure D.22 Stress-strain data from residual tests on $[0]_4$ coupons – nominal test temperature of 400°C.

D.2 STRENGTH RESPONSE

Table D.5 Load and strength data from $[90]_{12}$ at-temperature coupons

Test Temperature (°C)	Test Date	Coupon Width (m)	Coupon Thickness (m)	Maximum Load (N)	Ultimate Stress (MPa)
25	8/8/97	0.05080	0.00182	1803	19.50
25	9/15/97	0.05170	0.00150	2328	30.02
25	9/22/97	0.05060	0.00157	2760	34.74
150	8/11/97	0.05060	0.00168	1942.4	22.85
150	9/21/97	0.05058	0.00169	1051.8	12.30
150	10/24/97	0.05030	0.00168	2596	30.72
150	10/30/97	0.05040	0.00145	2268.8	31.04
200	8/18/97	0.05096	0.00178	1163.7	12.83
200	8/28/97	0.05090	0.00159	809.4	10.00
200	10/26/97	0.04996	0.00174	558	6.42
200	10/27/97	0.05052	0.00158	1806	22.60
250	8/22/97	0.05200	0.00148	237.0	3.08
250	9/11/97	0.05140	0.00175	84.5	0.94
250	9/19/97	0.05140	0.00164	141.6	1.68
300	8/26/97	0.04960	0.00163	58.1	0.72
300	9/19/97	0.05130	0.00185	7.7	0.08
300	9/22/97	0.05100	0.00164	37.1	0.44

Table D.6 Load and strength data from $[90]_{12}$ residual coupons

Test Temperature (°C)	Test Date	Coupon Width (m)	Coupon Thickness (m)	Maximum Load (N)	Ultimate Stress (MPa)
150	8/29/97	0.04920	0.00156	2220	28.94
150	9/17/97	0.05110	0.00180	1973	21.45
150	10/26/97	0.05072	0.00163	2906	35.15
200	8/26/97	0.05010	0.00151	2214	29.30
200	8/29/97	0.05130	0.00147	1785	23.70
200	9/22/97	0.05102	0.00158	2128	26.40
250	8/19/97	0.05100	0.00181	2092	22.66
250	9/21/97	0.05088	0.00148	2488	33.04
250	10/26/97	0.05040	0.00178	2404	26.80
300	8/27/97	0.05070	0.00163	129	1.56
300	9/17/97	0.05130	0.00174	189	2.11
300	9/19/97	0.05080	0.00165	157	1.88
300	10/27/97	0.05050	0.00168	116	1.37

Table D.7 Load and strength data from $[0]_4$ at-temperature coupons

Test Temperature (°C)	Test Date	Coupon Width (m)	Coupon Thickness (m)	Maximum Load (N)	Ultimate Stress (MPa)
25	9/10/97	0.05053	0.00058	40,051	1366.6
25	9/21/97	0.0508	0.00063	44,036	1376.0
25	9/22/97	0.05098	0.00057	27,231	937.1
150	8/27/97	0.0513	0.00057	37,400	1280.0
150	9/21/97	0.05105	0.00048	32,539	1327.9
150	10/29/97 #1	0.0504	0.00061	34,813	1132.3
150	10/29/97 #2	0.0503	0.00057	25,590	892.6
200	8/20/97	0.0532	0.00056	34,142	1146.0
200	8/28/97	0.0510	0.00055	33,202	1183.7
200	9/10/97	0.05094	0.00052	34,160	1289.6
200	10/22/97	0.051	0.0064	37,600	1151.5
200	10/30/97	0.05016	0.00060	24,528	815.2
250	8/19/97	0.0510	0.00061	28,659	921.2
250	9/15/97	0.05105	0.00059	39,027	1295.7
250	9/18/97	0.0506	0.00056	34,381	1213.3
300	8/18/97	0.0509	0.00057	23,115	796.7
300	9/16/97	0.0510	0.00053	23,809	880.9
300	10/29/97	0.0500	0.00061	23,006	754.3
350	8/22/97	0.0507	0.00062	16,500	524.5
350	9/19/97	0.0513	0.00062	17,104	537.8
350	9/21/97	0.0510	0.00058	23,660	799.9
350	10/17/97	0.05046	0.00055	18,900	681.7
400	8/27/97	0.05086	0.00064	24,046	738.7
400	9/16/97	0.0508	0.00056	23,800	837.9
400	9/20/97	0.05076	0.00064	24,112	742.2

Table D.8 Load and strength data from $[0]_4$ residual coupons

Test Temperature (°C)	Test Date	Coupon Width (m)	Coupon Thickness (m)	Maximum Load (N)	Ultimate Stress (MPa)
150	8/27/97	0.05098	0.00060	40,040	1308.9
150	9/22/97	0.05090	0.00057	37,225	1283.0
150	10/29/97	0.05050	0.00064	30,989	958.8
200	8/29/97	0.05110	0.00067	45,803	1337.8
200	9/17/97	0.05130	0.00059	33,400	1268.7
200	10/21/97	0.05082	0.00064	40,400	1241.4
250	8/25/97	0.05180	0.00056	37,400	1290.0
250	8/28/97	0.05130	0.00062	41,200	1290.0
250	10/26/97	0.05048	0.00054	37,559	1377.9
300	8/25/97	0.05100	0.00057	29,985	1016.0
300	9/15/97	0.05130	0.00058	47,894	1609.7
300	9/22/97	0.05101	0.00058	30,946	1046.0
300	10/30/97	0.05045	0.00047	24,561	1035.8
350	8/26/97	0.05100	0.00058	28,600	967.4
350	9/20/97	0.05110	0.00064	30,804	941.9
350	9/21/97	0.05110	0.00051	24,689	947.3
400	8/19/97	0.05108	0.00061	28,012	899.0
400	9/16/97	0.05080	0.00070	27,589	775.8
400	9/18/97	0.05100	0.00059	28,666	952.7

APPENDIX E

CLASSICAL LAMINATED PLATE THEORY

A laminated plate made of a composite material is exposed to a high temperature environment while being loaded by mechanical forces and moments. The temperature and degradation state of the material may vary through the thickness of the laminate. It is necessary to determine the stress distribution in the laminate, taking into account effects related to hygrothermal expansion, degradation-induced shrinkage, and strains induced by changes in internal pressure. Classical laminated plate theory, modified to include all of these effects, forms the basis of the mechanical response model.

E.1 CLASSICAL LAMINATED PLATE THEORY

In the material coordinate system of a laminate made of an orthotropic material, the stresses $\{\sigma\}$ in each ply are related to the mechanical strains in the ply, $\{\varepsilon\}^{mech}$, through the matrix of reduced stiffnesses:

$$\{\sigma\} = [Q]\{\varepsilon\}^{mech} \tag{E.1}$$

where

$$\{Q\} = \begin{bmatrix} Q_{11} & Q_{12} & 0 \\ Q_{12} & Q_{22} & 0 \\ 0 & 0 & Q_{66} \end{bmatrix} \tag{E.2}$$

The elements of the $[\mathbf{Q}]$ matrix for each ply are determined from the unidirectional ply properties. Properties may vary with the temperature and degradation state of the ply:

$$Q_{11} = \frac{E_L(T,\alpha)}{1-\nu_{LT}(T,\alpha)\nu_{TL}(T,\alpha)} \qquad Q_{22} = \frac{E_T(T,\alpha)}{1-\nu_{LT}(T,\alpha)\nu_{TL}(T,\alpha)}$$
$$Q_{12} = \nu_{LT}(T,\alpha)Q_{22} \qquad Q_{66} = G_{LT}(T,\alpha) \tag{E.3}$$

If the ply is oriented at an angle θ to the structural coordinates, the stresses and strains in the ply coordinate system are related to the stresses and strains in the structural coordinate system (denoted with bars over the vectors) through the transformation vector [T]:

$$\{\sigma\} = [\mathbf{T}]\{\bar{\sigma}\} \tag{E.4}$$

$$\{\varepsilon\}^{mech} = [\mathbf{T}]^{-T}\{\bar{\varepsilon}\}^{mech} \tag{E.5}$$

where

$$[\mathbf{T}] = \begin{bmatrix} \cos^2\theta & \sin^2\theta & 2\sin\theta\cos\theta \\ \sin^2\theta & \cos^2\theta & -2\sin\theta\cos\theta \\ -\sin\theta\cos\theta & \sin\theta\cos\theta & \cos^2\theta - \sin^2\theta \end{bmatrix} \tag{E.6}$$

and

$$[\mathbf{T}]^{-T} = \begin{bmatrix} \cos^2\theta & \sin^2\theta & \sin\theta\cos\theta \\ \sin^2\theta & \cos^2\theta & -\sin\theta\cos\theta \\ -2\sin\theta\cos\theta & 2\sin\theta\cos\theta & \cos^2\theta - \sin^2\theta \end{bmatrix} \tag{E.7}$$

The relationship between stress and strain in structural coordinates can thus be expressed

$$\{\bar{\sigma}\} = [\bar{Q}]\{\bar{\varepsilon}\}^{mech} \tag{E.8}$$

$$[\bar{Q}] = [T]^{-1}[Q][T]^{-T} \tag{E.9}$$

The ply mechanical strains are one component of the total ply strains, $\{\bar{\varepsilon}\}$. Mechanical strains can be isolated by subtracting ply strains induced by temperature changes, moisture absorption, degradation, and internal pressure from the total strains:

$$\{\bar{\varepsilon}\}^{mech} = \{\bar{\varepsilon}\} - \{\bar{\alpha}\}\Delta T - \{\bar{\beta}\}M - \{\bar{\chi}\}\alpha - \{\bar{\lambda}\}P \tag{E.10}$$

The second term on the right-hand side of Equation E.10 is the thermally-induced strain in the ply. The vector $\{\bar{\alpha}\}$ is the set of coefficients of thermal expansion (strain/°C), rotated into structural coordinates, while ΔT is the change in temperature (°C) from the stress-free temperature. The vectors $\{\bar{\alpha}\}$and $\{\alpha\}$, written in boldface, denote thermal expansion coefficients in structural and ply coordinates, respectively. The degradation state variable, α, is written in regular type. The next term is the moisture-induced strain, followed by the degradation-induced strain term. The vector $\{\bar{\beta}\}$ contains coefficients of moisture expansion (strain/moisture fraction) and is multiplied by M, the moisture content of the laminate expressed as a fraction of the total laminate weight. The vector $\{\bar{\chi}\}$ contains char expansion coefficients (strain) and is multiplied by α, the dimensionless degradation state. The final term is the strain induced by internal pressure and includes the vector of pressure compliances, $\{\bar{\lambda}\}$ (strain/Pa), and P, the pressure in the laminate (Pa). The coefficient vectors are rotated from ply coordinates into structural coordinates in the same way that strains are rotated:

$$\begin{aligned} \{\bar{\alpha}\} &= [\mathbf{T}]^T\{\alpha\} \quad \text{(a)} & \{\bar{\beta}\} &= [\mathbf{T}]^T\{\beta\} \quad \text{(b)} \\ \{\bar{\chi}\} &= [\mathbf{T}]^T\{\chi\} \quad \text{(c)} & \{\bar{\lambda}\} &= [\mathbf{T}]^T\{\lambda\} \quad \text{(d)} \end{aligned} \tag{E.11}$$

Temperature, moisture content, degradation state, and pressure may vary through the thickness, i.e. in the z-direction. Additionally, the elements of the coefficient vectors may change with the temperature, T, and/or degradation state, α, of the material:

$$\begin{aligned} \Delta T &= \Delta T(z) \quad \text{(a)} & M &= M(z) \quad \text{(b)} \\ \alpha &= \alpha(z) \quad \text{(c)} & P &= P(z) \quad \text{(d)} \end{aligned} \tag{E.12}$$

$$\begin{aligned} \{\alpha\} &= \{\alpha(\alpha)\} \quad \text{(a)} & \{\beta\} &= \{\beta(T,\alpha)\} \quad \text{(b)} \\ \{\chi\} &= \{\chi(T)\} \quad \text{(c)} & \{\lambda\} &= \{\lambda(T,\alpha)\} \quad \text{(d)} \end{aligned} \tag{E.13}$$

The ply strains in the structural coordinate system are determined from the laminate mid-plane strains $\{\varepsilon^\circ\}$ and laminate curvatures $\{\kappa\}$:

$$\{\bar{\varepsilon}\} = \{\varepsilon^\circ\} + z\{\kappa\} \tag{E.14}$$

where z is the vertical distance from the center of the laminate to the center of the ply. Assembling Equations E.8, E.10, and E.14, it can be stated that:

$$\{\bar{\sigma}\} = [\bar{Q}]\{\varepsilon^\circ\} + z[\bar{Q}]\{\kappa\} - [\bar{Q}]\{\bar{\alpha}\}\Delta T - [\bar{Q}]\{\bar{\beta}\}M - [\bar{Q}]\{\bar{\chi}\}\Delta\alpha - [\bar{Q}]\{\bar{\lambda}\}P \tag{E.15}$$

Integrating all of the terms in Equation E.15 through the thickness, an expression for the resultant forces is obtained:

$$\int\{\bar{\sigma}\}dz = \begin{array}{l} \int[\bar{Q}]dz\{\varepsilon^\circ\} + \int[\bar{Q}]zdz\{\kappa\} - \int[\bar{Q}]\{\bar{\alpha}\}\Delta T dz - \\ \int[\bar{Q}]\{\bar{\beta}\}Mdz - \int[\bar{Q}]\{\bar{\chi}\}\alpha dz - \int[\bar{Q}]\{\bar{\lambda}\}Pdz \end{array} \tag{E.16}$$

Similarly, multiplying through by z and integrating through the thickness gives an expression for the resultant moments:

$$\int \{\bar{\sigma}\} z dz = \int [\bar{Q}] z dz \{\varepsilon^o\} + \int [\bar{Q}] z^2 dz \{\kappa\} - \int [\bar{Q}] \{\bar{\alpha}\} \Delta T z dz - \int [\bar{Q}] \{\bar{\beta}\} M z dz - \int [\bar{Q}] \{\bar{\chi}\} \alpha z dz - \int [\bar{Q}] \{\bar{\lambda}\} P z dz \quad \text{(E.17)}$$

Equations E.16 and E.17 can be rewritten in matrix form:

$$\begin{Bmatrix} \mathbf{N} \\ \mathbf{M} \end{Bmatrix} = \begin{bmatrix} \mathbf{A} & \mathbf{B} \\ \mathbf{B} & \mathbf{D} \end{bmatrix} \begin{Bmatrix} \boldsymbol{\varepsilon}^o \\ \boldsymbol{\kappa} \end{Bmatrix} - \begin{Bmatrix} \mathbf{N}^T \\ \mathbf{M}^T \end{Bmatrix} - \begin{Bmatrix} \mathbf{N}^H \\ \mathbf{M}^H \end{Bmatrix} - \begin{Bmatrix} \mathbf{N}^C \\ \mathbf{M}^C \end{Bmatrix} - \begin{Bmatrix} \mathbf{N}^P \\ \mathbf{M}^P \end{Bmatrix} \quad \text{(E.18)}$$

where $\{\mathbf{N}\}$ and $\{\mathbf{M}\}$ are the vectors of resultant forces and moments, respectively:

$$\{\mathbf{N}\} = \int \{\bar{\sigma}\} dz \qquad \{\mathbf{M}\} = \int \{\bar{\sigma}\} z dz \quad \text{(E.19)}$$

$[\mathbf{A}]$, $[\mathbf{B}]$, and $[\mathbf{D}]$ are the matrices of extensional stiffnesses, extension-bending coupling stiffnesses, and bending stiffnesses, respectively:

$$[\mathbf{A}] = \int [\bar{Q}] dz \quad \text{(a)} \qquad [\mathbf{B}] = \int [\bar{Q}] z dz \quad \text{(b)} \qquad [\mathbf{D}] = \int [\bar{Q}] z^2 dz \quad \text{(c)} \quad \text{(E.20)}$$

The last four terms on the right hand side of Equation E.18 are the resultant forces and moments induced by temperature (T), moisture (H), degradation (C), and pressure (P) effects:

$$\{\mathbf{N}^T\} = \int [\bar{Q}] \{\bar{\alpha}\} \Delta T dz \qquad \{\mathbf{M}^T\} = \int [\bar{Q}] \{\bar{\alpha}\} \Delta T z dz \quad \text{(E.21)}$$

$$\{\mathbf{N}^H\} = \int [\bar{Q}] \{\bar{\beta}\} M dz \qquad \{\mathbf{M}^H\} = \int [\bar{Q}] \{\bar{\beta}\} M z dz \quad \text{(E.22)}$$

$$\{\mathbf{N}^C\} = \int [\overline{\mathbf{Q}}]\{\overline{\chi}\}\alpha dz \qquad \{\mathbf{M}^C\} = \int [\overline{\mathbf{Q}}]\{\overline{\chi}\}\alpha z dz \tag{E.23}$$

$$\{\mathbf{N}^P\} = \int [\overline{\mathbf{Q}}]\{\overline{\lambda}\}P dz \qquad \{\mathbf{M}^P\} = \int [\overline{\mathbf{Q}}]\{\overline{\lambda}\}P z dz \tag{E.24}$$

Rearranging Equation E.18, an expression for the mid-plane strains and curvatures is obtained:

$$\begin{Bmatrix} \boldsymbol{\varepsilon}^o \\ \boldsymbol{\kappa} \end{Bmatrix} = \begin{bmatrix} \mathbf{A} & \mathbf{B} \\ \mathbf{B} & \mathbf{D} \end{bmatrix}^{-1} \begin{Bmatrix} \mathbf{N} + \mathbf{N}^T + \mathbf{N}^H + \mathbf{N}^C + \mathbf{N}^P \\ \mathbf{M} + \mathbf{M}^T + \mathbf{M}^H + \mathbf{M}^C + \mathbf{M}^P \end{Bmatrix} \tag{E.25}$$

Thus, given applied resultant forces and moments $\{\mathbf{N}\}$ and $\{\mathbf{M}\}$ and laminate conditions $\Delta T(z)$, $M(z)$, $\alpha(z)$, and $P(z)$, the mid-plane strains and curvatures can be determined from Equation E.25. Stresses in each ply can then be calculated from Equation E.15.

E.2 DISCRETIZED MODEL

The laminate under consideration can be discretized into N nodes through the thickness. Each node i is located in a ply with angle θ_i, rotated stiffness matrix $[\overline{\mathbf{Q}}]_i$ and coefficient vectors $\{\alpha\}_i$, $\{\beta\}_i$, $\{\chi\}_i$, and $\{\lambda\}_i$. The top and bottom of the element associated with node i are located at z_i^+ and z_i^-, respectively, measured from the center line of the laminate. This geometry is illustrated in Figure E.1. The temperature and degradation state of the material may vary with i, but are assumed to be constant within each element. Furthermore, the material stiffnesses and other properties may vary with temperature and degradation state, hence they also vary with i.

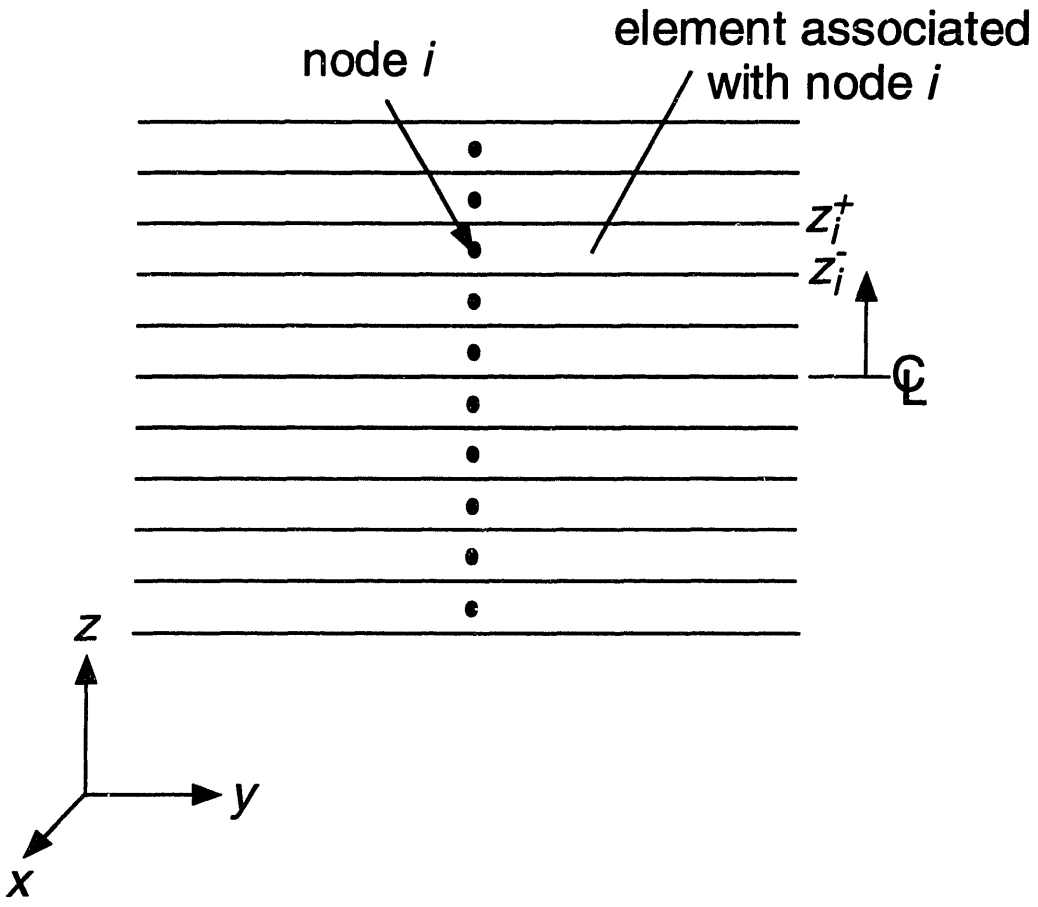

Figure E.E.1 Boundaries of element associated with node i

The expression relating ply stresses to laminate strains and curvatures and strains induced by thermal effects, etc., can be written in discretized form as follows:

$$\{\bar{\sigma}\}_i = [\bar{Q}]_i\{\varepsilon^o\} + \left(\frac{z_i^+ + z_i^-}{2}\right)[\bar{Q}]_i\{\kappa\} - [\bar{Q}]_i\{\alpha\}_i \Delta T_i \\ [\bar{Q}]_i\{\bar{\beta}\}_i M_i - [\bar{Q}]_i\{\bar{\chi}\}_i \alpha_i - [\bar{Q}]_i\{\bar{\lambda}\}_i P_i \tag{E.26}$$

Summing through the thickness, the following relations can be obtained:

$$\begin{Bmatrix} \mathbf{N} \\ \mathbf{M} \end{Bmatrix} = \begin{bmatrix} \mathbf{A} & \mathbf{B} \\ \mathbf{B} & \mathbf{D} \end{bmatrix} \begin{Bmatrix} \boldsymbol{\varepsilon}^o \\ \boldsymbol{\kappa} \end{Bmatrix} - \begin{Bmatrix} \mathbf{N}^T \\ \mathbf{M}^T \end{Bmatrix} - \begin{Bmatrix} \mathbf{N}^H \\ \mathbf{M}^H \end{Bmatrix} - \begin{Bmatrix} \mathbf{N}^C \\ \mathbf{M}^C \end{Bmatrix} - \begin{Bmatrix} \mathbf{N}^P \\ \mathbf{M}^P \end{Bmatrix} \tag{E.27}$$

The elements of Equation E.27 are written in discretized form as follows. The extensional stiffnesses, extension-bending coupling stiffnesses, and bending stiffnesses can be expressed as

$$[\mathbf{A}] = \sum_{i=1}^{N} [\bar{Q}]_i \left[z_i^+ - z_i^-\right] \tag{E.28}$$

$$[\mathbf{B}] = \frac{1}{2}\sum_{i=1}^{N} [\bar{Q}]_i \left[\left(z_i^+\right)^2 - \left(z_i^-\right)^2\right] \tag{E.29}$$

$$[\mathbf{D}] = \frac{1}{3}\sum_{i=1}^{N} [\bar{Q}]_i \left[\left(z_i^+\right)^3 - \left(z_i^-\right)^3\right] \tag{E.30}$$

The forces and moments induced by effects due to temperature, moisture, degradation, and pressure are written:

$$\{\mathbf{N}^T\} = \sum_{i=1}^{N} [\bar{Q}]_i \{\bar{\alpha}\}_i \Delta T_i \left(z_i^+ - z_i^-\right) \qquad \{\mathbf{M}^T\} = \sum_{i=1}^{N} [\bar{Q}]_i \{\bar{\alpha}\}_i \Delta T_i \left[\left(z_i^+\right)^2 - \left(z_i^-\right)^2\right] \tag{E.31}$$

$$\{\mathbf{N}^{\mathrm{H}}\}=\sum_{i=1}^{N}[\overline{\mathbf{Q}}]_i\{\overline{\boldsymbol{\beta}}\}_i M_i\left(z_i^+-z_i^-\right) \qquad \{\mathbf{M}^{\mathrm{H}}\}=\sum_{i=1}^{N}[\overline{\mathbf{Q}}]_i\{\overline{\boldsymbol{\beta}}\}_i M_i\left[\left(z_i^+\right)^2-\left(z_i^-\right)^2\right] \quad \text{(E.32)}$$

$$\{\mathbf{N}^{\mathrm{C}}\}=\sum_{i=1}^{N}[\overline{\mathbf{Q}}]_i\{\overline{\boldsymbol{\chi}}\}_i \alpha_i\left(z_i^+-z_i^-\right) \qquad \{\mathbf{M}^{\mathrm{C}}\}=\sum_{i=1}^{N}[\overline{\mathbf{Q}}]_i\{\overline{\boldsymbol{\chi}}\}_i \alpha_i\left[\left(z_i^+\right)^2-\left(z_i^-\right)^2\right] \quad \text{(E.33)}$$

$$\{\mathbf{N}^{\mathrm{P}}\}=\sum_{i=1}^{N}[\overline{\mathbf{Q}}]_i\{\overline{\boldsymbol{\lambda}}\}_i P_i\left(z_i^+-z_i^-\right) \qquad \{\mathbf{M}^{\mathrm{P}}\}=\sum_{i=1}^{N}[\overline{\mathbf{Q}}]_i\{\overline{\boldsymbol{\lambda}}\}_i P_i\left[\left(z_i^+\right)^2-\left(z_i^-\right)^2\right] \quad \text{(E.34)}$$

Rearranging Equation E.27, the following stress-strain relation is obtained:

$$\begin{Bmatrix}\boldsymbol{\varepsilon}^{\mathrm{o}}\\ \boldsymbol{\kappa}\end{Bmatrix}=\begin{bmatrix}\mathbf{A} & \mathbf{B}\\ \mathbf{B} & \mathbf{D}\end{bmatrix}^{-1}\begin{Bmatrix}\mathbf{N}+\mathbf{N}^{\mathrm{T}}+\mathbf{N}^{\mathrm{H}}+\mathbf{N}^{\mathrm{C}}+\mathbf{N}^{\mathrm{P}}\\ \mathbf{M}+\mathbf{M}^{\mathrm{T}}+\mathbf{M}^{\mathrm{H}}+\mathbf{M}^{\mathrm{C}}+\mathbf{M}^{\mathrm{P}}\end{Bmatrix} \quad \text{(E.35)}$$

Given applied forces and moments $\{\mathbf{N}\}$ and $\{\mathbf{M}\}$ and laminate conditions ΔT_i, M_i, α_i, and P_i, the mid-plane strains and curvatures are determined from Equation 4.93. Stresses in each element are then calculated from Equation E.26.

E.3 EVALUATION OF STRENGTH FRACTIONS

The determination of failure is not part of classical laminated plate theory, but a brief discussion of the calculation of strength fractions is included for completeness. The strength fraction is defined here as the ratio of the ply stresses calculated using Equation E.15 to the extensional and shear strengths of the ply. Calculations are based on the maximum stress failure criterion [59]. As the stresses approach the strengths, the strength fractions approach 1. Strength fractions are calculated as follows:

$$R_{xx} = \begin{cases} \dfrac{\sigma_{11}}{X^t(T,\alpha)} & \sigma_{11} > 0 \\ \dfrac{-\sigma_{11}}{X^c(T,\alpha)} & \sigma_{11} < 0 \end{cases} \tag{E.36}$$

$$R_{yy} = \begin{cases} \dfrac{\sigma_{22}}{Y^t(T,\alpha)} & \sigma_{22} > 0 \\ \dfrac{-\sigma_{22}}{Y^c(T,\alpha)} & \sigma_{22} < 0 \end{cases} \tag{E.37}$$

$$R_{xy} = \frac{|\sigma_{12}|}{S(T,\alpha)} \tag{E.38}$$

where X^t is the longitudinal tensile strength; X^c, the longitudinal compressive strength; Y^t, the transverse tensile strength; Y^c, the transverse compressive strength; and S, the shear strength of the ply. Like the stiffnesses and other material properties, the strengths may vary with the temperature and degradation state of the material.

When the structure is discretized as described in Section E.2, the strength fractions at each node i are determined as follows. Material strengths may vary with i:

$$(R_{xx})_i = \begin{cases} \dfrac{(\sigma_{11})_i}{(X^t)_i} & (\sigma_{11})_i > 0 \\ \dfrac{-(\sigma_{11})_i}{(X^c)_i} & (\sigma_{11})_i < 0 \end{cases} \tag{E.39}$$

$$(R_{yy})_i = \begin{cases} \dfrac{(\sigma_{22})_i}{(Y^t)_i} & (\sigma_{22})_i > 0 \\ \dfrac{-(\sigma_{22})_i}{(Y^c)_i} & (\sigma_{22})_i < 0 \end{cases} \tag{E.40}$$

$$(R_{xy})_i = \frac{|(\sigma_{12})_i|}{S_i} \tag{E.41}$$

APPENDIX F

AS4/3501-6 MATERIAL PROPERTY FILE

Following is a complete annotated listing of the AS4/3501-6 material property data file developed for use with CHARplus.

```
*************************************************************************
 ************************C  H  A  R  P  L  U  S************************
 *************************************************************************

 ************************  MATERIAL  PROPERTIES  ************************

 SOLID MATERIAL PROPERTIES FILE NAME = MAT.AS435016

 SOLID DENSITY  = 1.560E+03
 CHAR DENSITY   = 1.250E+03

 SOLID POROSITY = 1.000E-02
 CHAR  POROSITY = 3.300E-01

 SURFACE ABSORPTIVITY  = 5.300E-01
 SURFACE EMISSIVITY    = 5.300E-01


 NUMBER OF CHAR VOLUMES AT WHICH PERMEABILITIES ARE SPECIFIED = 11

 PERMEABILITIES OF UNDAMAGED MATERIAL-

   CHAR VOLUME        X           Y           Z
      0.000       5.000E-18   9.100E-18   3.900E-14
      0.100       5.800E-18   1.300E-17   3.900E-14
      0.200       1.500E-17   1.500E-17   3.900E-14
      0.300       3.900E-17   3.900E-17   3.900E-14
      0.400       1.120E-16   1.120E-16   3.900E-14
      0.500       3.200E-16   3.200E-16   3.900E-14
      0.600       9.400E-16   9.400E-16   3.900E-14
      0.700       2.700E-15   2.700E-15   3.900E-14
      0.800       7.800E-15   7.800E-15   3.900E-14
      0.900       2.300E-14   2.300E-14   3.900E-14
      1.000       6.500E-14   6.500E-14   3.900E-14

 PERMEABILITIES OF DAMAGED MATERIAL-

   CHAR VOLUME        X           Y           Z
      0.000       1.000E+00   1.000E+00   1.000E+00
      0.100       1.000E+00   1.000E+00   1.000E+00
      0.200       1.000E+00   1.000E+00   1.000E+00
      0.300       1.000E+00   1.000E+00   1.000E+00
      0.400       1.000E+00   1.000E+00   1.000E+00
      0.500       1.000E+00   1.000E+00   1.000E+00
      0.600       1.000E+00   1.000E+00   1.000E+00
      0.700       1.000E+00   1.000E+00   1.000E+00
```

0.800	1.000E+00	1.000E+00	1.000E+00
0.900	1.000E+00	1.000E+00	1.000E+00
1.000	1.000E+00	1.000E+00	1.000E+00

NUMBER OF CHAR VOLUMES AT WHICH CONDUCTITIES ARE SPECIFIED = 2
NUMBER OF TEMPERATURES AT WHICH CONDUCTITIES ARE SPECIFIED = 2

CONDUCTIVITIES OF UNDAMAGED MATERIAL-

CHAR VOLUME = 0.000E+00

TEMPERATURE	X	Y	Z
273.000	6.300E+00	7.000E-01	7.000E-01
3000.000	6.300E+00	7.000E-01	7.000E-01

CHAR VOLUME = 1.000E+00

TEMPERATURE	X	Y	Z
273.000	6.300E+00	2.000E-01	2.000E-01
3000.000	6.300E+00	2.000E-01	2.000E-01

CONDUCTIVITIES OF DAMAGED MATERIAL-

CHAR VOLUME = 0.000E+00

TEMPERATURE	X	Y	Z
273.000	6.300E+00	7.000E-01	7.000E-01
3000.000	6.300E+00	7.000E-01	7.000E-01

CHAR VOLUME = 1.000E+00

TEMPERATURE	X	Y	Z
273.000	6.300E+00	2.000E-01	2.000E-01
3000.000	6.300E+00	2.000E-01	2.000E-01

NUMBER OF TEMPERATURES AT WHICH SOLID AND
CHAR SPECIFIC HEATS ARE SPECIFIED = 2

SOLID AND CHAR SPECIFIC HEATS-

TEMPERATURE	SOLID	CHAR
273.000	1.8000E+03	1.8000E+03
3000.000	1.8000E+03	1.8000E+03

NUMBER OF CHAR VOLUMES AT WHICH MECHANICAL
PROPERTIES ARE SPECIFIED = 6
NUMBER OF TEMPERATURES AT WHICH MECHANICAL
PROPERTIES ARE SPECIFIED = 8

YOUNG'S MODULI OF UNDAMAGED MATERIAL-

CHAR VOLUME = 0.000E+00

TEMPERATURE	X	Y	Z
273.000	1.250E+11	8.400E+09	8.400E+09
298.000	1.250E+11	8.400E+09	8.400E+09
423.000	1.250E+11	8.400E+09	8.400E+09
473.000	1.250E+11	5.500E+09	5.500E+09
523.000	1.250E+11	1.000E+09	1.000E+09
573.000	1.250E+11	1.000E+08	1.000E+08
623.000	1.250E+11	1.000E+08	1.000E+08
3273.000	1.250E+11	1.000E+08	1.000E+08

CHAR VOLUME = 5.000E-08

TEMPERATURE	X	Y	Z
273.000	1.250E+11	8.400E+09	8.400E+09
298.000	1.250E+11	8.400E+09	8.400E+09
423.000	1.250E+11	8.400E+09	8.400E+09

473.000	1.250E+11	5.500E+09	5.500E+09
523.000	1.250E+11	1.000E+09	1.000E+09
573.000	1.250E+11	1.000E+08	1.000E+08
623.000	1.250E+11	1.000E+08	1.000E+08
3273.000	1.250E+11	1.000E+08	1.000E+08

CHAR VOLUME = 1.000E-05

TEMPERATURE	X	Y	Z
273.000	1.250E+11	8.400E+09	8.400E+09
298.000	1.250E+11	8.400E+09	8.400E+09
423.000	1.250E+11	8.400E+09	8.400E+09
473.000	1.250E+11	5.500E+09	5.500E+09
523.000	1.250E+11	1.000E+09	1.000E+09
573.000	1.250E+11	1.000E+08	1.000E+08
623.000	1.250E+11	1.000E+08	1.000E+08
3273.000	1.250E+11	1.000E+08	1.000E+08

CHAR VOLUME = 1.000E-03

TEMPERATURE	X	Y	Z
273.000	1.250E+11	8.000E+09	8.000E+09
298.000	1.250E+11	8.000E+09	8.000E+09
423.000	1.250E+11	8.000E+09	8.000E+09
473.000	1.250E+11	5.000E+09	5.000E+09
523.000	1.250E+11	8.000E+08	8.000E+08
573.000	1.250E+11	1.000E+08	1.000E+08
623.000	1.250E+11	1.000E+08	1.000E+08
3273.000	1.250E+11	1.000E+08	1.000E+08

CHAR VOLUME = 3.000E-02

TEMPERATURE	X	Y	Z
273.000	1.250E+11	5.800E+09	5.800E+09
298.000	1.250E+11	5.800E+09	5.800E+09
423.000	1.250E+11	5.800E+09	5.800E+09
473.000	1.250E+11	4.000E+09	4.000E+09
523.000	1.250E+11	4.000E+08	4.000E+08
573.000	1.250E+11	1.000E+08	1.000E+08
623.000	1.250E+11	1.000E+08	1.000E+08
3273.000	1.250E+11	1.000E+08	1.000E+08

CHAR VOLUME = 1.000E+00

TEMPERATURE	X	Y	Z
273.000	1.000E+11	1.000E+08	1.000E+08
298.000	1.000E+11	1.000E+08	1.000E+08
423.000	1.000E+11	1.000E+08	1.000E+08
473.000	1.000E+11	1.000E+08	1.000E+08
523.000	1.000E+11	1.000E+08	1.000E+08
573.000	1.000E+11	1.000E+08	1.000E+08
623.000	1.000E+11	1.000E+08	1.000E+08
3273.000	1.000E+11	1.000E+08	1.000E+08

YOUNG'S MODULI OF DAMAGED MATERIAL-

CHAR VOLUME = 0.000E+00

TEMPERATURE	X	Y	Z
273.000	1.250E+11	8.400E+09	8.400E+09
298.000	1.250E+11	8.400E+09	8.400E+09
423.000	1.250E+11	8.400E+09	8.400E+09
473.000	1.250E+11	5.500E+09	5.500E+09
523.000	1.250E+11	1.000E+09	1.000E+09
573.000	1.250E+11	1.000E+08	1.000E+08
623.000	1.250E+11	1.000E+08	1.000E+08
3273.000	1.250E+11	1.000E+08	1.000E+08

CHAR VOLUME = 5.000E-08

TEMPERATURE	X	Y	Z
273.000	1.250E+11	8.400E+09	8.400E+09
298.000	1.250E+11	8.400E+09	8.400E+09
423.000	1.250E+11	8.400E+09	8.400E+09
473.000	1.250E+11	5.500E+09	5.500E+09
523.000	1.250E+11	1.000E+09	1.000E+09
573.000	1.250E+11	1.000E+08	1.000E+08
623.000	1.250E+11	1.000E+08	1.000E+08
3273.000	1.250E+11	1.000E+08	1.000E+08

CHAR VOLUME = 1.000E-05

TEMPERATURE	X	Y	Z
273.000	1.250E+11	8.400E+09	8.400E+09
298.000	1.250E+11	8.400E+09	8.400E+09
423.000	1.250E+11	8.400E+09	8.400E+09
473.000	1.250E+11	5.500E+09	5.500E+09
523.000	1.250E+11	1.000E+09	1.000E+09
573.000	1.250E+11	1.000E+08	1.000E+08
623.000	1.250E+11	1.000E+08	1.000E+08
3273.000	1.250E+11	1.000E+08	1.000E+08

CHAR VOLUME = 1.000E-03

TEMPERATURE	X	Y	Z
273.000	1.250E+11	8.000E+09	8.000E+09
298.000	1.250E+11	8.000E+09	8.000E+09
423.000	1.250E+11	8.000E+09	8.000E+09
473.000	1.250E+11	5.000E+09	5.000E+09
523.000	1.250E+11	8.000E+08	8.000E+08
573.000	1.250E+11	1.000E+08	1.000E+08
623.000	1.250E+11	1.000E+08	1.000E+08
3273.000	1.250E+11	1.000E+08	1.000E+08

CHAR VOLUME = 3.000E-02

TEMPERATURE	X	Y	Z
273.000	1.250E+11	5.800E+09	5.800E+09
298.000	1.250E+11	5.800E+09	5.800E+09
423.000	1.250E+11	5.800E+09	5.800E+09
473.000	1.250E+11	4.000E+09	4.000E+09
523.000	1.250E+11	4.000E+08	4.000E+08
573.000	1.250E+11	1.000E+08	1.000E+08
623.000	1.250E+11	1.000E+08	1.000E+08
3273.000	1.250E+11	1.000E+08	1.000E+08

CHAR VOLUME = 1.000E+00

TEMPERATURE	X	Y	Z
273.000	1.000E+11	1.000E+08	1.000E+08
298.000	1.000E+11	1.000E+08	1.000E+08
423.000	1.000E+11	1.000E+08	1.000E+08
473.000	1.000E+11	1.000E+08	1.000E+08
523.000	1.000E+11	1.000E+08	1.000E+08
573.000	1.000E+11	1.000E+08	1.000E+08
623.000	1.000E+11	1.000E+08	1.000E+08
3273.000	1.000E+11	1.000E+08	1.000E+08

POISSON'S RATIOS OF UNDAMAGED MATERIAL-

CHAR VOLUME = 0.000E+00

TEMPERATURE	XY	XZ	YZ
273.000	3.000E-01	3.000E-01	3.000E-01
298.000	3.000E-01	3.000E-01	3.000E-01
423.000	3.000E-01	3.000E-01	3.000E-01
473.000	3.000E-01	3.000E-01	3.000E-01

523.000	3.000E-01	3.000E-01	3.000E-01
573.000	3.000E-01	3.000E-01	3.000E-01
623.000	3.000E-01	3.000E-01	3.000E-01
3273.000	3.000E-01	3.000E-01	3.000E-01

CHAR VOLUME = 5.000E-08

TEMPERATURE	XY	XZ	YZ
273.000	3.000E-01	3.000E-01	3.000E-01
298.000	3.000E-01	3.000E-01	3.000E-01
423.000	3.000E-01	3.000E-01	3.000E-01
473.000	3.000E-01	3.000E-01	3.000E-01
523.000	3.000E-01	3.000E-01	3.000E-01
573.000	3.000E-01	3.000E-01	3.000E-01
623.000	3.000E-01	3.000E-01	3.000E-01
3273.000	3.000E-01	3.000E-01	3.000E-01

CHAR VOLUME = 1.000E-05

TEMPERATURE	XY	XZ	YZ
273.000	3.000E-01	3.000E-01	3.000E-01
298.000	3.000E-01	3.000E-01	3.000E-01
423.000	3.000E-01	3.000E-01	3.000E-01
473.000	3.000E-01	3.000E-01	3.000E-01
523.000	3.000E-01	3.000E-01	3.000E-01
573.000	3.000E-01	3.000E-01	3.000E-01
623.000	3.000E-01	3.000E-01	3.000E-01
3273.000	3.000E-01	3.000E-01	3.000E-01

CHAR VOLUME = 1.000E-03

TEMPERATURE	XY	XZ	YZ
273.000	3.000E-01	3.000E-01	3.000E-01
298.000	3.000E-01	3.000E-01	3.000E-01
423.000	3.000E-01	3.000E-01	3.000E-01
473.000	3.000E-01	3.000E-01	3.000E-01
523.000	3.000E-01	3.000E-01	3.000E-01
573.000	3.000E-01	3.000E-01	3.000E-01
623.000	3.000E-01	3.000E-01	3.000E-01
3273.000	3.000E-01	3.000E-01	3.000E-01

CHAR VOLUME = 3.000E-02

TEMPERATURE	XY	XZ	YZ
273.000	3.000E-01	3.000E-01	3.000E-01
298.000	3.000E-01	3.000E-01	3.000E-01
423.000	3.000E-01	3.000E-01	3.000E-01
473.000	3.000E-01	3.000E-01	3.000E-01
523.000	3.000E-01	3.000E-01	3.000E-01
573.000	3.000E-01	3.000E-01	3.000E-01
623.000	3.000E-01	3.000E-01	3.000E-01
3273.000	3.000E-01	3.000E-01	3.000E-01

CHAR VOLUME = 1.000E+00

TEMPERATURE	XY	XZ	YZ
273.000	3.000E-01	3.000E-01	3.000E-01
298.000	3.000E-01	3.000E-01	3.000E-01
423.000	3.000E-01	3.000E-01	3.000E-01
473.000	3.000E-01	3.000E-01	3.000E-01
523.000	3.000E-01	3.000E-01	3.000E-01
573.000	3.000E-01	3.000E-01	3.000E-01
623.000	3.000E-01	3.000E-01	3.000E-01
3273.000	3.000E-01	3.000E-01	3.000E-01

POISSON'S RATIOS OF DAMAGED MATERIAL-

CHAR VOLUME = 0.000E+00

TEMPERATURE	XY	XZ	YZ
273.000	3.000E-01	3.000E-01	3.000E-01
298.000	3.000E-01	3.000E-01	3.000E-01
423.000	3.000E-01	3.000E-01	3.000E-01
473.000	3.000E-01	3.000E-01	3.000E-01
523.000	3.000E-01	3.000E-01	3.000E-01
573.000	3.000E-01	3.000E-01	3.000E-01
623.000	3.000E-01	3.000E-01	3.000E-01
3273.000	3.000E-01	3.000E-01	3.000E-01

CHAR VOLUME = 5.000E-08

TEMPERATURE	XY	XZ	YZ
273.000	3.000E-01	3.000E-01	3.000E-01
298.000	3.000E-01	3.000E-01	3.000E-01
423.000	3.000E-01	3.000E-01	3.000E-01
473.000	3.000E-01	3.000E-01	3.000E-01
523.000	3.000E-01	3.000E-01	3.000E-01
573.000	3.000E-01	3.000E-01	3.000E-01
623.000	3.000E-01	3.000E-01	3.000E-01
3273.000	3.000E-01	3.000E-01	3.000E-01

CHAR VOLUME = 1.000E-05

TEMPERATURE	XY	XZ	YZ
273.000	3.000E-01	3.000E-01	3.000E-01
298.000	3.000E-01	3.000E-01	3.000E-01
423.000	3.000E-01	3.000E-01	3.000E-01
473.000	3.000E-01	3.000E-01	3.000E-01
523.000	3.000E-01	3.000E-01	3.000E-01
573.000	3.000E-01	3.000E-01	3.000E-01
623.000	3.000E-01	3.000E-01	3.000E-01
3273.000	3.000E-01	3.000E-01	3.000E-01

CHAR VOLUME = 1.000E-03

TEMPERATURE	XY	XZ	YZ
273.000	3.000E-01	3.000E-01	3.000E-01
298.000	3.000E-01	3.000E-01	3.000E-01
423.000	3.000E-01	3.000E-01	3.000E-01
473.000	3.000E-01	3.000E-01	3.000E-01
523.000	3.000E-01	3.000E-01	3.000E-01
573.000	3.000E-01	3.000E-01	3.000E-01
623.000	3.000E-01	3.000E-01	3.000E-01
3273.000	3.000E-01	3.000E-01	3.000E-01

CHAR VOLUME = 3.000E-02

TEMPERATURE	XY	XZ	YZ
273.000	3.000E-01	3.000E-01	3.000E-01
298.000	3.000E-01	3.000E-01	3.000E-01
423.000	3.000E-01	3.000E-01	3.000E-01
473.000	3.000E-01	3.000E-01	3.000E-01
523.000	3.000E-01	3.000E-01	3.000E-01
573.000	3.000E-01	3.000E-01	3.000E-01
623.000	3.000E-01	3.000E-01	3.000E-01
3273.000	3.000E-01	3.000E-01	3.000E-01

CHAR VOLUME = 1.000E+00

TEMPERATURE	XY	XZ	YZ
273.000	3.000E-01	3.000E-01	3.000E-01
298.000	3.000E-01	3.000E-01	3.000E-01
423.000	3.000E-01	3.000E-01	3.000E-01
473.000	3.000E-01	3.000E-01	3.000E-01
523.000	3.000E-01	3.000E-01	3.000E-01
573.000	3.000E-01	3.000E-01	3.000E-01
623.000	3.000E-01	3.000E-01	3.000E-01

3273.000	3.000E-01	3.000E-01	3.000E-01

SHEAR MODULI OF UNDAMAGED MATERIAL-

CHAR VOLUME = 0.000E+00

TEMPERATURE	XY	XZ	YZ
273.000	6.000E+09	3.800E+09	6.000E+09
298.000	6.000E+09	3.800E+09	6.000E+09
423.000	6.000E+09	3.800E+09	6.000E+09
473.000	3.900E+09	2.500E+09	3.900E+09
523.000	7.100E+08	4.500E+08	7.100E+08
573.000	7.100E+07	4.500E+07	7.100E+07
623.000	7.100E+07	4.500E+07	7.100E+07
3273.000	7.100E+07	4.500E+07	7.100E+07

CHAR VOLUME = 5.000E-08

TEMPERATURE	XY	XZ	YZ
273.000	6.000E+09	3.800E+09	6.000E+09
298.000	6.000E+09	3.800E+09	6.000E+09
423.000	6.000E+09	3.800E+09	6.000E+09
473.000	3.900E+09	2.500E+09	3.900E+09
523.000	7.100E+08	4.500E+08	7.100E+08
573.000	7.100E+07	4.500E+07	7.100E+07
623.000	7.100E+07	4.500E+07	7.100E+07
3273.000	7.100E+07	4.500E+07	7.100E+07

CHAR VOLUME = 1.000E-05

TEMPERATURE	XY	XZ	YZ
273.000	6.000E+09	3.800E+09	6.000E+09
298.000	6.000E+09	3.800E+09	6.000E+09
423.000	6.000E+09	3.800E+09	6.000E+09
473.000	3.900E+09	2.500E+09	3.900E+09
523.000	7.100E+08	4.500E+08	7.100E+08
573.000	7.100E+07	4.500E+07	7.100E+07
623.000	7.100E+07	4.500E+07	7.100E+07
3273.000	7.100E+07	4.500E+07	7.100E+07

CHAR VOLUME = 1.000E-03

TEMPERATURE	XY	XZ	YZ
273.000	5.700E+09	3.600E+09	5.700E+09
298.000	5.700E+09	3.600E+09	5.700E+09
423.000	5.700E+09	3.600E+09	5.700E+09
473.000	3.600E+09	2.300E+09	3.600E+09
523.000	5.700E+08	3.600E+08	5.700E+08
573.000	7.100E+07	4.500E+07	7.100E+07
623.000	7.100E+07	4.500E+07	7.100E+07
3273.000	7.100E+07	4.500E+07	7.100E+07

CHAR VOLUME = 3.000E-02

TEMPERATURE	XY	XZ	YZ
273.000	4.100E+09	2.600E+09	4.100E+09
298.000	4.100E+09	2.600E+09	4.100E+09
423.000	4.100E+09	2.600E+09	4.100E+09
473.000	2.900E+09	1.800E+09	2.900E+09
523.000	2.900E+08	1.800E+08	2.900E+08
573.000	7.100E+07	4.500E+07	7.100E+07
623.000	7.100E+07	4.500E+07	7.100E+07
3273.000	7.100E+07	4.500E+07	7.100E+07

CHAR VOLUME = 1.000E+00

TEMPERATURE	XY	XZ	YZ
273.000	7.100E+07	4.500E+07	7.100E+07
298.000	7.100E+07	4.500E+07	7.100E+07

423.000	7.100E+07	4.500E+07	7.100E+07
473.000	7.100E+07	4.500E+07	7.100E+07
523.000	7.100E+07	4.500E+07	7.100E+07
573.000	7.100E+07	4.500E+07	7.100E+07
623.000	7.100E+07	4.500E+07	7.100E+07
3273.000	7.100E+07	4.500E+07	7.100E+07

SHEAR MODULI OF DAMAGED MATERIAL-

CHAR VOLUME = 0.000E+00

TEMPERATURE	XY	XZ	YZ
273.000	6.000E+09	3.800E+09	6.000E+09
298.000	6.000E+09	3.800E+09	6.000E+09
423.000	6.000E+09	3.800E+09	6.000E+09
473.000	3.900E+09	2.500E+09	3.900E+09
523.000	7.100E+08	4.500E+08	7.100E+08
573.000	7.100E+07	4.500E+07	7.100E+07
623.000	7.100E+07	4.500E+07	7.100E+07
3273.000	7.100E+07	4.500E+07	7.100E+07

CHAR VOLUME = 5.000E-08

TEMPERATURE	XY	XZ	YZ
273.000	6.000E+09	3.800E+09	6.000E+09
298.000	6.000E+09	3.800E+09	6.000E+09
423.000	6.000E+09	3.800E+09	6.000E+09
473.000	3.900E+09	2.500E+09	3.900E+09
523.000	7.100E+08	4.500E+08	7.100E+08
573.000	7.100E+07	4.500E+07	7.100E+07
623.000	7.100E+07	4.500E+07	7.100E+07
3273.000	7.100E+07	4.500E+07	7.100E+07

CHAR VOLUME = 1.000E-05

TEMPERATURE	XY	XZ	YZ
273.000	6.000E+09	3.800E+09	6.000E+09
298.000	6.000E+09	3.800E+09	6.000E+09
423.000	6.000E+09	3.800E+09	6.000E+09
473.000	3.900E+09	2.500E+09	3.900E+09
523.000	7.100E+08	4.500E+08	7.100E+08
573.000	7.100E+07	4.500E+07	7.100E+07
623.000	7.100E+07	4.500E+07	7.100E+07
3273.000	7.100E+07	4.500E+07	7.100E+07

CHAR VOLUME = 1.000E-03

TEMPERATURE	XY	XZ	YZ
273.000	5.700E+09	3.600E+09	5.700E+09
298.000	5.700E+09	3.600E+09	5.700E+09
423.000	5.700E+09	3.600E+09	5.700E+09
473.000	3.600E+09	2.300E+09	3.600E+09
523.000	5.700E+08	3.600E+08	5.700E+08
573.000	7.100E+07	4.500E+07	7.100E+07
623.000	7.100E+07	4.500E+07	7.100E+07
3273.000	7.100E+07	4.500E+07	7.100E+07

CHAR VOLUME = 3.000E-02

TEMPERATURE	XY	XZ	YZ
273.000	4.100E+09	2.600E+09	4.100E+09
298.000	4.100E+09	2.600E+09	4.100E+09
423.000	4.100E+09	2.600E+09	4.100E+09
473.000	2.900E+09	1.800E+09	2.900E+09
523.000	2.900E+08	1.800E+08	2.900E+08
573.000	7.100E+07	4.500E+07	7.100E+07
623.000	7.100E+07	4.500E+07	7.100E+07
3273.000	7.100E+07	4.500E+07	7.100E+07

CHAR VOLUME = 1.000E+00

TEMPERATURE	XY	XZ	YZ
273.000	7.100E+07	4.500E+07	7.100E+07
298.000	7.100E+07	4.500E+07	7.100E+07
423.000	7.100E+07	4.500E+07	7.100E+07
473.000	7.100E+07	4.500E+07	7.100E+07
523.000	7.100E+07	4.500E+07	7.100E+07
573.000	7.100E+07	4.500E+07	7.100E+07
623.000	7.100E+07	4.500E+07	7.100E+07
3273.000	7.100E+07	4.500E+07	7.100E+07

THERMAL EXPANSION STRAIN OF UNDAMAGED MATERIAL-

CHAR VOLUME = 0.000E+00

TEMPERATURE	X	Y	Z
273.000	6.480E-05	-5.180E-03	-5.180E-03
298.000	5.580E-05	-4.460E-03	-4.460E-03
423.000	1.080E-05	-8.640E-04	-8.640E-04
473.000	-7.200E-06	5.760E-04	5.760E-04
523.000	-2.520E-05	2.020E-03	2.020E-03
573.000	-4.320E-05	3.460E-03	3.460E-03
623.000	-6.120E-05	4.900E-03	4.900E-03
3273.000	-1.020E-03	8.120E-02	8.120E-02

CHAR VOLUME = 5.000E-08

TEMPERATURE	X	Y	Z
273.000	6.480E-05	-5.180E-03	-5.180E-03
298.000	5.580E-05	-4.460E-03	-4.460E-03
423.000	1.080E-05	-8.640E-04	-8.640E-04
473.000	-7.200E-06	5.760E-04	5.760E-04
523.000	-2.520E-05	2.020E-03	2.020E-03
573.000	-4.320E-05	3.460E-03	3.460E-03
623.000	-6.120E-05	4.900E-03	4.900E-03
3273.000	-1.020E-03	8.120E-02	8.120E-02

CHAR VOLUME = 1.000E-05

TEMPERATURE	X	Y	Z
273.000	6.480E-05	-5.180E-03	-5.180E-03
298.000	5.580E-05	-4.460E-03	-4.460E-03
423.000	1.080E-05	-8.640E-04	-8.640E-04
473.000	-7.200E-06	5.760E-04	5.760E-04
523.000	-2.520E-05	2.020E-03	2.020E-03
573.000	-4.320E-05	3.460E-03	3.460E-03
623.000	-6.120E-05	4.900E-03	4.900E-03
3273.000	-1.020E-03	8.120E-02	8.120E-02

CHAR VOLUME = 1.000E-03

TEMPERATURE	X	Y	Z
273.000	6.480E-05	-5.180E-03	-5.180E-03
298.000	5.580E-05	-4.460E-03	-4.460E-03
423.000	1.080E-05	-8.640E-04	-8.640E-04
473.000	-7.200E-06	5.760E-04	5.760E-04
523.000	-2.520E-05	2.020E-03	2.020E-03
573.000	-4.320E-05	3.460E-03	3.460E-03
623.000	-6.120E-05	4.900E-03	4.900E-03
3273.000	-1.020E-03	8.120E-02	8.120E-02

CHAR VOLUME = 3.000E-02

TEMPERATURE	X	Y	Z
273.000	6.480E-05	-5.180E-03	-5.180E-03
298.000	5.580E-05	-4.460E-03	-4.460E-03
423.000	1.080E-05	-8.640E-04	-8.640E-04

473.000	-7.200E-06	5.760E-04	5.760E-04
523.000	-2.520E-05	2.020E-03	2.020E-03
573.000	-4.320E-05	3.460E-03	3.460E-03
623.000	-6.120E-05	4.900E-03	4.900E-03
3273.000	-1.020E-03	8.120E-02	8.120E-02

CHAR VOLUME = 1.000E+00

TEMPERATURE	X	Y	Z
273.000	6.480E-05	-5.180E-03	-5.180E-03
298.000	5.580E-05	-4.460E-03	-4.460E-03
423.000	1.080E-05	-8.640E-04	-8.640E-04
473.000	-7.200E-06	5.760E-04	5.760E-04
523.000	-2.520E-05	2.020E-03	2.020E-03
573.000	-4.320E-05	3.460E-03	3.460E-03
623.000	-6.120E-05	4.900E-03	4.900E-03
3273.000	-1.020E-03	8.120E-02	8.120E-02

THERMAL EXPANSION STRAIN OF DAMAGED MATERIAL-

CHAR VOLUME = 0.000E+00

TEMPERATURE	X	Y	Z
273.000	6.480E-05	-5.180E-03	-5.180E-03
298.000	5.580E-05	-4.460E-03	-4.460E-03
423.000	1.080E-05	-8.640E-04	-8.640E-04
473.000	-7.200E-06	5.760E-04	5.760E-04
523.000	-2.520E-05	2.020E-03	2.020E-03
573.000	-4.320E-05	3.460E-03	3.460E-03
623.000	-6.120E-05	4.900E-03	4.900E-03
3273.000	-1.020E-03	8.120E-02	8.120E-02

CHAR VOLUME = 5.000E-08

TEMPERATURE	X	Y	Z
273.000	6.480E-05	-5.180E-03	-5.180E-03
298.000	5.580E-05	-4.460E-03	-4.460E-03
423.000	1.080E-05	-8.640E-04	-8.640E-04
473.000	-7.200E-06	5.760E-04	5.760E-04
523.000	-2.520E-05	2.020E-03	2.020E-03
573.000	-4.320E-05	3.460E-03	3.460E-03
623.000	-6.120E-05	4.900E-03	4.900E-03
3273.000	-1.020E-03	8.120E-02	8.120E-02

CHAR VOLUME = 1.000E-05

TEMPERATURE	X	Y	Z
273.000	6.480E-05	-5.180E-03	-5.180E-03
298.000	5.580E-05	-4.460E-03	-4.460E-03
423.000	1.080E-05	-8.640E-04	-8.640E-04
473.000	-7.200E-06	5.760E-04	5.760E-04
523.000	-2.520E-05	2.020E-03	2.020E-03
573.000	-4.320E-05	3.460E-03	3.460E-03
623.000	-6.120E-05	4.900E-03	4.900E-03
3273.000	-1.020E-03	8.120E-02	8.120E-02

CHAR VOLUME = 1.000E-03

TEMPERATURE	X	Y	Z
273.000	6.480E-05	-5.180E-03	-5.180E-03
298.000	5.580E-05	-4.460E-03	-4.460E-03
423.000	1.080E-05	-8.640E-04	-8.640E-04
473.000	-7.200E-06	5.760E-04	5.760E-04
523.000	-2.520E-05	2.020E-03	2.020E-03
573.000	-4.320E-05	3.460E-03	3.460E-03
623.000	-6.120E-05	4.900E-03	4.900E-03
3273.000	-1.020E-03	8.120E-02	8.120E-02

CHAR VOLUME = 3.000E-02

TEMPERATURE	X	Y	Z
273.000	6.480E-05	-5.180E-03	-5.180E-03
298.000	5.580E-05	-4.460E-03	-4.460E-03
423.000	1.080E-05	-8.640E-04	-8.640E-04
473.000	-7.200E-06	5.760E-04	5.760E-04
523.000	-2.520E-05	2.020E-03	2.020E-03
573.000	-4.320E-05	3.460E-03	3.460E-03
623.000	-6.120E-05	4.900E-03	4.900E-03
3273.000	-1.020E-03	8.120E-02	8.120E-02

CHAR VOLUME = 1.000E+00

TEMPERATURE	X	Y	Z
273.000	6.480E-05	-5.180E-03	-5.180E-03
298.000	5.580E-05	-4.460E-03	-4.460E-03
423.000	1.080E-05	-8.640E-04	-8.640E-04
473.000	-7.200E-06	5.760E-04	5.760E-04
523.000	-2.520E-05	2.020E-03	2.020E-03
573.000	-4.320E-05	3.460E-03	3.460E-03
623.000	-6.120E-05	4.900E-03	4.900E-03
3273.000	-1.020E-03	8.120E-02	8.120E-02

MOISTURE EXPANSION COEFFICIENTS OF UNDAMAGED MATERIAL-

CHAR VOLUME	X	Y	Z
0.000	0.000E+00	0.000E+00	0.000E+00
0.000	0.000E+00	0.000E+00	0.000E+00
0.000	0.000E+00	0.000E+00	0.000E+00
0.001	0.000E+00	0.000E+00	0.000E+00
0.030	0.000E+00	0.000E+00	0.000E+00
1.000	0.000E+00	0.000E+00	0.000E+00

MOISTURE EXPANSION COEFFICIENTS OF UNDAMAGED MATERIAL-

CHAR VOLUME	X	Y	Z
0.000	0.000E+00	0.000E+00	0.000E+00
0.000	0.000E+00	0.000E+00	0.000E+00
0.000	0.000E+00	0.000E+00	0.000E+00
0.001	0.000E+00	0.000E+00	0.000E+00
0.030	0.000E+00	0.000E+00	0.000E+00
1.000	0.000E+00	0.000E+00	0.000E+00

CHAR EXPANSION STRAIN OF UNDAMAGED MATERIAL-

CHAR VOLUME	X	Y	Z
0.000	0.000E+00	0.000E+00	0.000E+00
0.000	0.000E+00	0.000E+00	0.000E+00
0.000	0.000E+00	0.000E+00	0.000E+00
0.001	0.000E+00	0.000E+00	0.000E+00
0.030	0.000E+00	0.000E+00	0.000E+00
1.000	0.000E+00	0.000E+00	0.000E+00

CHAR EXPANSION STRAIN OF UNDAMAGED MATERIAL-

CHAR VOLUME	X	Y	Z
0.000	0.000E+00	0.000E+00	0.000E+00
0.000	0.000E+00	0.000E+00	0.000E+00
0.000	0.000E+00	0.000E+00	0.000E+00
0.001	0.000E+00	0.000E+00	0.000E+00
0.030	0.000E+00	0.000E+00	0.000E+00
1.000	0.000E+00	0.000E+00	0.000E+00

PRESSURE COMPLIANCE OF UNDAMAGED MATERIAL-

CHAR VOLUME = 0.000E+00

TEMPERATURE	X	Y	Z
273.000	0.000E+00	0.000E+00	0.000E+00
298.000	0.000E+00	0.000E+00	0.000E+00
423.000	0.000E+00	0.000E+00	0.000E+00
473.000	0.000E+00	0.000E+00	0.000E+00
523.000	0.000E+00	0.000E+00	0.000E+00
573.000	0.000E+00	0.000E+00	0.000E+00
623.000	0.000E+00	0.000E+00	0.000E+00
3273.000	0.000E+00	0.000E+00	0.000E+00

CHAR VOLUME = 5.000E-08

TEMPERATURE	X	Y	Z
273.000	0.000E+00	0.000E+00	0.000E+00
298.000	0.000E+00	0.000E+00	0.000E+00
423.000	0.000E+00	0.000E+00	0.000E+00
473.000	0.000E+00	0.000E+00	0.000E+00
523.000	0.000E+00	0.000E+00	0.000E+00
573.000	0.000E+00	0.000E+00	0.000E+00
623.000	0.000E+00	0.000E+00	0.000E+00
3273.000	0.000E+00	0.000E+00	0.000E+00

CHAR VOLUME = 1.000E-05

TEMPERATURE	X	Y	Z
273.000	0.000E+00	0.000E+00	0.000E+00
298.000	0.000E+00	0.000E+00	0.000E+00
423.000	0.000E+00	0.000E+00	0.000E+00
473.000	0.000E+00	0.000E+00	0.000E+00
523.000	0.000E+00	0.000E+00	0.000E+00
573.000	0.000E+00	0.000E+00	0.000E+00
623.000	0.000E+00	0.000E+00	0.000E+00
3273.000	0.000E+00	0.000E+00	0.000E+00

CHAR VOLUME = 1.000E-03

TEMPERATURE	X	Y	Z
273.000	0.000E+00	0.000E+00	0.000E+00
298.000	0.000E+00	0.000E+00	0.000E+00
423.000	0.000E+00	0.000E+00	0.000E+00
473.000	0.000E+00	0.000E+00	0.000E+00
523.000	0.000E+00	0.000E+00	0.000E+00
573.000	0.000E+00	0.000E+00	0.000E+00
623.000	0.000E+00	0.000E+00	0.000E+00
3273.000	0.000E+00	0.000E+00	0.000E+00

CHAR VOLUME = 3.000E-02

TEMPERATURE	X	Y	Z
273.000	0.000E+00	0.000E+00	0.000E+00
298.000	0.000E+00	0.000E+00	0.000E+00
423.000	0.000E+00	0.000E+00	0.000E+00
473.000	0.000E+00	0.000E+00	0.000E+00
523.000	0.000E+00	0.000E+00	0.000E+00
573.000	0.000E+00	0.000E+00	0.000E+00
623.000	0.000E+00	0.000E+00	0.000E+00
3273.000	0.000E+00	0.000E+00	0.000E+00

CHAR VOLUME = 1.000E+00

TEMPERATURE	X	Y	Z
273.000	0.000E+00	0.000E+00	0.000E+00
298.000	0.000E+00	0.000E+00	0.000E+00
423.000	0.000E+00	0.000E+00	0.000E+00
473.000	0.000E+00	0.000E+00	0.000E+00
523.000	0.000E+00	0.000E+00	0.000E+00

573.000	0.000E+00	0.000E+00	0.000E+00
623.000	0.000E+00	0.000E+00	0.000E+00
3273.000	0.000E+00	0.000E+00	0.000E+00

PRESSURE COMPLIANCE OF DAMAGED MATERIAL-

CHAR VOLUME = 0.000E+00

TEMPERATURE	X	Y	Z
273.000	0.000E+00	0.000E+00	0.000E+00
298.000	0.000E+00	0.000E+00	0.000E+00
423.000	0.000E+00	0.000E+00	0.000E+00
473.000	0.000E+00	0.000E+00	0.000E+00
523.000	0.000E+00	0.000E+00	0.000E+00
573.000	0.000E+00	0.000E+00	0.000E+00
623.000	0.000E+00	0.000E+00	0.000E+00
3273.000	0.000E+00	0.000E+00	0.000E+00

CHAR VOLUME = 5.000E-08

TEMPERATURE	X	Y	Z
273.000	0.000E+00	0.000E+00	0.000E+00
298.000	0.000E+00	0.000E+00	0.000E+00
423.000	0.000E+00	0.000E+00	0.000E+00
473.000	0.000E+00	0.000E+00	0.000E+00
523.000	0.000E+00	0.000E+00	0.000E+00
573.000	0.000E+00	0.000E+00	0.000E+00
623.000	0.000E+00	0.000E+00	0.000E+00
3273.000	0.000E+00	0.000E+00	0.000E+00

CHAR VOLUME = 1.000E-05

TEMPERATURE	X	Y	Z
273.000	0.000E+00	0.000E+00	0.000E+00
298.000	0.000E+00	0.000E+00	0.000E+00
423.000	0.000E+00	0.000E+00	0.000E+00
473.000	0.000E+00	0.000E+00	0.000E+00
523.000	0.000E+00	0.000E+00	0.000E+00
573.000	0.000E+00	0.000E+00	0.000E+00
623.000	0.000E+00	0.000E+00	0.000E+00
3273.000	0.000E+00	0.000E+00	0.000E+00

CHAR VOLUME = 1.000E-03

TEMPERATURE	X	Y	Z
273.000	0.000E+00	0.000E+00	0.000E+00
298.000	0.000E+00	0.000E+00	0.000E+00
423.000	0.000E+00	0.000E+00	0.000E+00
473.000	0.000E+00	0.000E+00	0.000E+00
523.000	0.000E+00	0.000E+00	0.000E+00
573.000	0.000E+00	0.000E+00	0.000E+00
623.000	0.000E+00	0.000E+00	0.000E+00
3273.000	0.000E+00	0.000E+00	0.000E+00

CHAR VOLUME = 3.000E-02

TEMPERATURE	X	Y	Z
273.000	0.000E+00	0.000E+00	0.000E+00
298.000	0.000E+00	0.000E+00	0.000E+00
423.000	0.000E+00	0.000E+00	0.000E+00
473.000	0.000E+00	0.000E+00	0.000E+00
523.000	0.000E+00	0.000E+00	0.000E+00
573.000	0.000E+00	0.000E+00	0.000E+00
623.000	0.000E+00	0.000E+00	0.000E+00
3273.000	0.000E+00	0.000E+00	0.000E+00

CHAR VOLUME = 1.000E+00

TEMPERATURE	X	Y	Z

273.000	0.000E+00	0.000E+00	0.000E+00
298.000	0.000E+00	0.000E+00	0.000E+00
423.000	0.000E+00	0.000E+00	0.000E+00
473.000	0.000E+00	0.000E+00	0.000E+00
523.000	0.000E+00	0.000E+00	0.000E+00
573.000	0.000E+00	0.000E+00	0.000E+00
623.000	0.000E+00	0.000E+00	0.000E+00
3273.000	0.000E+00	0.000E+00	0.000E+00

PRESSURE-STRESS COUPLING FACTOR OF UNDAMAGED MATERIAL-

CHAR VOLUME	X	Y	Z
0.000	1.000E+00	1.000E+00	1.000E+00
0.000	1.000E+00	1.000E+00	1.000E+00
0.000	1.000E+00	1.000E+00	1.000E+00
0.001	1.000E+00	1.000E+00	1.000E+00
0.030	1.000E+00	1.000E+00	1.000E+00
1.000	1.000E+00	1.000E+00	1.000E+00

PRESSURE-STRESS COUPLING FACTOR OF DAMAGED MATERIAL-

CHAR VOLUME	X	Y	Z
0.000	1.000E+00	1.000E+00	1.000E+00
0.000	1.000E+00	1.000E+00	1.000E+00
0.000	1.000E+00	1.000E+00	1.000E+00
0.001	1.000E+00	1.000E+00	1.000E+00
0.030	1.000E+00	1.000E+00	1.000E+00
1.000	1.000E+00	1.000E+00	1.000E+00

TENSILE STRENGTH OF UNDAMAGED MATERIAL-

CHAR VOLUME = 0.000E+00

TEMPERATURE	X	Y	Z
273.000	2.000E+09	5.520E+07	5.520E+07
298.000	2.000E+09	5.520E+07	5.520E+07
423.000	2.000E+09	4.400E+07	4.400E+07
473.000	1.800E+09	1.300E+07	1.300E+07
523.000	1.650E+09	4.000E+06	4.000E+06
573.000	1.500E+09	1.000E+05	1.000E+05
623.000	1.350E+09	1.000E+05	1.000E+05
3273.000	1.200E+09	1.000E+05	1.000E+05

CHAR VOLUME = 5.000E-08

TEMPERATURE	X	Y	Z
273.000	2.000E+09	5.520E+07	5.520E+07
298.000	2.000E+09	5.520E+07	5.520E+07
423.000	2.000E+09	4.400E+07	4.400E+07
473.000	1.800E+09	1.300E+07	1.300E+07
523.000	1.650E+09	4.000E+06	4.000E+06
573.000	1.500E+09	1.000E+05	1.000E+05
623.000	1.350E+09	1.000E+05	1.000E+05
3273.000	1.200E+09	1.000E+05	1.000E+05

CHAR VOLUME = 1.000E-05

TEMPERATURE	X	Y	Z
273.000	2.000E+09	5.520E+07	5.520E+07
298.000	2.000E+09	5.520E+07	5.520E+07
423.000	2.000E+09	4.400E+07	4.400E+07
473.000	1.800E+09	1.300E+07	1.300E+07
523.000	1.650E+09	4.000E+06	4.000E+06
573.000	1.500E+09	1.000E+05	1.000E+05
623.000	1.350E+09	1.000E+05	1.000E+05
3273.000	1.200E+09	1.000E+05	1.000E+05

CHAR VOLUME = 1.000E-03

TEMPERATURE	X	Y	Z
273.000	1.800E+09	4.000E+07	4.000E+07
298.000	1.800E+09	4.000E+07	4.000E+07
423.000	1.800E+09	3.200E+07	3.200E+07
473.000	1.620E+09	9.400E+06	9.400E+06
523.000	1.400E+09	2.900E+06	2.900E+06
573.000	1.200E+09	1.000E+05	1.000E+05
623.000	1.200E+09	1.000E+05	1.000E+05
3273.000	1.080E+09	1.000E+05	1.000E+05

CHAR VOLUME = 3.000E-02

TEMPERATURE	X	Y	Z
273.000	1.200E+09	1.700E+06	1.700E+06
298.000	1.200E+09	1.700E+06	1.700E+06
423.000	1.200E+09	1.300E+06	1.300E+06
473.000	1.080E+09	4.000E+05	4.000E+05
523.000	9.900E+08	1.000E+05	1.000E+05
573.000	9.000E+09	1.000E+05	1.000E+05
623.000	8.100E+08	1.000E+05	1.000E+05
3273.000	7.500E+08	1.000E+05	1.000E+05

CHAR VOLUME = 1.000E+00

TEMPERATURE	X	Y	Z
273.000	8.750E+08	1.000E+05	1.000E+05
298.000	8.750E+08	1.000E+05	1.000E+05
423.000	8.750E+08	1.000E+05	1.000E+05
473.000	8.500E+08	1.000E+05	1.000E+05
523.000	8.100E+08	1.000E+05	1.000E+05
573.000	8.100E+08	1.000E+05	1.000E+05
623.000	8.100E+08	1.000E+05	1.000E+05
3273.000	7.500E+08	1.000E+05	1.000E+05

COMPRESSIVE STRENGTH OF UNDAMAGED MATERIAL-

CHAR VOLUME = 0.000E+00

TEMPERATURE	X	Y	Z
273.000	2.000E+09	5.520E+07	5.520E+07
298.000	2.000E+09	5.520E+07	5.520E+07
423.000	1.590E+09	4.400E+07	4.400E+07
473.000	4.710E+08	1.300E+07	1.300E+07
523.000	1.450E+08	4.000E+06	4.000E+06
573.000	2.170E+07	1.000E+05	1.000E+05
623.000	3.620E+06	1.000E+05	1.000E+05
3273.000	3.620E+06	1.000E+05	1.000E+05

CHAR VOLUME = 5.000E-08

TEMPERATURE	X	Y	Z
273.000	2.000E+09	5.520E+07	5.520E+07
298.000	2.000E+09	5.520E+07	5.520E+07
423.000	1.590E+09	4.400E+07	4.400E+07
473.000	4.710E+08	1.300E+07	1.300E+07
523.000	1.450E+08	4.000E+06	4.000E+06
573.000	2.170E+07	1.000E+05	1.000E+05
623.000	3.620E+06	1.000E+05	1.000E+05
3273.000	3.620E+06	1.000E+05	1.000E+05

CHAR VOLUME = 1.000E-05

TEMPERATURE	X	Y	Z
273.000	2.000E+09	5.520E+07	5.520E+07
298.000	2.000E+09	5.520E+07	5.520E+07
423.000	1.590E+09	4.400E+07	4.400E+07

473.000	4.710E+08	1.300E+07	1.300E+07
523.000	1.450E+08	4.000E+06	4.000E+06
573.000	2.170E+07	1.000E+05	1.000E+05
623.000	3.620E+06	1.000E+05	1.000E+05
3273.000	3.620E+06	1.000E+05	1.000E+05

CHAR VOLUME = 1.000E-03

TEMPERATURE	X	Y	Z
273.000	1.450E+09	4.000E+07	4.000E+07
298.000	1.450E+09	4.000E+07	4.000E+07
423.000	1.160E+09	3.200E+07	3.200E+07
473.000	3.410E+08	9.400E+06	9.400E+06
523.000	1.050E+08	2.900E+06	2.900E+06
573.000	1.450E+07	1.000E+05	1.000E+05
623.000	3.620E+06	1.000E+05	1.000E+05
3273.000	3.620E+06	1.000E+05	1.000E+05

CHAR VOLUME = 3.000E-02

TEMPERATURE	X	Y	Z
273.000	6.160E+07	1.700E+06	1.700E+06
298.000	6.160E+07	1.700E+06	1.700E+06
423.000	4.710E+07	1.300E+06	1.300E+06
473.000	1.450E+07	4.000E+05	4.000E+05
523.000	3.620E+06	1.000E+05	1.000E+05
573.000	3.620E+06	1.000E+05	1.000E+05
623.000	3.620E+06	1.000E+05	1.000E+05
3273.000	3.620E+06	1.000E+05	1.000E+05

CHAR VOLUME = 1.000E+00

TEMPERATURE	X	Y	Z
273.000	3.620E+06	1.000E+05	1.000E+05
298.000	3.620E+06	1.000E+05	1.000E+05
423.000	3.620E+06	1.000E+05	1.000E+05
473.000	3.620E+06	1.000E+05	1.000E+05
523.000	3.620E+06	1.000E+05	1.000E+05
573.000	3.620E+06	1.000E+05	1.000E+05
623.000	3.620E+06	1.000E+05	1.000E+05
3273.000	3.620E+06	1.000E+05	1.000E+05

SHEAR STRENGTH OF UNDAMAGED MATERIAL-

CHAR VOLUME = 0.000E+00

TEMPERATURE	XY	XZ	YZ
273.000	1.050E+08	1.050E+08	1.050E+08
298.000	1.050E+08	1.050E+08	1.050E+08
423.000	8.370E+07	8.370E+07	8.370E+07
473.000	2.470E+07	2.470E+07	2.470E+07
523.000	7.610E+06	7.610E+06	7.610E+06
573.000	1.140E+06	1.140E+06	1.140E+06
623.000	1.900E+05	1.900E+05	1.900E+05
3273.000	1.900E+05	1.900E+05	1.900E+05

CHAR VOLUME = 5.000E-08

TEMPERATURE	XY	XZ	YZ
273.000	1.050E+08	1.050E+08	1.050E+08
298.000	1.050E+08	1.050E+08	1.050E+08
423.000	8.370E+07	8.370E+07	8.370E+07
473.000	2.470E+07	2.470E+07	2.470E+07
523.000	7.610E+06	7.610E+06	7.610E+06
573.000	1.140E+06	1.140E+06	1.140E+06
623.000	1.900E+05	1.900E+05	1.900E+05
3273.000	1.900E+05	1.900E+05	1.900E+05

CHAR VOLUME = 1.000E-05

TEMPERATURE	XY	XZ	YZ
273.000	1.050E+08	1.050E+08	1.050E+08
298.000	1.050E+08	1.050E+08	1.050E+08
423.000	8.370E+07	8.370E+07	8.370E+07
473.000	2.470E+07	2.470E+07	2.470E+07
523.000	7.610E+06	7.610E+06	7.610E+06
573.000	1.140E+06	1.140E+06	1.140E+06
623.000	1.900E+05	1.900E+05	1.900E+05
3273.000	1.900E+05	1.900E+05	1.900E+05

CHAR VOLUME = 1.000E-03

TEMPERATURE	XY	XZ	YZ
273.000	7.610E+07	7.610E+07	7.610E+07
298.000	7.610E+07	7.610E+07	7.610E+07
423.000	6.090E+07	6.090E+07	6.090E+07
473.000	1.790E+07	1.790E+07	1.790E+07
523.000	5.520E+06	5.520E+06	5.520E+06
573.000	7.610E+05	7.610E+05	7.610E+05
623.000	1.900E+05	1.900E+05	1.900E+05
3273.000	1.900E+05	1.900E+05	1.900E+05

CHAR VOLUME = 3.000E-02

TEMPERATURE	XY	XZ	YZ
273.000	3.230E+06	3.230E+06	3.230E+06
298.000	3.230E+06	3.230E+06	3.230E+06
423.000	2.470E+06	2.470E+06	2.470E+06
473.000	7.610E+05	7.610E+05	7.610E+05
523.000	1.900E+05	1.900E+05	1.900E+05
573.000	1.900E+05	1.900E+05	1.900E+05
623.000	1.900E+05	1.900E+05	1.900E+05
3273.000	1.900E+05	1.900E+05	1.900E+05

CHAR VOLUME = 1.000E+00

TEMPERATURE	XY	XZ	YZ
273.000	1.900E+05	1.900E+05	1.900E+05
298.000	1.900E+05	1.900E+05	1.900E+05
423.000	1.900E+05	1.900E+05	1.900E+05
473.000	1.900E+05	1.900E+05	1.900E+05
523.000	1.900E+05	1.900E+05	1.900E+05
573.000	1.900E+05	1.900E+05	1.900E+05
623.000	1.900E+05	1.900E+05	1.900E+05
3273.000	1.900E+05	1.900E+05	1.900E+05

********** VOLATILE PROPERTIES **********

NUMBER OF TEMPERATURES AT WHICH VOLATILE
SPECIFIC HEAT IS SPECIFIED = 2

VOLATILE SPECIFIC HEATS-

TEMPERATURE	SPECIFIC HEAT
0.000	2.0000E+03
3000.000	2.0000E+03

NUMBER OF TEMPERATURES AT WHICH VOLATILE
VISCOSITY IS SPECIFIED = 2

VOLATILE VISCOSITIES-

TEMPERATURE	VISCOSITY
0.000	7.9750E-06
3000.000	8.2975E-05

```
VOLATILE MOLECULAR WEIGHT  = 2.522E-44

****************************  REACTIONS  ****************************

CHARRING REACTION IS TEMPERATURE DEPENDENT

ACTIVATION ENERGY      1.8500E+08
RATE CONSTANT          3.9000E+12
REACTION ORDER         1.0000E+00

HEAT OF REACTION IS CONSTANT
HEAT OF REACTION =  -2.3400E+05
```

APPENDIX G

SHEAR AND COMPRESSION MATERIAL PROPERTY MODELS

A full set of property models for other mechanical material properties not measured in the course of this investigation, including shear properties and compressive strengths, can be constructed from the models in Figures 6.35 through 6.38 based on observed trends. Data from previous work, presented in Chapter 2, shows that shear modulus and shear strength exhibit the same temperature dependence as transverse properties: both drop significantly at temperatures around 200°C. Since shear properties of graphite/epoxy plies, like transverse properties, are very sensitive to the condition of the epoxy matrix, it is reasonable to assume that conditions that cause a decrease in transverse modulus or strength will cause a similar drop in shear modulus or strength. The temperature- and degradation-dependence of shear properties are therefore modeled using scaled versions of the transverse property models in Figures 6.35 and 6.36. The models in Figures 6.35 and 6.36 are scaled by the baseline shear properties of graphite/epoxy given in Table 6.6. Conditions that cause a 25% drop in transverse modulus are modeled as causing a 25% drop in shear modulus, and so on. The shear models appear in Figures G.1 and G.2.

Similarly, models of the temperature and degradation dependencies of the transverse and longitudinal compressive strengths of graphite/epoxy can be developed. Transverse compressive strength, like all other transverse properties, is dominated by the

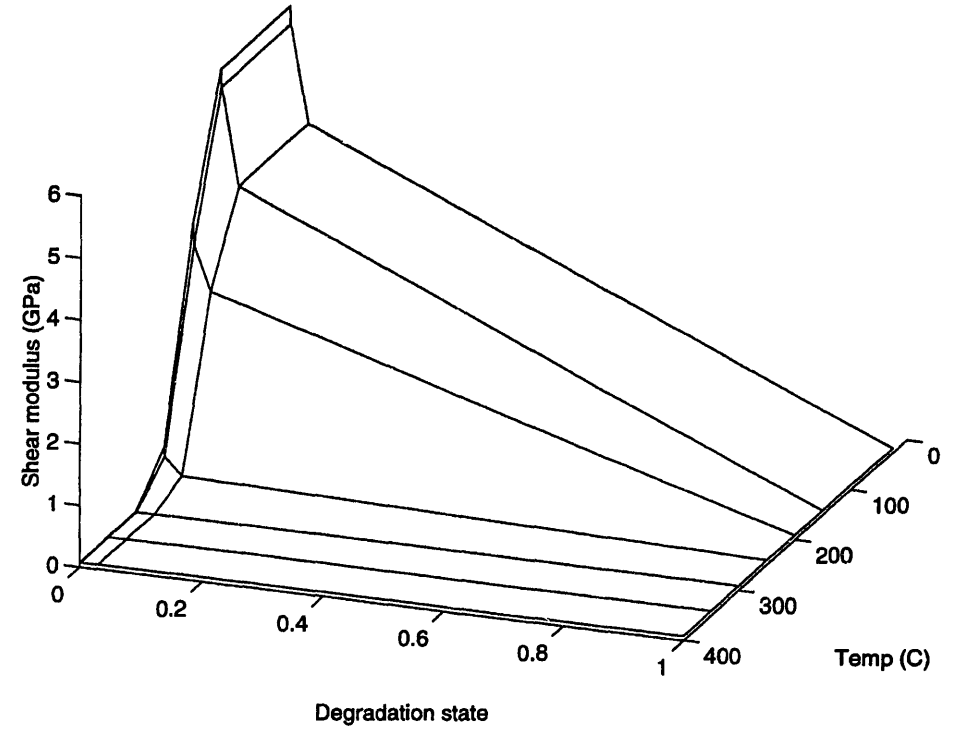

Figure G.1 Shear modulus model

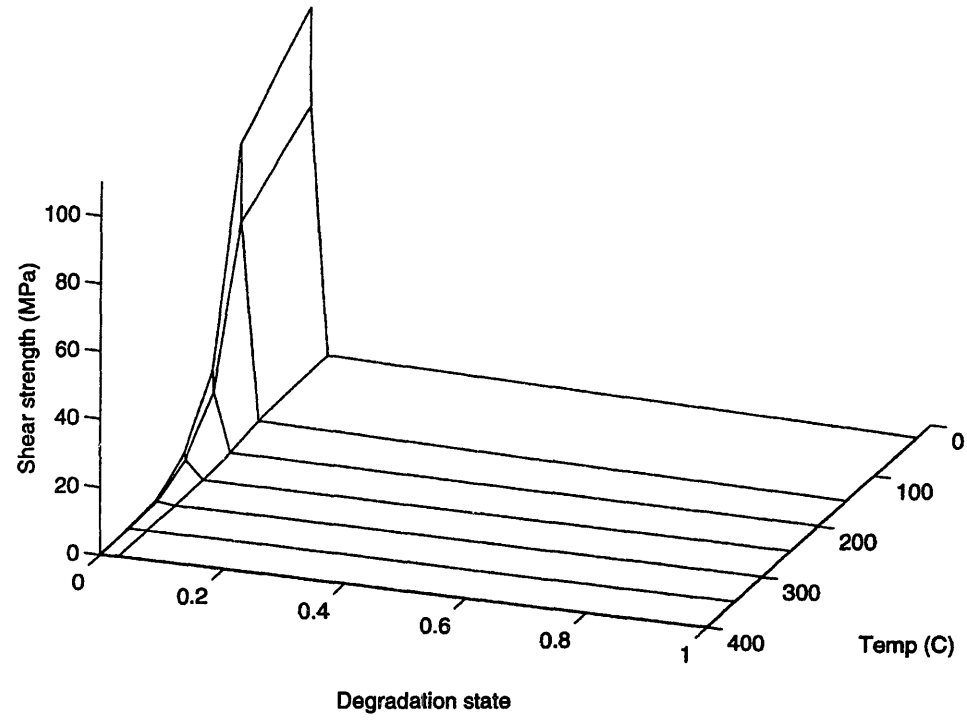

Figure G.2 Shear strength model

properties of the epoxy matrix. It is therefore reasonable to model the temperature- and degradation dependence of this property using a scaled version of the transverse tensile strength model. The model in Figure 6.36 is scaled by the nominal value of transverse compressive strength cited in Table 6.6, and the resulting transverse compressive strength model is plotted in Figure G.3.

It was noted in Chapter 2 that longitudinal compressive strength is sensitive to matrix degradation. For example, Frame, et al. [36] found that compressive strength dropped by 90% following a one-hour exposure at 287°C. The degradation state resulting from this exposure, as calculated from the degradation model developed in this work, would be 0.08. While the properties of the graphite fibers dominate trends in longitudinal tensile strength, the loss in compressive longitudinal strength is due to the fact that matrix loss makes it difficult for the degradation-insensitive fibers to support compressive loads. This loss in strength with increasing degradation is similar to the loss in transverse tensile strength. Compressive longitudinal strength is therefore modeled using a scaled version of the transverse tensile strength model in Figure 6.36. The model is scaled by the baseline longitudinal compressive strength cited in Table 6.6, and the resulting longitudinal compressive model is plotted in Figure G.4.

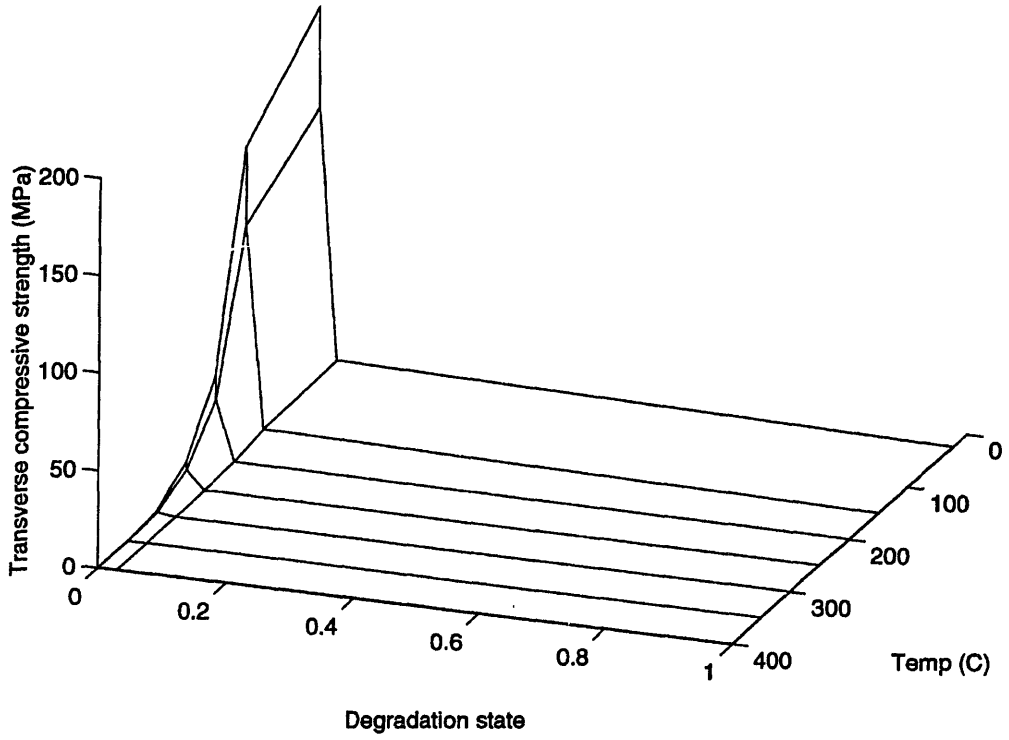

Figure G.3 Transverse compressive strength model

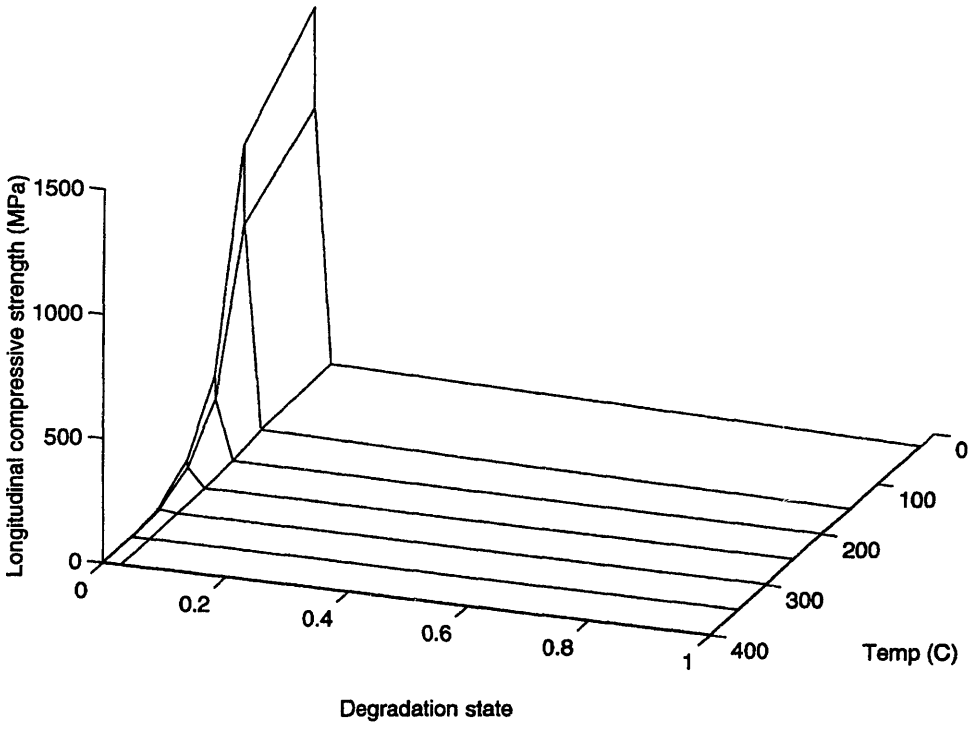

Figure G.4 Longitudinal compressive strength model.